

University of Southampton Research Repository ePrints Soton

Copyright © and Moral Rights for this thesis are retained by the author and/or other copyright owners. A copy can be downloaded for personal non-commercial research or study, without prior permission or charge. This thesis cannot be reproduced or quoted extensively from without first obtaining permission in writing from the copyright holder/s. The content must not be changed in any way or sold commercially in any format or medium without the formal permission of the copyright holders.

When referring to this work, full bibliographic details including the author, title, awarding institution and date of the thesis must be given e.g.

AUTHOR (year of submission) "Full thesis title", University of Southampton, name of the University School or Department, PhD Thesis, pagination

UNIVERSITY OF SOUTHAMPTON

FACULTY OF NATURAL AND ENVIRONMENTAL SCIENCES

Chemistry

**Chalcogenoether Complexes with Group 13 Halides and Development of Single
Source Precursors for Chemical Vapour Deposition of III-V and III-VI Thin Films**

by

Kathryn George

Thesis for the degree of Doctor of Philosophy

September 2013

UNIVERSITY OF SOUTHAMPTON

ABSTRACT

FACULTY OF NATURAL AND ENVIRONMENTAL SCIENCES

Chemistry

Thesis for the degree of Doctor of Philosophy

CHALCOGENOETHER COMPLEXES WITH GROUP 13 HALIDES AND DEVELOPMENT OF SINGLE SOURCE PRECURSORS FOR CHEMICAL VAPOUR DEPOSITION OF III-V AND III-VI THIN FILMS

Kathryn George

GaCl₃ can react with macrocyclic thio- and seleno-ethers to give complexes with coordination numbers and geometries that were previously not accessible by using acyclic chalcogenoether ligands. [MCl₂([16]aneE₄)] [MCl₄] (M = Ga, In; E = S, Se) exhibit distorted octahedral geometry at M, whereas [GaCl₃([14]aneS₄)] is the first example of trigonal bipyramidal coordination at Ga with three planar chlorides. GaCl₃ was also found to promote the one and two electron oxidation of [8]aneSe₂ to [{"8]aneSe₂}₂][GaCl₄]₂ and [{"8]aneSe₂Cl}][GaCl₄].

The coordination complexes [GaCl₃(ⁿBu₂E)] and (GaCl₃)₂{ⁿBuE(CH₂)_nEⁿBu} (E = Se, n = 2; E = Te, n = 3) have been found to be effective single source precursors for the LPCVD of Ga₂E₃ at 773 K. The films were shown to be stoichiometric and have low levels of impurities by EDX. It is possible to preferentially deposit Ga₂Te₃ onto TiN rather than SiO₂. This is the first reported example of a precursor based on a telluroether and the first single source precursor to deposit single phase Ga₂Te₃.

[Ga(SⁱPr)₂(μ-SⁱPr)]₂ can be used to deposit cubic Ga₂S₃ at 723 K, which can be annealed to give monoclinic Ga₂S₃. *In situ* XRD shows that the phase transition occurs between 773 and 873 K. The phase change also causes a change in the resistivity of the thin film. It is also possible to induce a phase change by laser annealing. Microfocus XRD and subsequent phase refinement was used to quantify the percentage conversion to the monoclinic phase, with higher laser powers giving a higher fraction of the monoclinic phase.

The reaction of AlX₃ (X = Cl, Br, I) with acyclic chalcogenoethers yielded a range of coordination numbers and geometries. [AlX₃(Me₂E)] (E = S, Se, Te) had distorted tetrahedral coordination at Al; [AlCl₃(MeC(CH₂SMe)₃)] formed a 1D chain polymer with trigonal bipyramidal coordination; [AlX₂(MeECH₂CH₂EMe)₂][AlX₄] exhibited 6-coordinate Al. The reaction of AlCl₃ with macrocyclic ligands formed [AlCl₃([9]aneS₃)], [AlCl₂([14]aneS₄)][AlCl₄] and [AlCl₂([16]aneSe₄)][AlCl₄]. All complexes were very air and moisture sensitive and AlCl₃ was found to promote the formation of selenonium and telluronium species. [AlCl₃(ⁿBu₂E)] (E = Se, Te) were found to be unsuitable precursors for LPCVD of aluminium chalcogenide thin films.

[ⁿBu₂Ga(μ-EⁿBu)₂GaⁿBu₂] (E = P, As) were used to deposit thin films of GaP and GaAs *via* LPCVD. The films were crystalline and had low levels of C and O contamination. The thin films of GaP were found to exhibit photoluminescence comparable to that of a single crystal reference, whereas GaAs exhibited some sub-band gap luminescence. [Ga(PⁿBu)₃] was investigated as a single source precursor but was found to be unsuitable due to poor volatility.

Contents

List of tables.....	vii
List of figures.....	ix
Declaration of authorship.....	xv
Acknowledgements.....	xvii
Definitions and abbreviations.....	xix
Chapter 1 – Introduction.....	1
1.1 III-V and III-VI thin films.....	1
1.2 Thin film deposition.....	5
1.2.1 Physical vapour deposition.....	5
1.2.2 Atomic layer deposition.....	6
1.2.3 Molecular beam epitaxy.....	6
1.2.4 Chemical vapour deposition.....	7
1.3 Coordination chemistry of Group 13 metals.....	11
1.3.1 Coordination chemistry of aluminium halides.....	11
1.3.2 Coordination chemistry of gallium halides.....	13
1.3.3 Coordination chemistry of indium halides.....	17
1.4 Chalcogenoether synthesis.....	25
1.5 Characterisation of coordination complexes.....	27
1.5.1 Nuclear magnetic resonance spectroscopy.....	27
1.5.2 Vibrational spectroscopy.....	28
1.5.3 Single crystal X-ray diffraction.....	30
1.6 Thin film characterisation.....	33
1.6.1 Thin film X-ray diffraction.....	33
1.6.2 Raman spectroscopy.....	34
1.6.3 X-ray photoelectron spectroscopy.....	35
1.6.4 Scanning electron microscopy and energy dispersive X-ray spectroscopy...35	
1.6.5 Atomic force microscopy.....	36

1.6.6 Photoluminescence.....	37
1.6.7 Electronic characterisation.....	38
1.7 References.....	41
Chapter 2 – Coordination Complexes of Gallium and Indium Trichloride with Thio- and Selenoether Macrocycles.....	51
2.1 Introduction.....	51
2.1.1 Macrocycle synthesis.....	51
2.1.2 Thioether and selenoether macrocyclic p-block complexes.....	55
2.2 Results and discussion.....	59
2.2.1 Cyclic diselenoether ligand complexes.....	59
2.2.2 Tetrathioether and tetraselenoether macrocyclic ligand complexes.....	64
2.2.3 Conclusions.....	72
2.3 Experimental.....	73
2.4 References.....	79
Chapter 3 – Low Pressure Chemical Vapour Deposition of Gallium Selenide and Gallium Telluride Thin Films.....	83
3.1 Introduction.....	83
3.1.1 Single source precursors for III-VI materials.....	84
3.2 Results and discussion.....	87
3.2.1 Synthesis and characterisation of precursors.....	87
3.2.2 Deposition and characterisation of gallium selenide thin films.....	90
3.2.3 Deposition and characterisation of gallium telluride thin films.....	94
3.2.4 Hall measurements.....	98
3.2.5 Selective deposition.....	99
3.2.6 Attempted LPCVD of gallium sulfide.....	100
3.2.7 Conclusions.....	102
3.3 Experimental.....	103

3.4 References.....	109
Chapter 4 – Chemical Vapour Deposition of Gallium Sulfide.....	113
4.1 Introduction.....	113
4.1.1 Properties of gallium sulfide.....	113
4.1.2 Structure of Ga ₂ S ₃	114
4.1.3 CVD of gallium sulfide.....	116
4.2 Results and discussion.....	119
4.2.1 Precursor synthesis.....	119
4.2.2 Thin film deposition and characterisation.....	120
4.2.3 [Ga(S ^t Bu) ₂ (μ-S ^t Bu)] ₂	126
4.2.4 Microfocus XRD experiments.....	126
4.2.5 Conclusions.....	132
4.3 Experimental.....	133
4.4 References.....	135
Chapter 5 – Coordination Complexes of Aluminium Halides with Acyclic and Macrocyclic Chalcogenoethers.....	137
5.1 Introduction.....	137
5.1.1 Uses of aluminium compounds.....	137
5.1.2 Coordination complexes with macrocycles.....	138
5.2 Results and discussion.....	141
5.2.1 Complexes with monodentate ligands.....	142
5.2.2 Complexes with bi- and tri- dentate ligands.....	148
5.2.3 Complexes with macrocyclic ligands.....	160
5.2.4 Chemical vapour deposition.....	163
5.2.5 Conclusions.....	164
5.3 Experimental.....	165

5.4 References.....	177
Chapter 6 – Chemical Vapour Deposition of Gallium Arsenide and Gallium Phosphide Thin Films.....	181
6.1 Introduction.....	181
6.1.1 LPCVD of III-V materials using single source precursors.....	182
6.1.2 Supercritical fluid deposition.....	184
6.2 Results and discussion.....	187
6.2.1 Dimeric [$n\text{Bu}_2\text{Ga}(\text{E}^i\text{Bu}_2)_2\text{Ga}^n\text{Bu}_2$] precursors.....	187
6.2.2 [$\text{Ga}(\text{P}^i\text{Bu}_2)_3$] precursor.....	195
6.2.3 Conclusions.....	197
6.3 Experimental.....	199
6.4 References.....	201
Chapter 7 – Conclusions and Outlook.....	205
Appendix 1 – General Experimental Techniques.....	209

List of tables

- Table 1.1** Properties of selected NMR nuclei
- Table 1.2** IR and Raman active stretches for $[\text{MCl}_4]^-$ (M = Al, Ga, In)
- Table 2.1** Selected bond lengths (\AA) and angles ($^\circ$) for $[\{[\text{8}]_{\text{ane}}\text{Se}_2\}_2]^{2+}$
- Table 2.2** Selected bond lengths (\AA) and angles ($^\circ$) for $[\{[\text{8}]_{\text{ane}}\text{Se}_2\text{Cl}\}]^+$
- Table 2.3** Selected bond lengths (\AA) and angles ($^\circ$) for $[\text{GaCl}_2([\text{16}]_{\text{ane}}\text{S}_4)]^+$
- Table 2.4** Selected bond lengths (\AA) and angles ($^\circ$) for $[\text{GaCl}_2([\text{16}]_{\text{ane}}\text{Se}_4)]^+$
- Table 2.5** Selected bond lengths (\AA) and angles ($^\circ$) for $[\text{InCl}_2([\text{16}]_{\text{ane}}\text{Se}_4)]^+$
- Table 2.6** Selected bond lengths (\AA) and angles ($^\circ$) for $[\text{GaCl}_3([\text{14}]_{\text{ane}}\text{S}_4)]$
- Table 2.7** Crystal data and structure refinement details
- Table 3.1** Selected bond lengths (\AA) and angles ($^\circ$) for $[(\text{GaCl}_3)_2\{\text{'BuTe}(\text{CH}_2)_3\text{Te'Bu}\}]$
- Table 3.2** Selected bond lengths (\AA) and angles ($^\circ$) for $[(\text{GaCl}_3)_2(\text{EtS}(\text{CH}_2)_2\text{SEt})]$
- Table 4.1** Crystal phases of Ga_2S_3
- Table 4.2** Acidities of dimethyl amide, methoxide and methyl thiolate
- Table 4.3** Refined phase fractions and lattice parameters for thin film samples of Ga_2S_3 laser annealed at 90, 100 and 110 mA

- Table 5.1** Selected bond distances (Å) and angles (°) for [AlCl₃(Me₂Se)] and [AlCl₃(Me₂Te)]
- Table 5.2** Selected bond distances (Å) and angles (°) for [AlBr₃(Me₂Te)]
- Table 5.3** Selected bond distances (Å) and angles (°) for [AlCl₂(CH₃S(CH₂)₂SCH₃)₂]⁺ and [AlCl₂(CH₃Se(CH₂)₂SeCH₃)₂]⁺
- Table 5.4** Selected bond distances (Å) and angles (°) for [AlI₂(CH₃S(CH₂)₂SCH₃)₂]⁺
- Table 5.5** Selected bond distances (Å) and angles (°) for [^tBuTe(CH₂)₃Te(^tBu)Te(CH₂)₃Te^tBu]⁺
- Table 5.6** Selected bond lengths (Å) and angles (°) for [(AlCl₃)₂(*o*-C₆H₄(CH₂SEt)₂)]
- Table 5.7** Selected bond lengths (Å) and angles (°) for [*o*-C₆H₄CH₂Se(Me)CH₂]⁺
- Table 5.8** Selected bond distances (Å) and angles (°) for [AlCl₃(MeC(CH₂SMe)₃)]
- Table 5.9** Selected bond lengths and angles for [AlCl₂([14]aneS₄)]⁺
- Table 5.10** Crystal data and structure refinement details
- Table 6.1** EDX data for GaE films deposited by LPCVD from [ⁿBu₂Ga(μ-E^tBu₂)₂GaⁿBu₂] (E = P or As)

List of figures

- Figure 1.1** Diagram illustrating the processes in a chemical vapour deposition reaction
- Figure 1.2** Structure of the cation in the selenonium tetrachlorogallate salt [o - $C_6H_4CH_2Se(Me)CH_2$][$GaCl_4$]
- Figure 1.3** Structure of $[(GaBr_3)_2\{\mu$ - o - $C_6H_4(CH_2P(O)Ph_2)_2\}]$
- Figure 1.4** View of the cation in cis - $[Cl_2Ga(dmbpy)_2][GaCl_4]$ ($dmbpy$ = 4,4'-dimethyl-2,2'-bipyridine)
- Figure 1.5** Structures of (a) $\{[MeC(CH_2AsMe_2)_3-\kappa As:\kappa^2 As'As''] (GaCl_3)(GaCl_2)\}^+$; (b) $\{[Me_2AsCH_2C(Me)(CH_2AsMe_2)_2-\kappa^2 AsAs'] GaCl_2\}^+$; (c) $\{[\mu_3$ - $MeC(CH_2AsMe_2)_3-\kappa As:\kappa As':\kappa As'''] (GaI_3)_3\}$
- Figure 1.6** Structures of (a) $[InCl_2\{^iPrS(CH_2)_2S^iPr\}_2]^+$; (b) $[InCl_2([14]aneS_4)]^+$; (c) $[In_2Cl_6\{CH_3Se(CH_2)_2SeCH_3\}_2]$
- Figure 1.7** Crystal structure of the complex $[(InCl_3)_4\{o$ - $C_6H_4(CH_2SEt)_2\}_3]$
- Figure 1.8** Structure of $[(InCl_3)_2(Me_3AsO)_3]$
- Figure 1.9** Structure of $[(InCl_3)_2(DME)_3]$
- Figure 1.10** Structure of $[InBr_2(1,4,7,10$ -tetraazabicyclo[5.5.2]tetradecane)] $^+$
- Figure 1.11** Structures of (a) $[(InI_3)_2(dppe)]$; (b) $[(InI_3)_2(dppe)_3]$
- Figure 1.12** Structures of (a) $[InBr_2(o$ - $C_6H_4(PMe_2)_2)]^+$; (b) $[InBr_2\{o$ - $C_6H_4(PMe_2)_2\}_2]^+$; (c) $[InI_2\{o$ - $C_6H_4(PMe_2)_2\}_2][InI_4\{o$ - $C_6H_4(PMe_2)_2\}]$; (d) $[In_2Cl_6\{o$ - $C_6H_4(PMe_2)_2\}_2]$; (e) part of the chain polymer $[In_2Cl_5\{o$ - $C_6H_4(PMe_2)_2\}_2]_n^+$
- Figure 1.13** Structures of (a) $[In_2Cl_6\{o$ - $C_6H_4(AsMe_2)_2\}_2]$; (b) $[InI_2(o$ - $C_6H_4(AsMe_2)_2)]^+$; (c) $[In_2Cl_5\{o$ - $C_6H_4(AsMe_2)_2\}_2]_n^+$
- Figure 1.14** Schematic diagram of Rayleigh and Raman scattering

- Figure 2.1** Synthesis of selenoether macrocycles using a direct synthesis route
- Figure 2.2** High dilution syntheses of [12]aneSe₃ and [20]aneSe₅
- Figure 2.3** Synthesis of [12]aneSe₃, benzo-[11]aneSe₃ and benzo-[13]aneSe₃ using a high dilution method
- Figure 2.4** 2D sheet polymer of [(GeCl₂)₂([14]aneS₄)]
- Figure 2.5** Crystal structure of [(AsCl₃)₄[24]aneSe₆]
- Figure 2.6** 3c-4e bonding model
- Figure 2.7** Reactions of GaCl₃ with [8]aneSe₂
- Figure 2.8** Crystal structure of the dimeric cation in [{[8]aneSe₂}₂][GaCl₄]₂
- Figure 2.9** Crystal structure of the cation in [{[8]aneSe₂Cl}][GaCl₄]·CH₂Cl₂
- Figure 2.10** View of one of the cations in the asymmetric unit of [GaCl₂([16]aneS₄)]₂[GaCl₄]
- Figure 2.11** Crystal structure of the cation in [GaCl₂([16]aneSe₄)]₂[GaCl₄]
- Figure 2.12** View of the structure of the centrosymmetric cation in [InCl₂([16]aneSe₄)]₂[InCl₄]
- Figure 2.13** Crystal structure of a section of the [GaCl₃([14]aneS₄)] chain polymer
- Figure 2.14** Part of the extended 1D chain structure of [GaCl₃([14]aneS₄)]
- Figure 2.15** Structure of [InCl₂([14]aneS₄)]⁺ in [InCl₂([14]aneS₄)]₂[InCl₄]
- Figure 3.1** Structure of [Cp*Ga(μ₃-Se)]₄
- Figure 3.2** View of the crystal structure of [(GaCl₃)₂{^tBuTe(CH₂)₃Te^tBu}]
- Figure 3.3** Long intermolecular contacts between Cl and Te in [(GaCl₃)₂{^tBuTe(CH₂)₃Te^tBu}]

- Figure 3.4** Top and cross-sectional SEM images of a thin film of Ga₂Se₃ deposited from [(GaCl₃)₂{ⁿBuSeCH₂CH₂SeⁿBu}] at 773 K onto SiO₂
- Figure 3.5** EDX spectrum of a Ga₂Se₃ film showing no detectable chlorine content
- Figure 3.6** XRD pattern from a typical Ga₂Se₃ thin film (monoclinic, *Cc*) grown via LPCVD from [(GaCl₃)₂{ⁿBuSeCH₂CH₂SeⁿBu}] at 773 K onto SiO₂
- Figure 3.7** Raman spectrum of a thin film of Ga₂Se₃ grown from [(GaCl₃)₂{ⁿBuSeCH₂CH₂SeⁿBu}] at 773 K
- Figure 3.8** AFM images of a Ga₂Se₃ thin film grown via LPCVD using 5 mg of [(GaCl₃)₂{ⁿBuSeCH₂CH₂SeⁿBu}] at 773 K onto SiO₂
- Figure 3.9** Top and cross-sectional SEM images of a thin film of Ga₂Te₃ deposited from [GaCl₃(TeⁿBu₂)] at 773 K onto SiO₂
- Figure 3.10** EDX spectrum of a Ga₂Te₃ film showing no detectable chlorine content
- Figure 3.11** Raman spectrum of a thin film of Ga₂Te₃
- Figure 3.12** Fit to XRD pattern for Ga₂Te₃ in *F*-43*m*
- Figure 3.13** AFM images of a Ga₂Te₃ thin film grown via LPCVD using 20 mg of [GaCl₃(TeⁿBu₂)] at 773 K onto SiO₂
- Figure 3.14** Diagram of photolithographically patterned SiO₂/TiN substrates
- Figure 3.15** - SEM image showing the preferential deposition of Ga₂Te₃ onto the TiN surface relative to the SiO₂ surface of a patterned TiN/SiO₂ substrate *via* LPCVD using 5 mg of [GaCl₃(TeⁿBu₂)] at 773 K
- Figure 3.16** Crystal structure of [(GaCl₃)₂(EtS(CH₂)₂SEt)]
- Figure 4.1** XRD pattern of γ -Ga₂S₃ deposited at different temperatures onto glass showing an increase in crystallinity with temperature
- Figure 4.2** Molecular structure of [Ga(SⁱPr)₂(μ -SⁱPr)]₂

- Figure 4.3** Top and cross-sectional SEM images of a thin film of Ga₂S₃ deposited from [Ga(SⁱPr)₂(μ-SⁱPr)]₂ at 723 K onto SiO₂
- Figure 4.4** XRD pattern of Ga₂S₃ thin film deposited at 400 °C with background subtraction and peak positions corresponding to *F-43m* Ga₂S₃
- Figure 4.5** XRD pattern of Ga₂S₃ thin film deposited at 400 °C with background subtraction and peak positions corresponding to *Cc* Ga₂S₃
- Figure 4.6** Phase transition of Ga₂S₃ as annealing temperature increases
- Figure 4.7** Raman spectra of a Ga₂S₃ thin film before and after annealing
- Figure 4.8** Thin film of Ga₂S₃ deposited onto a patterned substrate at 723 K showing no evidence of selectivity
- Figure 4.9** Uncorrected XRD profile of a Ga₂S₃ thin film laser annealed at 110 mA
- Figure 4.10** Stacked plot showing how phase composition of the film changes with laser annealing power
- Figure 4.11** Phase fit for Ga₂S₃ annealed at 90 mA
- Figure 4.12** Phase fit for Ga₂S₃ annealed at 100 mA
- Figure 4.13** Phase fit for Ga₂S₃ annealed at 110 mA
- Figure 5.1** Structure of [(μ₃-AlEt)₂(1,4,8,11-tetraazacyclotetradecane-1,4,8,11-tetraide)(AlCl₂Et)₂]
- Figure 5.2** Crystal structures of [AlCl₃(Me₂Se)] and [AlCl₃(Me₂Te)]
- Figure 5.3** Structure of [Me₂SH][AlCl₄]
- Figure 5.4** Crystal structure of [AlBr₃(Me₂Te)]
- Figure 5.5** View of the cations in [AlCl₂(CH₃E(CH₂)₂ECH₃)₂][AlCl₄] (E = S, Se)

- Figure 5.6** View along the *a* axis of the packing diagrams of $[\text{AlCl}_2(\text{CH}_3\text{S}(\text{CH}_2)_2\text{SCH}_3)_2][\text{AlCl}_4]$ and $[\text{AlCl}_2(\text{CH}_3\text{Se}(\text{CH}_2)_2\text{SeCH}_3)_2][\text{AlCl}_4]$
- Figure 5.7** Crystal structure of the cation in $[\text{AlI}_2(\text{CH}_3\text{S}(\text{CH}_2)_2\text{SCH}_3)_2][\text{AlI}_4]$
- Figure 5.8** Crystal structure of the cation in $[\text{tBuTe}(\text{CH}_2)_3\text{Te}(\text{tBu})\text{Te}(\text{CH}_2)_3\text{Te}(\text{tBu})][\text{AlCl}_4]$
- Figure 5.9** Structure of $[\{o\text{-C}_6\text{H}_4(\text{CH}_2\text{SEt})_2\}(\text{AlCl}_3)_2]$
- Figure 5.10** Structure of one of the cations in $[\text{C}_{17}\text{H}_{19}\text{Se}]_2[\text{TiCl}_6]$
- Figure 5.11** View of the cation in $[o\text{-C}_6\text{H}_4\text{CH}_2\text{Se}(\text{Me})\text{CH}_2][\text{AlCl}_4]$
- Figure 5.12** Calculated mass spectrometry isotope pattern for $[o\text{-C}_6\text{H}_4\text{CH}_2\text{Se}(\text{Me})\text{CH}_2]^+$
- Figure 5.13** View of part of the 1D chain polymer $[\text{AlCl}_3(\text{MeC}(\text{CH}_2\text{SMe})_3)]$
- Figure 5.14** View of one of the cations in $[\text{AlCl}_2([\text{14}]ane\text{S}_4)][\text{AlCl}_4]$
-
- Figure 6.1** Structure of $[\text{nBu}_2\text{Ga}(\mu\text{-P}^t\text{Bu}_2)_2\text{Ga}^n\text{Bu}_2]$
- Figure 6.2** XRD pattern obtained from a GaP thin film grown on silica at 773 K by LPCVD from $[\text{nBu}_2\text{Ga}(\mu\text{-P}^t\text{Bu}_2)_2\text{Ga}^n\text{Bu}_2]$
- Figure 6.3** XRD pattern obtained from a GaAs thin film grown on silica at 773 K by LPCVD from $[\text{nBu}_2\text{Ga}(\mu\text{-As}^t\text{Bu}_2)_2\text{Ga}^n\text{Bu}_2]$
- Figure 6.4** XRD patterns from GaAs thin films deposited from $[\text{nBu}_2\text{Ga}(\mu\text{-As}^t\text{Bu}_2)_2\text{Ga}^n\text{Bu}_2]$ at 673, 773 and 823 K and GaP thin films (b) deposited from $[\text{nBu}_2\text{Ga}(\mu\text{-P}^t\text{Bu}_2)_2\text{Ga}^n\text{Bu}_2]$ at 673, 773 and 823 K
- Figure 6.5** Raman spectra of GaP and GaAs thin films grown by LPCVD at 773 K from $[\text{nBu}_2\text{Ga}(\mu\text{-E}^t\text{Bu}_2)_2\text{Ga}^n\text{Bu}_2]$

- Figure 6.6** SEM cross-section images of GaP and GaAs films deposited on silica at 773 K by LPCVD from $[\text{}^n\text{Bu}_2\text{Ga}(\mu\text{-E}^t\text{Bu}_2)_2\text{Ga}^n\text{Bu}_2]$
- Figure 6.7** 3D AFM image (20 μm x 20 μm) of a GaP film grown at 773 K
- Figure 6.8** 3D AFM image (20 μm x 20 μm) of a GaAs film grown at 773 K
- Figure 6.9** Luminescence spectrum of GaP film grown at 773 K by LPCVD from $[\text{}^n\text{Bu}_2\text{Ga}(\mu\text{-P}^t\text{Bu}_2)_2\text{Ga}^n\text{Bu}_2]$
- Figure 6.10** Transmission spectrum of GaAs film grown at 773 K
- Figure 6.11** Diffuse reflectance spectrum of GaP film grown at 773 K
- Figure 6.12** Structure of $[\text{Ga}(\text{P}^t\text{Bu}_2)_3]$
- Figure 6.13** XRD pattern from GaP film deposited from $\text{Ga}(\text{P}^t\text{Bu}_2)_3$ at 773 K

DECLARATION OF AUTHORSHIP

I, Kathryn George, declare that the thesis entitled “Chalcogenoether Complexes with Group 13 Halides and Development of Single Source Precursors for Chemical Vapour Deposition of III-V and III-VI Thin Films” and the work presented in the thesis are both my own, and have been generated by me as the result of my own original research. I confirm that:

- this work was done wholly or mainly while in candidature for a research degree at this University;
- where any part of this thesis has previously been submitted for a degree or any other qualification at this University or any other institution, this has been clearly stated;
- where I have consulted the published work of others, this is always clearly attributed;
- where I have quoted from the work of others, the source is always given. With the exception of such quotations, this thesis is entirely my own work;
- I have acknowledged all main sources of help;
- where the thesis is based on work done by myself jointly with others, I have made clear exactly what was done by others and what I have contributed myself;
- parts of this work have been published as:

Chemical Vapor Deposition of GaP and GaAs Thin Films From [ⁿBu₂Ga(μ-E^tBu₂)₂GaⁿBu₂] (E = P or As) and Ga(P^tBu₂)₃, Cheng, F.; George, K.; Hector, A. L.; Jura, M.; Kroner, A.; Levason, W.; Nesbitt, J.; Reid, G.; Smith, D. C.; Wilson, J. W. *Chem. Mater.* **2011**, *23*, 5217

Unexpected Reactivity and Coordination in Gallium(III) and Indium(III) Chloride Complexes With Geometrically Constrained Thio- and Selenoether Ligands, George, K.; Jura, M.; Levason, W.; Light, M. E.; Ollivere, L. P.; Reid, G. *Inorg. Chem.* **2012**, *51*, 2231

Telluroether and Selenoether Complexes as Single Source Reagents for Low Pressure Chemical Vapor Deposition of Crystalline Ga₂Te₃ and Ga₂Se₃ Thin Films, George, K.; de Groot, C. H.; Gurnani, C.; Hector, A. L.; Huang, R.; Jura, M.; Levason, W.; Reid, G. *Chem. Mater.* **2013**, 25, 1829

Low Pressure Chemical Vapour Deposition of Crystalline Ga₂Te₃ and Ga₂Se₃ Thin Films from Single Source Precursors Using Telluroether and Selenoether Complexes, George, K.; Groot, C. H. d.; Gurnani, C.; Hector, A. L.; Huang, R.; Jura, M.; Levason, W.; Reid, G., *Physics Procedia* **2013**, 46, 142

Figures have been reproduced with copyright permission.

Signed:

Date:.....

Acknowledgements

I would not have been able to complete my PhD without the help of a range of people, whom I would like to acknowledge. I want to thank the EPSRC and CMSD at ISIS, STFC for providing the funding for this research. Professors Gill Reid and Bill Levason, my academic supervisors, have helped me with support, advice and suggestions throughout the PhD, as well as running multinuclear NMR spectra. Dr Marek Jura, my industrial supervisor at ISIS, has also given me plenty of advice and provided access to and training on the instruments in the Materials Characterisation Laboratory at ISIS. I appreciate the time and patience of Dr Andrew Hector, my advisor, in explaining some of the materials chemistry and assisting with XRD data analysis. Ruomeng Huang has provided most of the CVD substrates and collected selected SEM images, EDX data, Raman spectra and Hall measurements. John Nesbitt collected the photoluminescence data. I am grateful for the help provided by Drs Mike Webster, Mark Light, Wenjian Zhang with crystallography and to the members of NCS for their helpful suggestions in collecting crystal data. I also need to thank the Reid/Levason group, past and present, for day to day help and entertainment. Particular acknowledgement must go to Drs Sophie Benjamin and David Pugh for advice and help on a wide range of subjects. Finally, I want to acknowledge my family, friends (particularly Lauren Dackombe, Chris Andrews and Dan Heggs), and SUWRFC, who may not have helped directly with the chemistry in this thesis but have been invaluable in providing support, distraction and generally keeping me going throughout the last three years.

Definitions and Abbreviations

[6]aneN ₃	1,3,5-triazacyclohexane
[8]aneSe ₂	1,5-diselenacyclooctane
[8]aneTe ₂	1,5-ditelluracyclooctane
[9]aneN ₃	1,4,7-triazacyclononane
[9]aneS ₃	1,4,7-trithiacyclononane
[12]aneS ₄	1,4,7,10-tetrathiacyclododecane
[12]aneSe ₃	1,5,9-triselenacyclododecane
[14]aneS ₄	1,4,8,11-tetrathiacyclotetradecane
[14]aneSe ₄	1,4,8,11-tetraselenacyclotetradecane
[16]aneS ₄	1,5,9,13-tetrathiacyclohexadecane
[16]aneSe ₄	1,5,9,13-tetraselenacyclohexadecane
[20]aneSe ₅	1,5,9,13,17-pentaseleacyclocosane
[24]aneSe ₆	1,5,9,13,17,21-hexaselenacyclotetracosane
15-crown-5	1,4,7,10,13-pentaoxacyclopentadecane
18-crown-6	1,4,7,10,13,16-hexaoxacyclooctadecane
AACVD	aerosol assisted chemical vapour deposition
acac	acetylacetonate
AFM	atomic force microscopy
ALD	atomic layer deposition
bipy	2,2'-bipyridine
Cp*	pentamethylcyclopentadienyl
CVD	chemical vapour deposition

Cy	cyclohexyl
cyclam	1,4,8,11-tetraazacyclotetradecane
cyclen	1,4,7,10-tetraazacyclododecane
dmbpy	4,4'-dimethyl-2,2'-bipyridine
DME	1,2-dimethoxyethane
dmf	dimethylformamide
dmpy	3,5-dimethylpyridine
DMSe	3,3-dimethylselenetane
DMSO	dimethylsulfoxide
dppe	bis(diphenylphosphino)ethane
EDX	energy dispersive X-ray spectroscopy
en	1,2-diaminoethane
ESI	electrospray ionisation
FETISH	field effect transistor with an insulating sulfide heterojunction
FWHM	full width half maximum
GST	germanium antimony telluride
IR	infra-red
LED	light emitting diode
LO	longitudinal optical
LPCVD	low pressure chemical vapour deposition
MBE	molecular beam epitaxy
MOCVD	metal organic chemical vapour deposition
MS	mass spectrometry

NMR	nuclear magnetic resonance
OMCVD	organometallic chemical vapour deposition
PCM	phase change memory
PL	photoluminescence
PVD	physical vapour deposition
py	pyridine
RMS	root mean square
SCFD	supercritical chemical fluid deposition
SEM	scanning electron microscopy
terpy	2,2',2''-terpyridyl
TGA	thermogravimetric analysis
thf	tetrahydrofuran
tmen	N,N,N',N'-tetramethylethylenediamine
TO	transverse optical
TsO	p-toluenesulfonate
XPS	X-ray photoelectron spectroscopy
XRD	X-ray diffraction
YSZ	yttria-stabilised zirconia

1 Introduction

This thesis aims to synthesise and characterise single source precursors based on coordination complexes of Group 13 and Group 15/16 elements for the low pressure chemical vapour deposition of III-V and III-VI thin films. As part of this, the films will be characterised by a range of techniques, which are described in this chapter. In order to develop these precursors it will also be necessary to enhance the current understanding of the coordination chemistry of the Group 13 elements. Therefore this thesis will also explore some of the coordination chemistry of Group 13 halides with Group 16 donor ligands.

1.1 III-V and III-VI thin films

III-V and III-VI thin films have attracted significant interest due to their semiconducting properties. The modern electronics industry is heavily reliant on semiconductors, which are the focus of a large volume of research. This large field of research has been well documented in more specialised texts.¹⁻⁵

The dominant material for semiconductor device fabrication is silicon. Compound semiconductors made from Group 13 and Group 15 or 16 elements, such as GaP and GaAs, are also widely used and offer several advantages over silicon, the major one being that they have direct bandgaps. This makes these materials efficient light emitters, enabling their use in photonic devices. A direct bandgap semiconductor has the lowest minimum electron energy of the conduction band located at the zone centre of the Brillouin zone and the maximum electron energy in the valence band is aligned vertically in energy vs. k space. The transition that occurs in a direct bandgap semiconductor is thus conserved by either a photon absorption or emission, depending on the direction of the transition. The process of an electron recombining with a hole in the valence band, with the associated emission of a photon is known as radiative recombination. For an indirect bandgap semiconductor the lowest minimum electron energy of the conduction is not aligned in k space with the maximum electron energy of

the conduction band. Therefore transitions between the valence and conduction bands of an indirect bandgap semiconductor require a change in momentum that is not necessary for a direct bandgap semiconductor. Indirect bandgap semiconductors must undergo non-radiative recombination processes as radiative recombination requires recombining carriers with the correct energy to satisfy both the transition energy and momentum values. The long waiting time for these carriers means that the probability of an indirect bandgap semiconductor undergoing radiative recombination is exceptionally low. The non-radiative recombination occurs instead *via* transitions *via* defects and Auger recombination.⁶

As well as having a direct bandgap, the energy of the bandgap of III-V materials is better suited to optoelectronic applications than Si. For example GaAs has a direct bandgap energy of 1.42 eV, which corresponds to a wavelength of 0.9 μm , falling within the infra-red region of the electromagnetic spectrum.⁷ III-V devices also have a lower defect generation rate than Si devices when exposed to high-energy ionising radiation. GaAs devices are also able to operate at higher powers than silicon devices.

The semiconducting properties of III-V compounds were first discovered by Welker in the 1950s.⁸ During the 1970s GaP and GaAs were in use in mass market LED devices and the volume and diversity of their use has increased since then. GaAs now finds uses in LEDs, laser diodes and solar cells. The development of single source precursors for III-V thin films was intensively researched from the early 1980s to the mid-1990s.⁹

There is also considerable interest in developing III-VI, V-VI and ternary chalcogenide materials for phase change memory (PCM) applications in solid state memory devices.¹⁰⁻¹⁵ PCM works by using a material that can easily switch between amorphous and crystalline states by heating *via* use of an electric current. The two forms of PCM that have been developed are optical PCM, where there is a difference in the optical constants of the crystalline and amorphous phases, and electrical PCM, where there is a difference in the resistivity of the two phases.¹⁶ The two different phases effectively act as a binary '1' or '0', enabling data to be stored and read. Over the last couple of

decades the technology has developed sufficiently to be able to compete with incumbent technology such as flash memory.¹² PCM devices have strong potential as they can offer low power, high endurance, good data retention properties, fast programming, are scalable below 22 nm and are a non-volatile form of memory.¹¹ Chalcogenide materials are particularly important as PCM materials, with germanium antimony telluride (GST) alloys being the materials that have attracted the most attention, due to their fast crystallisation speeds, good crystallisation and melting temperatures and ease of deposition by physical vapour deposition (PVD). Ideal electrical PCM materials have several properties:

- Large difference in resistance between crystalline and amorphous phases
- High enough crystallisation temperature for the amorphous phase to be stable at the device operating temperature (80 – 150 °C) over a long time period (~10 years)
- Ability to switch to a crystalline phase on a nanosecond time scale
- Low melting temperature, which determines the power required to reamorphise the crystalline material
- Ability to withstand repeated crystallisation cycles without a decrease in performance

The switching ability of Ga₂Se₃ single crystals was identified in the 1970s¹⁷ and many studies have been undertaken since then into the switching behaviour of Group 13 chalcogenides, including the fabrication of switchable PCM cells.¹⁸⁻²¹ Recently a significant volume of work has focussed on fabricating In₂Se₃ nanowires and understanding their switching behaviour with positive results.²²⁻²⁵ Ga₂Te₃ has also attracted interest as a low power PCM material.²⁶

III-VI materials have also been used to passivate the surface of III-V materials.²⁷⁻³¹ This includes the use of a single source precursor [¹BuGaS]₄ to deposit a layer of GaS on GaAs, which enhances the photoluminescence of GaAs due to a decrease in surface recombination.²⁸ This led to a new class of GaAs based transistors that were termed FETISH (field effect transistor with an insulating sulfide heterojunction).³¹ GaS is a

suitable material for GaAs passivation as its lattice constant ($a = 5.4 \text{ \AA}$) is within 5% of the lattice constant for GaAs (5.63 \AA). Selenium vapour has also been used to create a layer of Ga_2Se_3 on the surface of a GaAs substrate, increasing the smoothness of the substrate surface at the atomic level as well as allowing for the deposition of more oriented GaAs in subsequent layers.²⁹

1.2 Thin film deposition

There are multiple methods to produce thin films of III-V and III-VI materials, including physical vapour deposition (PVD), chemical vapour deposition (CVD), atomic layer deposition (ALD) and molecular beam epitaxy (MBE).³²⁻⁴⁴

1.2.1 Physical vapour deposition

Physical vapour deposition (PVD) is a common, widely used technique for thin film growth due to its simplicity.⁴⁵⁻⁴⁸ There are several methods that can be used to produce a PVD coating. In the classic method, a crucible of an elemental material is vaporised either by heating or directing a laser or electron beam at the material. Film growth proceeds *via* the following steps:

1. Vaporisation of a solid
2. Transportation of the gas from the source to the substrate
3. Adsorption of the gas on the surface
4. Nucleation and film growth

The substrate can be kept at a lower temperature than the vapour, allowing for the deposition of films onto substrates that have low thermal stability, such as organic polymers. The material is only deposited on surfaces directly facing the source and cannot diffuse across the surface so even coverage of non-flat surfaces is not achievable. The requirement of ultra-high vacuum conditions is also expensive.

Sputter coating works by ejecting material from a target, typically using an ion beam, onto a substrate. It is also possible to use a reactive gas to sputter coat metal oxides or metal nitrides, for example. As the target does not need to be vaporised, this process allows for the use of elements with very high melting points.

Pulsed laser desorption is PVD technique in which a high power, pulsed laser beam is directed at a target either under ultrahigh vacuum conditions or in the presence of a reactive gas. The use of a high energy laser beams results in the formation of a plasma, formed of charged and neutral species, which expands away from the target and deposits a thin film on the substrate. By controlling the number and length of the laser pulses, the film thickness can be controlled and multilayer films can be grown by switching targets. The stoichiometry of the target is retained, allowing for the use of this technique to transform large pieces of bulk material into more complex thin films.

1.2.2 Atomic layer deposition

Atomic layer deposition (ALD) is used to form thin films by growing the film one atomic layer at a time.⁴⁹⁻⁵² ALD has some similarities to CVD but only one precursor is introduced into the chamber at any time and the chamber purged after each precursor pulse in order to remove excess precursor before the next precursor pulse. The growth of each layer is self-limiting, allowing for control over growth rate. ALD is capable of growing homogenous, crystalline films over large areas with good control. Film growth, however, is slow due to the requirement to switch between precursors at frequent intervals.⁵³

1.2.3 Molecular beam epitaxy

Molecular beam epitaxy (MBE) is a simple process, similar to PVD.⁴¹⁻⁴³ Elemental sources are evaporated independently and at a controlled rate to form molecular beams, which intercept at the surface of the substrate. This is carried out under ultrahigh vacuum conditions with relatively low growth rates. Films can be produced with very high purity. It is possible to create complex layer structures and doped thin films using this process.⁵³

1.2.4 Chemical vapour deposition

Chemical vapour deposition (CVD) involves the chemical reaction of one or more vapour phase precursor(s) to form a solid thin film.^{35, 44, 54, 55} Precursors can either be single source or multiple source. Single source precursors incorporate the necessary elements required to deposit the thin film within one molecule e.g. $[\text{Ga}(\text{P}^t\text{Bu}_2)_3]$. Often there is already a bond between the elements that will be forming the thin film so that in the gas phase the reactions occurring are predominantly the elimination of the organic side chains. Dual source precursors are where two separate precursors are used, each of which incorporates a different element of the thin film e.g. GaMe_3 and PH_3 . Dual source precursors are the most commonly used in industry due to their lower cost and ability to produce very high purity films. Single source precursors have been found to be more useful in specialist applications such as quantum dot formation and nanowire growth (see 6.1.1).

The key steps involved in a CVD reaction (Figure 1.1) are as follows⁵⁵:

1. Evaporation and transport of precursors into the reactor
2. Vapour phase reactions of precursors to produce reactive intermediates
3. Transport of reactants to the substrate
4. Adsorption of reactants onto the substrate
5. Film formation *via* surface diffusion, nucleation and surface chemical reactions
6. Desorption and transport of remaining decomposition fragments from the reactor

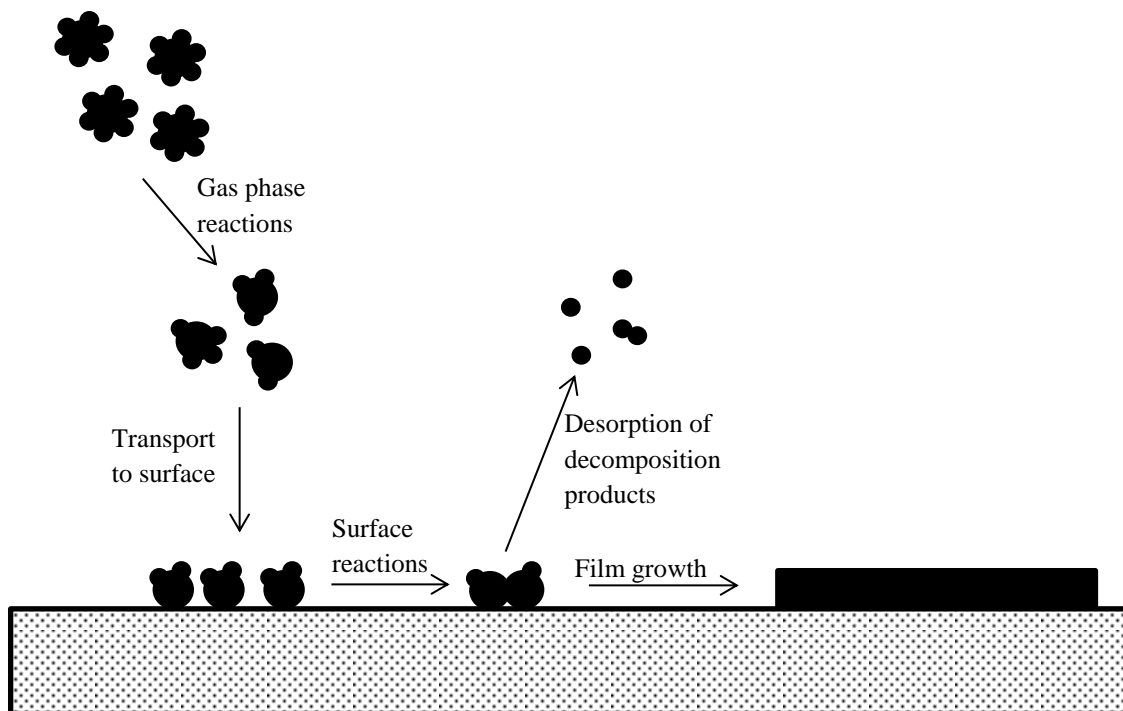


Figure 1.1 – Diagram illustrating the processes in a chemical vapour deposition reaction

CVD has the advantage of being able to easily deposit films with uniform distribution over large areas as well as depositing conformal films into pores and channels. The higher flow rates of precursors in CVD systems also allow for faster deposition of thin films. However, CVD precursors can be more expensive and more difficult to handle than PVD precursors and the higher temperatures often required can be unsuitable for structures already fabricated on substrates.

Important properties to be considered when designing a precursor include:

- high purity synthesis to avoid defects in the thin film
- simple, scalable synthesis so that several grams can be made at a time
- volatility if being used for low pressure (LP) CVD
- solubility if being used for aerosol assisted (AA) CVD

- a sufficiently large temperature difference between evaporation and decomposition
- stability to be stored over a period of months or years

It is also advantageous if the precursor is non-toxic, non-pyrophoric and air and moisture stable, although in practice this combination is often difficult to achieve.⁶ A recent review by O'Brien *et al.* gives a comprehensive review of precursors for main group semiconductors.⁶

There are several modifications to the CVD process to allow for different methods of delivering the precursor into the reactor. These include low pressure (LP) CVD, where the system is under vacuum. This method can only be used if the precursors are sufficiently volatile. Aerosol assisted (AA) CVD uses a solvent to dissolve the precursor, which is then nebulised and sprayed into the reaction chamber. This method is better suited to involatile precursors, although they must have solubility in a suitable solvent. Readers are directed to a recent article by Carmalt *et al.* for a more detailed overview of AACVD as a thin film deposition technique.⁵⁶

Development of precursors for the CVD of III-VI thin films occurred much later than for III-V thin films with the first report of an indium thiolate complex being suggested as a potential OMCVD precursor in 1989.⁵⁷ The development of III-VI materials has increased in recent years due to political pressure to eliminate the use of cadmium and mercury, found in II-VI thin films, which also have semiconducting properties.³⁴ Many single source precursors are organometallic or coordination complexes of Group 13 metal ions.

1.3 Coordination chemistry of Group 13 metals

Compounds of the Group 13 elements typically assume the +3 oxidation state. These trivalent compounds with six valence electrons make the Group 13 elements good electron acceptors, with Lewis acidity decreasing down the group. The +1 oxidation state is also encountered, due to the ns^2np^1 electronic configuration. However, thallium is the only element in the group that is more commonly found in the +1 oxidation state than the +3 oxidation. In(I) is more common than Ga(I) but both are powerful reducing agents and prone to disproportionation in solution.⁵⁸

The coordination chemistry of aluminium, gallium and indium trihalides will be discussed here. A more extensive discussion of the chemistry of the Group 13 metals can be found in books by Downs,⁵⁸ Aldridge and Downs,⁵⁹ Cotton, Wilkinson *et al.*,⁶⁰ the relevant chapters of Comprehensive Coordination Chemistry (25.1 and 25.2)⁶¹⁻⁶³ and Comprehensive Coordination Chemistry II (3.4 and 3.5)⁶⁴⁻⁶⁶

1.3.1 Coordination chemistry of aluminium halides

There is limited work reported in the literature for AlX_3 ($X = Cl, Br, I$) complexes with chalcogenoethers. AlF_3 is polymeric and is not yet known to form complexes with chalcogenoethers.⁶⁷ Richards and Thompson reported some examples of complexes of $AlCl_3$ with Me_2S , Et_2S and C_4H_8S in 1967 but little work has been performed since.⁶⁸ Reaction of $AlCl_3$ with one equivalent of ligand leads to the formation of a monomeric, tetrahedral species and addition of a second equivalent of ligand is believed to lead to the formation of a pentacoordinate monomeric complex.

A larger volume of research has been performed on the coordination complexes of AlX_3 with phosphine chalcogenide or pnictogen ligands. Burford and co-workers have synthesised phosphine oxide complexes of AlX_3 ($X = Cl, Br$).⁶⁹ Single crystal X-ray diffraction shows the formation of neutral complexes of the type $[AlX_3(R_3PO)]$ adopting a distorted tetrahedral geometry at the aluminium centre with angles close to 109° and linear bonding of R_3PO , in contrast to the analogous complexes of BF_3 that

adopt a bent geometry at oxygen. In a later publication Burford and co-workers also examined coordination complexes of R_3PE ($E = S, Se$) with $AlCl_3$.⁷⁰ These isostructural complexes are also neutral with distorted tetrahedral coordination at the aluminium centre but with a bent geometry at the chalcogen.

Early work on the coordination chemistry of AlX_3 ($X = Cl, Br$) with nitrogen donor ligands was carried out by Carty and co-workers, who synthesised complexes of AlX_3 with 2,2',2''-terpyridyl (terpy).⁷¹ The $[AlCl_3(terpy)]$ complex adopts a distorted octahedral geometry at the aluminium centre. White and co-workers investigated the coordination chemistry of $AlCl_3$ with a wider range of nitrogen donor ligands and thf.⁷² All the complexes synthesised were mononuclear with either a 1:1 (2-methylpyridine, 2-diphenylmethylpyridine, quinoline, thf) or 1:2 (piperidine) Al:ligand ratio. $[AlCl_3(thf)_2]$ ⁷³ and the six coordinate $[AlCl_2(thf)_4]^+$ cation⁷⁴ have also been reported. This is similar to other reported complexes of $AlCl_3$ with nitrogen donor ligands such as the 1:2 adduct of $AlCl_3$ with Me_3N ⁷⁵ and the 1:3 adduct with pyridine⁷⁶. The complex obtained from the 2:1 reaction of pyridine with $AlCl_3$, however, is ionic with the formula *trans*- $[AlCl_2(py)_4][AlCl_4]$ ⁷⁶. The product crystallised from the reaction of $AlCl_3$ with MeCN is also ionic with a six-coordinate aluminium centre and the formula $[AlCl(MeCN)_5][AlCl_4]_2 \cdot MeCN$.⁷⁷ Studies involving the coordination complexes AlX_3 ($X = Br, I$) with the bidentate nitrogen donor ligands ethylenediamine (en) and N,N,N',N' -tetramethylethylenediamine (tmen) indicate that the formation of ionic structures of the type $[AlX_2(L)]^+[AlX_4]^-$ is favoured over the formation of a neutral, bridged structure.⁷⁸

Reported structures of AlX_3 ($X = Cl, Br$) with phosphine ligands show distorted tetrahedral coordination with one equivalent of ligand to give the complexes $[AlX_3(L)]$ ($X = Cl, L = PPh_3, P(2,4,6-C_6H_2Me_3)_3$; $X = Br, L = PH^tBu_2, PSiMe_3, P(2,4,6-C_6H_2Me_3)_3$).⁷⁹⁻⁸² There is also NMR spectroscopic evidence for the existence of $[AlX_3(PR_3)]$ ($X = Cl, Br; R = Me, Et$).⁸³ Reaction of AlX_3 with two equivalents of ligand leads to a trigonal bipyramidal structure with *trans* phosphine donors such as $[AlI_3(PEt_3)_2]$, which has been crystallographically characterised.⁸⁴ IR spectroscopy shows that the trigonal bipyramidal geometry is also present in $[AlCl_3(PMe_3)_2]$.^{75, 85}

NMR spectroscopy indicates that $[\text{AlX}_3(\text{PEt}_3)_2]$ ($\text{X} = \text{Cl}, \text{Br}$) can be formed but that only the 1:1 adduct of AlX_3 with PPh_3 exists and $[\text{AlX}_3(\text{PPh}_3)_2]$ cannot be formed.⁸⁶

1.3.2 Coordination chemistry of gallium halides

Previous work in the Southampton group has investigated the coordination chemistry of gallium trihalides with neutral mono- and bi-dentate thio- and seleno-ethers.⁸⁷ The majority of these complexes were characterised by single crystal X-ray diffraction but ^{71}Ga , $^{77}\text{Se}\{^1\text{H}\}$ and $^{125}\text{Te}\{^1\text{H}\}$ NMR spectroscopic measurements (where appropriate) also yielded useful information. $[\text{GaCl}_4]^-$ is readily identifiable by ^{71}Ga NMR spectroscopy due to its sharp resonance at 251 ppm (in CH_2Cl_2),⁸⁸ allowing it to be distinguished from $[\text{GaCl}_3(\text{L})]$ complexes, which exhibit a broader peak, due to the lower symmetry environment, between 230 and 271 ppm.⁸⁷ These complexes adopt distorted tetrahedral geometries at the metal centre with the bidentate ligands preferring to adopt a 2:1 GaX_3 to ligand stoichiometry with the neutral ligand bridging rather than having five coordinate gallium centres or halide displacement to form an ionic coordination complex. Although it would be predicted that a monodentate ligand such as EMe_2 ($\text{E} = \text{S}, \text{Se}, \text{Te}$) would form a neutral tetrahedral complex, it is surprising that the use of bi- and tri-dentate ligands does not form 5- and 6- coordinate species or lead to halide displacement and the formation of ionic species. This contrasts with previous work on the coordination chemistry of gallium halides with diphosphane and diarsane ligands.⁸⁹ There is, however, the first reported example of the cleavage of C-Se bonds by gallium in the selenonium tetrachlorogallate salt $[\text{o-C}_6\text{H}_4\text{CH}_2\text{Se}(\text{Me})\text{CH}_2][\text{GaCl}_4]$ that forms if $[(\text{GaCl}_3)_2\{\mu\text{-o-C}_6\text{H}_4(\text{CH}_2\text{SeMe})_2\}]$ is left to stand in CH_2Cl_2 solution (Figure 1.2).

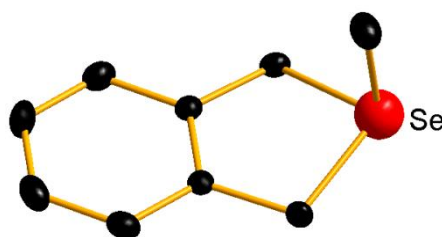


Figure 1.2 - Structure of the cation in the selenonium tetrachlorogallate salt $[\text{o-C}_6\text{H}_4\text{CH}_2\text{Se}(\text{Me})\text{CH}_2][\text{GaCl}_4]$

Other research groups have also investigated the coordination chemistry of gallium halides with chalcogenoethers. Mishra *et al.* synthesised dimethyl selenide precursors of copper, gallium and indium halides as potential single source CVD precursors, although their use for CVD is not discussed.⁹⁰ They isolated $[\text{GaI}_3(\text{SeMe}_2)]$, which is isomorphous with $[\text{GaCl}_3(\text{SeMe}_2)]$.⁸⁷

The coordination chemistry of GaCl_3 with constrained thio- and seleno-ethers has also been investigated.⁹¹ The reactions of GaCl_3 with the tetradentate ligands $\text{C}(\text{CH}_2\text{SMe})_4$ and $1,2,4,5\text{-C}_6\text{H}_2(\text{CH}_2\text{SMe})_4$ yield $[(\text{GaCl}_3)_4(\text{L})]$ with distorted tetrahedral coordination at Ga, as seen previously with non-constrained (with saturated aliphatic linking groups) thioethers. The reaction of GaCl_3 with the semi-rigid $o\text{-C}_6\text{H}_4(\text{SMe})_2$ forms a ligand-bridged dimer $[(\text{GaCl}_3)_2\{o\text{-C}_6\text{H}_4(\text{SMe})_2\}]$ and again contains distorted tetrahedral Ga(III). This complex, however, is unusually reactive towards CH_2Cl_2 and, after several days, produces the bis-sulfonium species $[\{o\text{-C}_6\text{H}_4(\text{SMeCH}_2\text{Cl})_2\}][\text{GaCl}_4]_2$. The equivalent reaction with the xylyl-based dithioether forms $[(\text{GaCl}_3)_2\{o\text{-C}_6\text{H}_4(\text{CH}_2\text{SEt})_2\}]$, which is more stable and shows no evidence for the formation of the sulfonium complex.

GaF_3 has a polymeric structure and there are very few examples of coordination complexes of GaF_3 . These include several examples of neutral and ionic, 4-, 5- and 6-coordinate complexes with NH_3 , including $[\text{GaF}_3(\text{NH}_3)]$ and $[\text{GaF}_3(\text{NH}_3)_2]$; *mer*- $[\text{GaF}_3(\text{py})_3]$; $[\text{GaF}_3(4,4'\text{-bipy})]$ and a complex with a functionalised [9]aneN₃ macrocycle $[\text{GaF}_3(\text{L})]$ (L = 1,4,7-tris(2-amino-3,5-di-*tert*-butylbenzyl)1,4,7-triazacyclononane).^{67, 92}

There are some reported structures of gallium halides with oxygen donor ligands. Reaction of GaX_3 with thf can produce either a 4-coordinate, distorted tetrahedral species $[\text{GaCl}_3(\text{thf})]^{93}$ or a 5-coordinate, trigonal bipyramidal complex $[\text{GaBr}_3(\text{thf})_2]$ with *trans* thf donors.⁹⁴ Reaction of GaCl_3 with 1,4-dioxane also produces a 5-coordinate species with GaCl_3 bridged by dioxane molecules to produce an infinite 1D chain structure.⁹⁵ Reaction of GaCl_3 with the diether $\text{MeO}(\text{CH}_2)_2\text{OMe}$ produces an ionic

species $[\text{GaCl}_2(\text{MeO}(\text{CH}_2)_2\text{OMe})_2][\text{GaCl}_4]$ with 6-coordinate Ga.⁹⁶ GaX_3 (X = Cl, Br) has been complexed with the phosphine oxide ligands R_3PO (R = Ph, NMe_2 , PhO).⁶⁹ $[\text{GaCl}_3(\text{OPPh}_3)]$ was structurally characterised by X-ray crystallography and was isostructural with the AlX_3 complexes (X = Cl, Br). The phosphine oxide ligands Me_3PO and $o\text{-C}_6\text{H}_4(\text{CH}_2\text{P}(\text{O})\text{Ph}_2)_2$ were reacted with GaX_3 (X = Cl, Br, I) in a study by Levason, Reid and co-workers.⁹⁷ These form neutral, distorted tetrahedral coordination complexes of the form $[\text{GaX}_3(\text{OPMe}_3)]$ and $[(\text{GaX}_3)_2\{\mu\text{-}o\text{-C}_6\text{H}_4(\text{CH}_2\text{P}(\text{O})\text{Ph}_2)_2\}]$ (Figure 1.3), although $[\text{GaI}_2(\text{OPMe}_3)_2][\text{GaI}_4]$ was also crystallographically characterised it was not representative of the bulk product. The 18-crown-6 complex of GaI_3 is an ionic species with the formula $[\text{GaI}_2(18\text{-crown-6})][\text{GaI}_4]$.⁹⁸ Spectroscopic data on the complex matches that of $[\text{InI}_2(18\text{-crown-6})][\text{InI}_4]$, which has been characterised by X-ray crystallography and been shown to have *trans* iodine atoms in the $[\text{InI}_2]^+$ unit.

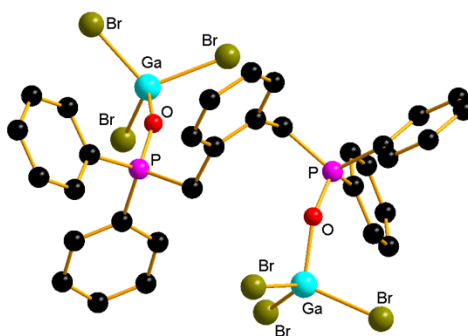


Figure 1.3 – Structure of $[(\text{GaBr}_3)_2\{\mu\text{-}o\text{-C}_6\text{H}_4(\text{CH}_2\text{P}(\text{O})\text{Ph}_2)_2\}]$

Reactions of GaX_3 with Group 15 donor ligands yield a range of complexes. Reactions with nitrogen donor ligands can yield 4-, 5- or 6-coordinate gallium species. A series of adducts of the formula $\text{X}_3\text{Ga}\{\text{NH}(\text{R})(\text{R}')\}$ (X = Cl, R = R' = SiMe_3 , SiMe_2Ph , R = ^tBu , R' = SiMe_3 ; X = Br, R = R' = SiMe_3 , SiMe_2Ph) were synthesised, exhibiting 4-coordinate, distorted tetrahedral Ga centres.⁹⁹ Reaction of GaX_3 (X = Cl, I) with the bidentate N donor ligands en and tmen yields 4-coordinate, ionic species $[\text{GaX}_2\text{L}][\text{GaCl}_4]$ (L = en, tmen).⁷⁸ The reaction of GaCl_3 with 2,2'-bipyridyl (bipy) yields the 6-coordinate ionic species *cis*- $[\text{Cl}_2\text{Ga}(\text{bipy})_2][\text{GaCl}_4]$.¹⁰⁰ An analogous structure was reported for the reaction of GaCl_3 with 4,4'-dimethyl-2,2'-bipyridine

(dmbpy) (Figure 1.4).¹⁰¹ The majority of 5-coordinate gallium halide coordination complexes are accessed by using macrocycles or porphyrins as the ligand which leads to a square based pyramidal geometry.¹⁰²⁻¹⁰⁵ Some trigonal bipyramidal complexes have also been reported.¹⁰⁶

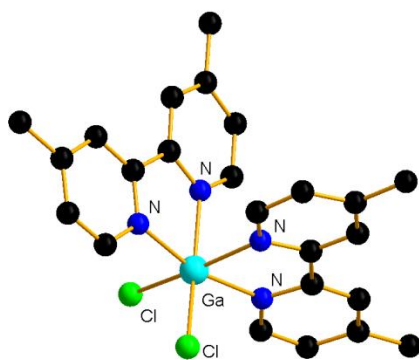


Figure 1.4 – View of the cation in *cis*-[GaCl₂(dmbpy)₂][GaCl₄]

Similarly to the coordination chemistry of GaX₃ with chalcogenoethers, the reaction of GaX₃ with phosphine ligands yields neutral complexes with distorted tetrahedral coordination at the Ga centre in the majority of examples.⁹⁷ Crystallographic studies with mono- and bi-dentate alkyl- and aryl-phosphines also indicate that distorted tetrahedral coordination at gallium is the preferred mode of coordination in these types of complex.¹⁰⁷⁻¹⁰⁹ The use of *o*-C₆H₄(PMe₂)₂ as a ligand to GaX₃ (X = Cl, Br, I) in a 1:1 stoichiometry leads to the formation of *trans*-[GaX₂{*o*-C₆H₄(PMe₂)₂}₂][GaX₄], which features an octahedral Ga cation, whereas the reaction with two equivalents of GaX₃ to one *o*-C₆H₄(PMe₂)₂ forms [GaX₂{*o*-C₆H₄(PMe₂)₂}][GaX₄], which has a distorted tetrahedral cation.¹¹⁰ An analogous structure was obtained by using the ligand *o*-C₆H₄(PPh₂)₂, which has sufficient steric bulk to prevent the formation of a complex with two ligands chelating to [GaX₂]⁺.

The coordination chemistry of GaX₃ with arsines also shows the preference for Ga to adopt a 4-coordinate, tetrahedral geometry. The reaction of GaX₃ with R₃As (R = Ph, Me) forms complexes with distorted tetrahedral coordination at Ga.^{89, 97, 111} Reaction

with *o*-C₆H₄(AsMe₂)₂ produces the ionic species [GaX₂{*o*-C₆H₄(AsMe₂)₂}][GaX₄], which exhibits 4-coordinate Ga. The bidentate ligand Ph₂As(CH₂)₂AsPh₂ also adopts a distorted tetrahedral geometry at Ga in the complex [GaI₃{*μ*-Ph₂As(CH₂)₂AsPh₂}GaI₃]. The tripodal arsine MeC(CH₂AsMe₂)₃, however, showed differing coordination modes dependant on the halide.¹¹² GaCl₃ forms either [{MeC(CH₂AsMe₂)₃-κAs:κ²As'As''}(GaCl₃)(GaCl₂)]⁺[GaCl₄]⁻ (Figure 1.5a) in which the triarsine forms a bidentate chelate to the GaCl₂⁺ and the third As donor binds to an additional GaCl₃ or [{Me₂AsCH₂C(Me)(CH₂AsMe₂)₂-κ²AsAs'}GaCl₂]⁺[GaCl₄]⁻ (Figure 1.5b) with bidentate chelation to the GaCl₂⁺ and the third As donor remaining uncoordinated. GaI₃ forms [{*μ*₃-MeC(CH₂AsMe₂)₃-κAs:κAs':κAs''}(GaI₃)₃], a 3:1 adduct with one GaI₃ coordinating in a distorted tetrahedral geometry at each As donor (Figure 1.5c).

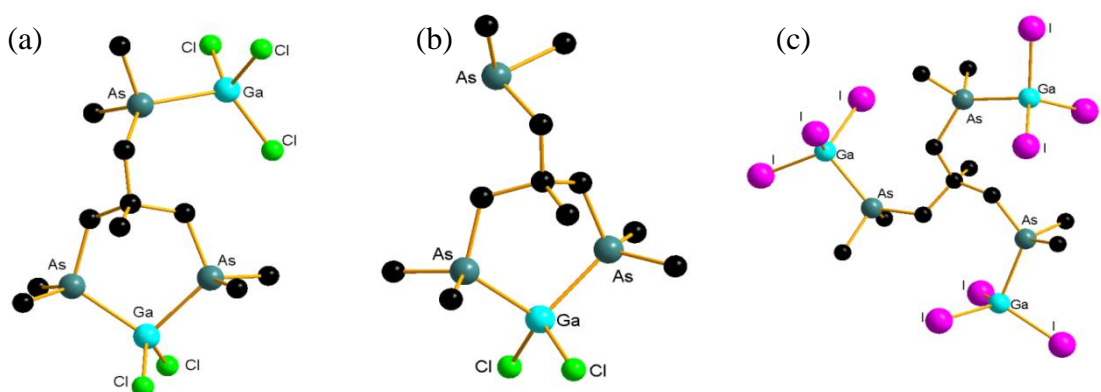


Figure 1.5 – Structures of (a) [{MeC(CH₂AsMe₂)₃-κAs:κ²As'As''}(GaCl₃)(GaCl₂)]⁺; (b) [{Me₂AsCH₂C(Me)(CH₂AsMe₂)₂-κ²AsAs'}GaCl₂]⁺; (c) [{*μ*₃-MeC(CH₂AsMe₂)₃-κAs:κAs':κAs''}(GaI₃)₃]

1.3.3 Coordination complexes of indium halides

Early work on the complexation of InX₃ (X = Cl, Br, I) with Me₂S, Et₂S and tetrahydrothiophene reported that stable 1:2 complexes formed, with 1:1 and 1:3

complexes also possible for InI_3 , although no structural data was reported.¹¹³ Later IR spectroscopic data were reported, leading to assignment of the $[\text{InX}_3(\text{Et}_2\text{S})_2]$ ($\text{X} = \text{Cl}, \text{Br}$) complexes as having D_{3h} symmetry.¹¹⁴

Previous work in the Southampton group has also investigated the coordination chemistry of indium trihalides with neutral mono- and bi-dentate thio- and selenoethers.¹¹⁵ In contrast to the analogous reactions with GaX_3 , the indium halide complexes show a much wider variety of coordination geometries and coordination numbers. Four-, five- and six- coordinate neutral complexes of mono-, bi- and tri-dentate ligands; ionic complexes of the form $[\text{InX}_2\text{L}][\text{InX}_4]$ with some bidentate and macrocyclic ligands, for example $[\text{InCl}_2\{\text{}^i\text{PrS}(\text{CH}_2)_2\text{S}^i\text{Pr}\}_2][\text{InCl}_4]$ (Figure 1.6a) and $[\text{InCl}_2([\text{14}]\text{aneS}_4)][\text{InCl}_4]$ (Figure 1.6b); and indium(III) halo-bridged octahedral dimers with bidentate ligands $[\text{InX}_2(\text{L-L})(\mu\text{-X})_2\text{InX}_2(\text{L-L})]$ (Figure 1.6c) were characterised. The ability to access higher coordination numbers for indium may be explained by the significantly larger ionic radius (0.80 Å) of indium(III) compared with that of gallium(III) (0.62 Å).⁵⁸

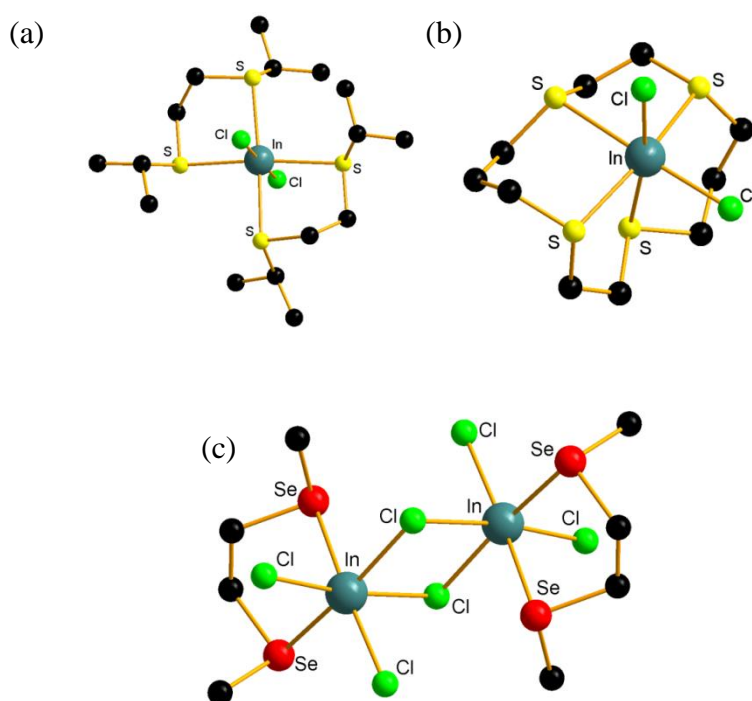


Figure 1.6 – Structures of (a) $[\text{InCl}_2\{\text{}^i\text{PrS}(\text{CH}_2)_2\text{S}^i\text{Pr}\}_2]^+$; (b) $[\text{InCl}_2([\text{14}]\text{aneS}_4)]^+$; (c) $[\text{In}_2\text{Cl}_6\{\text{CH}_3\text{Se}(\text{CH}_2)_2\text{SeCH}_3\}_2]$

The reaction of InCl_3 with constrained chalcogenoethers yields a much wider range of chemistry.⁹¹ For example, reaction of InCl_3 with $o\text{-C}_6\text{H}_4(\text{CH}_2\text{SEt})_2$ forms a 4:3 complex $[(\text{InCl}_3)_4\{o\text{-C}_6\text{H}_4(\text{CH}_2\text{SEt})_2\}_3]$ (Figure 1.7), consisting of discrete tetranuclear moieties in which the central In atom is octahedrally coordinated to six bridging Cl's, while the three In atoms on the edges have two bridging Cl's, two terminal Cl's and two mutually *trans* S-donor atoms from different dithioether ligands.

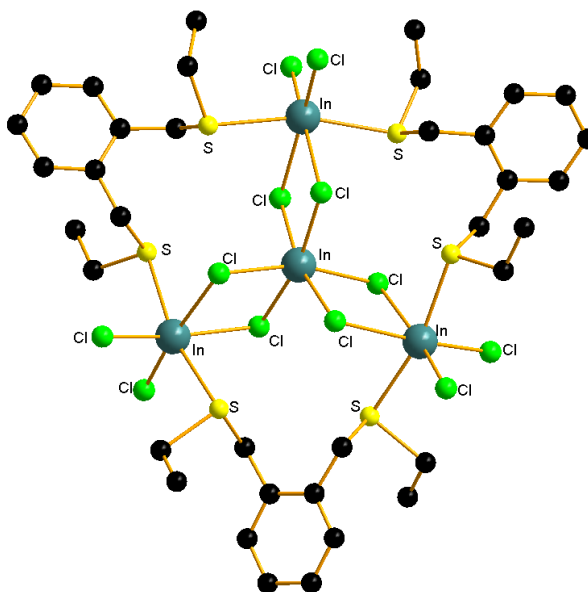


Figure 1.7 – Crystal structure of the complex $[(\text{InCl}_3)_4\{o\text{-C}_6\text{H}_4(\text{CH}_2\text{SEt})_2\}_3]$

Wieghardt *et al.* reported the synthesis of $[\text{InCl}_3([\text{9}]ane\text{S}_3)]$, which is characterised by elemental analysis and IR spectroscopy.¹¹⁶ The authors also describe the reaction of indium halides with $[\text{9}]ane\text{N}_3$ and $\text{Me}_3[\text{9}]ane\text{N}_3$. All complexes contain 6-coordinate $\text{In}(\text{III})$, which sits above the plane of the macrocycle with facial chlorides. More recent attempts to crystallise $[\text{InCl}_3([\text{9}]ane\text{S}_3)]$ have failed due to its poor solubility but other characterisation data support the assignment of a *fac*-octahedral structure.¹¹⁵

There are large number of reported crystal structures of coordination complexes of indium(III) halides with oxygen donor ligands. Coordination of InX_3 with thf yield the 5-coordinate species $[\text{InCl}_3(\text{thf})_2]$ ¹¹⁷⁻¹¹⁹ and $[\text{InBr}_3(\text{thf})_2]$ ¹²⁰ which have a trigonal

bipyramidal structure with axial thf coordination. A 6-coordinate, distorted octahedral species $[\text{InCl}_3(\text{thf})_3]$ is also accessible.^{121, 122} Use of DMSO as an oxygen donor yields $[\text{InX}_3(\text{Me}_2\text{SO})_3]$ ($\text{X} = \text{Cl}, \text{Br}$)¹²³ and $[\text{InI}_2(\text{Me}_2\text{SO})_4][\text{InI}_4]$ ¹²⁴ although conductivity measurements suggest that this is not indicative of the solution behaviour for the iodide complex. Coordination complexes of InX_3 with phosphine oxide ligands can form either neutral or ionic species. $[\text{InCl}_3(\text{OPMe}_3)_3]$ has *mer* octahedral geometry, whereas $[\text{InX}_2(\text{OPPh}_3)_4][\text{InX}_4]$ ($\text{X} = \text{Cl}, \text{Br}$) have an octahedral cation with *trans* halides.¹²³ Using $\text{OP}(\text{Me}_2\text{N})_3$ as a ligand for InI_3 results in the formation of an octahedral cation with *trans* iodine atoms in $[\text{InI}_2(\text{OP}(\text{Me}_2\text{N})_3)_4]\text{I}$.¹²⁵ Reaction of InI_3 with $(\text{MeOC}_6\text{H}_4)_3\text{PO}$ yields a 5-coordinate complex with two phosphine oxide ligands *trans* in a trigonal bipyramidal geometry.¹²⁶ Similarly $\text{OP}((\text{CH}_3)_2\text{N})_3$ gives a 5-coordinate, $[\text{InCl}_3][\text{OP}((\text{CH}_3)_2\text{N})_3)_2]$ with *cis* chlorides in a trigonal bipyramidal geometry.¹²⁷ Using OAsMe_3 as a ligand gives a ligand bridged dimer with the formula $[(\text{InX}_3)_2(\text{OAsMe}_3)_3]$ ($\text{X} = \text{Cl}, \text{Br}$) (Figure 1.8).^{123, 128}

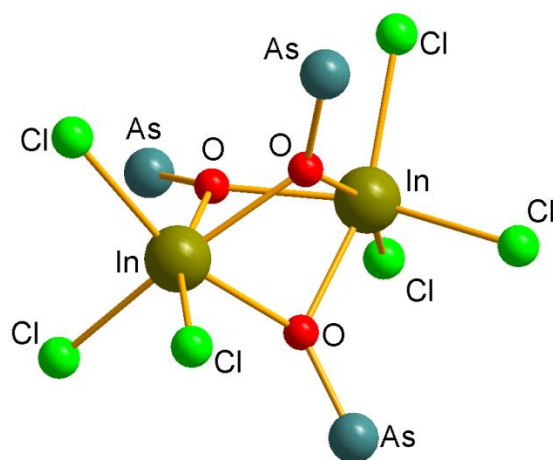


Figure 1.8 – Structure of $[(\text{InCl}_3)_2(\text{OAsMe}_3)_3]$. Methyl groups omitted for clarity.

There are also some examples of coordination complexes using bidentate oxygen donor ligands. 1,2-dimethoxyethane (DME) forms a complex with InCl_3 with the formula $[(\text{InCl}_3)_2(\text{DME})_3]$.¹²⁹ This complex has 6-coordinate indium with one DME chelating at each indium centre and a further DME bridging between the two $\text{InCl}_3(\text{DME})$ units (Figure 1.9). $[\text{InBr}_3(\text{DME})(\text{MeCN})]$, which has a chelating DME, can be obtained from

the reaction of ${}^i\text{PrInBr}_2$ with DME in MeCN.¹³⁰ In thf, acetylacetonate (acac) will form a chelate complex with the formula $[\text{InBr}_2(\text{acac})(\text{thf})_2]$ with distorted octahedral coordination, featuring *trans* thf donors and *cis* Br atoms.^{131, 132}

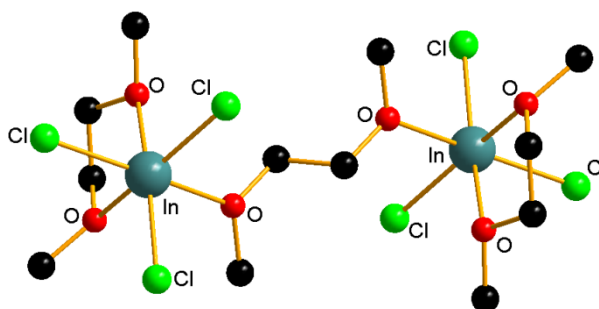


Figure 1.9 – Structure of $[(\text{InCl}_3)_2(\text{DME})_3]$

A range of coordination complexes of indium halides with Group 15 donor ligands have also been characterised. The use of mono-, bi- and tridentate N donor ligands has yielded complexes with distorted tetrahedral, trigonal bipyramidal and octahedral coordination geometries.¹³³⁻¹³⁵ *Trans* trigonal bipyramidal coordination was also observed by using two equivalents of a monodentate donor.¹³⁶ Reaction of InBr_3 with the cyclic N donor ligands $\text{Me}_3[6]\text{aneN}_3$ and $\text{Me}_3[9]\text{aneN}_3$ give octahedral complexes with *fac* coordination of the ligand.¹²⁰ In contrast, use of the cyclic cross-bridged tetradentate ligands based on $[12]\text{aneN}_4$ and $[14]\text{aneN}_4$ yield ionic species with the formula $[\text{InBr}_2(\text{L})]\text{Br}$ (Figure 1.10).¹³⁷

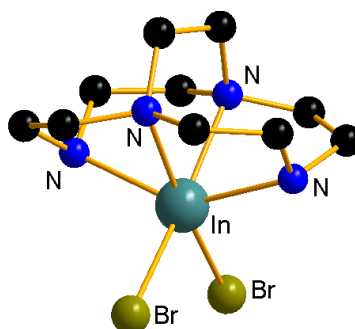


Figure 1.10 – Structure of $[\text{InBr}_2(1,4,7,10\text{-tetraazabicyclo}[5.5.2]\text{tetradecane})]^+$

The use of phosphine donors yields a wider variety of coordination geometries. InCl_3 reacts with tris(2,4,6-trimethoxyphenyl)phosphine to give a distorted tetrahedral complex.¹²⁶ Neutral, distorted tetrahedral species were reported from the 1:1 reaction of InI_3 with secondary and tertiary phosphines¹³⁸ whereas the reaction of two equivalents of Ph_2MeP or PhMe_2P with InX_3 ($\text{X} = \text{Br}, \text{I}$) yields a distorted trigonal bipyramidal species with *trans* phosphine donors.¹³⁹ Other work has confirmed that, depending on the stoichiometry of phosphine to indium halide, both 1:1 and 2:1 adducts are accessible.¹⁴⁰⁻¹⁴³ The bidentate ligand bis(diphenylphosphino)ethane (dppe) has been shown to coordinate in two crystallographically distinct ways. One reaction gave a ligand bridged species with two InI_3 moieties attached to each P donor (Figure 1.11a)¹⁴⁴ whereas another reaction gave a species with the formula $[(\text{InI}_3)_2(\text{dppe})_3]$, which has one dppe bridging between each InI_3 unit with one further dppe coordinated *trans* on each InI_3 via only one P donor (Figure 1.11b).¹⁴⁵

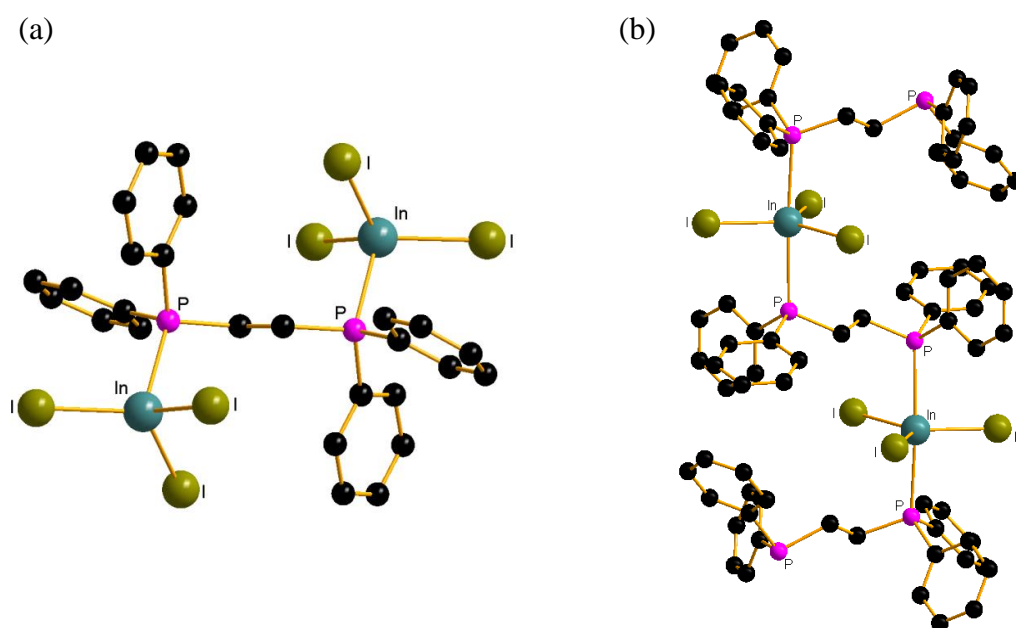


Figure 1.11 – Structures of (a) $[(\text{InI}_3)_2(\text{dppe})]$; (b) $[(\text{InI}_3)_2(\text{dppe})_3]$

Reaction of InCl_3 with $o\text{-C}_6\text{H}_4(\text{PPh}_2)_2$ gave a bis-chelated cation $[\text{InCl}_2(o\text{-C}_6\text{H}_4(\text{PPh}_2)_2)_2][\text{InCl}_4]$ whereas the 1:1 reaction of InX_3 ($\text{X} = \text{Br}, \text{I}$) with the same ligand gave a neutral species $[\text{InX}_3(o\text{-C}_6\text{H}_4(\text{PPh}_2)_2)]$. Using two equivalents of InX_3 ($\text{X} = \text{Cl}, \text{Br}, \text{I}$) gave no new species for $\text{X} = \text{Cl}$, but produced $[\text{InX}_2(o\text{-C}_6\text{H}_4(\text{PPh}_2))][\text{InX}_4]$ for X

= Br or I.¹⁴⁶ Reacting InX_3 with $o\text{-C}_6\text{H}_4(\text{PMe}_2)_2$ yielded the ionic species $[\text{InX}_2(o\text{-C}_6\text{H}_4(\text{PMe}_2)_2)]^+[\text{InX}_4]^-$ ($\text{X} = \text{Cl}, \text{Br}, \text{I}$) (Figure 1.12a), $[\text{InBr}_2\{o\text{-C}_6\text{H}_4(\text{PMe}_2)_2\}_2]^+[\text{InBr}_4]^-$ (Figure 1.12b), $[\text{InI}_2\{o\text{-C}_6\text{H}_4(\text{PMe}_2)_2\}_2]^+[\text{InI}_4\{o\text{-C}_6\text{H}_4(\text{PMe}_2)_2\}]^-$ (Figure 1.12c) as well as the chloro-bridged dimer $[\text{In}_2\text{Cl}_6\{o\text{-C}_6\text{H}_4(\text{PMe}_2)_2\}_2]$ (Figure 1.12d). $[\text{In}_2\text{Cl}_5\{o\text{-C}_6\text{H}_4(\text{PMe}_2)_2\}_2]_n^+[\text{InCl}_4]_n^-$ (Figure 1.12e) was also crystallographically characterised but was not a major product.¹¹⁰

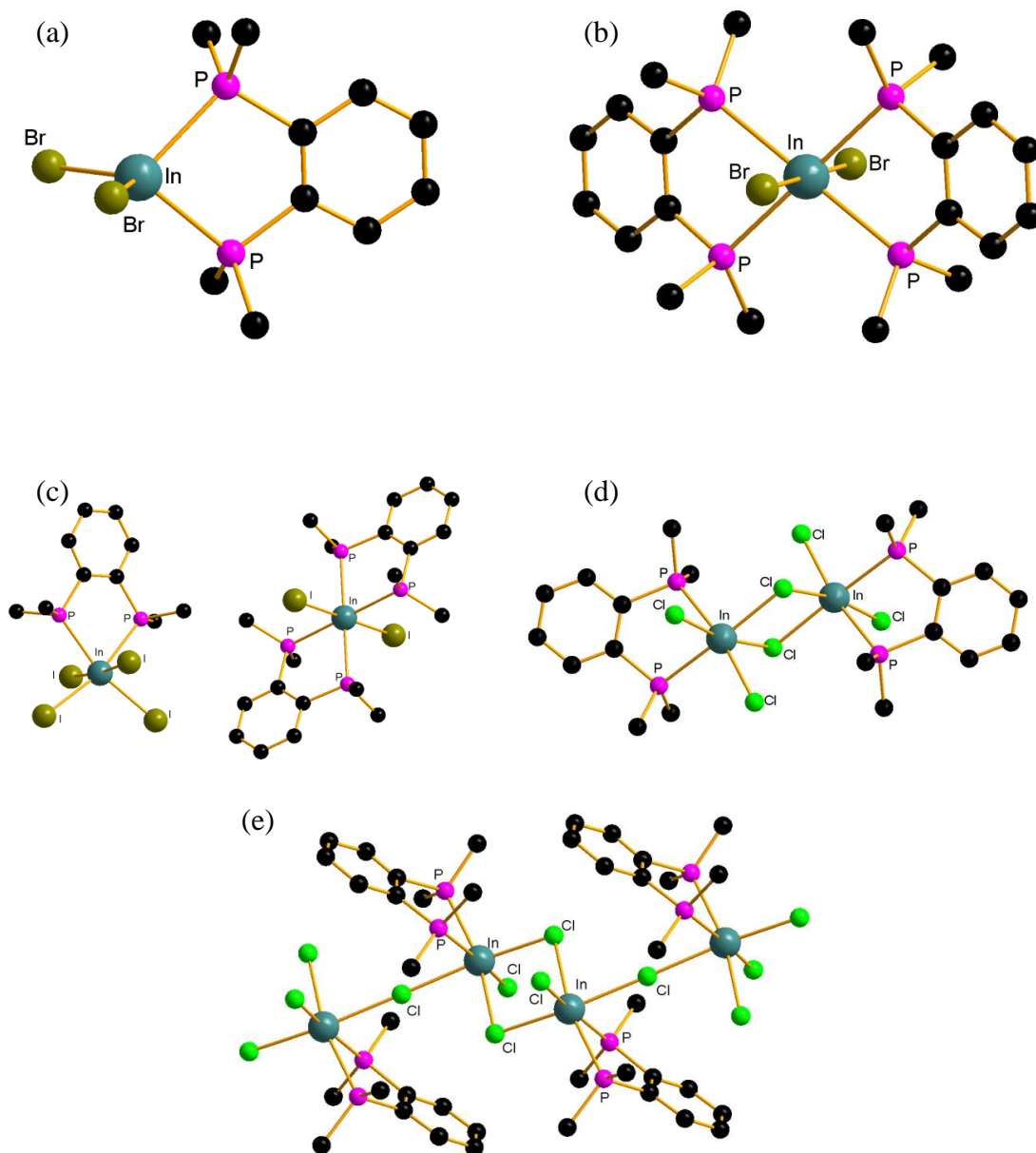


Figure 1.12 – Structures of (a) $[\text{InBr}_2(o\text{-C}_6\text{H}_4(\text{PMe}_2)_2)]^+$; (b) $[\text{InBr}_2\{o\text{-C}_6\text{H}_4(\text{PMe}_2)_2\}_2]^+$; (c) $[\text{InI}_2\{o\text{-C}_6\text{H}_4(\text{PMe}_2)_2\}_2]^+[\text{InI}_4\{o\text{-C}_6\text{H}_4(\text{PMe}_2)_2\}]^-$; (d) $[\text{In}_2\text{Cl}_6\{o\text{-C}_6\text{H}_4(\text{PMe}_2)_2\}_2]$; (e) part of the chain polymer $[\text{In}_2\text{Cl}_5\{o\text{-C}_6\text{H}_4(\text{PMe}_2)_2\}_2]_n^+$

There are fewer reports of coordination complexes of In(III) halides with arsines. Reaction of Ph_3As with InI_3 yields both $[\text{InI}_3(\text{AsPh}_3)]$ and $[\text{InI}_3(\text{AsPh}_3)_2]$.¹⁴¹ The reaction of InX_3 with the ligand $o\text{-C}_6\text{H}_4(\text{AsMe}_2)_2$ yields a large number of different coordination complexes.¹¹⁰ The 1:1 reaction produces $[\text{In}_2\text{X}_6\{o\text{-C}_6\text{H}_4(\text{AsMe}_2)_2\}_2]$ for $\text{X} = \text{Cl}$ or Br (Figure 1.13a) and $[\text{InI}_2\{o\text{-C}_6\text{H}_4(\text{AsMe}_2)_2\}_2][\text{InI}_4\{o\text{-C}_6\text{H}_4(\text{AsMe}_2)_2\}]$ for $\text{X} = \text{I}$. In all cases these can further react to give $[\text{InX}_2\{o\text{-C}_6\text{H}_4(\text{AsMe}_2)_2\}_2][\text{InX}_4]$ ($\text{X} = \text{Cl}, \text{Br}, \text{I}$). The 2:1 reaction of InX_3 with $o\text{-C}_6\text{H}_4(\text{AsMe}_2)_2$ produces $[\text{InX}_2(o\text{-C}_6\text{H}_4(\text{AsMe}_2)_2)][\text{InX}_4]$ (Figure 1.13b). By reacting >3 equivalents of InCl_3 with $o\text{-C}_6\text{H}_4(\text{AsMe}_2)_2$ it was possible to isolate the species $[\text{In}_2\text{Cl}_5\{o\text{-C}_6\text{H}_4(\text{AsMe}_2)_2\}_2]_n[\text{InCl}_4]_n$, which has a polymeric cation (Figure 1.13c).^{110, 147}

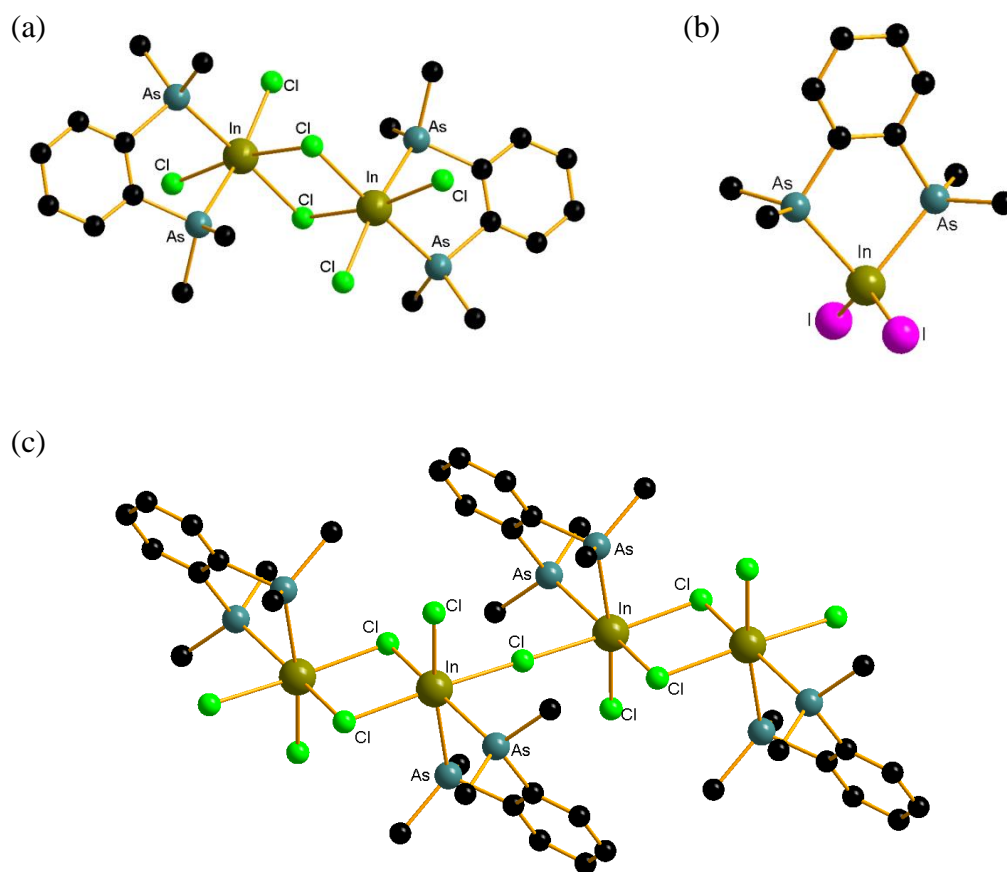


Figure 1.13 – Structures of (a) $[\text{In}_2\text{Cl}_6\{o\text{-C}_6\text{H}_4(\text{AsMe}_2)_2\}_2]$; (b) $[\text{InI}_2(o\text{-C}_6\text{H}_4(\text{AsMe}_2)_2)][\text{InI}_4(o\text{-C}_6\text{H}_4(\text{AsMe}_2)_2)]^+$; (c) $[\text{In}_2\text{Cl}_5\{o\text{-C}_6\text{H}_4(\text{AsMe}_2)_2\}_2]_n^+$

1.4 Chalcogenoether synthesis

Thioethers are typically prepared by the reaction of a thiol with an alkyl halide or an alkene.¹⁴⁸⁻¹⁵⁰ Many of the simple, dialkyl thioethers are commercially available, unlike the corresponding seleno- or telluro-ethers.

The acyclic chalcogenoethers R_2E ($E = Se, Te$) can be synthesised in good yield by the reaction of freshly ground selenium or tellurium in thf with RLi , followed by the addition of RCl . The reaction mixture is frozen in a liquid N_2 bath before addition of RLi , then allowed to warm to room temperature, forming a colourless solution of $RELi$, which is then refrozen and RCl added. By performing the reaction at low temperatures, the formation of diselenide species is less favoured. The reaction is then allowed to warm to room temperature again and stirred for 2 hours before removal of all solvent *in vacuo*, extraction with hexane and purification by distillation. In order to prepare the bidentate ligands $RE(CH_2)_nER$, a stoichiometric quantity of $Cl(CH_2)_nCl$ is added after the formation of $RELi$.¹⁵¹⁻¹⁵³ It is not possible to synthesise $RTe(CH_2)_2TeR$ due to the weak $Te-C$ bond, which leads to the elimination of ethene and the formation of R_2Te_2 instead, however $RTe(CH_2)_nTeR$ ($n = 1,3$) are accessible.¹⁵³ This route works best for ligands where $R = Me, ^nBu, ^tBu$ or Ph as solutions of these alkyl lithiums are most stable and therefore commercially available. Alternative methods for the synthesis of dialkyl chalcogenides includes the reaction of a dialkyl dichalcogenide (R_2E_2) with a Grignard reagent ($R'MgCl$); the reaction of the elemental chalcogen with sodium and $NaBH_4$ to form E^{2-} followed by addition of an alkyl halide; or the reaction of the elemental chalcogen (S, Se or Te) in $Na/NH_3(l)$ with an alkyl halide.^{154, 155}

All the chalcogenoethers are malodorous due to their volatility, although typically less so than the corresponding thiols, selenols and tellurols. Selenoethers and telluroethers are toxic and must be handled carefully. Thioethers and selenoethers are air and moisture stable, whereas telluroethers are stable to moisture but are mildly air sensitive.

For a discussion of the synthesis of macrocyclic chalcogenoethers see 2.1.1.

1.5 Characterisation of coordination complexes

This section will describe some of the characterisation techniques used to identify the coordination complexes and single source precursors synthesised as part of this thesis. These techniques can be used to provide compositional and structural information.

1.5.1 Nuclear magnetic resonance spectroscopy

^1H , ^{13}C , ^{27}Al , ^{71}Ga , ^{77}Se , ^{115}In and ^{125}Te NMR spectroscopy are used throughout this project to characterise the compounds synthesised. The property of the nucleus responsible for the NMR effect is called nuclear spin (I). The ease with which NMR spectra can be obtained is affected by several factors, including the natural abundance of the isotope studied, the chemical shift range and, for nuclei with $I > 1/2$, the quadrupole moment of the isotope being observed.⁸⁸

An asymmetric environment surrounding the nucleus will lead to differences in the electron density, which cause an electric field gradient. The nucleus will always try to orientate itself to the lowest energy position. For nuclei with $I = 1/2$, this is possible, however, nuclei with $I > 1/2$ will not be able to find an orientation with minimum energy and will therefore keep moving to try to orientate the nucleus, causing a loss in energy. This very fast loss of energy means that quadrupolar relaxation is very fast and so the nucleus quickly returns to the ground state. As the lifetime of the excited state is very small, the associated uncertainty in the lifetime is very small. This causes line broadening due to the Heisenberg uncertainty principle, which states that the more precisely the position of a particle is known, the less precisely its energy can be determined, and *vice versa*. As the uncertainty in the relaxation time is very small, there is an increase in the uncertainty in the position of the NMR signal, leading to line broadening. In some cases the line broadening is so severe that it is broader than the NMR window and no signal can be observed. Nuclei in a symmetric environment will have a uniform electric field gradient, leading to a relaxation time longer than that of nuclei in an asymmetric environment, hence reducing line broadening. This often allows species such as $[\text{GaCl}_4]^-$ to be observed in $^{71}\text{Ga}\{^1\text{H}\}$ NMR spectra whereas lower symmetry species may not be observable due to line broadening. It is sometimes

possible to observe complexes with C_{3v} symmetry as the electric field gradient can be close to zero. This has allowed ^{71}Ga NMR spectra to be obtained for most complexes of GaX_3 ($X = \text{Cl, Br, I}$) with acyclic chalcogenoethers, which have C_{3v} symmetry at gallium, although linewidths are typically 2000-9000 Hz ($W_{1/2}$).⁸⁷ Table 1.1 lists the natural abundance, spin and, where applicable, quadrupole moment for the NMR nuclei studied in this thesis.

Isotope	Natural Abundance (%)	Spin	Quadrupole Moment (10^{-28} m^2)	Resonant frequency (MHz)
^1H	99.99	1/2	n/a	100
^{13}C	1.11	1/2	n/a	25.1
^{27}Al	100	5/2	0.14	26.1
^{71}Ga	39.6	3/2	0.11	30.6
^{77}Se	7.58	1/2	n/a	19.1
^{115}In	95.72	9/2	0.86	22.0
^{125}Te	6.99	1/2	n/a	31.5

Table 1.1 – Properties of selected NMR nuclei⁸⁸

The NMR shift is also dependent on external factors such as temperature and solvent, which may change the electronic environment around the nuclei.⁸⁸ It is important to ensure that NMR resonances are correctly referenced. Typically ^1H and ^{13}C NMR spectroscopy is referenced to an internal standard i.e. the residual proton signals of a deuterated solvent. ^{27}Al , ^{71}Ga and ^{115}In are referenced to an external standard of aqueous $[\text{M}(\text{H}_2\text{O})_6]^{3+}$ at $\text{pH} = 1$. ^{77}Se and ^{125}Te are referenced to external, neat Me_2E . These are used neat as their shifts are dependent on concentration. When selecting a reference it is important that it is easily available, has a consistent chemical shift with a sharp signal with no coupling.

1.5.2 Vibrational spectroscopy

Vibrational spectroscopy comprises the complementary techniques of Infra-Red (IR) and Raman spectroscopy.¹⁵⁶ These spectroscopic techniques can provide information about the types of bonds present and the symmetry of the species.

When radiation of a specific energy corresponding to vibrational transitions in a molecule is absorbed and a change in dipole occurs, IR absorptions are produced. Raman spectra are produced when light is scattered leading to a Stokes or anti-Stokes emission from a molecule occurs, leading to a change in the polarisability of the molecule. Stokes and anti-Stokes emissions occur when energy is absorbed and then reemitted minus or plus a quantum of vibrational energy corresponding to the excitation energy.¹⁵⁶ Figure 1.14 shows the changes that occur when the system is excited by incoming light. In the majority of cases there is no energy lost (Rayleigh scattering) and so the system returns to the same vibrational level, whereas Stokes scattering leads to a loss of energy and hence a return to a higher vibrational level. Anti-Stokes scattering leads to a gain in energy and a return to a lower vibrational energy level, requiring the electron to be in a vibrational level that is higher than the ground state. As the higher energy states are less populated than the ground state, there is less anti-Stokes scattering and so the emissions are weaker than for Stokes scattering.

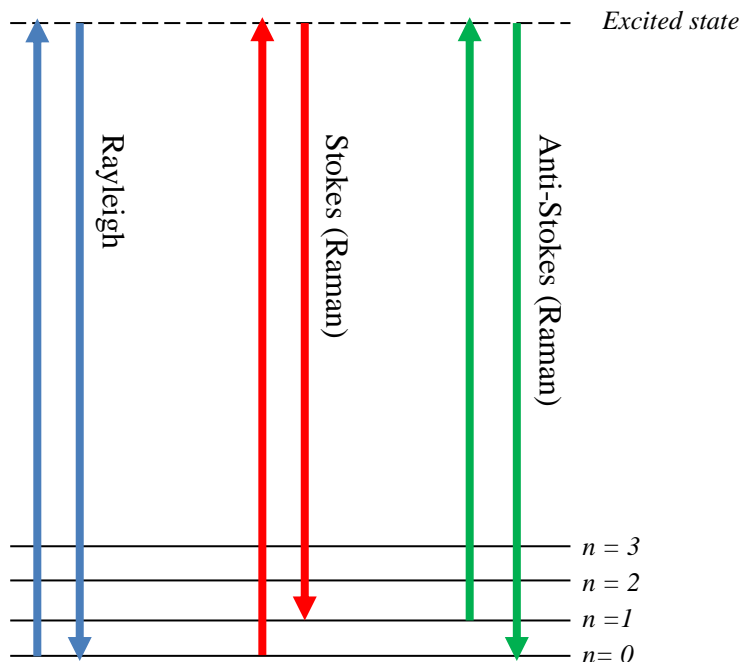


Figure 1.14 – Schematic diagram of Rayleigh and Raman scattering

The tetrahedral $[\text{MCl}_4]^-$ anions ($\text{M} = \text{Al}, \text{Ga}, \text{In}$) have characteristic stretches that can be identified in IR and Raman spectra (Table 1.2).¹⁵⁷ The vibrational stretches of a more complex molecule, however, may be more difficult to interpret.

	$\text{a}_1 - \text{Raman active} / \text{cm}^{-1}$	$\text{t}_2 - \text{Raman and IR active} / \text{cm}^{-1}$
$[\text{AlCl}_4]^-$	348	498
$[\text{GaCl}_4]^-$	343	370
$[\text{InCl}_4]^-$	321	337

Table 1.2 – IR and Raman active stretches for $[\text{MCl}_4]^-$ ($\text{M} = \text{Al}, \text{Ga}, \text{In}$)

Group theory can be used to deduce the symmetry of the molecule being studied and therefore to work out how many IR and Raman active stretches will be observed. Samples do not need to be soluble, conferring a significant advantage over NMR spectroscopy.

1.5.3 Single crystal X-ray diffraction

Single crystal X-ray diffraction is a very useful technique as it can provide a significant amount of information on the structure of a molecule, including atom types and positions, bond lengths and bond angles. It is necessary, however, to grow a single crystal of the molecule to be studied, which is not always achievable. Single crystal X-ray structures must also be used in conjunction with other spectroscopic data in order to ascertain that the crystal structure is representative of the bulk product.

In a single crystal, all molecules are highly ordered and related by symmetry. When X-rays are directed at an atom, the electrons oscillate in the electric field of the X-ray beam and radiate X-rays at the same frequency as the incident beam. This process is known as Thomson scattering and the X-rays can be used to create a diffraction pattern. Heavier atoms, containing more electrons, diffract more strongly than lighter atoms so atom types can be identified relative to others in the molecule. As the molecules in the

crystal are arranged in a lattice, the diffraction pattern produced will have symmetry. From the diffraction pattern it is possible to produce an electron density map, which indicates the position of the atoms and their relative sizes. Through several cycles of refinement, the precise atom types and positions can be identified. By using indicators of the quality of the fit of the data, such as temperature factors and R values, it is possible to see how well the proposed suggestion matches the data and therefore if a correct structural determination has been made.¹⁵⁸

1.6 Thin film characterisation

This section will describe the techniques used to characterise the thin film samples that are discussed in this thesis. These techniques allow identification of the elements present in the thin film, analysis of its purity and provide information on the morphology of the surface. A brief overview of each technique is given herein. A more detailed description of the techniques is available in the Encyclopaedia of Materials Characterization: Surfaces, Interfaces, Thin Films¹⁵⁹ or more specific texts for each technique.¹⁶⁰⁻¹⁶⁶

1.6.1 Thin film X-ray diffraction

Powder X-Ray Diffraction (XRD) is a useful technique for the identification of polycrystalline materials that are not suitable for single crystal X-ray diffraction.^{167, 168} The diffraction pattern acquired depends upon the cell dimensions, cell symmetry and atom positions therefore powder XRD patterns can act as fingerprints for crystalline solids and database matching can allow for relatively simple assignment of a pattern.¹⁵⁶ It is also possible to identify the components of a mixture of crystalline substances.

Crystallites diffract the incident X-ray beam and, as they are randomly orientated in all directions, a diffraction pattern of circles is generated. Using the Bragg equation (Equation 1.1), it is possible to calculate the layer spacings that gave rise to the diffraction pattern and match them to a database. The intensities of the peaks can also yield information about the arrangement of the atoms in the crystal structure and heavier atoms will produce more intense peaks. By calculating the structure factor, which is related to the intensity of a peak, it is possible to derive atom positions, using the scattering factor for the atom in conjunction with the peak intensity. The phase problem arises as it is necessary to take the square root of the intensity hence the magnitude of the structure factor is known but not its sign, losing information about the phase, which is necessary to calculate the electron density distribution and atomic positions. In some cases, the sample has preferred orientation of crystallites due to the growth conditions. This will result in non-uniform circles in the diffraction pattern as well as non-standard intensities in the diffraction pattern generated.

$$n\lambda = 2d \sin \theta$$

Equation 1.1 – The Bragg equation. λ is the incident wavelength, d is the spacing between planes in the atomic lattice, θ is the scattering angle

The depth that the X-rays can penetrate into the sample is controlled by the incident angle of the X-rays. For thin film samples that are only a few microns thick, it is necessary to use a low incident angle (typically less than 5°) in order to avoid any contribution from the substrate, which would otherwise dominate the diffraction pattern. The X-ray beam also has an increased path length through the film, increasing the intensity of the diffraction. This technique is known as glancing angle or grazing incidence XRD.

XRD can also provide information on the crystallite size. The Scherrer equation (Equation 1.2) relates peak width to crystallite size with smaller crystallites producing broader peaks due to incoherent scattering from the edges of the crystallites. This equation does not account for instrumental broadening but this can be calculated by running a standard using the same conditions.

$$\tau = \frac{K\lambda}{\beta \cos \theta}$$

Equation 1.2 – The Scherrer equation for determining crystallite size. τ is the mean crystallite size, K is the Scherrer constant, λ is the X-ray wavelength, β is the FWHM line broadening, θ is the Bragg angle.

1.6.2 Raman spectroscopy

Raman spectroscopy, when applied to thin films, is able to measure the crystallinity of the sample.¹⁶⁷ Polycrystalline, particularly nanocrystalline, samples will lead to Raman spectra with broader lines than single crystal samples and amorphous samples have

lines so broad as to be unobservable.^{169, 170} The wavelength of the light scattered from the sample can also be compared to known wavelengths and the identity of the sample confirmed. Small shifts in the frequency occur due to stress and strain in the sample^{171, 172} as well as sample microcrystallinity.^{169, 173} By using a very focussed laser beam, it is possible to examine very small areas of a sample.

Raman spectroscopy of crystalline solids differs from molecular vibrational spectroscopy in that it deals with phonons. There are two main types of phonon – acoustic (in phase) and optical (out of phase). These can either be longitudinal (when wave polarisation and wave propagation act in the same direction) or transverse (when wave polarisation and wave propagation are perpendicular).

1.6.3 X-ray photoelectron spectroscopy

X-Ray Photoelectron Spectroscopy (XPS) provides information about the elements in a sample and the environment in which they are in. A beam of X-rays is directed at the surface of the sample, interacting with the core level electrons and causing some of the electrons to be ejected from the inner orbitals of the atoms. As these electrons have specific energies that correlate to the atom they were ejected from, it is possible to measure the elements present in the sample. The energies of the electrons also vary slightly dependent on the environment of the atom, making it possible to identify elements in different oxidation states or bonded to different elements. It is necessary to do this under high vacuum to stop the electrons from interacting with the air. Although the X-rays can penetrate far into the sample, XPS can only give information on the top few nm as electrons cannot escape from a greater depth. As this method samples the top 5 nm of a sample, it can be necessary to etch the surface before XPS analysis to remove any surface oxide.¹⁶⁷

1.6.4 Scanning electron microscopy and energy dispersive X-ray spectroscopy

Scanning Electron Microscopy (SEM) is used to create a magnified image of the surface of thin film samples using an electron beam.¹⁶⁷ If the thin film to be studied is poorly or

non-conductive, it can be coated with a thin layer of a conductive material such as gold or carbon to prevent build-up of charge during the experiment. A narrow beam of electrons is then focussed at a point on the surface, causing electrons to be ejected from the surface of the thin film, which are detected by a positively charged grid placed above the sample. As this process is carried out across the sample, an image of the entire surface can be generated. This technique has advantages over optical microscopy as the electron wavelengths are much smaller than the photon wavelengths so a greater magnification and resolution can be achieved.

Energy Dispersive X-ray spectroscopy (EDX) is often carried out in conjunction with SEM. As the electrons from the SEM interact with the atoms in the surface, they cause excitation of electrons from lower to higher energy orbitals. As the electrons fall back to the lower energy orbitals, they emit X-rays that are characteristic of that atom and so it is possible to determine the elemental composition of the material being examined. EDX is not well suited to the study of light elements (<Na) as they produce fewer X-rays, favouring emission of Auger electrons instead. Technological problems can also limit the detection or accurate quantification of light elements, such as the detector window material, which often cannot allow X-ray transmission below certain energies. Recent developments in technology, however, have allowed for easier study of films containing light elements.¹⁷⁴ There can also be problems in obtaining accurate quantitative measurements from a sample if the X-ray peaks of the elements of interest overlap. In these circumstances Wavelength Dispersive X-ray spectroscopy (WDX) can be more useful as its higher resolution can identify the separate peaks. WDX is also better for accurately quantifying light atoms than EDX but is more time consuming and expensive to use.

1.6.5 Atomic force microscopy

Atomic Force Microscopy (AFM) is another method of studying the surface of a thin film.^{166, 175} A tip is attached to a cantilever and is moved over the surface.¹⁶⁷ The tip moves vertically in response to attractive and repulsive forces. The movement of the tip is amplified by a laser, which is attached to the cantilever, enabling a larger picture of

the topography of the surface to be generated. AFM can also be done in tapping mode. In tapping mode the tip is moved up and down at regular intervals and the interaction with the surface measured. Using tapping mode reduces the twisting of the tip that can occur due to lateral forces that also affect the tip. The effectiveness and resolution of AFM depends on the size of the tip used, with smaller tips giving better resolution. AFM has some advantages over SEM in that it doesn't need a coating for electronic conductivity and samples do not need to be under high vacuum to be studied.

The roughness of a surface studied by AFM can be quantified by measuring the deviation from a perfectly flat surface. There are several methods used to quantify the roughness. Root mean squared (RMS) roughness is the method used in this thesis. RMS roughness is given by the standard deviation of the z-values (height) of the sample. Due to the different methods used to calculate surface roughness, as well as the different methods of acquiring AFM data, it is difficult to compare surface roughness values reported in the literature. In this thesis all AFM samples were collected using the same method and all roughness values were calculated using the RMS method, allowing for comparison between the different thin film samples deposited.

1.6.6 Photoluminescence

Good quality semiconductors with very low levels of impurities will exhibit photoluminescence (PL). Photoluminescence is generated by the radiative relaxation of electronic excitations. The electronic excitations occur when the sample is excited with an optical source, generally a laser, which creates electron-hole pairs. When the electron-hole pairs recombine, photons can be emitted and detected. This process is known as radiative recombination and gives rise to a signal in the PL spectrum. It is also possible for non-radiative recombination to occur, which does not result in photons being emitted and hence does not yield any PL information. Surface recombination is usually non-radiative and modification of the surface, for example by etching or oxidation, can affect the PL intensity. It is also possible for photons to be reabsorbed within the sample; therefore it is important that the majority of the recombination processes are radiative. Typically the absorption depth is a few microns, so the bulk of a

thin film sample can be probed. A PL spectrum can give information about transition energies and can be used to determine electronic energy levels. To obtain the best quality spectral data, PL should be conducted at 5K, however good quality data can be obtained at room temperature.^{165, 167}

1.6.7 Electronic characterisation

The van der Pauw method can be used to measure the sheet resistance and Hall coefficient of a sample, which can provide information on the resistivity, carrier density and hole mobility of a material.^{176, 177} A four point probe is used to measure the voltage of an arbitrarily shaped area of a thin film with uniform thickness by applying a current. This allows the resistance of the sample to be calculated and, if the thickness is known, the resistivity can be calculated. A high resistivity for a crystalline thin film sample is important for PCM devices as it means a low reset current will be required, lowering the power consumption of the device.

By applying a magnetic field to the sample, the Hall voltage can also be measured, which can be used to determine carrier density, assuming that the current, magnetic field and film thickness are known. The measurement of the Hall voltage arises from the Hall effect, where a charged particle (in this case an electron) travelling in a magnetic field experiences a Lorentz force which is proportional to the strength of the field and its travelling velocity.

$$F_L = qvB$$

Equation 1.3 – Calculation of Lorentz force (F_L). q = particle charge; v = travelling velocity; B = magnetic field strength

For a semiconducting sample, the carrier velocity is proportional to the current applied on the sample.

$$v = \frac{I}{n_m A q}$$

Equation 1.4 – Calculation of carrier velocity (v). I = current; n_m = carrier density; A = cross sectional area of the material; q = elementary charge

After an external magnetic field is applied perpendicular to the direction of current flow, the experienced Lorentz force of the carriers will accumulate at one edge of the sample, allowing the Lorentz force in this case to be written as:

$$F_L = \frac{IB}{n_m A}$$

Equation 1.5 – Lorentz force experienced by carriers after the application of an external magnetic field

The accumulation of carriers at one edge of the sample will create an electric field across the material due to the uneven distribution of charge resulting in a potential difference across the sample known as the Hall voltage (V_H). The electric field exerted on the carrier counteracts the Lorentz force to reach a balance where current will only flow along the material. Therefore the strength of the electric field can be obtained and the Hall voltage calculated. Once the Hall voltage has been calculated it is possible to calculate the carrier density.

$$V_H = wE = \frac{wIB}{qn_m A} = \frac{IB}{qn_m t}$$

Equation 1.6 – Calculation of Hall voltage (V_H). w = width of the material; E = electric field force; t = thickness of the material

The majority carrier mobility can also be calculated using the formula of semiconductor resistivity. The mobility is a measure of how easily the carriers can move under the influence of an electrical field.

$$\rho = \frac{1}{qn_m\mu_m}$$

Equation 1.7 – Formula of semiconductor resistivity (ρ). μ_m = majority carrier mobility

A high purity semiconductor will have a low carrier density and a high carrier mobility.

1.7 References

1. Yu, P. Y.; Cardona, M., *Fundamentals of Semiconductors*. Fourth ed.; Springer: Heidelberg, Germany, 2010.
2. Grundmann, M., *The Physics of Semiconductors*. Second ed.; Springer: Heidelberg, Germany, 2010.
3. Sealy, B. J., *J. I. Electron. Rad. Eng.* **1987**, *57*, S2.
4. Malik, R. J., *III-V Semiconductor Materials and Devices*. Elsevier Science: Amsterdam, The Netherlands, 1989; Vol. Seven.
5. Joyce, H. J.; Gao, Q.; Hoe Tan, H.; Jagadish, C.; Kim, Y.; Zou, J.; Smith, L. M.; Jackson, H. E.; Yarrison-Rice, J. M.; Parkinson, P.; Johnston, M. B., *Prog. Quant. Electron.* **2011**, *35*, 23-75.
6. Malik, M. A.; Afzaal, M.; O'Brien, P., *Chem. Rev.* **2010**, *110*, 4417-4446.
7. Woods, R. C.; Powell, A. L., *Eng. Sci. Educ. J.* **1994**, *3*, 271-275.
8. Welker, H. J., *IEEE Trans. Electron. Dev.* **1976**, *23*, 664-674.
9. Gleizes, A. N., *Chem. Vap. Deposition* **2000**, *6*, 155-173.
10. Raoux, S.; Wuttig, M., *Phase Change Materials*. Springer: New York, USA, 2009.
11. Breitwisch, M. J. In *Phase Change Memory, Interconnect Technology Conference, 2008. IITC 2008. International, 1-4 June 2008, 2008*; 2008; pp 219-221.
12. Wong, H. S. P.; Raoux, S.; SangBum, K.; Jiale, L.; Reifenberg, J. P.; Rajendran, B.; Asheghi, M.; Goodson, K. E., *Proc. IEEE* **2010**, *98*, 2201-2227.
13. Burr, G. W.; Breitwisch, M. J.; Franceschini, M.; Garetto, D.; Gopalakrishnan, K.; Jackson, B.; Kurdi, B.; Lam, C.; Lastras, L. A.; Padilla, A.; Rajendran, B.; Raoux, S.; Shenoy, R. S., *J. Vac. Sci. Technol. B* **2010**, *28*, 223-262.
14. Raoux, S., *Ann. Rev. Mater. Res.* **2009**, *39*, 25-48.
15. Caldwell, M. A.; Jeyasingh, R. G. D.; Wong, H. S. P.; Milliron, D. J., *Nanoscale* **2012**, *4*, 4382-4392.
16. Lee, B.-S.; Bishop, S., Optical and Electrical Properties of Phase Change Materials. In *Phase Change Materials*, Raoux, S.; Wuttig, M., Eds. Springer US: 2009; pp 175-198.
17. Persin, M.; Celustka, B., *Fizika (Zagreb)* **1976**, *8*, Suppl., 92-4.

18. Heon, L.; Young Keun, K.; Donghwan, K.; Dae-Hwan, K., *IEEE Trans. Magn.* **2005**, *41*, 1034-1036.
19. Bekheet, A. E., *Eur. Phys. J. - Appl. Phys.* **2001**, *16*, 187-193.
20. Bekheet, A. E., *J. Electron. Mater.* **2008**, *37*, 540-544.
21. Lee, H.; Kang, D.-H.; Tran, L., *Mater. Sci. Eng., B* **2005**, *119*, 196-201.
22. Yu, B.; Ju, S.; Sun, X.; Ng, G.; Nguyen, T. D.; Meyyappan, M.; Janes, D. B., *Appl. Phys. Lett.* **2007**, *91*, 133119.
23. Mafi, E.; Soudi, A.; Gu, Y., *J. Phys. Chem. C* **2012**, *116*, 22539-22544.
24. Baek, C.-K.; Kang, D.; Kim, J.; Jin, B.; Rim, T.; Park, S.; Meyyappan, M.; Jeong, Y.-H.; Lee, J.-S., *Solid-State Electron.* **2013**, *80*, 10-13.
25. Jin, B.; Kang, D.; Kim, J.; Meyyappan, M.; Lee, J.-S., *J. Appl. Phys.* **2013**, *113*, 164303-6.
26. Zhu, H.; Yin, J.; Xia, Y.; Liu, Z., *Appl. Phys. Lett.* **2010**, *97*, 083504-3.
27. Barron, A. R., *Adv. Mater. Opt. Electron.* **1995**, *5*, 245-258.
28. MacInnes, A. N.; Power, M. B.; Barron, A. R.; Jenkins, P. P.; Hepp, A. F., *Appl. Phys. Lett.* **1993**, *62*, 711-713.
29. Bezryadin, N. N.; Kotov, G. I.; Kuzubov, S. V.; Arsent'ev, I. N.; Tarasov, I. S.; Starodubtsev, A. A.; Sysoev, A. B., *Tech. Phys. Lett.* **2008**, *34*, 428-430.
30. Plis, E. A.; Kutty, M. N.; Krishna, S., *Laser Photonics Rev.* **2013**, *7*, 45-59.
31. Pernot, P. J.; Barron, A. R., *Chem. Vap. Deposition* **1995**, *1*, 75-78.
32. Kenty, J. L., *J. Electron. Mater.* **1973**, *2*, 239-254.
33. Chung, T.; Walter, G.; Holonyak, N., *J. Appl. Phys.* **2005**, *97*.
34. Afzaal, M.; O'Brien, P., *J. Mater. Chem.* **2006**, *16*, 1597-1602.
35. Ludowise, M. J., *J. Appl. Phys.* **1985**, *58*, R31-R55.
36. Zaouk, A.; Salvetat, E.; Sakaya, J.; Maury, F.; Constant, G., *J. Cryst. Growth* **1981**, *55*, 135-144.
37. Ozeki, M.; Haraguchi, T.; Takeuchi, T.; Maeda, K., *J. Cryst. Growth* **2005**, *276*, 374-380.
38. Ruiz, A.; Gonzalez, L.; Mazuelas, A.; Briones, F., *Appl. Phys. A-Mater. Sci. Process.* **1989**, *49*, 543-545.
39. Bertone, D., *J. Electron. Mater.* **1992**, *21*, 265-268.
40. Pi, B.; Shu, Y. C.; Lin, Y. W.; Sun, J. M.; Qu, S. C.; Yao, J. H.; Xing, X. D.; Xu, B.; Shu, Q.; Wang, Z. G.; Xu, J., *J. Cryst. Growth* **2007**, *299*, 243-247.
41. Ploog, K., *Annu. Rev. Mater. Sci.* **1982**, *12*, 123-148.

42. Spirkoska, D.; Colombo, C.; Heiß, M.; Heigoldt, M.; Abstreiter, G.; Fontcuberta i Morral, A., Growth Methods and Properties of High Purity III-V Nanowires by Molecular Beam Epitaxy. In *Advances in Solid State Physics*, Haug, R., Ed. Springer: Berlin, Germany, 2009; Vol. 48.
43. Joyce, B. A., *Rep. Prog. Phys.* **1985**, *48*, 1637.
44. Dupuis, R. D., *Science* **1984**, *226*, 623-629.
45. Auciello, O.; Kingon, A. I. In *A critical review of physical vapor deposition techniques for the synthesis of ferroelectric thin films*, Applications of Ferroelectrics, 1992. ISAF '92., Proceedings of the Eighth IEEE International Symposium on, 30 Aug-2 Sep 1992, 1992; 1992; pp 320-331.
46. Mattox, D. M., *Handbook of Physical Vapor Deposition Processing*. Noyes Publications: New Jersey, USA, 1998.
47. Mahan, J. E., *Physical Vapor Deposition of Thin Films*. John Wiley & Sons: New York, USA, 2000.
48. Reichelt, K.; Jiang, X., *Thin Solid Films* **1990**, *191*, 91-126.
49. Knisley, T. J.; Kalutarage, L. C.; Winter, C. H., *Coord. Chem. Rev.* **2013**.
50. Delft, J. A. v.; Garcia-Alonso, D.; Kessels, W. M. M., *Semicond. Sci. Technol.* **2012**, *27*, 074002.
51. Kim, H., *J. Vac. Sci. Technol. B* **2003**, *21*, 2231-2261.
52. Puurunen, R. L., *J. Appl. Phys.* **2005**, *97*, 121301-52.
53. Schubert, U.; Huesing, N., *Synthesis of Inorganic Materials*. Third ed.; Wiley-VCH: Weinheim, Germany, 2012.
54. Choy, K. L., *Prog. Mater. Sci.* **2003**, *48*, 57-170.
55. Jones, A. C.; Hitchman, M. L., *Chemical Vapour Deposition: Precursors, Processes and Applications*. RSC: Cambridge, UK, 2008.
56. Marchand, P.; Hassan, I. A.; Parkin, I. P.; Carmalt, C. J., *Dalton Trans.* **2013**, *42*, 9406-9422.
57. Nomura, R.; Inazawa, S. j.; Kanaya, K.; Matsuda, H., *Polyhedron* **1989**, *8*, 763-767.
58. Downs, A. J., *Chemistry of Aluminium, Gallium, Indium and Thallium*. Blackie Academic and Professional: Glasgow, UK, 1993.
59. Aldridge, S.; Downs, A. J., *The Group 13 Metals Aluminium, Gallium, Indium and Thallium*. Wiley: Chichester, UK, 2011.

60. Cotton, F. A.; Wilkinson, G.; Murillo, C. A.; Bochmann, M., *Advanced Inorganic Chemistry*. Sixth ed.; John Wiley and Sons: New York, USA, 1999.
61. Wilkinson, G.; Gillard, R. D.; McCleverty, J. A., *Comprehensive Coordination Chemistry*. First ed.; Pergamon: Oxford, UK, 1987.
62. Taylor, M. J., Aluminium and Gallium. In *Comprehensive Coordination Chemistry*, Wilkinson, G.; Gillard, R. D.; McCleverty, J. A., Eds. Pergamon Press: Oxford, UK, 1987; Vol. 3, pp 105-152.
63. Tuck, D. G., Indium and Thallium. In *Comprehensive Coordination Chemistry*, Wilkinson, G.; Gillard, R. D.; McCleverty, J. A., Eds. Pergamon Press: Oxford, UK, 1987; Vol. 3, pp 153-182.
64. Parkin, G. F. R., *Comprehensive Coordination Chemistry II*. Pergamon: Oxford, UK, 2003.
65. Robinson, G. H., 3.4 - Aluminum and Gallium. In *Comprehensive Coordination Chemistry II*, Editors-in-Chief: , J. A. M.; Meyer, T. J., Eds. Pergamon: Oxford, UK, 2003; pp 347-382.
66. Rasika Dias, H. V., 3.5 - Indium and Thallium. In *Comprehensive Coordination Chemistry II*, Editors-in-Chief: , J. A. M.; Meyer, T. J., Eds. Pergamon: Oxford, UK, 2003; pp 383-463.
67. Benjamin, S. L.; Levason, W.; Reid, G., *Chem. Soc. Rev.* **2013**, 42, 1460-1499.
68. Richards, R. L.; Thompson, A., *J. Chem. Soc. A* **1967**, 1248-1252.
69. Burford, N.; Royan, B. W.; Spence, R. E. v. H.; Cameron, T. S.; Linden, A.; Rogers, R. D., *J. Chem. Soc., Dalton Trans.* **1990**, 1521-1528.
70. Burford, N.; Royan, B. W.; Spence, R. E. v. H.; Rogers, R. D., *J. Chem. Soc., Dalton Trans.* **1990**, 2111-2117.
71. Beran, G.; Dymock, K.; Patel, H. A.; Carty, A. J.; Boorman, P. M., *Inorg. Chem.* **1972**, 11, 896-898.
72. Engelhardt, L. M.; Junk, P. C.; Raston, C. L.; Skelton, B. W.; White, A. H., *J. Chem. Soc., Dalton Trans.* **1996**, 3297-3301.
73. Cowley, A. H.; Cushner, M. C.; Davis, R. E.; Riley, P. E., *Inorg. Chem.* **1981**, 20, 1179-1181.
74. Sluka, R.; Necas, M.; Sindelar, P., *Acta Crystallogr. E* **2004**, 60, m447-m448.
75. Beattie, I. R.; Ozin, G. A.; Blayden, H. E., *J. Chem. Soc. A* **1969**, 2535-2536.
76. Pullmann, P.; Hensen, K.; Bats, J. W., *Z. Naturforsch., B: Chem. Sci.* **1982**, 37, 1312-1315.

77. Beattie, I. R.; Jones, P. J.; Howard, J. A. K.; Smart, L. E.; Gilmore, C. J.; Akitt, J. W., *J. Chem. Soc., Dalton Trans.* **1979**, 528-535.
78. Trinh, C.; Bodensteiner, M.; Virovets, A. V.; Peresyphkina, E. V.; Scheer, M.; Matveev, S. M.; Timoshkin, A. Y., *Polyhedron* **2010**, *29*, 414-424.
79. Ménard, G.; Stephan, D. W., *J. Am. Chem. Soc.* **2010**, *132*, 1796-1797.
80. Wells, R. L.; McPhail, A. T.; Laske, J. A.; White, P. S., *Polyhedron* **1994**, *13*, 2737-2744.
81. Dornhaus, F.; Scholz, S.; Sängler, I.; Bolte, M.; Wagner, M.; Lerner, H.-W., *Z. Anorg. Allg. Chem.* **2009**, *635*, 2263-2272.
82. Timoshkin, A. Y.; Bodensteiner, M.; Sevastianova, T. N.; Lisovenko, A. S.; Davydova, E. I.; Scheer, M.; Graßl, C.; Butlak, A. V., *Inorg. Chem.* **2012**, *51*, 11602-11611.
83. Vriezen, W. H. N.; Jellinek, F., *Chem. Phys. Lett.* **1967**, *1*, 284.
84. Ecker, A.; Schnöckel, H., *Z. Anorg. Allg. Chem.* **1998**, *624*, 813-816.
85. Beattie, I. R.; Ozin, G. A., *J. Chem. Soc. A* **1968**, 2373-2377.
86. Vriezen, W. H. N.; Jellinek, F., *Recl. Trav. Chim. Pays-Bas* **1970**, *89*, 1306-1312.
87. Gurnani, C.; Levason, W.; Ratnani, R.; Reid, G.; Webster, M., *Dalton Trans.* **2008**, 6274-6282.
88. Mason, J., *Multinuclear NMR*. Plenum Press: New York, USA, 1989.
89. Cheng, F.; Hector, A. L.; Levason, W.; Reid, G.; Webster, M.; Zhang, W. J., *Inorg. Chem.* **2007**, *46*, 7215-7223.
90. Mishra, S.; Jeanneau, E.; Daniele, S., *Polyhedron* **2010**, *29*, 500-506.
91. George, K.; Jura, M.; Levason, W.; Light, M. E.; Ollivere, L. P.; Reid, G., *Inorg. Chem.* **2012**, *51*, 2231-2240.
92. Weyhermuller, T.; Wieghardt, K., *Chem. Commun.* **1998**, 557-558.
93. Scholz, S.; Lerner, H.-W.; Bolte, M., *Acta Crystallogr. E* **2002**, *58*, m586-m587.
94. Nogai, S. D.; Schmidbaur, H., *Dalton Trans.* **2003**, 2488-2495.
95. Boardman, A.; Jeffs, S. E.; Small, R. W. H.; Worrall, I. J., *Inorg. Chim. Acta* **1984**, *87*, L27-L28.
96. Bock, S.; Noth, H.; Wietelmann, A., *Z. Naturforsch. B* **1990**, *45*, 979-984.
97. Cheng, F.; Codgbrook, H. L.; Hector, A. L.; Levason, W.; Reid, G.; Webster, M.; Zhang, W., *Polyhedron* **2007**, *26*, 4147-4155.
98. A. Kloo, L.; J. Taylor, M., *J. Chem. Soc., Dalton Trans.* **1997**, 2693-2696.

99. Carmalt, C. J.; Mileham, J. D.; White, A. J. P.; Williams, D. J., *Dalton Trans.* **2003**, 4255-4260.
100. Restivo, R.; Palenik, G. J., *J. Chem. Soc., Dalton Trans.* **1972**, 341-344.
101. Sofetis, A.; Raptopoulou, C. P.; Terzis, A.; Zafiropoulos, T. F., *Inorg. Chim. Acta* **2006**, *359*, 3389-3395.
102. Yamasaki, K.; Okada, O.; Inami, K.; Oka, K.; Kotani, M.; Yamada, H., *J. Phys. Chem. B* **1997**, *101*, 13-19.
103. Donzello, M. P.; Agostinetto, R.; Ivanova, S. S.; Fujimori, M.; Suzuki, Y.; Yoshikawa, H.; Shen, J.; Awaga, K.; Ercolani, C.; Kadish, K. M.; Stuzhin, P. A., *Inorg. Chem.* **2005**, *44*, 8539-8551.
104. Coutsolelos, A.; Guillard, R.; Bayeul, D.; Lecomte, C., *Polyhedron* **1986**, *5*, 1157-1164.
105. Barnard, P. J.; Holland, J. P.; Bayly, S. R.; Wadas, T. J.; Anderson, C. J.; Dilworth, J. R., *Inorg. Chem.* **2009**, *48*, 7117-7126.
106. Zantias, S.; Raptopoulou, C. P.; Terzis, A.; Zafiropoulos, T. F., *Inorg. Chem. Commun.* **1999**, *2*, 48-51.
107. Carter, J. C.; Jugie, G.; Enjalbert, R.; Galy, J., *Inorg. Chem.* **1978**, *17*, 1248-1254.
108. Cheng, F.; Hector, A. L.; Levason, W.; Reid, G.; Webster, M.; Zhang, W., *Acta Crystallogr. E* **2007**, *63*, m1761.
109. Weigand, J. J.; Burford, N.; Decken, A., *Eur. J. Inorg. Chem.* **2008**, *2008*, 4343-4347.
110. Cheng, F.; Hector, A. L.; Levason, W.; Reid, G.; Webster, M.; Zhang, W., *Inorg. Chem.* **2008**, *47*, 9691-9700.
111. Baker, L. J.; Rickard, C. E. F.; Taylor, M. J., *J. Organomet. Chem.* **1994**, *464*, C4-C6.
112. Cheng, F.; Hector, A. L.; Levason, W.; Reid, G.; Webster, M.; Zhang, W., *Dalton Trans.* **2007**, 2207-2210.
113. Fairbrother, F.; Flitcroft, N., *J. Less Common Met.* **1962**, *4*, 504-511.
114. Evans, C. A.; Taylor, M. J., *J. Chem. Soc. A* **1969**, 1343-1344.
115. Gurnani, C.; Jura, M.; Levason, W.; Ratnani, R.; Reid, G.; Webster, M., *Dalton Trans.* **2009**, 1611-1619.
116. Wiegardt, K.; Kleine-Boymann, M.; Nuber, B.; Weiss, J., *Inorg. Chem.* **1986**, *25*, 1654-1659.

117. Self, M. F.; McPhail, A. T.; Wells, R. L., *Polyhedron* **1993**, *12*, 455-459.
118. Whittlesey, B. R.; Ittycheriah, I. P., *Acta Crystallogr. C* **1994**, *50*, 693-695.
119. Dias, H. V. R.; Jin, W., *Inorg. Chem.* **1996**, *35*, 267-268.
120. Willey, G. R.; Aris, D. R.; Haslop, J. V.; Errington, W., *Polyhedron* **2001**, *20*, 423-429.
121. Wells, R. L.; Kher, S. S.; Baldwin, R. A.; White, P. S., *Polyhedron* **1994**, *13*, 2731-2735.
122. Dashti, A.; Niediek, K.; Werner, B.; Neumüller, B., *Z. Anorg. Allg. Chem.* **1997**, *623*, 394-402.
123. Robinson, W. T.; Wilkins, C. J.; Zeying, Z., *J. Chem. Soc., Dalton Trans.* **1990**, 219-227.
124. Einstein, F. W. B.; Tuck, D. G., *J. Chem. Soc. Chem. Comm.* **1970**, 1182-1183.
125. Malyarick, M. A.; Ilyuhin, A. B.; Petrosyants, S. P., *Polyhedron* **1993**, *12*, 2403-2409.
126. Chen, F.; Ma, G.; Cavell, R. G.; Terskikh, V. V.; Wasylshen, R. E., *Chem. Commun.* **2008**, 5933-5935.
127. Sinha, S. P.; Pakkanen, T. T.; Pakkanen, T. A.; Niinistö, L., *Polyhedron* **1982**, *1*, 355-359.
128. Groves, A. G.; Robinson, W. T.; Wilkins, C. J., *Inorg. Chim. Acta* **1986**, *114*, L29-L31.
129. Carta, G.; Benetollo, F.; Sitran, S.; Rossetto, G.; Braga, F.; Zanella, P., *Polyhedron* **1995**, *14*, 1923-1928.
130. Werner, B.; Kräter, T.; Neumüller, B., *Z. Anorg. Allg. Chem.* **1995**, *621*, 346-358.
131. Tyrra, W. E., *J. Fluorine Chem.* **2001**, *112*, 149-152.
132. Tyrra, W.; Wickleder, M. S., *J. Organomet. Chem.* **2003**, *677*, 28-34.
133. Chitsaz, S.; Breyhan, T.; Pauls, J.; Neumüller, B., *Z. Anorg. Allg. Chem.* **2002**, *628*, 956-964.
134. Itazaki, M.; Ujihara, R.; Nakazawa, H., *Acta Crystallogr. E* **2006**, *62*, m1649-m1650.
135. Butcher, R. J.; George, C.; Muratore, N.; Purdy, A. P., *Acta Crystallogr. E* **2003**, *59*, m1107-m1109.
136. Karia, R.; Willey, G. R.; Drew, M. G. B., *Acta Crystallogr. C* **1986**, *42*, 558-560.

137. Niu, W.; Wong, E. H.; Weisman, G. R.; Sommer, R. D.; Rheingold, A. L., *Inorg. Chem. Commun.* **2002**, *5*, 1-4.
138. Alcock, N. W.; Degnan, I. A.; Howarth, O. W.; Wallbridge, M. G. H., *J. Chem. Soc., Dalton Trans.* **1992**, 2775-2780.
139. Clegg, W.; Norman, N. C.; Pickett, N. L., *Acta Crystallogr. C* **1994**, *50*, 36-38.
140. Chen, F.; Ma, G.; Bernard, G. M.; Cavell, R. G.; McDonald, R.; Ferguson, M. J.; Wasylshen, R. E., *J. Am. Chem. Soc.* **2010**, *132*, 5479-5493.
141. Baker, L. J.; Kloos, L. A.; Rickard, C. E. F.; Taylor, M. J., *J. Organomet. Chem.* **1997**, *545-546*, 249-255.
142. Veidis, M. V.; Palenik, G. J., *J. Chem. Soc. Chem. Comm.* **1969**, 586b-587.
143. Brown, M. A.; Tuck, D. G.; Wells, E. J., *Can. J. Chem.* **1996**, *74*, 1535-1549.
144. Sigl, M.; Schier, A.; Schmidbaur, H., *Z. Naturforsch., B: Chem. Sci.* **1999**, *54*, 21-25.
145. Degnan, I. A.; Alcock, N. W.; Roe, S. M.; Wallbridge, M. G. H., *Acta Crystallogr. C* **1992**, *48*, 995-999.
146. Sigl, M.; Schier, A.; Schmidbaur, H., *Eur. J. Inorg. Chem.* **1998**, 1998, 203-210.
147. Nyholm, R. S.; Ulm, K., *J. Chem. Soc.* **1965**, 4199-4203.
148. Campbell, J. R., *J. Org. Chem.* **1964**, *29*, 1830-1833.
149. Khurana, J. M.; Sahoo, P. K., *Synth. Commun.* **1992**, *22*, 1691-1702.
150. McAllan, D. T.; Cullum, T. V.; Dean, R. A.; Fidler, F. A., *J. Am. Chem. Soc.* **1951**, *73*, 3627-3632.
151. Gulliver, D. J.; Hope, E. G.; Levason, W.; Murray, S. G.; Potter, D. M.; Marshall, G. L., *J. Chem. Soc. Perkin Trans. 2* **1984**, 429-434.
152. Hope, E. G.; Kemmitt, T.; Levason, W., *Organometallics* **1987**, *6*, 206-207.
153. Hope, E. G.; Kemmitt, T.; Levason, W., *Organometallics* **1988**, *7*, 78-83.
154. O'Brien, D. H.; Dereu, N.; Huang, C. K.; Irgolic, K. J.; Knapp, F. F., *Organometallics* **1983**, *2*, 305-307.
155. Brandsma, L.; Wijers, H. E., *Recl. Trav. Chim. Pays-Bas* **1963**, *82*, 68-74.
156. Ebsworth, E. A. V.; Rankin, D. W. H.; Cradock, S., *Structural Methods in Inorganic Chemistry*. Blackwell Scientific: Chichester, UK, 1987.
157. Nakamoto, K., *Infrared and Raman Spectra of Inorganic and Coordination Compounds*. Fourth ed.; Wiley-Interscience: New York, USA, 1986.

158. Blake, A. J.; Clegg, W.; Cole, J. M.; Evans, J. O.; Main, P.; Parsons, S.; Watkin, D. J., *Crystal Structure Analysis - Principles and Practice*. Second Edition ed.; Oxford University Press: Oxford, UK, 2009.
159. Brundle, C. R.; Evans, C. A., Jr.; Wilson, S., *Encyclopedia of Materials Characterization - Surfaces, Interfaces, Thin Films*. In Elsevier: 1992.
160. Birkholz, M., *Thin Film Analysis by X-Ray Scattering*. Wiley: Weinheim, Germany, 2006.
161. Harris, K. D. M., Powder Diffraction Crystallography of Molecular Solids. In *Advanced X-Ray Crystallography*, Rissanen, K., Ed. Springer Berlin, Germany, 2012; Vol. 315, pp 133-177.
162. Mulvaney, S. P.; Keating, C. D., *Anal. Chem.* **2000**, *72*, 145-158.
163. Lyon, L. A.; Keating, C. D.; Fox, A. P.; Baker, B. E.; He, L.; Nicewarner, S. R.; Mulvaney, S. P.; Natan, M. J., *Anal. Chem.* **1998**, *70*, 341-362.
164. Newbury, D. E., Energy Dispersive Spectrometry. In *Characterization of Materials*, John Wiley & Sons, Inc.: Chichester, UK, 2002.
165. Gfroerer, T. H., Photoluminescence in Analysis of Surfaces and Interfaces. In *Encyclopedia of Analytical Chemistry*, Meyers, R. A., Ed. John Wiley & Sons Ltd: Chichester, UK, 2000; pp 9209–9231.
166. Meyer, E., *Prog. Surf. Sci.* **1992**, *41*, 3-49.
167. Schroder, D. K., *Semiconductor Material and Device Characterisation*. Second Edition ed.; John Wiley & Sons: New Jersey, USA, 1998.
168. Bruce, D. W.; O'Hare, D., *Inorganic Materials*. Second Edition ed.; John Wiley and Sons: Chichester, UK, 1996.
169. Fujii, M.; Hayashi, S.; Yamamoto, K., *Jpn. J. Appl. Phys. Part 1 - Regul. Pap. Short Notes Rev. Pap.* **1991**, *30*, 687-694.
170. Yang, C.-H.; Ma, Z.-Q., *Appl. Opt.* **2012**, *51*, 5438-5441.
171. Loechelt, G. H.; Cave, N. G.; Menendez, J., *Appl. Phys. Lett.* **1995**, *66*, 3639-3641.
172. De Wolf, I., *Semicond. Sci. Technol.* **1996**, *11*, 139.
173. Richter, H.; Wang, Z. P.; Ley, L., *Solid State Commun.* **1981**, *39*, 625-629.
174. McCarthy, J.; Friel, J.; Camus, P., *Microsc. Microanal.* **2009**, *15*, 484-490.
175. Binnig, G.; Quate, C. F.; Gerber, C., *Phys. Rev. Lett.* **1986**, *56*, 930-933.
176. van der Pauw, L. J., *Philips Research Reports* **1958**, *13*, 1-9.
177. van der Pauw, L. J., *Philips Technical Review* **1958**, *20*, 220-224.

2 Coordination Complexes of Gallium and Indium Trichloride with Thio- and Seleno-ether Macrocycles

2.1 Introduction

The aims of this chapter are to develop the understanding of the coordination chemistry of gallium and indium trichloride with chalcogenoethers. The use of chalcogenoether macrocycles builds on the work described in 1.3.2 and 1.3.3, which focussed on the use of acyclic ligands. Previously, reactions of gallium(III) halides with chalcogenoethers yielded only 4-coordinate, distorted tetrahedral species, whereas reacting indium(III) halides with the same ligands yielded a much wider range of coordination geometries.^{1, 2}

Chapter summary: The novel compounds $[(MCl_3)_2([8]aneSe_2)]$ ($M = Ga, In$), $[[8]aneSe_2]Cl[GaCl_4] \cdot CH_2Cl_2$, $[[8]aneSe_2]_2[GaCl_4]_2$, $[GaCl_2([16]aneE_4)][GaCl_4]$ ($E = S, Se$), $[InCl_2([16]aneSe_4)][InCl_4]$ and $[GaCl_3([14]aneS_4)]$ were synthesised and characterised. The unsuccessful reactions of MCl_3 with $[12]aneS_4$ ($M = Ga$) and $[24]aneSe_6$ ($M = Ga, In$) are also discussed. All other compounds discussed, including the macrocycles, have previously been synthesised.

2.1.1 Macrocycle synthesis

The synthesis of macrocycles is typically more challenging than the synthesis of acyclic ligands, requiring careful control of the reaction conditions in order to promote cyclisation over polymerisation.

The synthesis of thioether macrocycles is generally based on a high dilution method using Cs_2CO_3 in dmf to deprotonate a dithiol in order to react with a dibromoalkane.^{3, 4} Other methods to synthesise thioether macrocycles have also been reported but the use of potent vesicants as intermediates in the reaction has limited their utilisation.⁵ A small number of thioether macrocycles are available to purchase from commercial suppliers

but these are limited to macrocycles containing 3 or 4 sulfur donors. It is also possible to synthesise functionalised saturated and unsaturated thioether macrocycles,⁶⁻¹⁰ some of which are liquid crystals.¹¹

There are no selenoether macrocycles available to purchase from commercial suppliers and many of the organoselenium precursors required in the synthesis of the macrocycles are also unavailable e.g. $\text{NCSe}(\text{CH}_2)_3\text{SeCN}$. Figure 2.1 illustrates the synthesis route for the selenoether macrocycles that are used in this work. The synthesis was first reported by Pinto and co-workers in 1989.¹² Careful temperature control is needed to prevent polymerisation becoming the dominant reaction pathway, while still ensuring that the temperature is high enough to allow the reaction to proceed. The reaction produces a mixture of products ($[\text{8}]_{\text{ane}}\text{Se}_2$, $[\text{16}]_{\text{ane}}\text{Se}_4$ and $[\text{24}]_{\text{ane}}\text{Se}_6$) from [1+1], [2+2] and [3+3] cyclisations. The products are purified by column chromatography, although $[\text{8}]_{\text{ane}}\text{Se}_2$ can also be separated from the crude product by vacuum distillation.

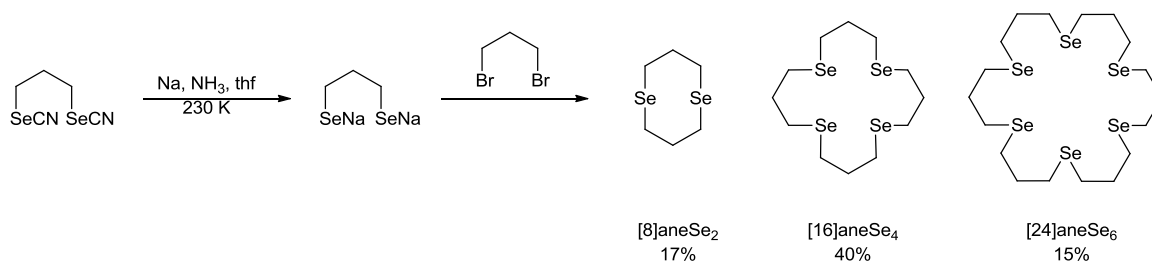


Figure 2.1 – Synthesis of selenoether macrocycles using a direct synthesis route¹²

The synthesis of the macrocycle $[\text{14}]_{\text{ane}}\text{Se}_4$ is also reported, using an identical synthesis route but with sodium ethane-1,2-bis(selenolate) (prepared *in situ*) in place of sodium propane-1,3-bis(selenolate).¹² There are no reports of this ligand being used for coordination chemistry due to the propensity to eliminate the C₂ linkage and form the diselenide.

It is also possible to synthesise selenoether macrocycles containing 3 and 5 Se donor atoms. [12]aneSe₃ and [20]aneSe₅ can be synthesised *via* high dilution cyclisation of NaSe(CH₂)₃SeNa with TsO(CH₂)₃{Se(CH₂)₃}_nOTs (*n* = 1, 3) (Figure 3.2).¹³

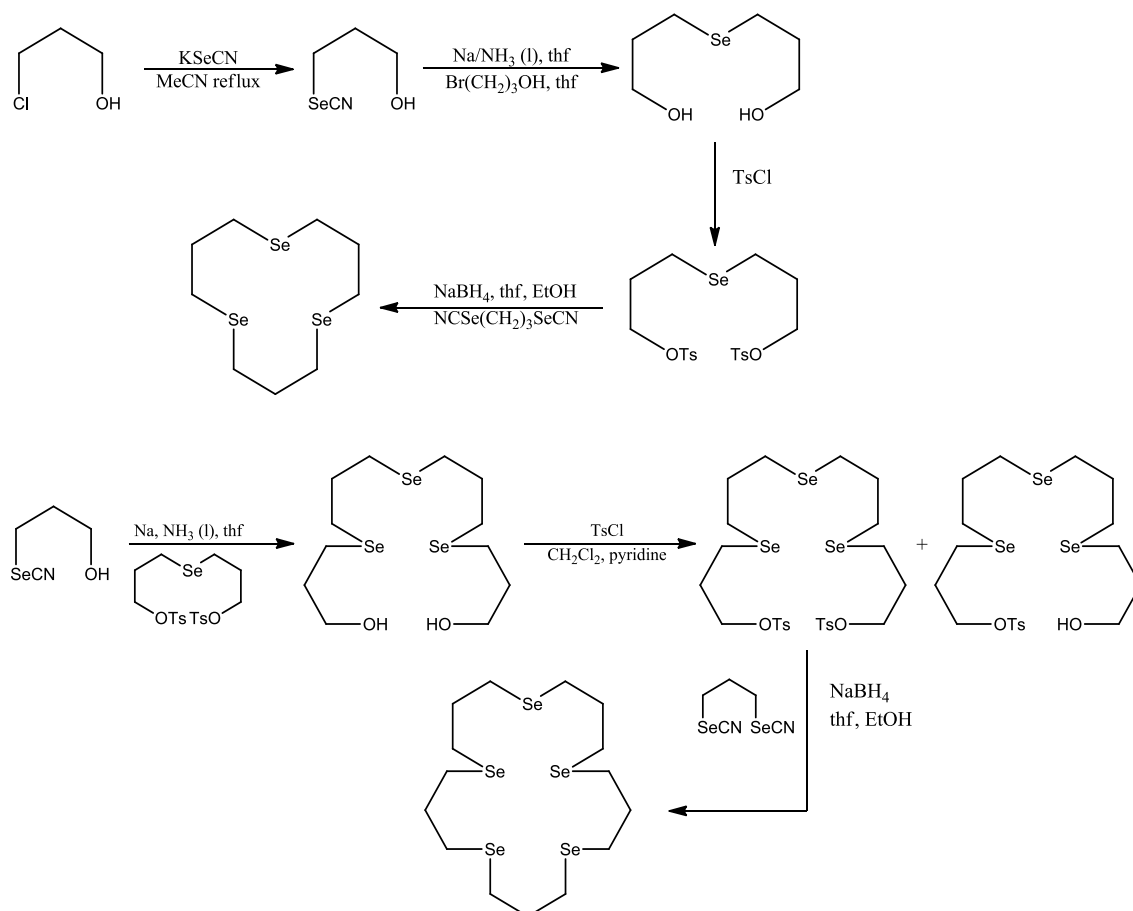


Figure 2.2 – High dilution syntheses of [12]aneSe₃ (top) and [20]aneSe₅ (bottom).

The syntheses of other Se₃-donor macrocycles [12]aneSe₃, benzo-[11]aneSe₃ and benzo-[13]aneSe₃ have also been reported using a high dilution, room temperature reaction in thf and ethanol with NaBH₄ (Figure 2.3).¹⁴ A small range of functionalised selenoether macrocycles also exist, including naphthalene functionalised Se₃- and Se₄- donor macrocycles^{15, 16} and Me₄[8]aneSe₂, Me₆[12]aneSe₃ and Me₈[16]aneSe₄,¹⁷ which are synthesised by the ring-opening macrocyclisation of 3,3-dimethylselenetane (DMSe) by the complex [Re₂(CO)₉(DMSe)].

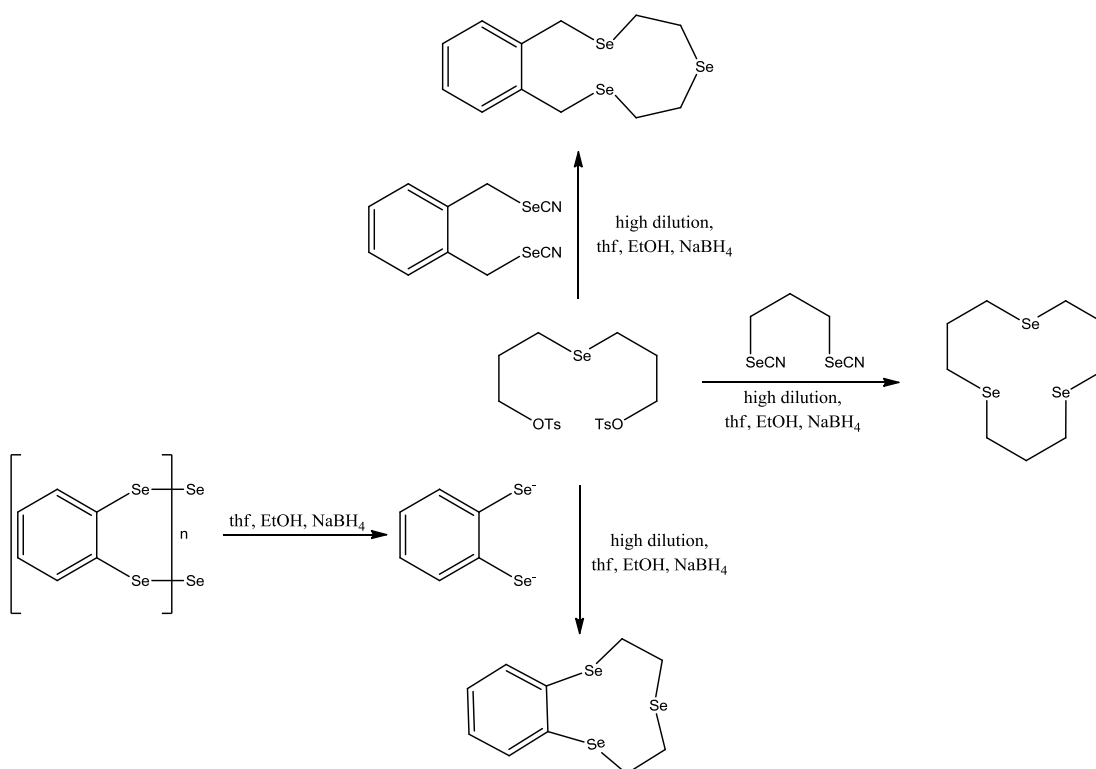


Figure 2.3 – Synthesis of [12]aneSe₃, benzo-[11]aneSe₃ and benzo-[13]aneSe₃ using a high dilution method¹⁴

In contrast to the large number of sulfur and selenium containing macrocycles, there are still very few reported tellurium containing macrocycles. Telluroethers are much more sensitive to oxidation and light than the corresponding thio- and seleno-ethers. This is mainly due to the much weaker Te-C bond strength compared to that of Se-C or S-C, making it much more reactive and prone to eliminating the carbon backbone and forming elemental tellurium. This arises from the much poorer orbital overlap between Te and C compared to that of S and C as the bonding orbitals get larger and more diffuse as Group 16 is descended. The difference in electronegativity between carbon and tellurium also polarises the Te-C bond.¹⁸ The only cyclic tellurium ligands reported are [8]aneTe₂ and [12]aneTe₃, although a wider range of mixed donor macrocycles exist.¹⁸

2.1.2 Thioether and selenoether macrocyclic p-block complexes

The work reported here focuses on complexes of GaCl₃ and InCl₃ with the cyclic ligands [8]aneSe₂, [16]aneSe₄, [14]aneS₄ and [16]aneS₄. These ligands were selected over [12]aneE₃ and [20]aneE₅ (E = S, Se) as they have been most widely used in studies of coordination complexes and will therefore lead to easier comparison with other p-block macrocyclic complexes. This is due to their commercial availability (E = S) or easier synthesis (E = Se).

Previous studies have investigated the coordination chemistry of thioether and selenoether macrocycles with other p-block halides, leading to a wide range of coordination geometries and extended 1-D and 2-D networks. Examples of these are discussed in more detail by Levason and Reid.^{19, 20}

Reactions of GeX₂ with thioether macrocycles led to the formation of exocyclically coordinated chain and sheet polymers (Figure 2.4).^{21, 22} Similarly, the analogous reactions with macrocyclic selenoethers yielded 2-D sheet polymers with exocyclic coordination at selenium and long range interactions between Ge centres and Cl on adjacent GeCl₂ units.²¹ The reactions of SnX₄ with thioether macrocycles yielded exocyclically coordinated chain polymers, with the sulfur coordination either *cis* (X = Cl and X = Br, L = [12]aneS₄) or *trans* (X = Br, L = [14]aneS₄, [16]aneS₄).²³ The reactions of SnX₄ with [8]aneSe₂ (X = Cl) and [16]aneSe₄ (X = Cl, Br) yielded 1:1 complexes as evidenced by microanalysis data but these have not been structurally characterised. ⁷⁷Se NMR spectroscopy of [SnCl₄([16]aneSe₄)] showed two resonances, supporting the formation of a 1:1 adduct with a distorted octahedral donor set from Cl₄Se₂ and two uncoordinated Se atoms. The work done with lead halides is much more limited and most examples feature mixed donor thia-oxa macrocycles.²⁰ The structure of [Pb([10]aneS₃)(H₂O)(ClO₄)₂] has been reported, which has a facially capping [10]aneS₃ ligand, coordinated H₂O and weak interactions from two [ClO₄]⁻ units.²⁴

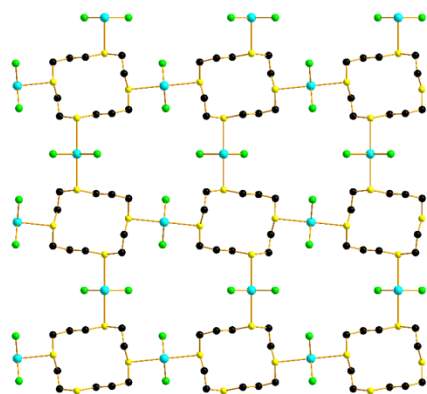


Figure 2.4 – 2D sheet polymer of $[(\text{GeCl}_2)_2([14]\text{aneS}_4)]$. Ge = turquoise, Cl = green, S = yellow, C = black.

The thioether and selenoether macrocycle complexes of AsX_3 show more variety in their coordination geometries. $[\text{AsCl}_3([9]\text{aneS}_3)]$ is a monomeric complex with weak *fac* coordination from three sulfur atoms whereas $[\text{AsCl}_3([14]\text{aneS}_4)]$ adopts a 2-D sheet polymer structure with exocyclic coordination of the macrocycle and bridging Cl ligands. $[24]\text{aneSe}_6$ exhibits both exocyclic and endocyclic coordination with an As_2Cl_6 dimer complexed to two *cis* Se donors per As within the macrocycle and two AsCl_3 molecules complexed exocyclically on each of the remaining two *trans* Se atoms (Figure 2.5). Interesting structural trends are also observed for the series of $[\text{MCl}_3([8]\text{aneSe}_2)]$ ($\text{M} = \text{As}, \text{Sb}, \text{Bi}$).²⁵ $[\text{AsCl}_3([8]\text{aneSe}_2)]$ adopts an infinite one-dimensional ladder structure with As_2Cl_6 linked by bridging $[8]\text{aneSe}_2$ molecules. The $[\text{SbCl}_3([8]\text{aneSe}_2)]$ complex takes the form of $[\text{Sb}_2\text{Cl}_6(\kappa^1[8]\text{aneSe}_2)_2]$ dimers. Long range Sb–Se interactions link the dimers into an infinite ladder structure.

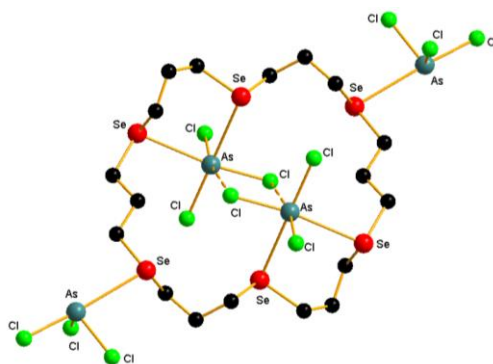


Figure 2.5 – Crystal structure of $[(\text{AsCl}_3)_4[24]\text{aneSe}_6]$ exhibiting both endo- and exocyclic coordination

There is some debate about the bonding models used to describe the hypervalency seen in p-block coordination complexes.²⁶⁻²⁸ This type of interaction is also known as secondary bonding, a term introduced by Alcock.²⁹ The traditional 2 centre – 2 electron (2c-2e) model has fallen out of favour as calculations have shown that higher energy d-orbitals cannot contribute to the bonding as significantly as previously believed. The alternative treatment that has been developed is a 3 centre – 4 electron (3c-4e) model. For a linear X–M–X unit, the central M uses one empty p-orbital and combines this with one filled donor orbital on each X. This generates three molecular orbitals; bonding, nonbonding and antibonding (in order of increasing energy), with the two electron pairs occupying the bonding and nonbonding orbitals (Figure 2.6).

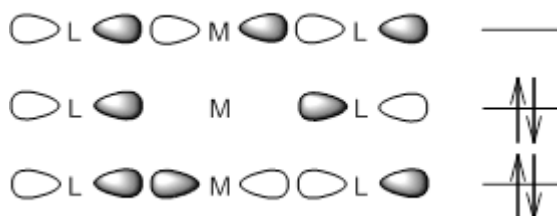


Figure 2.6 - 3c-4e bonding model adapted from Benjamin, Levason and Reid³⁰

If the groups around the central metal atom are different, e.g. X-M-Y, the model can be adapted so that the primary M-X bond dominates and polarises the bonding orbital towards X, and the M-X antibonding orbital becomes polarised towards M. As the M-X antibonding orbital is empty, it can then behave as an acceptor orbital for an electron pair from Y. If the M-X bonding significantly dominates and M-Y bonding is very weak, this is often known as “secondary bonding”. It is these secondary bonding interactions that contribute to the extended structures seen in many p-block complexes. A more comprehensive review on this subject is available from Hoffmann and co-workers.^{28, 31}

2.2 Results and discussion

2.2.1 Cyclic diselenoether ligand complexes

GaCl₃ and InCl₃ were reacted with [8]aneSe₂ in anhydrous CH₂Cl₂. The reaction scheme (Figure 2.7) shows an overview of the products obtained for the reaction of GaCl₃ with [8]aneSe₂.

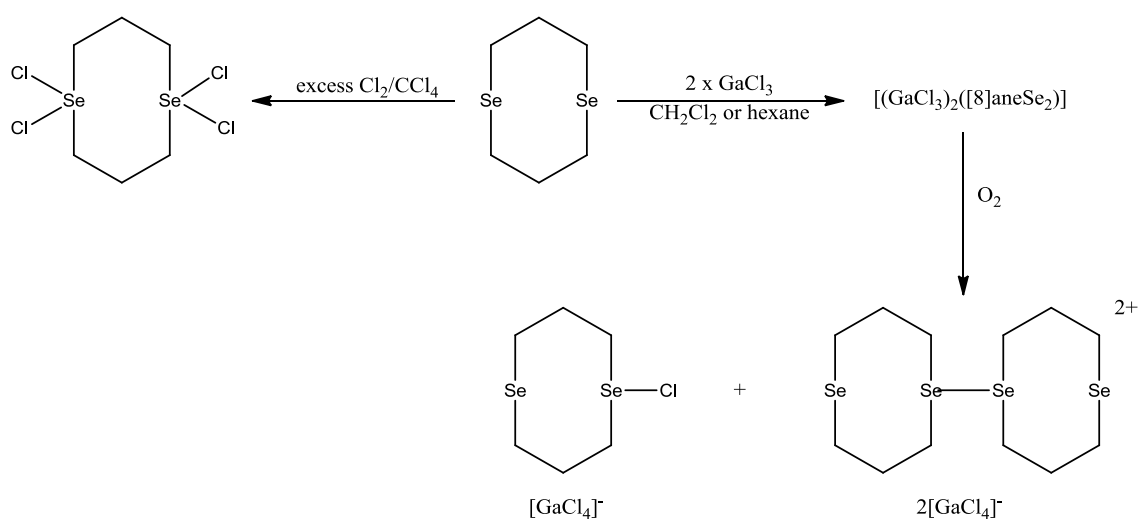


Figure 2.7 – Reactions of GaCl₃ with [8]aneSe₂

The 2:1 reaction of GaCl₃ with [8]aneSe₂ yielded a highly air sensitive, white crystalline solid from a pale yellow solution. The product is believed to be [(GaCl₃)₂([8]aneSe₂)] with each GaCl₃ in a distorted tetrahedral environment coordinated to one of the Se atoms. The NMR spectroscopic data support the assignment of a distorted tetrahedral coordination environment, although they cannot provide confirmation of the stoichiometry. The ¹H NMR spectrum shows high frequency shifts (by 0.3 - 0.4 ppm) relative to free ligand. The ⁷¹Ga{¹H} NMR spectrum shows a broad (w_{1/2} = 4500 Hz) resonance at 237 ppm, which is in agreement with the distorted tetrahedral environment of [GaCl₃(L)] (L = [8]aneSe₂).^{1, 32} The ⁷⁷Se{¹H} NMR spectrum at 293 K shows a significant low frequency shift at 119 ppm relative to free ligand at 137 ppm.¹² When the sample is cooled to 203 K, there is a further low frequency shift to 112 ppm. The IR

spectrum indicates the presence of coordinated GaCl_3 with stretches at 386 and 360 cm^{-1} with no evidence for the presence of $[\text{GaCl}_4]^-$, which would be observed at 370 cm^{-1} .³³ Attempts to obtain microanalysis data to confirm the stoichiometry were unsuccessful as the sample decomposed in transit to an external microanalysis company. The microanalysis company stated that a colour change from white to orange had occurred when they received the sample, indicating oxidation.

When the reaction of GaCl_3 with $[\text{8}]_{\text{ane}}\text{Se}_2$ was carried out in a 1:1 stoichiometry, the solution turned deep yellow and red and yellow crystals formed after keeping the solution at $-18\text{ }^\circ\text{C}$ for several days. Single crystal X-ray diffraction showed that the red crystals were $\{[\text{8}]_{\text{ane}}\text{Se}_2\}_2[\text{GaCl}_4]_2$, which contained a dimeric cation formed by the coupling of two mono oxidised $[\text{8}]_{\text{ane}}\text{Se}_2$ rings (Figure 2.8) and the yellow crystals were $\{[\text{8}]_{\text{ane}}\text{Se}_2\text{Cl}\}[\text{GaCl}_4]\cdot\text{CH}_2\text{Cl}_2$, containing a doubly oxidised $[\text{8}]_{\text{ane}}\text{Se}_2$ ring (Figure 2.9). In order to study the formation of these products, an NMR spectroscopic experiment was conducted. A sample of the white product from the 2:1 reaction was dissolved in $\text{CDCl}_3/\text{CH}_2\text{Cl}_2$ and the $^{77}\text{Se}\{^1\text{H}\}$ and $^{71}\text{Ga}\{^1\text{H}\}$ NMR spectra were obtained as previously described. The sample then had dry O_2 bubbled through it for approximately one minute, causing the colourless solution to change to orange-red. A red precipitate rapidly formed, leaving a colourless solution. A unit cell determination on the crystals from this precipitate showed that they matched the red crystals in Figure 2.8. The previous resonances in the $^{77}\text{Se}\{^1\text{H}\}$ and $^{71}\text{Ga}\{^1\text{H}\}$ NMR spectra had disappeared and no new resonances were visible. The red precipitate that had formed was then dissolved in $(\text{CH}_3)_2\text{CO}$, forming a yellow solution which turned colourless after a few minutes and remained colourless. This may indicate that a further reaction has occurred, possibly a second oxidation. The ^{71}Ga NMR spectrum of this solution shows the presence of $[\text{GaCl}_4]^-$ with a strong, sharp singlet at 250 ppm ³² but no signal was observed by ^{77}Se NMR spectroscopy either at 298 K or 183 K , even after long data acquisitions and a wide scan range ($-200 - 1500\text{ ppm}$).

The reaction of GaCl_3 with $[\text{8}]_{\text{ane}}\text{Se}_2$ in a 2:1 stoichiometry was also repeated in anhydrous hexane to ensure that CH_2Cl_2 played no role in the oxidation reaction. A white product was isolated initially and confirmed by IR and ^1H NMR spectroscopy to

be the same product as from the 2:1 reaction in CH_2Cl_2 . The white solid was then redissolved in hexane and exposed to air, causing a red solid to precipitate from the solution, which was confirmed to be $\{[\text{8}]ane\text{Se}_2\}_2[\text{GaCl}_4]_2$ by $^{71}\text{Ga}\{^1\text{H}\}$ NMR spectroscopy, which exhibited a sharp peak at 250 ppm, indicative of $[\text{GaCl}_4]^-$ and negative electrospray ionisation (ESI) mass spectrometry ($M^- = 211$).³² Although no resonances were visible in the ^{77}Se NMR spectrum, ESI⁺ MS showed a distinctive isotope pattern consistent with the calculated spectrum of a singly charged cation containing two Se atoms ($M^+ = 244$), confirming the presence of $\{[\text{8}]ane\text{Se}_2\}^+$.

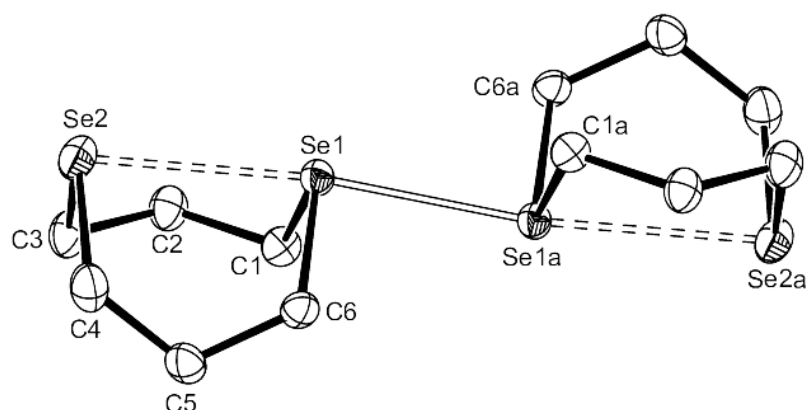


Figure 2.8 – Crystal structure of the dimeric cation in $\{[\text{8}]ane\text{Se}_2\}_2[\text{GaCl}_4]_2$ with atom numbering scheme. Ellipsoids are shown at the 50% probability level and H atoms are omitted for clarity. Symmetry operation: $a = -x, -y, -z$

Se1–C1	1.980(3)	Se2–C3	1.957(3)
Se1–C6	1.981(3)	Se2–C4	1.962(3)
Se1–Se1a	2.666(1)	C1–Se1–C6	99.69(13)
Se1⋯Se2	2.891(1)	C3–Se2–C4	99.71(15)

Table 2.1 - Selected bond lengths (Å) and angles ($^\circ$) for $\{[\text{8}]ane\text{Se}_2\}_2^{2+}$ (Figure 2.8)

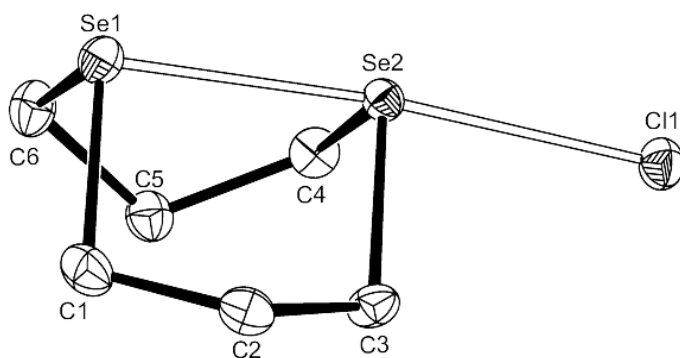


Figure 2.9 – Crystal structure of the cation in $[[[8]aneSe_2Cl][GaCl_4] \cdot CH_2Cl_2]$ with atom numbering scheme. Ellipsoids are shown at the 50% probability level and H atoms are omitted for clarity

Se2–Cl1	2.535(1)	C1–Se1–C6	99.66(9)
Se1–C1	1.970(2)	C3–Se2–C4	101.93(9)
Se1–C6	1.967(2)	C4–Se2–Cl1	89.39(6)
Se1–Se2	2.523(1)	C3–Se2–Cl1	88.09(6)
Se2–C3	1.981(2)	Se1–Se2–Cl1	175.23(2)
Se2–C4	1.978(2)		

Table 2.2 - Selected bond lengths (Å) and angles ($^{\circ}$) for $[[[8]aneSe_2Cl]]^+$ (Figure 2.9)

A solution of $[8]aneSe_2$ in CH_2Cl_2 is indefinitely stable in air therefore the oxidation of the ligand must be promoted by the presence of $GaCl_3$. The mechanism by which the oxidation occurs is unclear.

It has been previously shown that it is possible to generate the dication $[[8]aneSe_2]^{2+}$ by chemical oxidation using $NOPF_6$,³⁴ $NOBF_4$ ³⁵ or $[Cu(SO_3CF_3)_2]$ ³⁶. The monocationic radical species $[[8]aneSe_2]^+$ may have also been observed by EPR spectroscopy but details of the features of the EPR spectrum are not reported.³⁷ The macrocycle was also shown to exhibit reversible electrochemical oxidation to the dication in acetonitrile. The cyclic voltammogram for this system shows only a single oxidation peak and a single reduction peak, which is explained by the stepwise formation of first the monocation and then the dication, but at such similar potentials that the oxidation peaks overlap to form a single peak, and the reverse procedure for the reduction. The $[[8]aneSe_2]^{2+}$ cation

and the $[[8]aneSe_2]^+$ monocation radical have been studied by Furukawa *et al.*^{38,39} who have shown that it is possible to obtain both species by chemical and electrochemical oxidation. They have isolated the $[[8]aneSe_2]^{2+}$ dication as a monomeric species, with two BF_4^- counterions, and with a Se-Se bond distance of 2.382(2) Å. This is just within twice the covalent radius of selenium (2.40 Å)⁴⁰ and it is also shorter than the Se1-Se2 distance in Figure 2.8 of 2.667(1) Å, which still lies significantly within the sum of the van der Waals radii (3.8 Å).⁴¹ The monocation in $[[8]aneSe_2]Cl][GaCl_4] \cdot CH_2Cl_2$ has a shorter Se-Se bond distance of 2.535(1) Å.

In a separate experiment $NOBF_4$ was added to a solution of $[(GaCl_3)_2([8]aneSe_2)]$ in anhydrous CH_2Cl_2 under an N_2 atmosphere in order to show that the same oxidation product could be obtained by use of an alternative oxidising agent. $NOBF_4$ was selected as the oxidant as it is an effective one electron oxidising agent with a non-coordinating anion. Addition of $NOBF_4$ led to a rapid red coloration, which dissipated over *ca.* one minute to a yellow solution, suggesting a similar process occurs with other oxidants. However, oxidation of a CH_2Cl_2 solution of $[8]aneSe_2$ by addition of an excess of Cl_2 -saturated CCl_4 caused a bright yellow precipitate to form (in the absence of $GaCl_3$). NMR spectroscopic studies (1H , $^{13}C\{^1H\}$ and $^{77}Se\{^1H\}$ ($\delta = 656$ ppm)) on this product were consistent with the formation of the tetrachloride derivative, $[[8]aneSe_2Cl_4]$ and supported by microanalytical data. This is in agreement with previous work on halogen adducts of diorganyl chalcogenides, which showed significant high frequency shifts in 1H and ^{77}Se NMR spectra.⁴² Se(IV) compounds typically have significantly higher frequency chemical shifts than Se(II) compounds in ^{77}Se NMR spectroscopy, for example, Me_2Se has a shift of 0 ppm (standard ^{77}Se NMR spectroscopy reference) whereas Me_2SeCl_2 has a shift of 448 ppm.³²

The reaction of $InCl_3$ with $[8]aneSe_2$ yielded a white, crystalline solid. Microanalysis data showed the compound to have the formula $[InCl_3([8]aneSe_2)_2]$. Raman and IR spectroscopy do not indicate the presence of $[InCl_4]^-$ (321 (Raman only) and 337 cm^{-1})³³ however comparison of IR and Raman spectra with known compounds did not allow for assignment of the coordination geometry. The 1H NMR spectroscopic data show shifts of less than 0.1 ppm relative to free ligand. Attempts to grow crystals suitable for single

crystal X-ray diffraction were unsuccessful and so the structure and coordination geometry of this complex are unknown.

2.2.2 Tetrathioether and tetraselenoether macrocyclic ligand complexes

The reactions of GaCl₃ with [n]aneS₄ (n = 12, 14, 16) and MCl₃ (M = Ga, In) with [16]aneSe₄ in anhydrous CH₂Cl₂ were carried out. The reaction of GaCl₃ with [12]aneS₄ yielded inconclusive characterisation data. Multiple microanalysis results showed much lower levels of carbon than expected. IR spectra showed a broad peak at 368 cm⁻¹, which could be assigned as a Ga-Cl stretch in [GaCl₃(L)] rather than [GaCl₄]⁻. Poor solubility hindered attempts to acquire informative ¹H NMR spectroscopic data. Attempts to grow crystals suitable for single crystal X-ray diffraction yielded only [12]aneS₄ therefore this reaction was not pursued further.

The complexes obtained from the reaction of MCl₃ with [16]aneE₄ were found to be isostructural, with a *trans* [MCl₂]⁺ fragment complexed within the macrocycle in a distorted octahedral geometry, and a tetrahedral [MCl₄]⁻ counterion present for charge balance (Figures 2.10 – 2.12). These products were obtained from both the reaction of one equivalent of MCl₃ with [16]aneE₄ and the reaction of two equivalents of MCl₃ with [16]aneE₄.

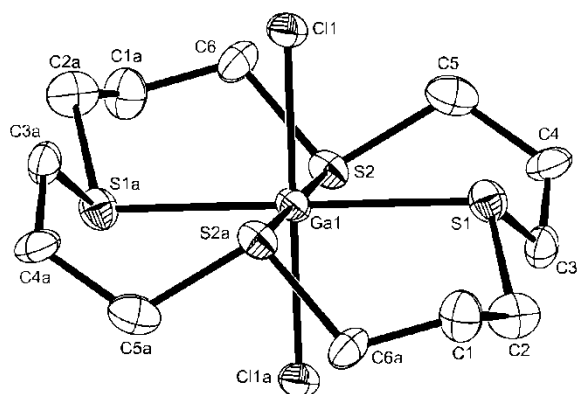


Figure 2.10 - View of one of the cations in the asymmetric unit of $[\text{GaCl}_2([\text{16}]aneS_4)][\text{GaCl}_4]$ with representative atom numbering scheme. Ellipsoids are shown at the 50% probability level and H atoms are omitted for clarity. The other cation is similar. Symmetry operation: $a = 2 - x, -y, 1 - z$

Ga1–Cl1	2.276(3)	Cl1–Ga1–S1	88.28(12)
Ga2–Cl2	2.293(3)	Cl1–Ga1–S2	92.27(12)
Ga3–Cl3	2.296(3)	Cl2–Ga2–S3	88.35(12)
Ga4–Cl4	2.292(3)	Cl2–Ga2–S4	91.81(13)
Ga1–S1	2.518(4)	Cl3–Ga3–S5	91.83(12)
Ga1–S2	2.492(4)	Cl3–Ga3–S6	91.24(12)
Ga2–S3	2.515(4)	Cl4–Ga4–S7	91.19(12)
Ga2–S4	2.464(4)	Cl4–Ga4–S8	92.01(14)
Ga3–S5	2.486(4)	S1–Ga1–S2	90.60(12)
Ga3–S6	2.499(4)	S3–Ga2–S4	89.57(12)
Ga4–S7	2.496(4)	S5–Ga3–S6	90.40(13)
Ga4–S8	2.482(4)	S7–Ga4–S8	90.02(13)

Table 2.3 - Selected bond lengths (Å) and angles ($^\circ$) for $[\text{GaCl}_2([\text{16}]aneS_4)]^+$ (Figure 2.10)

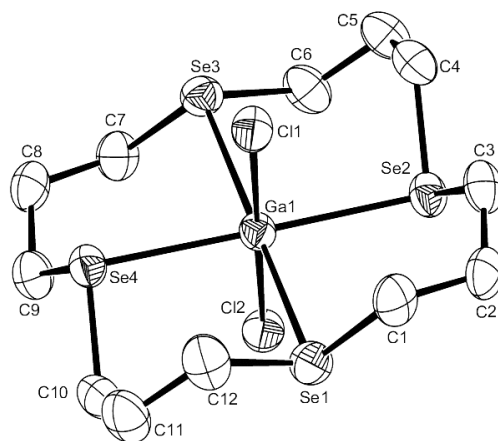


Figure 2.11 – Crystal structure of the cation in $[\text{GaCl}_2([\text{16]aneSe}_4)][\text{GaCl}_4]$ with atom numbering scheme. Ellipsoids are shown at the 50% probability level and H atoms are omitted for clarity.

Ga1–Cl1	2.322(1)	Ga1–Cl2	2.306(1)
Ga1–Se1	2.611(1)	Ga1–Se2	2.603(1)
Ga1–Se3	2.610(1)	Ga1–Se4	2.591(1)
Cl1–Ga1–Cl2	178.96(5)	Cl1–Ga1–Se1	91.85(4)
Cl1–Ga1–Se2	92.20(3)	Cl1–Ga1–Se3	85.86(4)
Cl1–Ga1–Se4	87.13(3)	Cl2–Ga1–Se1	89.11(4)
Cl2–Ga1–Se2	87.41(3)	Cl2–Ga1–Se3	93.19(4)
Cl2–Ga1–Se4	93.26(3)	Se1–Ga1–Se2	88.56(2)
Se1–Ga1–Se3	177.60(3)	Se1–Ga1–Se4	91.71(2)
Se2–Ga1–Se3	92.23(2)	Se2–Ga1–Se4	179.28(3)
Se3–Ga1–Se4	87.47(2)		

Table 2.4 - Selected bond lengths (Å) and angles ($^\circ$) for $[\text{GaCl}_2([\text{16]aneSe}_4)]^+$ (Figure 2.11)

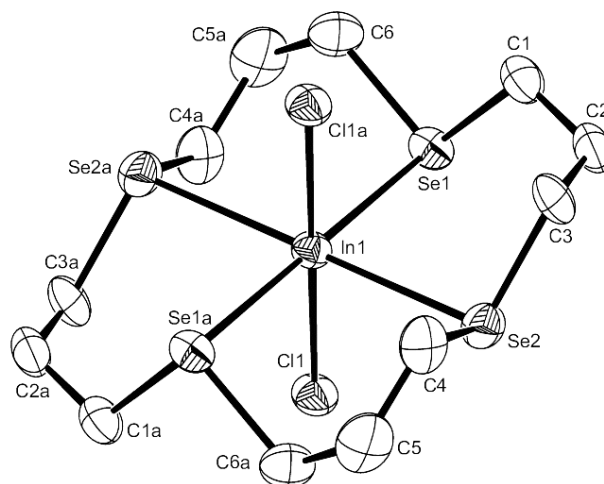


Figure 2.12 - View of the structure of the centrosymmetric cation in $[\text{InCl}_2([\text{16]aneSe}_4)][\text{InCl}_4]$ with atom numbering scheme. Ellipsoids are shown at the 40% probability level and H atoms are omitted for clarity. Symmetry operation: $a = -x, 1 - y, 2 - z$.

In1–Cl1	2.475(2)	Cl1–In1–Se1	88.04(6)
In1–Se1	2.719(1)	Cl1–In1–Se2	88.10(6)
In1–Se2	2.739(1)		

Table 2.5 - Selected bond lengths (Å) and angles ($^\circ$) for $[\text{InCl}_2([\text{16]aneSe}_4)]^+$ (Figure 2.12)

The single crystal X-ray structures of $[\text{GaCl}_2([\text{16]aneE}_4)]^+$ ($E = \text{S}, \text{Se}$) (Figures 2.10-11) show that gallium adopts a six-coordinate *pseudo*-octahedral geometry with displacement of one chloride, which is very unusual when compared to prior examples of thio- and seleno-ethers of gallium halides, which have solely exhibited distorted tetrahedral coordination of GaCl_3 *via* a single chalcogen donor group.¹ The six-coordinate octahedral geometry of $[\text{InCl}_2([\text{16]aneSe}_4)]^+$ (Figure 2.12) is not so unusual since previous examples show that indium complexes generally exhibit a wider range of coordination numbers and geometries than gallium complexes.² The structure of $[\text{InCl}_2([\text{14]aneS}_4)][\text{InCl}_4]$ has been determined previously and has been found to have a distorted octahedral geometry at In in $[\text{InCl}_2([\text{14]aneS}_4)]$ but with *cis* coordination of the chloride ligands.² The M-E

distances within each complex are non-identical, showing that the metal is positioned asymmetrically within the coordination sphere of the macrocycle. The Ga-Cl distances in $[\text{GaCl}_2([\text{16}]ane\text{Se}_4)]^+$ are also non-equivalent. Conversely, the same cannot be said for $[\text{GaCl}_2([\text{16}]ane\text{S}_4)]^+$ and $[\text{InCl}_2([\text{16}]ane\text{Se}_4)]^+$ as the Cl atoms are related by a symmetry operation. The bond angles also indicate that the structure is not perfectly octahedral as typical Cl-M-E angles are approximately 88 or 92°. As expected, the In-Cl (2.475(2) Å) and In-Se (2.719(1) Å) bond lengths are longer than the Ga-Cl (2.306(1) – 2.322(1) Å) and Ga-Se (2.591(1) – 2.611(1) Å) bond lengths, due to the larger covalent radius of In (1.42 vs. 1.22 Å).⁴⁰ The Ga-Se bond lengths are also longer than the Ga-S (2.464(4) – 2.518(4) Å) bond lengths due to the larger radius of Se compared with S (1.20 vs. 1.05 Å). In $[\text{GaCl}_2([\text{16}]ane\text{Se}_4)]^+$, the Ga atom sits only ~0.03 Å out of the plane of Se atoms, suggesting a very good size match between Ga(III) and the macrocyclic binding cavity. The Ga–Se bond distances, however, are significantly longer than in the previously reported tetrahedral complexes of $[\text{GaCl}_3(\text{SeMe}_2)]$ (2.464 (1) Å) and $[(\text{GaCl}_3)_2\{\text{}^n\text{BuSe}(\text{CH}_2)_2\text{Se}^n\text{Bu}\}]$ (2.468(1) Å).¹ This may be due to the increased coordination number or the constraints imposed by the more rigid macrocyclic ligand compared with the acyclic ligands.

IR and Raman spectroscopy confirm the presence of $[\text{MCl}_4]^-$ with strong, sharp peaks. The $[\text{MCl}_4]^-$ anions have tetrahedral symmetry so, using literature data, group theory allows assignment of the IR and Raman active stretches (cm^{-1}) as $a_1 = 346$ (Raman), $t_2 = 370$ (Raman and IR) for $[\text{GaCl}_4]^-$ and $a_1 = 321$ (Raman), $t_2 = 337$ (Raman and IR) for $[\text{InCl}_4]^-$.³³ Multinuclear NMR spectroscopy was also able to confirm the presence of $[\text{MCl}_4]^-$ for the $[\text{GaCl}_2([\text{16}]ane\text{S}_4)][\text{GaCl}_4]$ and $[\text{InCl}_2([\text{16}]ane\text{Se}_4)][\text{InCl}_4]$ complexes in CH_2Cl_2 . It would also have been expected that a solution of the $[\text{GaCl}_2([\text{16}]ane\text{Se}_4)][\text{GaCl}_4]$ complex in CH_2Cl_2 would exhibit a sharp peak for $[\text{GaCl}_4]^-$ in the $^{71}\text{Ga}\{^1\text{H}\}$ NMR spectra of the complex but this was not observed, possibly due to poor solubility. When this complex was dissolved in CH_3CN , a sharp singlet corresponding to $[\text{GaCl}_4]^-$ was observed. $^{71}\text{Ga}\{^1\text{H}\}$ and $^{115}\text{In}\{^1\text{H}\}$ NMR spectroscopic measurements were unable to observe a resonance for the $[\text{MCl}_2([\text{16}]ane\text{E}_4)]^+$ units. This is unsurprising due to the asymmetric environment of the quadrupolar nuclei, which could lead to line broadening to the extent that the resonance becomes too broad to observe. $^{77}\text{Se}\{^1\text{H}\}$ NMR

spectroscopy of $[\text{GaCl}_2([\text{16}]ane\text{Se}_4)][\text{GaCl}_4]$ in (non-coordinating) CH_2Cl_2 showed a low frequency coordination shift with a singlet at 134 ppm compared to 158 ppm in the free ligand.¹² In CH_3CN the resonance is a very sharp singlet at 158 ppm, suggesting that the ligand is extensively dissociated in the more competitive CH_3CN solvent. $[\text{InCl}_2([\text{16}]ane\text{Se}_4)][\text{InCl}_4]$ also appears to be extensively dissociated with a singlet at 158 ppm even in non-coordinating CH_2Cl_2 . ^1H NMR spectra exhibited a slight high frequency shift (approx. 0.2 ppm) relative to the free ligand. This is consistent with the NMR spectroscopic data obtained on complexes of InX_3 with acyclic chalcogenoether ligands, which also exhibited small, high frequency coordination shifts in ^1H NMR spectra and difficulty in obtaining ^{77}Se NMR spectra.²

In contrast, the reaction of GaCl_3 with $[\text{14}]ane\text{S}_4$ yielded a 1:1 complex, which was confirmed by CHN microanalysis. Although a distorted tetrahedral structure based on monomeric $[\text{GaCl}_3(\text{L})]$ was considered likely based on previous work (see 1.4.2), IR and Raman spectra indicate local D_{3h} symmetry (trigonal bipyramidal Cl_3S_2 coordination at Ga), showing the predicted e' mode at 381 and the a_1' mode at 331 cm^{-1} for the GaCl_3 unit. This is confirmed by the crystal structure showing an infinite polymeric chain with GaCl_3 in a distorted trigonal bipyramidal geometry with axial S atoms from bridging $[\text{14}]ane\text{S}_4$ molecules (Figures 2.13 and 2.14). A τ value of 0.99 shows that the complex is very close to ideal trigonal bipyramidal geometry (angles at 90 and 120°).⁴³ This is the first reported example of complexed GaCl_3 with the three Cl ligands adopting trigonal planar coordination sites. This structure also contrasts with the previously reported structure of *cis*- $[\text{InCl}_2([\text{14}]ane\text{S}_4)][\text{InCl}_4]$ where the macrocycle adopts a folded conformation to bind endocyclically to the $[\text{InCl}_2]^+$ unit with distorted octahedral coordination (Figure 2.15).² The In-S ($2.610(4) - 2.725(4)\text{ \AA}$) bond lengths in this structure are longer than the Ga-S ($2.574(1)\text{ \AA}$), which can mostly be attributed to the larger covalent radius of In vs. Ga. The In-Cl ($2.406(4), 2.418(4)\text{ \AA}$) bond lengths are also longer compared with the Ga-Cl bond lengths ($2.183(1)\text{ \AA}$).

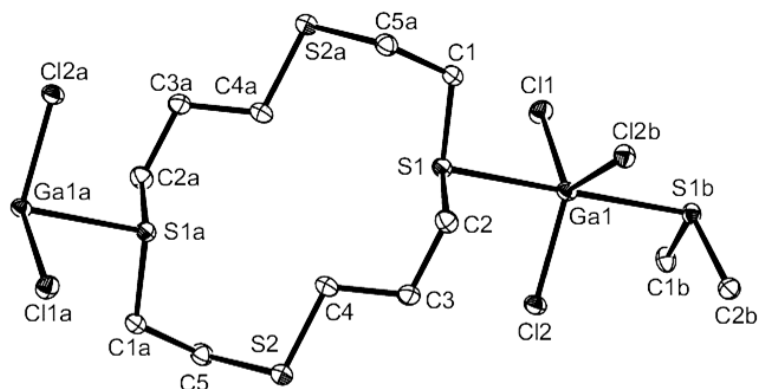


Figure 2.13 – Crystal structure of a section of the $[\text{GaCl}_3([\text{14}]ane\text{S}_4)]$ chain polymer with atom numbering scheme. Ellipsoids are shown at the 50% probability level and H atoms are omitted for clarity. Symmetry operators: $a = \frac{1}{2} - x, \frac{1}{2} - y, -z$; $b = 1 - x, y, \frac{1}{2} - z$

Ga1–Cl1	2.183(1)	Ga1–Cl2	2.184(1)
Ga1–S1	2.574(1)	Cl1–Ga1–Cl2	119.68(1)
Cl2–Ga1–Cl2b	120.64(3)	Cl1–Ga1–S1	89.65(1)
Cl2–Ga1–S1	88.54(2)	Cl1–Ga1–S1b	89.65(1)
Cl2–Ga1–S1b	91.81(2)	S1–Ga1–S1b	179.31(2)

Table 2.6 - Selected bond lengths (Å) and angles ($^\circ$) for $[\text{GaCl}_3([\text{14}]ane\text{S}_4)]$ (Figure 2.13)

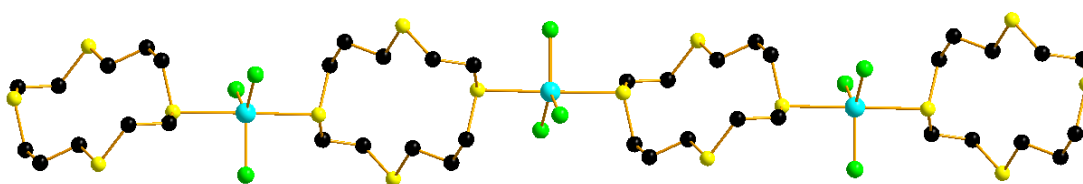


Figure 2.14 – Part of the extended 1D chain structure of $[\text{GaCl}_3([\text{14}]ane\text{S}_4)]$

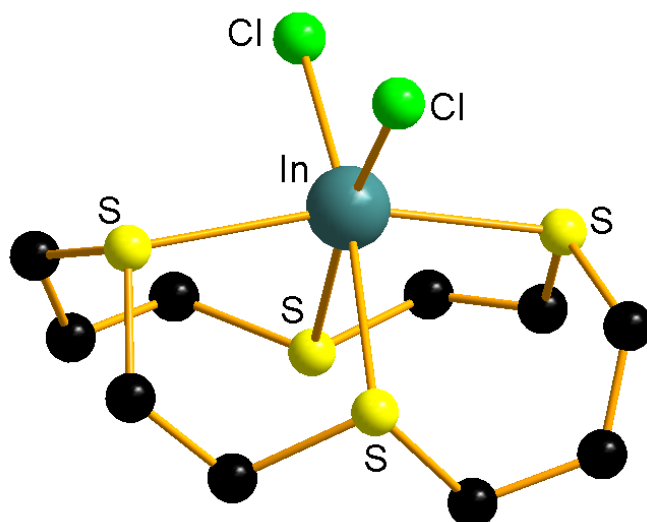


Figure 2.15 – Structure of $[\text{InCl}_2([\text{14}]ane\text{S}_4)]^+$ in $[\text{InCl}_2([\text{14}]ane\text{S}_4)][\text{InCl}_4]$

Compared with other complexes previously reported in the literature, the Ga–S distances ($2.5744(6) \text{ \AA}$) are considerably longer than those in the bidentate complexes of $[(\text{GaCl}_3)_2(\text{PhS}(\text{CH}_2)_2\text{SPh})]$ ($2.389(1) \text{ \AA}$) and $[(\text{GaCl}_3)_2(o\text{-C}_6\text{H}_4(\text{CH}_2\text{SMe})_2)]$ ($2.357(2) \text{ \AA}$).¹ A similar trend also exists for the Ga–Cl bond lengths but is less pronounced. This may be caused by the higher coordination number in $[\text{GaCl}_3([\text{14}]ane\text{S}_4)]$ compared with the 4-coordinate species previously characterised.

The reaction of GaCl_3 with $[\text{14}]ane\text{S}_4$ was also carried out as a 2:1 reaction. Comparison of the spectroscopic data of the product from this reaction with that of the 1:1 reaction shows that the product differs. Due to the complexities of the IR and NMR spectra, however, it has not been possible to identify the product. The IR spectrum shows evidence for the formation of more than one species, exhibiting a broad peak with distinguishable features at $401, 388, 368$ and 359 cm^{-1} , which indicates a mixture of Ga–Cl stretches probably arising from $[\text{GaCl}_3(\text{L})]$ ($401, 388, 359 \text{ cm}^{-1}$) and $[\text{GaCl}_4]^-$ (368 cm^{-1}). ^1H NMR spectroscopy reveals a more complicated spectrum than free ligand, with some additional peak multiplicity and overlapping of peaks. $^{71}\text{Ga}\{^1\text{H}\}$ NMR spectroscopy shows a sharp peak at 251 ppm , corresponding to that of $[\text{GaCl}_4]^-$. The spectroscopic data suggest that using a 2:1 ratio of GaCl_3 may produce a species that contains $[\text{GaCl}_4]^-$, possibly related to the complex of $[\text{GaCl}_2([\text{16}]ane\text{S}_4)][\text{GaCl}_4]$, but that

another species, probably the 1-D chain polymer (Figure 2.13) is present. The CHN elemental analysis data do not fit for either a 1:1 or a 2:1 complex, nor can it be easily assigned as a complex with an alternative M:L ratio.

The reactions of GaCl₃ with the tetradentate ligands [16]aneE₄ (E = S, Se) and [14]aneS₄ have shown some unusual and unexpected coordination modes. By constraining the donor atoms within a macrocyclic environment, it has been possible to access both six-coordinate octahedral geometries and five-coordinate trigonal bipyramidal coordination. Characterisation by multinuclear NMR, IR and Raman spectroscopies and microanalysis confirm that the crystal structures observed are representative of the bulk products.

The reactions of GaCl₃ and InCl₃ with [24]aneSe₆ were also carried out but the products remain unidentified. Attempts at collecting NMR spectroscopic data were hampered by the insolubility of the complexes and microanalysis could not identify the M:L stoichiometry. Raman and IR spectroscopy did not yield sufficient information for characterisation and so the decision was taken not to pursue the synthesis and characterisation of these complexes.

2.2.3 Conclusions

The use of macrocyclic ligands has allowed access to coordination geometries of GaCl₃ that have not been previously observed with chalcogenoether ligands. Both 6-coordinate octahedral and 5-coordinate trigonal bipyramidal geometries have been characterised. The crystal structures are supported by IR, Raman and multinuclear NMR spectroscopy on the bulk samples. GaCl₃ has also been found to promote the one and two electron oxidations of [8]aneSe₂ in air.

2.3 Experimental

[GaCl₃([14]aneS₄)]

[14]aneS₄ (0.053 g, 0.20 mmol) was dissolved in CH₂Cl₂ (5 mL) and added to a solution of GaCl₃ (0.035 g, 0.20 mmol) dissolved in CH₂Cl₂ (5 mL) with constant stirring. After 45 minutes the volume of the solvent was reduced *in vacuo* to ~5 mL. Colourless crystals suitable for X-ray diffraction studies were obtained from the solution which was kept at -18 °C for 48 hours. Yield: 0.073 g, 83%. Anal. Calcd for C₁₀H₂₀Cl₃GaS₄·½CH₂Cl₂: C, 25.9; H, 4.3. Found: C, 26.0, H, 4.0%. ¹H NMR (CD₂Cl₂, 295 K): 2.07 (quin, [4H], CH₂CH₂CH₂), 2.90 (t, [8H], SCH₂CH₂), 3.01 (s, [8H], SCH₂CH₂S), 5.3 (s, CH₂Cl₂). IR (cm⁻¹, Nujol): 381 (s,br). Raman (cm⁻¹): 386 (w), 331 (s).

[GaCl₂([16]aneS₄)] [GaCl₄]

[16]aneS₄ (0.025 g, 0.08 mmol) was dissolved in anhydrous CH₂Cl₂ (10 mL) and added to a solution of GaCl₃ (0.030 g, 0.17 mmol) in anhydrous MeCN (5 mL) with constant stirring. After 30 minutes the volume of the solvent was reduced *in vacuo* to ~7 mL. A white precipitate was obtained from the solution which was kept at -18 °C overnight. Colourless crystals suitable for X-ray diffraction studies were also obtained from the solution. Yield: 0.037 g, 68%. ¹H NMR (CD₂Cl₂, 295 K): 2.14 (quin, [8H], SCH₂CH₂), 2.95 (t, [16H], SCH₂CH₂). ⁷¹Ga{¹H} NMR (CD₃CN, 295 K) 252. IR (cm⁻¹, Nujol): 368 (br), 301 (br). Raman (cm⁻¹): 370 (w), 346(s). Yield: 0.037 g, 68%. Microanalytical measurements showed variable %C and %H values, but always lower than predicted, and data on the crystals gave %C and %H values which decreased steadily over time, suggesting decomposition.

[(GaCl₃)₂([8]aneSe₂)]

[8]aneSe₂ (0.069 g, 0.28 mmol) was dissolved in anhydrous CH₂Cl₂ (5 mL) and added to a solution of GaCl₃ (0.100 g, 0.57 mmol) in anhydrous CH₂Cl₂ (5 mL) with constant stirring to give a pale yellow solution. After 30 minutes a white precipitate had formed, which was collected by filtration and dried *in vacuo*. Yield: 0.082 g, 46%. ¹H NMR

(CDCl₃, 295 K): 2.47 (quin, [4H], SeCH₂CH₂), 3.23 (t, [8H], SeCH₂CH₂). ⁷¹Ga NMR (CDCl₃, 295 K): 237 (w_{1/2} = 4500 Hz). ⁷⁷Se{¹H} NMR (CDCl₃, 203 K): 112.1. IR spectrum (cm⁻¹, Nujol): 386 (s), 360 (m). Raman: not obtained as sample turned orange in the laser. Satisfactory microanalyses were not obtained due to the extreme sensitivity of this complex, leading to severe difficulties in handling the solid.

[GaCl₂([16]aneSe₄)]GaCl₄

[16]aneSe₄ (0.07 g, 0.14 mmol) was dissolved in CH₂Cl₂ (10 mL) and added to a solution of GaCl₃ (0.05 g, 0.28 mmol) in CH₂Cl₂ (5 mL) with constant stirring. After 45 minutes the volume of the solvent was reduced *in vacuo* to ~7 mL. Colourless crystals suitable for X-ray diffraction studies were obtained from the solution which was kept at -18 °C for 48 hours. Yield: 0.059 g, 50%. Anal. Calcd for C₁₂H₂₄Cl₆Ga₂Se₄: C, 17.2; H, 2.9. Found: C, 16.9, H, 2.6%. ¹H NMR (CDCl₃, 295 K): 2.15 (quin, [8H], CH₂CH₂CH₂), 2.85 (t, [16H], SeCH₂). ⁷⁷Se{¹H} NMR (CD₂Cl₂, 295 K) 138. IR (cm⁻¹, Nujol): 371 (s). Raman (cm⁻¹): 373 (w), 346 (s).

[InCl₃([8]aneSe₂)₂]

[8]aneSe₂ (0.121 g, 0.50 mmol) was dissolved in CH₂Cl₂ (5 mL) and added to a suspension of InCl₃ (0.111 g, 0.50 mmol) in CH₂Cl₂ (5 mL) with constant stirring. After 30 minutes the white solid was collected by filtration, washed with CH₂Cl₂ and dried *in vacuo*. Yield: 0.062 g, 35% (based on [8]aneSe₂). Anal. Calcd for C₁₂H₂₄Cl₃InSe₄: C, 20.4; H, 3.4. Found: C, 20.9, H, 3.8%. ¹H NMR (CD₃CN, 295 K): 2.23 (quin, [4H], CH₂CH₂CH₂), 2.89 (t, [8H], SeCH₂). IR (cm⁻¹, Nujol): 298 (m), 283 (s). Raman (cm⁻¹): 278 (s), 252 (m).

[InCl₂([16]aneSe₄)]InCl₄

[16]aneSe₄ (0.22 g, 0.45 mmol) was dissolved in CH₂Cl₂ (5 mL) and added to a suspension of InCl₃ (0.10 g, 0.45 mmol) in CH₂Cl₂ (5 mL) with constant stirring. After 30 minutes the white solid was collected by filtration. The volume of the filtrate was reduced *in vacuo* to

~5 mL. Colourless crystals suitable for X-ray diffraction studies were obtained from the filtrate which was kept at -18 °C for 48 hours. Yield: 0.127 g, 40%. Anal. Calcd for $C_{12}H_{24}Cl_6In_2Se_4$: C, 15.5; H, 2.6. Found: C, 15.3, H, 2.4%. 1H NMR ($CDCl_3$, 295 K): 2.07 (quin, [8H], $CH_2CH_2CH_2$), 2.71 (t, [16H], $SeCH_2$). $^{77}Se\{^1H\}$ NMR (CD_2Cl_2 , 295 K): 158. ^{115}In NMR (CD_2Cl_2 , 298 K): 446 ($[InCl_4]^-$). IR (cm^{-1} , Nujol): 338 (s), 323 (m), 275 (m). Raman (cm^{-1}) 346 (w), 336 (w), 320 (s), 281 (s), 242 (s).

[[8]aneSe₂Cl₄]: [8]aneSe₂ (0.040 g, 0.16 mmol) was added to a saturated solution of Cl₂ in CCl₄ (6 mL) with stirring. A pale yellow precipitate formed immediately. After 1 hour the reaction mixture was filtered to yield a pale yellow solid, which was washed with CH₂Cl₂ (2 x 2 mL) and dried *in vacuo*. Yield: essentially quantitative. Anal. Calcd for $C_6H_{12}Cl_4Se_2$: C, 18.8; H, 3.2. Found: C, 19.5; H, 3.2%. $^{13}C\{^1H\}$ NMR ($(CD_3)_2SO$, 295 K): 49.1 ($SeCH_2$), 44.2 ($CH_2CH_2CH_2$). $^{77}Se\{^1H\}$ NMR ($(CD_3)_2SO$, 295 K): 656.5 (s).

Table 2.7 Crystal data and structure refinement details^a

Compound	[GaCl ₃ ([14]aneS ₄)]	[GaCl ₂ ([16]aneS ₄)]GaCl ₄	[GaCl ₂ ([16]aneSe ₄)]GaCl ₄
Formula	C ₁₀ H ₂₀ Cl ₃ GaS ₄	C ₁₂ H ₂₄ Cl ₆ Ga ₂ S ₄	C ₁₂ H ₂₄ Cl ₆ Ga ₂ Se ₄
<i>M</i>	444.57	648.69	836.29
crystal system	monoclinic	monoclinic	orthorhombic
Space group	<i>C2/c</i> (no. 15)	<i>P2₁/n</i> (no. 14)	<i>Pbca</i> (no. 61)
<i>a</i> [Å]	21.781(4)	14.503(4)	9.9535(10)
<i>b</i> [Å]	6.537(1)	21.168(5)	21.461(4)
<i>c</i> [Å]	12.307(2)	15.591(3)	23.331(4)
β [deg]	108.56(1)	100.711(10)	90
<i>U</i> [Å ³]	1661.2(5)	4703.1(18)	4983.7(14)
<i>Z</i>	4	8	8
μ(Mo Kα) [mm ⁻¹]	2.622	3.325	8.646
total reflns	10950	31853	31334
unique reflns	1897	8246	5697
<i>R</i> _{int}	0.027	0.123	0.055
no. of params, restraints	123, 0	439, 0	217, 0
<i>R</i> ₁ ^b [<i>I</i> _o > 2σ(<i>I</i> _o)]	0.019	0.098	0.037
<i>R</i> ₁ [all data]	0.021	0.189	0.056
<i>wR</i> ₂ ^b [<i>I</i> _o > 2σ(<i>I</i> _o)]	0.041	0.210	0.075
<i>wR</i> ₂ [all data]	0.042	0.267	0.085

^a Common items: temperature = 120 K; wavelength (Mo Kα) = 0.71073 Å; θ(max) = 27.5°.

^b $R_1 = \sum ||F_o| - |F_c|| / \sum |F_o|$. $wR_2 = [\sum w(F_o^2 - F_c^2)^2 / \sum wF_o^4]^{1/2}$

Table 2.7 cont.

Compound	[InCl ₂ ([16]aneSe ₄)] [InCl ₄]	[[8]aneSe ₂) ₂][GaCl ₄] ₂	[[8]aneSe ₂]Cl][GaCl ₄]·CH ₂ Cl ₂
Formula	C ₁₂ H ₂₄ Cl ₆ In ₂ Se ₄	C ₁₂ H ₂₄ Cl ₈ Ga ₂ Se ₄	C ₇ H ₁₄ Cl ₇ GaSe ₂
<i>M</i>	926.49	907.19	573.97
crystal system	monoclinic	monoclinic	monoclinic
Space group	<i>P</i> 2 ₁ / <i>m</i> (no. 11)	<i>P</i> 2 ₁ / <i>n</i> (no. 14)	<i>P</i> 2 ₁ / <i>n</i> (no. 14)
<i>a</i> [Å]	6.9436(15)	9.0156(15)	7.3566(10)
<i>b</i> [Å]	22.508(5)	14.148(3)	12.521(2)
<i>c</i> [Å]	8.4877(15)	10.4855(15)	18.670(3)
β [deg]	100.735(10)	99.204(10)	93.107(10)
<i>U</i> [Å ³]	1303.3(4)	1320.2(4)	1717.2(4)
<i>Z</i>	2	2	4
μ(Mo Kα) [mm ⁻¹]	7.967	8.365	6.908
total no. reflns	14834	16831	17301
unique reflns	3064	3030	3907
<i>R</i> _{int}	0.082	0.042	0.035
no. of params, restraints	115, 0	118, 0	154, 0
<i>R</i> ₁ ^b [<i>I</i> _o > 2σ(<i>I</i> _o)]	0.065	0.027	0.020
<i>R</i> ₁ [all data]	0.118	0.036	0.024
<i>wR</i> ₂ ^b [<i>I</i> _o > 2σ(<i>I</i> _o)]	0.101	0.053	0.049
<i>wR</i> ₂ [all data]	0.120	0.056	0.051

2.4 References

1. Gurnani, C.; Levason, W.; Ratnani, R.; Reid, G.; Webster, M., *Dalton Trans.* **2008**, 6274-6282.
2. Gurnani, C.; Jura, M.; Levason, W.; Ratnani, R.; Reid, G.; Webster, M., *Dalton Trans.* **2009**, 1611-1619.
3. Buter, J.; Kellogg, R. M., *J. Org. Chem.* **1981**, *46*, 4481-4485.
4. Setzer, W. N.; Afshar, S.; Burns, N. L.; Ferrante, L. A.; Hester, A. M.; Meehan, E. J.; Grant, G. J.; Isaac, S. M.; Laudeman, C. P.; Lewis, C. M.; VanDerveer, D. G., *Heteroat. Chem.* **1990**, *1*, 375-387.
5. Ochrymowycz, L. A.; Mak, C.-P.; Michna, J. D., *J. Org. Chem.* **1974**, *39*, 2079-2084.
6. Champness, N. R.; Bruce, D. W.; Schroder, M., *New J. Chem.* **1999**, *23*, 671-674.
7. Mlinarić-Majerski, K.; Pavlović, D.; Luić, M.; Kojić-Prodić, B., *Chem. Ber.* **1994**, *127*, 1327-1329.
8. Berko, A.; Horton, P. N.; Hursthouse, M. B.; Packer, R. J.; Went, M. J., *Inorg. Chem. Commun.* **2005**, *8*, 488-490.
9. Comba, P.; Fath, A.; Nuber, B.; Peters, A., *J. Org. Chem.* **1997**, *62*, 8459-8462.
10. Neve, F.; Ghedini, M., *Inorg. Chim. Acta* **1994**, *217*, 1-2.
11. Blake, A. J.; Bruce, D. W.; Fallis, I. A.; Parsons, S.; Schroder, M., *J. Chem. Soc. Chem. Comm.* **1994**, 2471-2473.
12. Batchelor, R. J.; Einstein, F. W. B.; Gay, I. D.; Gu, J. H.; Johnston, B. D.; Pinto, B. M., *J. Am. Chem. Soc.* **1989**, *111*, 6582-6591.
13. Cordova-Reyes, I.; VandenHoven, E.; Mohammed, A.; Pinto, B. M., *Can. J. Chem.* **1995**, *73*, 113-116.
14. Levason, W.; Manning, J. M.; Reid, G.; Tuggey, M.; Webster, M., *Dalton Trans.* **2009**, 4569-77.
15. Fujihara, H.; Yabe, M.; Furukawa, N., *J. Chem. Soc., Perkin Trans. 1* **1996**, 1783-1785.
16. Fujihara, H.; Yabe, M.; Ikemori, M.; Furukawa, N., *J. Chem. Soc., Perkin Trans. 1* **1993**, 2145-2146.
17. Adams, R. D.; McBride, K. T.; Rogers, R. D., *Organometallics* **1997**, *16*, 3895-3901.

18. Panda, A., *Coord. Chem. Rev.* **2009**, *253*, 1947-1965.
19. Levason, W.; Reid, G., *J. Chem. Soc., Dalton Trans.* **2001**, 2953-2960.
20. Levason, W.; Reid, G.; Zhang, W., *Dalton Trans.* **2011**, *40*, 8491-8506.
21. Hector, A. L.; Levason, W.; Reid, G.; Webster, M.; Zhang, W., *Dalton Trans.* **2011**, *40*, 694-700.
22. Cheng, F.; Hector, A. L.; Levason, W.; Reid, G.; Webster, M.; Zhang, W., *Chem. Commun.* **2008**, 5508-5510.
23. Levason, W.; Matthews, M. L.; Patel, R.; Reid, G.; Webster, M., *New J. Chem.* **2003**, *27*, 1784-1788.
24. Helm, M.; Loveday, K.; Combs, C.; Bentzen, E.; VanDerveer, D.; Rogers, R.; Grant, G., *J. Chem. Crystallogr.* **2003**, *33*, 447-455.
25. Hill, N. J.; Levason, W.; Patel, R.; Reid, G.; Webster, M., *Dalton Trans.* **2004**, 980-981.
26. Norman, N. C.; Pickett, N. L., *Coord. Chem. Rev.* **1995**, *145*, 27-54.
27. Starbuck, J.; C. Norman, N.; Guy Orpen, A., *New J. Chem.* **1999**, *23*, 969-972.
28. Landrum, G. A.; Hoffmann, R., *Angew. Chem. Int. Ed.* **1998**, *37*, 1887-1890.
29. Alcock, N. W., Secondary Bonding to Nonmetallic Elements. In *Advances in Inorganic Chemistry and Radiochemistry*, Emeléus, H. J.; Sharpe, A. G., Eds. Academic Press: 1972; Vol. Volume 15, pp 1-58.
30. Benjamin, S. L.; Levason, W.; Reid, G., *Chem. Soc. Rev.* **2013**, *42*, 1460-1499.
31. A. Landrum, G.; Goldberg, N.; Hoffmann, R., *J. Chem. Soc., Dalton Trans.* **1997**, 3605-3613.
32. Mason, J., *Multinuclear NMR*. Plenum Press: New York, USA, 1989.
33. Nakamoto, K., *Infrared and Raman Spectra of Inorganic and Coordination Compounds*. Fourth ed.; Wiley-Interscience: New York, USA, 1986.
34. Fujihara, H.; Akaishi, R.; Erata, T.; Furukawa, N., *J. Chem. Soc. Chem. Comm.* **1989**, 1789-1790.
35. Fujihara, H.; Akaishi, R.; Furukawa, N., *Tetrahedron* **1993**, *49*, 1605-1618.
36. Batchelor, R. J.; Einstein, F. W. B.; Gay, I. D.; Gu, J. H.; Mehta, S.; Pinto, B. M.; Zhou, X. M., *Inorg. Chem.* **2000**, *39*, 2558-2571.
37. Evans, D. H.; Gruhn, N. E.; Jin, J.; Li, B.; Lorange, E.; Okumura, N.; Macias-Ruvalcaba, N. A.; Zakai, U. I.; Zhang, S.-Z.; Block, E.; Glass, R. S., *J. Org. Chem.* **2010**, *75*, 1997-2009.

38. Fujihara, H.; Akaishi, R.; Nakamura, A.; Furukawa, N., *Tetrahedron Lett.* **1990**, *31*, 6375-6378.
39. Furukawa, N., *Bull. Chem. Soc. Jpn.* **1997**, *70*, 2571-2591.
40. Cordero, B.; Gomez, V.; Platero-Prats, A. E.; Reves, M.; Echeverria, J.; Cremades, E.; Barragan, F.; Alvarez, S., *Dalton Trans.* **2008**, 2832-2838.
41. Mantina, M.; Chamberlin, A. C.; Valero, R.; Cramer, C. J.; Truhlar, D. G., *J. Phys. Chem. A* **2009**, *113*, 5806-5812.
42. Nakanishi, W.; Hayashi, S.; Tukada, H.; Iwamura, H., *J. Phys. Org. Chem.* **1990**, *3*, 358-368.
43. Addison, A. W.; Rao, T. N.; Reedijk, J.; van Rijn, J.; Verschoor, G. C., *J. Chem. Soc., Dalton Trans.* **1984**, 1349-1356.

3 Low Pressure Chemical Vapour Deposition of Gallium Selenide and Gallium Telluride Thin Films

3.1 Introduction

The coordination chemistry of gallium(III) halides with seleno- and telluro-ether ligands has been discussed in Chapters 1 and 2. The work in this chapter aims to investigate whether neutral chalcogenoether complexes of GaX_3 ($\text{X} = \text{Cl}, \text{Br}$) are suitable single source precursors for the chemical vapour deposition of gallium chalcogenide thin films. A range of chalcogenoether complexes of GaX_3 have previously been characterised.¹ As part of that work $[(\text{GaCl}_3)_2\{\mu\text{-}o\text{-C}_6\text{H}_4(\text{CH}_2\text{SeMe})_2\}]$ was investigated as a possible single source LPCVD precursor but decomposed before vaporisation occurred. Similar single source precursors with the formula $[\text{SnCl}_4\{\text{}^n\text{BuSe}(\text{CH}_2)_x\text{Se}^n\text{Bu}\}]$ ($x = 2$ or 3), which are coordination complexes obtained from the reaction of SnCl_4 with $\text{}^n\text{BuSe}(\text{CH}_2)_x\text{Se}^n\text{Bu}$ ($x = 2$ or 3), have been used to deposit SnSe_2 into holes in patterned substrates (Figure 3.14) with high selectivity of thin film growth onto TiN rather than SiO_2 .² The deposition of these thin films of the IV-VI material SnSe_2 was carried out using a similar methodology to that reported herein.

Chapter summary: $[\text{GaX}_3\{\text{}^n\text{Bu}_2\text{Se}\}]$ ($\text{X} = \text{Cl}, \text{Br}$), $[\text{GaCl}_3\{\text{Te}^n\text{Bu}_2\}]$, $[(\text{GaCl}_3)_2\{\text{}^n\text{BuTe}(\text{CH}_2)_3\text{Te}^n\text{Bu}\}]$, $[(\text{GaCl}_3)_2\{\text{}^t\text{BuTe}(\text{CH}_2)_3\text{Te}^t\text{Bu}\}]$ and $[(\text{GaCl}_3)_2\{\text{EtS}(\text{CH}_2)_2\text{SEt}\}]$ are novel coordination complexes, whereas $[(\text{GaCl}_3)_2\{\text{}^n\text{BuSeCH}_2\text{CH}_2\text{Se}^n\text{Bu}\}]$ has previously been synthesised and characterised. None of the complexes have previously been used as CVD precursors. LPCVD experiments were typically conducted at 0.1 mmHg and 773 K using 100 mg of precursor.

3.1.1 Single source precursors for III-VI materials

III-VI materials, such as Ga₂Se₃ and Ga₂Te₃, are important due to their semiconducting properties, which makes them useful in optoelectronic devices, as well as being potential candidates for phase change memory materials. For a more detailed discussion see section 1.1.

There are several examples of metal thiolates, selenolates and tellurolates being used for the CVD of metal chalcogenide thin films such as TiS₂, ZnTe, CdTe and HgTe.^{3, 4} Dialkyldithiocarbamate and dialkyldiselenocarbamate complexes have also been developed as single source precursors for InS, InSe and SnS for example [Et₂In(S₂CNMeⁿBu)] has been used as a single source precursor for AACVD.^{5, 6} There are also a small number of examples of neutral selenoether complexes being used for the LPCVD of TiSe₂ and SnSe₂ such as [TiCl₄(SeEt₂)₂], [TiCl₄(*o*-C₆H₄(CH₂EMe)₂)] (E = S, Se) and [SnCl₄(ⁿBuSe(CH₂)_xSeⁿBu)] (x = 2 or 3).^{2, 7, 8} The deposition of SnSe₂ was carried out within the research group at Southampton, using the same CVD rig and the same deposition conditions that were used to deposit the thin films reported in this chapter (773 K, 0.05 mmHg). The work also investigated using photolithographically patterned substrates (also reported herein) to selectively deposit SnSe₂ onto TiN with very high selectivity.

The first examples of CVD precursors for III-VI materials were single source, unlike the dual source routes employed for III-V materials (see 6.1),^{9, 10} although dual source routes have also been reported.^{11, 12} The first precursors used bulky alkyl and thiolate groups to produce monomeric indium thiolate complexes such as [ⁿBuIn(SⁱPr)₂], which deposited In₂S₃ at 300 – 400 °C and In₆S₇ at 450 °C.¹³ A similar, dimeric thiolate complex [(^tBu)₂In(μ-S^tBu)]₂ has been used to deposit InS.^{14, 15} O'Brien and co-workers have developed a range of single source precursors for Group 13 chalcogenide thin films in recent years. M₂Se₃ (M = Ga, In) thin films have been deposited by AACVD in toluene and LP-MOCVD (~10⁻² Torr, 673 – 748 K) from mixed alkyl/dialkylselenophosphorylamides of the type [R₂M(SePⁱPr₂)₂N].¹⁶ The Ga₂Se₃ films were found to be slightly selenium rich (64% Se) and the In₂Se₃ films had some

phosphorus content from the precursor (<1%). In₂Se₃ has also been deposited *via* AACVD (thf) and LP-MOCVD (~10⁻² Torr, 673 – 798 K) from a precursor utilising similar ligands [In{(SePⁱPr₂)₂N}₂Cl].¹⁷ These films also had some phosphorus contamination from the precursor but levels of other contaminants (O, Cl) were low. By using AACVD, lower deposition temperatures could be achieved than for LP-MOCVD.

Experiments using gallium and indium complexes of mixed alkyl thiocarbamates showed that both the alkyl group and the deposition temperature used has a significant effect on the phase and stoichiometry of the material deposited.¹⁸ [Me₂In(S₂CNEt₂)] deposits InS and In₆S₇ at 400 – 425 °C whereas In₂S₃ is deposited at 325 °C. In contrast, [Et₂In(S₂CNEt₂)] deposits In₂S₃ at 350 – 400 °C and the analogous neopentyl indium complex deposits In₆S₇. In₂E₃ has been grown from a tris-(dialkyldiselenocarbamate) precursor [In(E₂CNMeR)₃] (E = S, R = ⁿBu or ⁿHex; E = Se, R = ⁿHex).^{19, 20} [Et₂In(S₂CNMeⁿBu)] has been used to deposit nanorods of In₂S₃ that are ~20 nm in diameter and ~400 – 500 nm in length without the use of a template.²¹ Other precursors that have successfully been used to deposit In₂S₃ include [In(S₂COⁱPr)₃], which produces thin films at temperatures as low as 210 °C;²² [In(SOCNR₂)₃] (R = Et, ⁱPr) have been used to deposit tetragonal (R = ⁱPr)²³ and cubic (R = Et)²⁴ In₂S₃.

Barron and co-workers have also reported a gallium-chalcogen heterocubane precursor [Cp*Ga(μ₃-E)]₄ (Figure 3.1) for the MOCVD of Ga₂E₃ (E = S, Se), which is amorphous when deposited at 290 – 310 °C but crystallises upon annealing at 500 °C.²⁵ They have also used the cubane precursors [^tBuGaSe]₄ and [(EtMe₂C)InSe]₄ for the deposition of GaSe, using APCVD at 603 K, and InSe nanoparticles, using LPCVD (10⁻³ Torr, 563 K).²⁶ The GaSe nanoparticles had a mean diameter of 42 nm whereas the InSe nanoparticles had a mean diameter of 88 nm. Bourret and co-workers used [In{SeC(SiMe₃)₃}]₃ for the deposition of In₂Se₃ at temperatures between 330 °C and 500 °C at 10⁻² Torr.²⁷ Depositions at 330 °C produced hexagonal In₂Se₃ whereas depositions at 500 °C produced cubic In₂Se₃. Between these temperatures a mixture of hexagonal and cubic In₂Se₃ formed. There are also a number of additional reported single source precursors for the deposition of films with a 1:1 ratio of metal:chalcogenide.²⁸⁻³⁰

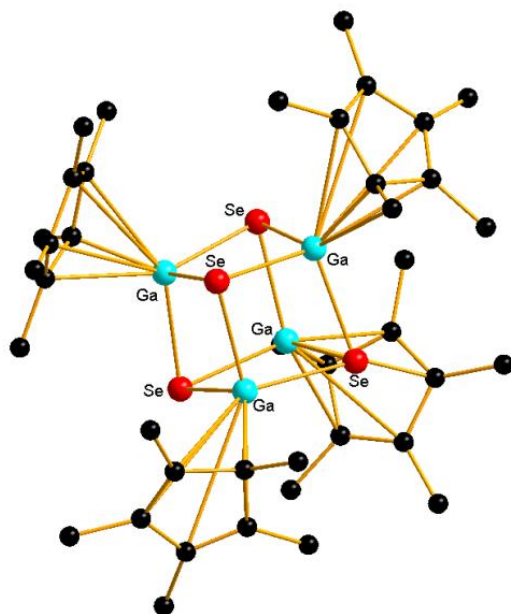


Figure 3.1 – Structure of $[\text{Cp}^*\text{Ga}(\mu_3\text{-Se})]_4$

Literature examples of single source precursors for gallium telluride are extremely limited. A 1995 review by Barron features $[\text{}^1\text{BuGaTe}]_4$ as the only single source precursor used to deposit GaTe and no precursors for the deposition of Ga_2Te_3 are included.³¹ O'Brien and co-workers also report a number of gallium telluride cubane precursors of the form $[\text{RGa}(\mu_3\text{-Te})]_4$ ($\text{R} = \text{CMe}_3, \text{CEtMe}_2, \text{CEt}_2\text{Me}$) that have been used to deposit GaTe at 285 - 310°C.²⁹ O'Brien, Chivers and co-workers have reported deposition of M_2Te_3 ($\text{M} = \text{Ga}, \text{In}$) at 325 – 475 °C using single source precursors based upon metal complexes with the monoanionic ditelluroimidodiphosphinato ligand $[\text{N}(\text{}^i\text{Pr}_2\text{PTE})_2]^-$. $\{\text{In}(\mu\text{-Te})[\text{N}(\text{}^i\text{Pr}_2\text{PTE})_2]\}_3$ deposited solely In_2Te_3 but $\{\text{Ga}(\mu\text{-Te})[\text{N}(\text{}^i\text{Pr}_2\text{PTE})_2]\}_3$ deposited a mixture of cubic Ga_2Te_3 , monoclinic GaTe and hexagonal Te, as shown by XRD measurements. EDX showed the films to be heavily rich in tellurium and to be contaminated with phosphorus (15 – 20%).³² Metal complexes using this ligand have also been used successfully as single source precursors to other telluride materials such as Sb_2Te_3 and CdTe .^{33, 34} The previous work published shows that more success has been obtained using single source precursors to indium chalcogenide films and that gallium reagents have been less successful.

3.2 Results and discussion

3.2.1 Synthesis and characterisation of precursors

All precursors were synthesised in good yields by the direct reaction of a stoichiometric quantity of GaCl₃ with a chalcogenoether ligand in anhydrous CH₂Cl₂. Ligands with *n*-butyl terminal substituents were selected for use in precursor synthesis as these are more likely to be eliminated easily *via* CVD while also being easy to obtain synthetically. Hence the complexes [(GaCl₃)₂{ⁿBuSeCH₂CH₂SeⁿBu}], [GaX₃(ⁿBu₂Se)] (X = Cl, Br), [GaCl₃(TeⁿBu₂)] and [(GaCl₃)₂{ⁿBuTe(CH₂)₃TeⁿBu}] were selected as potential single source precursors. [(GaCl₃)₂{^tBuTe(CH₂)₃Te^tBu}] was also synthesised as it was thought that replacing *n*-butyl groups with *t*-butyl groups would lead to the formation of a solid precursor, which would allow for easier precursor characterisation and manipulation. [(GaCl₃)₂{ⁿBuSeCH₂CH₂SeⁿBu}] is easily obtained as a crystalline solid whereas [GaX₃(ⁿBu₂Se)] (X = Cl, Br) and [GaCl₃(TeⁿBu₂)] are yellow or orange oils respectively. [(GaCl₃)₂{ⁿBuTe(CH₂)₃TeⁿBu}] is an extremely viscous orange oil that is more easily handled as a solution in anhydrous CH₂Cl₂. [GaCl₃(TeMe₂)] was synthesised to validate the assumption that precursors with *n*-butyl substituents would be better single source precursors than precursors with methyl substituents.

Previous work has shown that complexes of GaCl₃ with acyclic chalcogenoethers adopt a four coordinate, distorted tetrahedral geometry at the gallium centre (See 1.3.2). The crystal structure of the dinuclear [(GaCl₃)₂{ⁿBuSeCH₂CH₂SeⁿBu}] has been determined previously and also adopts a four coordinate geometry.¹ Characterisation of all new complexes by IR, Raman, ¹H, ⁷¹Ga, ⁷⁷Se{¹H} and ¹²⁵Te{¹H} NMR spectroscopy and microanalysis as appropriate, show that the data are in very good agreement with that obtained for related complexes,¹ and multinuclear NMR spectra indicate the complexes remain associated in chlorocarbon solutions. IR spectroscopy was used to confirm that the precursors adopt a distorted tetrahedral geometry and negate the presence of [GaCl₄]⁻, which has a characteristic IR stretch.³⁵ ⁷¹Ga NMR spectroscopy also indicates that the precursors synthesised as part of this work also adopt a C_{3v} geometry with broad peaks at in the region of 249 - 234 ppm, indicative of four coordinate GaCl₃ with one donor from the ligand rather than sharp peaks indicative of [GaCl₄]⁻.³⁶

The selenoether complexes are stable for months under an inert atmosphere at room temperature, however, the telluroether complexes tend to darken over a few days to weeks if stored at room temperature even in the glove box, forming increasing amounts of black solid (elemental Te) over time. Storage of the precursors in the dark at low temperatures (-18 °C) slowed the degradation considerably. Spectroscopic analysis of a sample of $[\text{GaCl}_3(\text{Te}^n\text{Bu}_2)]$ stored in the glove box for four weeks revealed that complete decomposition had occurred, mainly producing $[\text{Te}^n\text{Bu}_3][\text{GaCl}_4]$ [^1H NMR: $\delta = 3.15$ (*t*, [2H], TeCH_2), 1.80 (*m*, [2H], CH_2), 1.49 (*m*, [2H], CH_2), 0.98 (*t*, [3H], CH_3); $^{125}\text{Te}\{^1\text{H}\}$ NMR (CDCl_3): $\delta = 491$; ES^+ MS (MeCN): $m/z = 301$; ES^- MS (MeCN): $m/z = 211$] and elemental Te. It was therefore preferable to use freshly made precursors for the deposition of Ga_2Te_3 as using older (several days or more) precursors led to the deposition of films with higher levels of tellurium content. Examination of the films deposited from old samples by scanning electron microscopy showed two types of crystallites, which EDX confirmed corresponded to Ga_2Te_3 and Te. XRD spectroscopy also showed a mixture of Ga_2Te_3 and Te.

The crystal structure of $[(\text{GaCl}_3)_2\{\text{BuTe}(\text{CH}_2)_3\text{TeBu}\}]$ (Figure 3.2) shows a discrete dinuclear moiety with each Ga coordinated *via* three Cl ligands and one Te atom from the bridging ditelluroether, leading to a distorted tetrahedral coordination environment. This is the first crystallographically characterised example of a telluroether complex of a gallium halide. The Ga–Te bond distances are *ca.* 2.63 Å, some 0.5 Å longer than $d(\text{Ga–Cl})$. Comparison with the Ga–Se distances in four-coordinate selenoether complexes of GaCl_3 , e.g. $[(\text{GaCl}_3)_2\{\mu\text{-}^n\text{BuSe}(\text{CH}_2)_2\text{Se}^n\text{Bu}\}]$ (Ga–Se = 2.4683(11) Å), shows the Ga–Te distances in $[(\text{GaCl}_3)_2\{\text{BuTe}(\text{CH}_2)_3\text{TeBu}\}]$ are *ca.* 0.16 Å longer.¹ This is less than expected based simply upon the difference in covalent radii of Te *vs.* Se (0.25 Å), suggesting that the Ga–Te bonds are stronger than the Ga – Se bonds in these systems. This is in agreement with the decreased electronegativity of Te compared to Se. Long intermolecular $\text{Te}\cdots\text{Cl}$ contacts (3.710(3), 3.805(3) and 3.955(3) Å) are also evident (Figure 3.3). These are close to the sum of the Van der Waals radii for Te and Cl (3.81 Å).³⁷

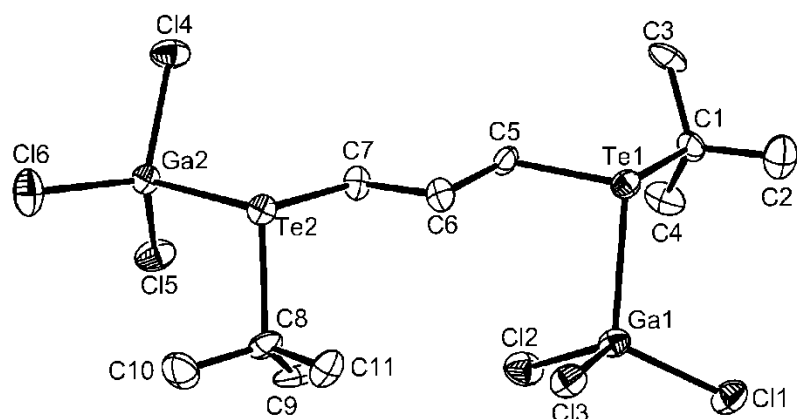


Figure 3.2 - View of the crystal structure of $[(\text{GaCl}_3)_2\{\text{tBuTe}(\text{CH}_2)_3\text{Te}'\text{Bu}\}]$ with atom numbering scheme. H atoms are omitted for clarity and ellipsoids are drawn at the 50% probability level.

Te1–Ga1	2.6378(14)	Cl3–Ga1–Cl2	109.27(11)
Te2–Ga2	2.6356(13)	Cl1–Ga1–Te1	111.74(9)
Ga1–Cl1	2.158(3)	Cl3–Ga1–Te1	102.92(8)
Ga1–Cl2	2.178(3)	Cl2–Ga1–Te1	108.26(8)
Ga1–Cl3	2.172(2)	Cl5–Ga2–Cl4	109.14(10)
Ga2–Cl4	2.181(3)	Cl6–Ga2–Cl4	111.84(12)
Ga2–Cl5	2.167(3)	Cl6–Ga2–Cl5	111.11(12)
Ga2–Cl6	2.159(3)	Cl4–Ga2–Te2	102.36(8)
Cl1–Ga1–Cl2	110.76(11)	Cl5–Ga2–Te2	112.07(8)
Cl1–Ga1–Cl3	113.52(10)	Cl6–Ga2–Te2	110.03(8)

Table 3.1 - Selected bond lengths (Å) and angles (°) for $[(\text{GaCl}_3)_2\{\text{tBuTe}(\text{CH}_2)_3\text{Te}'\text{Bu}\}]$ (Figure 3.2)

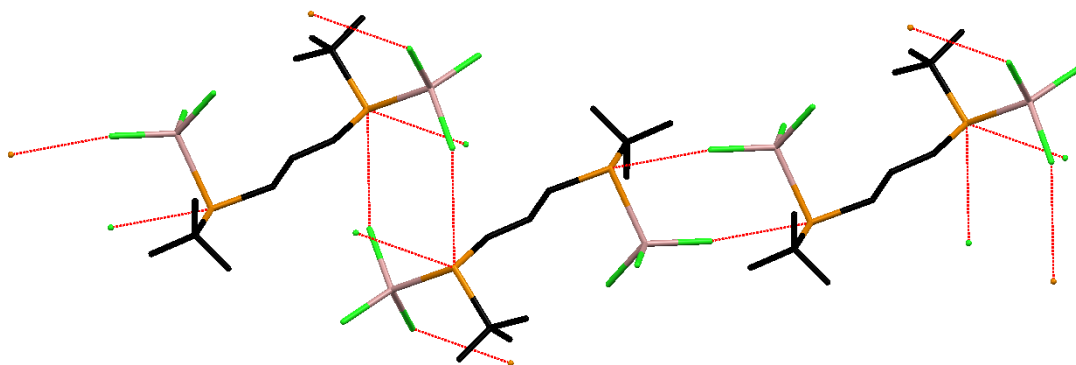


Figure 3.3 – Long intermolecular contacts (red) between Cl (green) and Te (brown) in $[(\text{GaCl}_3)_2\{\text{tBuTe}(\text{CH}_2)_3\text{Te}'\text{Bu}\}]$

3.2.2 Deposition and characterisation of gallium selenide thin films

Thermogravimetric analysis (TGA) of $[(\text{GaCl}_3)_2\{\text{}^n\text{BuSeCH}_2\text{CH}_2\text{Se}^n\text{Bu}\}]$ under a dry N_2 atmosphere revealed a two-step mass loss. The onset of the first step occurred at ~ 410 K, corresponding to a mass loss of 53%, while the second step occurs between ~ 550 and ~ 650 K, resulting in a further mass loss of 9%. This was used to guide the deposition temperature for the LPCVD experiments, suggesting that a temperature in excess of 650 K would be necessary.

LPCVD experiments using the selenoether complexes $[(\text{GaCl}_3)_2\{\text{}^n\text{BuSeCH}_2\text{CH}_2\text{Se}^n\text{Bu}\}]$ and $[\text{GaCl}_3(\text{}^n\text{Bu}_2\text{Se})]$ were undertaken at a pressure of 0.1 mmHg with the furnace temperature set at 773, 823 and 873 K. Due to a temperature gradient across the tube furnace, the temperature of the furnace at the precursor is ~ 605 K. Partial evaporation of the precursor compound occurred (some black solid residue remained) and there was deposition of orange coloured films onto SiO_2 or TiN substrates. The films produced by the two reagents, and also $[\text{GaBr}_3(\text{}^n\text{Bu}_2\text{Se})]$, were very similar in appearance (as well as structure and morphology), although the powdered solid $[(\text{GaCl}_3)_2\{\text{}^n\text{BuSeCH}_2\text{CH}_2\text{Se}^n\text{Bu}\}]$ proved more convenient to load into the CVD tube, hence this was used for the subsequent work. Initially depositions used *ca.* 100 mg of precursor, producing films over all the tiles except that closest to the precursor. These orange films were used for compositional and structural characterisation.

Scanning electron microscopy (SEM) images showed that the films are continuous comprised of small, cuboid crystallites with a regular morphology (Figure 3.4a). LPCVD using 100 mg of $[(\text{GaCl}_3)_2\{\text{}^n\text{BuSeCH}_2\text{CH}_2\text{Se}^n\text{Bu}\}]$ gave a film approximately $0.8 \mu\text{m}$ thick (Figure 3.4b), which was uniform across all films. EDX spectroscopy on these films showed a Ga:Se ratio of 1:1.50 (Ga_2Se_3), with negligible Cl or C content (Figure 3.5), whereas at lower deposition temperature (723 K) significantly higher Cl content was observed, hence all further depositions were carried out at 773 K.

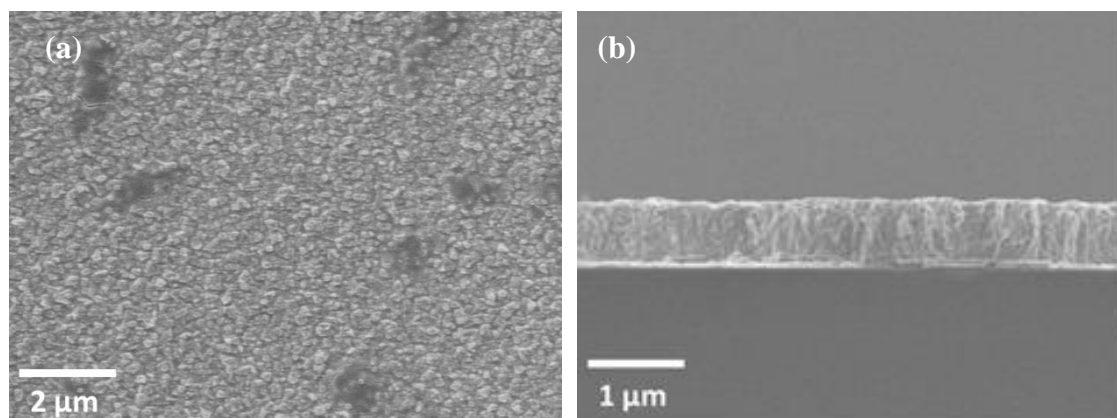


Figure 3.4 - (a) Top and (b) cross-sectional SEM images of a thin film of Ga_2Se_3 deposited from $[(\text{GaCl}_3)_2\{\text{nBuSeCH}_2\text{CH}_2\text{Se}^{\text{nBu}}\}]$ at 773 K onto SiO_2

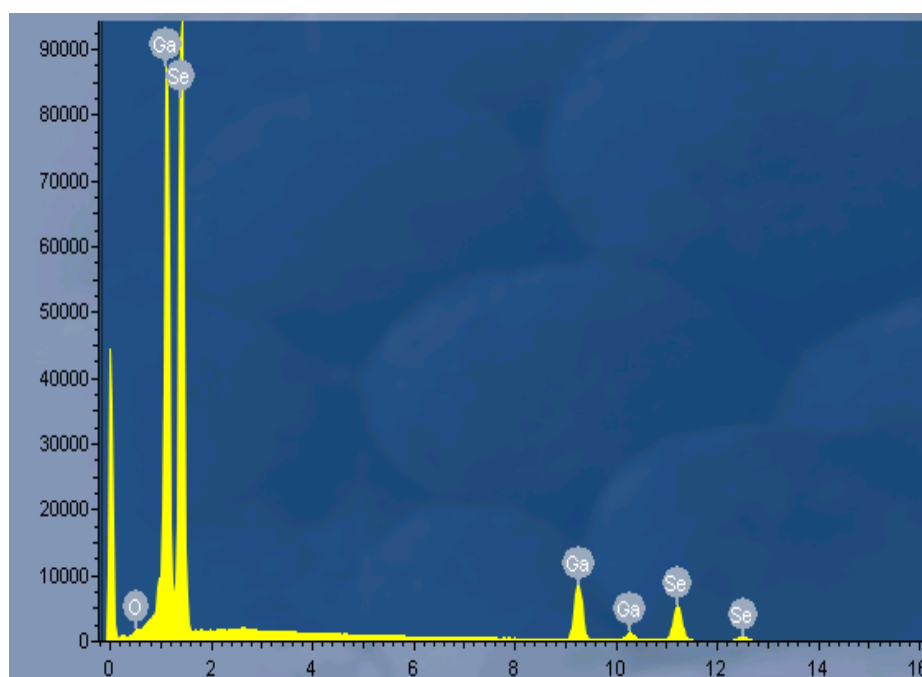


Figure 3.5 – EDX spectrum of a Ga_2Se_3 film showing no detectable chlorine content. Units: keV (x axis) and counts (y axis).

X-ray diffraction (XRD) measurements carried out on the films show that the films are crystalline monoclinic (*Cc*) Ga_2Se_3 , with the pattern matching well with literature data and showing no evidence of preferred orientation (Figure 3.6).³⁸ As the individual peak positions could not be resolved, it was not possible to do further refinements on the XRD data in order to compare lattice parameters with literature values.

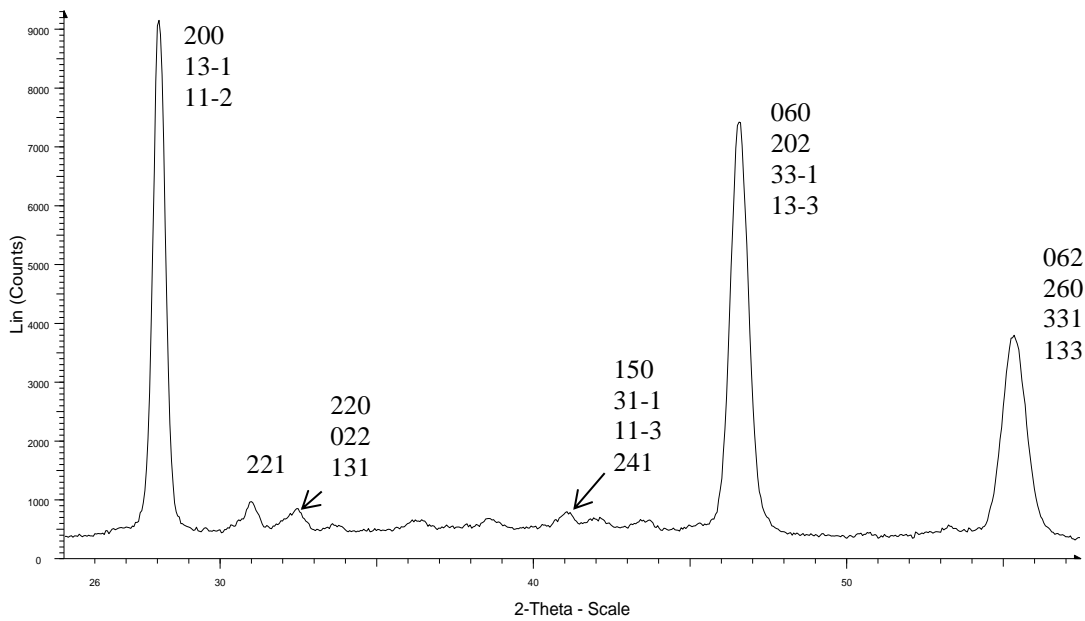


Figure 3.6 - XRD pattern from a typical Ga_2Se_3 thin film (monoclinic, Cc) grown via LPCVD from $[(\text{GaCl}_3)_2\{\text{}^n\text{BuSeCH}_2\text{CH}_2\text{Se}^n\text{Bu}\}]$ at 773 K onto SiO_2 . Only significant peaks have been indexed. Smaller features correspond to weaker reflections, which are not labeled for clarity.

Raman spectra were collected by Mr Ruomeng Huang. The Raman spectra of the films grown from $[(\text{GaCl}_3)_2\{\text{}^n\text{BuSeCH}_2\text{CH}_2\text{Se}^n\text{Bu}\}]$ and $[\text{GaCl}_3(\text{}^n\text{Bu}_2\text{Se})]$ confirmed that the films are crystalline, showing a sharp peak at 155 cm^{-1} and two broad peaks at 260 and 293 cm^{-1} , in agreement with the literature data (Figure 3.7).³⁹ Previous calculations indicate that the sharp peak at 155 cm^{-1} corresponds to the A_1 vibrational mode and the broad peaks at 260 and 293 cm^{-1} arise from transverse optical (TO) and longitudinal optical (LO) phonons, respectively, of Ga_2Se_3 .^{39, 40}

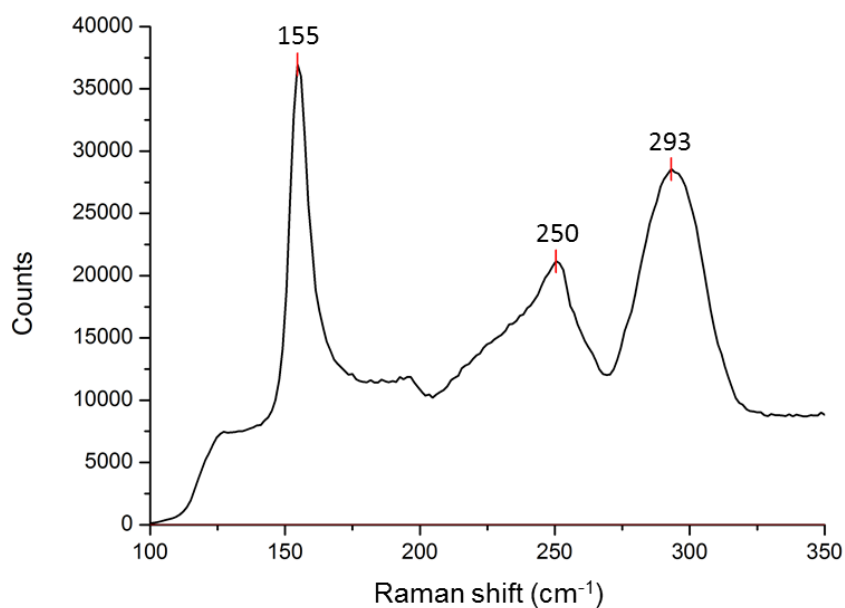


Figure 3.7 - Raman spectrum of a thin film of Ga_2Se_3 grown from $[(\text{GaCl}_3)_2\{\text{nBuSeCH}_2\text{CH}_2\text{Se}^{\text{nBu}}\}]$ at 773 K. Peaks marked on the graph match with literature values.

Atomic force microscopy (AFM) measurements confirm that there is uniform coverage across the substrate and also indicate that thinner films grown with limited quantities of reagent (~ 5 mg) are considerably smoother than thicker films. The thinner films (shown to be ~ 100 nm thick by cross-sectional SEM) had an RMS roughness of 18 nm (Figure 3.8).

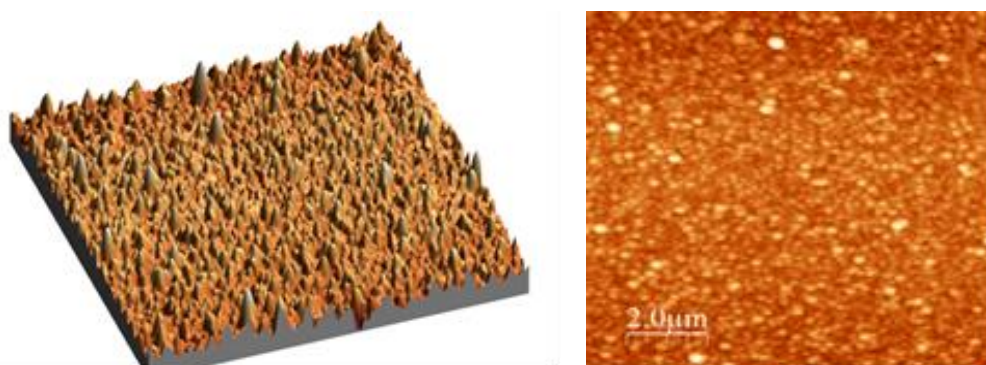


Figure 3.8 - AFM images of a Ga_2Se_3 thin film grown via LPCVD using 5 mg of $[(\text{GaCl}_3)_2\{\text{nBuSeCH}_2\text{CH}_2\text{Se}^{\text{nBu}}\}]$ at 773 K onto SiO_2 . RMS roughness = 18 nm.

3.2.3 Deposition and characterisation of gallium telluride thin films

LPCVD experiments were carried out at 773 K and 0.1 mm Hg using $[\text{GaCl}_3(\text{Te}^n\text{Bu}_2)]$, $[(\text{GaCl}_3)_2\{^n\text{BuTe}(\text{CH}_2)_3\text{Te}^n\text{Bu}\}]$, $[(\text{GaCl}_3)_2\{^t\text{BuTe}(\text{CH}_2)_3\text{Te}^t\text{Bu}\}]$ and $[\text{GaCl}_3(\text{Me}_2\text{Te})]$. $[\text{GaCl}_3(\text{Te}^n\text{Bu}_2)]$ and $[(\text{GaCl}_3)_2\{^n\text{BuTe}(\text{CH}_2)_3\text{Te}^n\text{Bu}\}]$ led to the deposition of grey films on 2 or 3 tiles, starting *ca.* 3 cm from the precursor (the temperature range across this region is 710 – 773 K), for both SiO_2 and TiN substrates. $[\text{GaCl}_3(\text{Te}^n\text{Bu}_2)]$ was chosen as the preferred precursor for depositions as it is a more mobile oil, allowing for easier loading into the CVD tube, although identical characterisation data were obtained on films deposited from $[(\text{GaCl}_3)_2\{^n\text{BuTe}(\text{CH}_2)_3\text{Te}^n\text{Bu}\}]$.

SEM images show that coverage of the substrate is uniform and the films are composed of microcrystallites approximately 1 μm in length (Figure 3.9a). LPCVD using 100 mg of precursor produces a film approximately 4 μm thick (Figure 3.9b). EDX measurements show a 1:1.50 ratio of Ga : Te, with no observable Cl, O or C impurities (Figure 3.10).

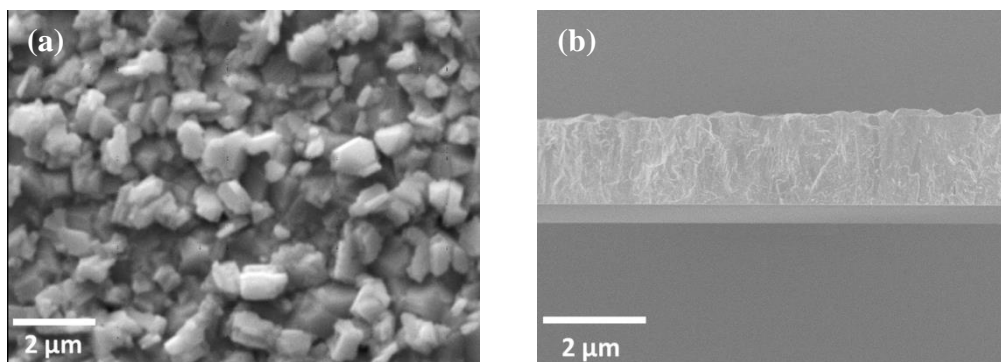


Figure 3.9 - (a) Top and (b) cross-sectional SEM images of a thin film of Ga_2Te_3 deposited from $[\text{GaCl}_3(\text{Te}^n\text{Bu}_2)]$ at 773 K onto SiO_2

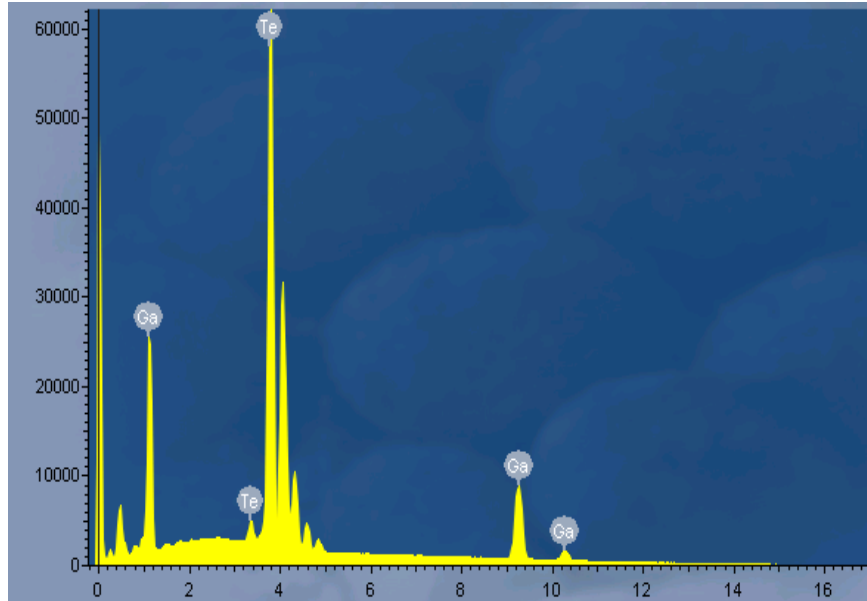


Figure 3.10 – EDX spectrum of a Ga₂Te₃ film showing no detectable chlorine content. Units: keV (x axis) and counts (y axis).

The Raman spectra of the films show peaks at 123 (A_g vibrational mode), 157 (E_g) and 226 (F_g) cm⁻¹ in agreement with literature data for Ga₂Te₃ (Figure 3.11), confirming that the thin films are crystalline Ga₂Te₃.⁴¹

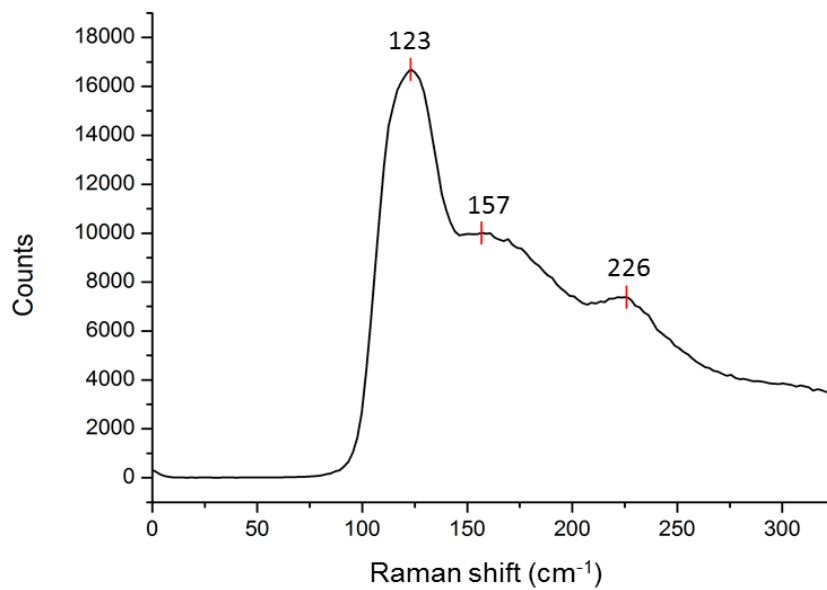


Figure 3.11 - Raman spectrum of a thin film of Ga₂Te₃. Peaks marked on the graph match with literature values.

XRD measurements on the thin films indicate that they are crystalline with a diffraction pattern that matches that reported for cubic ($F-43m$) Ga_2Te_3 . Indexing of the pattern and refining of the model against literature data by Dr Andrew Hector using GSAS software gives a lattice parameter $a = 5.8913(8) \text{ \AA}$ (Figure 3.12), which matches well with literature values (literature data from ICSD: $a = 5.886(5), 5.896(3) \text{ \AA}$ ⁴²⁻⁴⁴). There was no evidence for preferred orientation so this was not refined in the model.

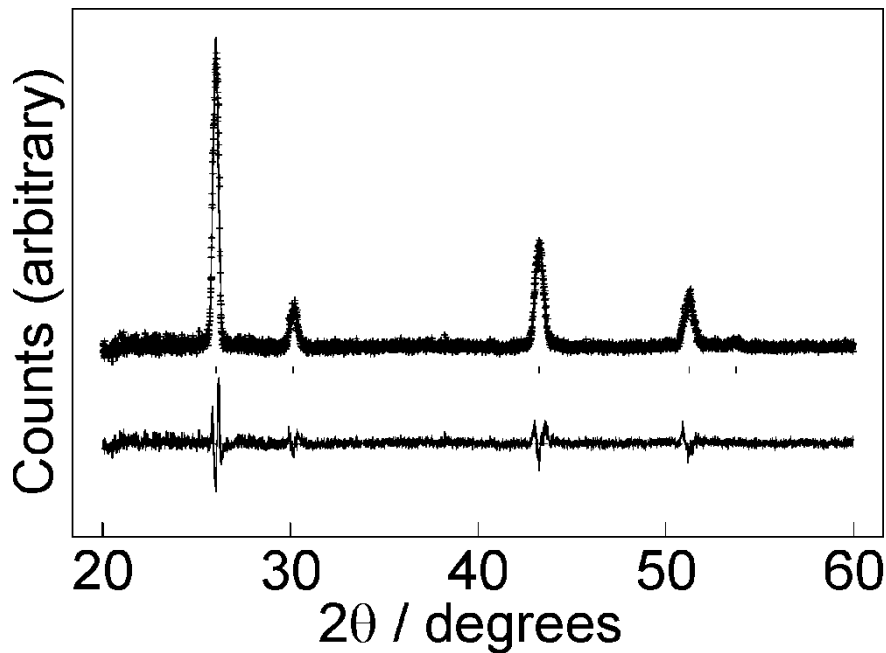


Figure 3.12 - Fit to XRD pattern for Ga_2Te_3 in $F-43m$ (zinc blende structure with 1/3 vacancies on Ga sites) with $a = 5.8913(8) \text{ \AA}$ ($R_{wp} = 18.2\%$, $R_p = 14.2\%$). Crosses mark the data points, the upper continuous line the fit and the lower continuous line the difference. Tick marks show the positions of allowed reflections.

AFM measurements also show that substrate coverage is uniform and roughness is relatively low (RMS roughness = 42 nm) for samples grown using smaller quantities of reagent (20 mg) (Figure 3.13).

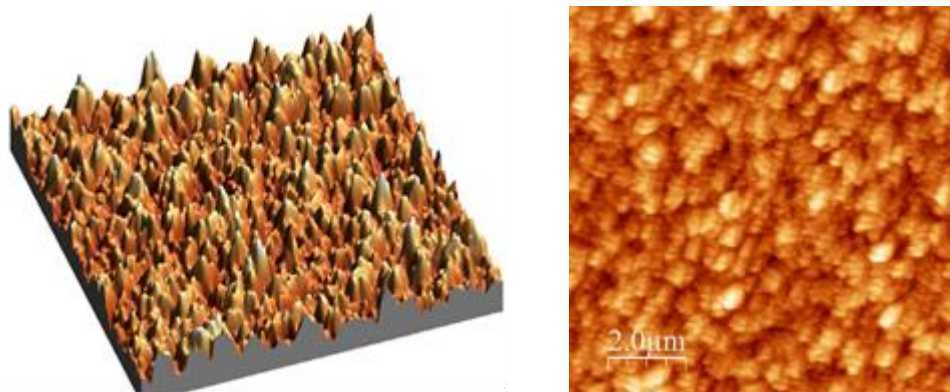


Figure 3.13 - AFM images of a Ga_2Te_3 thin film grown via LPCVD using 20 mg of $[\text{GaCl}_3(\text{Te}^n\text{Bu}_2)]$ at 773 K onto SiO_2 . RMS roughness = 42 nm.

$[(\text{GaCl}_3)_2\{\text{BuTe}(\text{CH}_2)_3\text{Te}^n\text{Bu}\}]$ was found to be insufficiently volatile to be a suitable LPCVD precursor as it pyrolysed where it was loaded into the tube furnace and did not deposit any material onto the tiles. XRD and EDX analysis of the pyrolysed precursor indicated that it formed Ga_2Te_3 but also had significant C and Cl contamination.

$[\text{GaCl}_3(\text{Me}_2\text{Te})]$ was synthesised according to the method published by Gurnani *et al.*¹ in order to validate the assumption that a complex with methyl substituents would be a less suitable single source precursor for the deposition of Ga_2Te_3 than a precursor with *n*-butyl substituents. 100 mg of $[\text{GaCl}_3(\text{Me}_2\text{Te})]$ was loaded into a CVD tube with fused silica tiles and heated to 773 K. The precursor melted and turned black, leaving some black residue and a black and metallic grey deposit at the far, cooler end of the tube. There was however negligible deposition on the silica tiles, with all but one tile having no film. XRD of the thin black film deposited gave no diffraction pattern. This therefore suggests that *n*-butyl substituents are more suitable for elimination, likely *via* a β -hydride elimination pathway, than methyl substituents, which would have to undergo radical elimination.⁴⁵ It is, however, difficult to state this definitively as other factors, such as thermal stability and ease of dissociation of the ligand from gallium, will also play a role in the decomposition of the single source precursor.

3.2.4 Hall measurements

Hall measurements were conducted by Mr Ruomeng Huang (ECS, University of Southampton) in order to measure the resistivity of the samples, which is an important property for phase change memory devices. For the Hall conductivity measurements, the Ga₂E₃ films were deposited on a SiO₂ coated Si substrate in order to insulate the current to the substrate. Films with thicknesses of 2.5 μm (E = Te) and 1.2 μm (E = Se) were used for the measurements. The experiments were performed under a magnetic field of 0.5 Tesla at 300 K.

The Ga₂Te₃ films were found to be a p-type semiconductor with a resistivity of 195±10 Ωcm and a carrier density of $5 \times 10^{15} \text{ cm}^{-3}$. The resistivity and carrier type are consistent with recent thermo-electric characterisation on bulk samples,^{46, 47} suggesting a close to stoichiometric compound. The hole mobility of the film was found to be in a range of 10 – 40 cm²/V-s.

The Ga₂Se₃ thin films are also p-type with a resistivity of $9 \pm 1 \times 10^3 \text{ Ωcm}$, a carrier density of $2 \times 10^{13} \text{ cm}^{-3}$, and a hole mobility of 20 – 80 cm²/V-s. The carrier type is in agreement with bulk measurements reported in the literature.^{48, 49} The resistivity is higher than for Ga₂Te₃, as expected from the difference in bandgap (approximately 2.0eV for Ga₂Se₃ and 1.1 eV for Ga₂Te₃).

Thin film conductivity sensitively depends on the exact composition and microstructure and for phase change materials, also the number of crystallisation cycles. The effect of the arrangement of the vacancies in the crystal structure may also play a role. Hence there is a large range of thin film data reported in the literature.^{41, 50-52} The non-uniformity of the Ga₂Se₃ film is also relevant, and hence the data for Ga₂Se₃ are indicative rather than authoritative.

3.2.5 Selective deposition

Photolithographically patterned TiN/SiO₂ substrates (Figure 3.14) were fabricated by Mr Ruomeng Huang (see Appendix 1 – Experimental). They have previously been used to show that SnSe₂ can be selectively deposited onto TiN rather than SiO₂.² This high selectivity was correlated to the relative hydrophobicities of the different substrates, as determined by measurements on the contact angle of a water droplet. The higher hydrophobicity of the TiN surface than the SiO₂ surface makes it more attractive to the hydrophobic alkyl substituents of the precursor. The ability to be able to deposit on to TiN, which is electrically conducting, in preference to SiO₂, which is electrically insulating, is an advantage as it makes device fabrication simpler and allows for characterising a known volume of material.

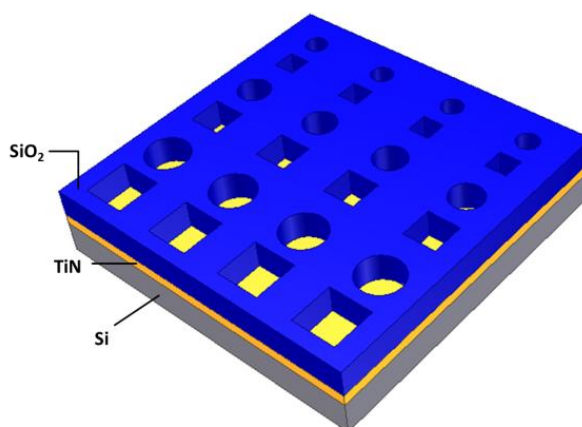


Figure 3.14 - Diagram of photolithographically patterned SiO₂/TiN substrates. The top SiO₂ layer is approximately 1 μm thick.

CVD experiments were carried out using limited quantities (5 – 10 mg) of [(GaCl₃)₂{ⁿBuSeCH₂CH₂SeⁿBu}] and [GaCl₃(TeⁿBu₂)]. The Ga₂Se₃ deposition showed no indication of selectivity, producing a uniform film that covered the entirety of the substrate. SEM images of Ga₂Te₃ deposited onto the patterned substrates showed a preference for deposition onto TiN over SiO₂ (Figure 3.15), although the selectivity was not quite as high as for SnSe₂. It may be possible to improve the selectivity by refining the LPCVD conditions, for example optimising the deposition temperature or adjusting the rate of precursor sublimation. It was the aim, however, of this work to prove

whether or not these coordination complexes would be suitable single source precursors, rather than achieve the best level of selectivity.

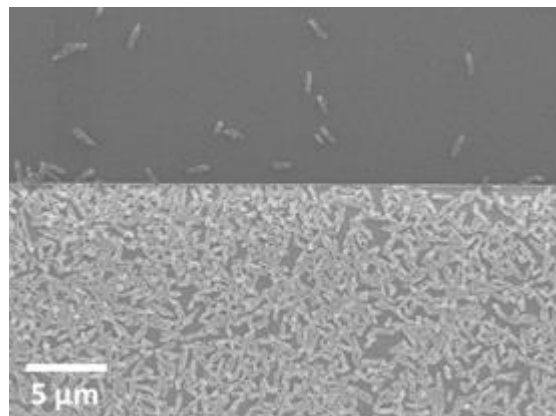


Figure 3.15 - SEM image showing the preferential deposition of Ga_2Te_3 onto the TiN surface (bottom half of image) relative to the SiO_2 surface (top half) of a patterned TiN/ SiO_2 substrate *via* LPCVD using 5 mg of $[\text{GaCl}_3(\text{Te}^n\text{Bu}_2)]$ at 773 K

3.2.6 Attempted LPCVD of gallium sulfide

In order to see whether thioether complexes of GaCl_3 were also suitable single source precursors for the deposition of Ga_2S_3 , three complexes were synthesised. $[\text{GaCl}_3(\text{R}_2\text{S})]$ ($\text{R} = \text{Et}, ^n\text{Bu}$), colourless oils, and $[(\text{GaCl}_3)_2\{\text{EtS}(\text{CH}_2)_2\text{SEt}\}]$, a white solid.

$[(\text{GaCl}_3)_2\{\text{EtS}(\text{CH}_2)_2\text{SEt}\}]$ was fully characterised, including a crystal structure (Figure 3.16) which confirmed the expected distorted tetrahedral coordination of one GaCl_3 at each S donor. ^{71}Ga NMR spectroscopy also confirmed the geometry with a broad ($W_{1/2} \sim 9000$ Hz) peak at 249 ppm, characteristic of distorted tetrahedral coordination.¹ The analogous complex $[(\text{GaCl}_3)_2\{\text{MeS}(\text{CH}_2)_2\text{SMe}\}]$ has a ^{71}Ga NMR spectroscopic shift of 265 ppm ($W_{1/2} \sim 8000$ Hz).¹ The difference in shifts may be due to the change from Me to Et substituents on the ligand but may also be influenced by the concentration of the NMR sample as all other conditions were consistent.

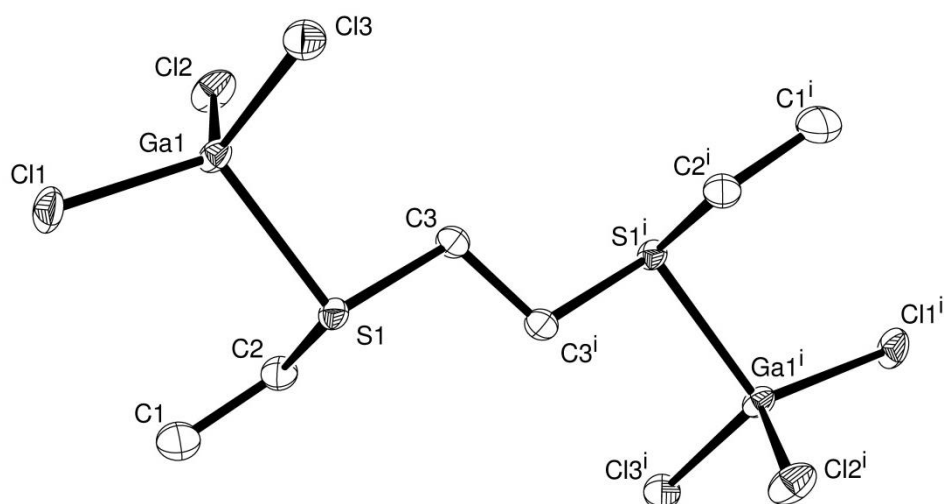


Figure 3.16 – Crystal structure of $[(\text{GaCl}_3)_2(\text{EtS}(\text{CH}_2)_2\text{SEt})]$ with atom numbering scheme. Ellipsoids are shown at the 50% probability level and H atoms are omitted for clarity. The molecule has 2-fold symmetry. Symmetry operation: $i = 2-x, 2-y, 2-z$.

S1-Ga1	2.362(2)	Cl1-Ga1-Cl3	113.43(7)
Cl1-Ga1	2.130(2)	Cl2-Ga1-Cl3	111.62(6)
Cl2-Ga1	2.152(2)	Cl1-Ga1-S1	108.76(6)
Cl3-Ga1	2.170(2)	Cl2-Ga1-S1	104.56(6)
Cl1-Ga1-Cl2	113.55(6)	Cl3-Ga1-S1	104.02(7)

Table 3.2 - Selected bond lengths (Å) and angles ($^\circ$) for $[(\text{GaCl}_3)_2(\text{EtS}(\text{CH}_2)_2\text{SEt})]$ (Figure 3.16)

LPCVD was carried out under similar conditions to the other precursors with depositions carried out 773 – 873 K, using 100 mg of reagent. Thin grey films were obtained, which were not crystalline by powder XRD. EDX measurements on several films deposited from all three precursors showed that the films, although containing gallium, had little or no sulfur content and very high levels of carbon and chlorine contamination. In these complexes the S-C bond is likely to be stronger than the Ga-S bond whereas for the seleno- and telluro-ethers the E-C (E = Se, Te) bond strength is weaker, allowing for easier elimination of the alkyl groups while maintaining the Ga-E interaction.

3.2.7 Conclusions

Seleno- and telluro- ether complexes of GaCl_3 have been shown to be effective single source precursors for the reproducible deposition of good quality thin films of Ga_2E_3 (E = Se, Te). This is the first reported example of a single source precursor based on a telluroether complex for the deposition of a metal telluride. Ga_2Te_3 can be deposited on to patterned substrates with preference for film growth on TiN over SiO_2 .

Characterisation of the thin films by XRD, Raman spectroscopy, SEM and EDX showed them to be crystalline with a 1:1.5 ratio of Ga:E. Electrical characterisation of the thin films showed that they are p-type semiconductors, with properties that agree well with literature values. The use of single source precursors to obtain stoichiometric Ga_2E_3 with no contamination from GaE or elemental chalcogen is a significant improvement, particularly for E = Te, over previously reported single source precursors. The ease of synthesis of the precursors is also a significant advantage. As the CVD conditions used could not deposit amorphous thin films, it was not possible to further explore the potential of the gallium chalcogenide films as phase change memory materials. The relatively high surface roughness also precludes easy device fabrication.

The analogous thioether complexes were not suitable single source precursors, failing to produce thin films of Ga_2S_3 . Alternative precursors for the deposition of Ga_2S_3 are discussed in Chapter 4.

3.3 Experimental

ⁿBuTe(CH₂)₃TeⁿBu

Freshly ground tellurium powder (8.9 g, 0.07 mol) in dry thf (140 mL) was frozen in a liquid nitrogen bath. ⁿBuLi (44 mL of 1.6 mol dm⁻³ solution in diethyl ether, 0.07 mol) was added and the mixture allowed to thaw. When all the tellurium had dissolved, the clear solution was refrozen (-196 °C) and 1,3-dichloropropane (3.6 mL, 4.28 g, 0.036 mol) added slowly dropwise. The mixture was allowed to warm to room temperature and hydrolysed with deoxygenated water, followed by separation, extraction with diethyl ether and drying (MgSO₄), under an inert atmosphere. The solvent was removed by distillation and the residue fractionated *in vacuo* (90 °C, 0.7 mmHg) to give an air-sensitive red oil. Yield: 8.0 g, 53%. ¹H NMR (CDCl₃): 0.91 (t, [6H], CH₃), 1.39 (m, [4H], CH₂), 1.72 (m, [4H], CH₂), 2.13 (m, [2H]), 2.68 (m, [8H], CH₂TeCH₂). ¹³C{¹H} NMR (CDCl₃): 3.85 (CH₂Te, ¹J_{TeC} = 150 Hz), 5.60 (CH₂Te, ¹J_{TeC} = 150 Hz), 14.48 (CH₃), 26.16 (CH₂), 35.42 (CH₂), 35.48 (CH₂). ¹²⁵Te{¹H} NMR (neat): 289 (s) ppm.

^tBuTe(CH₂)₃Te^tBu

Freshly ground Te (12.76 g, 0.1 mol) was suspended in anhydrous thf (150 mL) and frozen in a liquid N₂ bath. ^tBuLi (63 mL, 0.1 mol) was added and the solution allowed to warm to room temperature with stirring. After 30 minutes a yellow solution formed, which was frozen in a liquid N₂ bath and 1,3-dichloropropane added. The solution was allowed to warm to room temperature with stirring. After 30 minutes the solution had turned brown and a white precipitate had formed. After a further 30 minutes all solvent was removed *in vacuo*. The brown oil was extracted with anhydrous, degassed hexane (2 x 75 mL) and filtered through Celite. The hexane was removed *in vacuo* to give an orange oil, which was purified by vacuum distillation. ^tBuTe(CH₂)₃Te^tBu was collected as an orange-brown oil at 120°C at 0.1 mmHg. Yield: 16.2 g, 78%. ¹H NMR (CDCl₃, 295 K): 1.48 (s, [18H], CH₃), 2.11 (m, [2H], TeCH₂CH₂), 2.63 (t, [4H], TeCH₂). ¹³C{¹H} NMR (CDCl₃, 295 K): 5.75 (CH₃), 23.08 (TeCH₂CH₂), 34.28 (TeCH₂), 35.73 (CTe). ¹²⁵Te{¹H} NMR (CDCl₃, 295 K): 612 (s) ppm.

[(GaCl₃)₂(EtS(CH₂)₂SEt)]

GaCl₃ (0.44 g, 2.5 mmol) was dissolved in anhydrous CH₂Cl₂ (10 mL) and EtS(CH₂)₂SEt (0.188 g, 1.25 mmol) was added dropwise with stirring. After 30 mins., the volume of solution was reduced to ~5 mL *in vacuo*, causing a large quantity of white precipitate to form. The precipitate was collected by filtration, washed with CH₂Cl₂ (2 mL) and dried *in vacuo*. Colourless crystals suitable for X-ray diffraction were obtained by keeping the filtrate at -18 °C for 24 hours. Yield: 0.272 g, 43%. Anal. Calcd for C₆H₁₄Cl₆Ga₂S₂: C, 14.3; H, 2.8. Found: C, 13.4, H, 3.2%. ¹H NMR (CDCl₃, 295 K): 3.48 (s, 4 [H]), 3.17 (q, [4H]), 1.56 (t, [6H]). ⁷¹Ga NMR (CDCl₃, 295 K): 249 (W_{1/2} ~9000 Hz). IR (cm⁻¹, Nujol): 396 (s), 360 (s), 340 (s). Raman (cm⁻¹): 398 (w), 358 (s).

[GaCl₃(SeⁿBu₂)]

GaCl₃ (0.44 g, 2.5 mmol) was dissolved in anhydrous CH₂Cl₂ (10 mL) and a solution of SeⁿBu₂ (0.48 g, 2.5 mmol) in anhydrous CH₂Cl₂ (5 mL) was added with stirring. After 30 mins., all volatiles were removed *in vacuo* to give a pale yellow oil. Yield 0.75 g (82%). Anal. Calcd for C₈H₁₈Cl₃GaSe: C, 26.0; H, 4.9. Found: C, 26.7, H, 5.7%. ¹H NMR (CDCl₃, 295 K): 0.98 (t, [6H], CH₃), 1.50 (m, [4H], CH₂), 1.86 (m, [4H], CH₂), 3.16 (t, [4H], SeCH₂). ⁷⁷Se{¹H} NMR (CD₂Cl₂, 295 K): 135. ⁷¹Ga NMR (CD₂Cl₂, 295 K): 244 (W_{1/2} ~9000 Hz). IR (cm⁻¹, neat film): 395 (s), 371 (s), 356 (s). Raman (cm⁻¹): 396 (w), 373 (w), 355 (s).

[GaBr₃(SeⁿBu₂)]

Prepared similarly from SeⁿBu₂ and GaBr₃ (0.100 g, 0.32 mmol) in anhydrous CH₂Cl₂. Orange oil. Yield 0.152 g, 94%. Anal. Calcd for C₈H₁₈Br₃GaSe: C, 19.1; H, 3.6. Found: C, 19.6; H, 3.7%. ¹H NMR (CDCl₃, 295 K): 0.99 (t, [6H], CH₃), 1.49 (m, [4H], CH₂), 1.87 (m, [4H], CH₂), 3.08 (t, [4H], SeCH₂). ⁷⁷Se{¹H} NMR (CDCl₃, 295 K): 146. ⁷¹Ga NMR (CDCl₃, 295 K): 125 (W_{1/2} ~ 4200 Hz). IR (cm⁻¹, neat film): 299 (s), 237 (m). Raman (cm⁻¹): 285 (m), 235 (s).

[GaCl₃(TeⁿBu₂)]

GaCl₃ (0.29 g, 1.7 mmol) was dissolved in anhydrous CH₂Cl₂ (10 mL) and a solution of TeⁿBu₂ (0.40 g, 1.7 mmol) in anhydrous CH₂Cl₂ (10 mL) was added with stirring. After 30 minutes, all volatiles were removed *in vacuo* to give an orange oil, which was washed with cold hexane (5 mL) and dried *in vacuo*. Yield: 0.55 g, 80%. Anal. Calcd for C₈H₁₈Cl₃GaTe: C, 23.0; H, 4.3. Found: C, 23.0, H, 4.6%. ¹H NMR (CDCl₃, 295 K): 0.99 (t, [6H], CH₃), 1.48 (m, [4H], CH₂), 1.88 (m, [4H], CH₂), 3.08 (t, [4H], TeCH₂). ¹²⁵Te{¹H} NMR (CDCl₃, 295 K): 103 (s) ppm. ⁷¹Ga NMR (CDCl₃, 295 K): 234 (s, W_{1/2} ~3500 Hz) ppm. IR (cm⁻¹, Nujol): 387 (s,br), 349 (s). Raman (cm⁻¹): 398 (br), 350 (s).

[(GaCl₃)₂{ⁿBuTe(CH₂)₃TeⁿBu}]

GaCl₃ (0.44 g, 2.5 mmol) was dissolved in anhydrous CH₂Cl₂ (10 mL) and a solution of ⁿBuTe(CH₂)₃TeⁿBu (0.25 g, 1.25 mmol) in anhydrous CH₂Cl₂ (10 mL) was added with stirring to form an orange solution. After 30 mins., all volatiles were removed *in vacuo* to give a viscous brown oil, which was washed with cold hexane (5 mL) and dried *in vacuo*. Yield: 0.67 g, 73%. ¹H NMR (CDCl₃, 295 K): 1.00 (m, [6H], CH₃), 1.50 (m, [4H], CH₂), 1.90 (m, [4H], CH₂), 2.47 (m, [2H], CH₂), 3.09 (m, [4H], CH₂), 3.17 (m, [4H], CH₂). ¹²⁵Te{¹H} NMR (CDCl₃, 295 K): 129 (s) ppm. ⁷¹Ga NMR (CDCl₃, 295 K): 234 (s, W_{1/2} ~5000 Hz) ppm. IR (cm⁻¹, Nujol): 387 (s,br), 349 (s).

[(GaCl₃)₂{^tBuTe(CH₂)₃Te^tBu}]

GaCl₃ (0.44 g, 2.5 mmol) was dissolved in anhydrous CH₂Cl₂ (10 mL) and a solution of ^tBuTe(CH₂)₃Te^tBu (0.25 g, 1.25 mmol) in anhydrous CH₂Cl₂ (10 mL) was added with stirring to form an orange solution. The volume of solvent was reduced *in vacuo* to 10 mL and stored at 5°C overnight. Yellow, needle like crystals grew from the solution. Yield: 0.63 g, 69%. Anal. Calcd for C₁₁H₂₄Cl₆Ga₂Te₂: C, 17.3; H, 3.2. Found: C, 17.5, H, 3.0%. ¹H NMR (CDCl₃, 295 K): 1.85 (s, [18H], CH₃), 2.55 (m, [2H], TeCH₂), 3.14 (t, [4H], TeCH₂CH₂). IR (cm⁻¹, Nujol): 397 (m), 383 (s), 351 (m). Raman (cm⁻¹): 396 (w), 378 (w), 348 (s).

X-ray Crystallography

Crystals of $[(\text{GaCl}_3)_2\{\text{tBuTe}(\text{CH}_2)_3\text{Te}^t\text{Bu}\}]$ and $[(\text{GaCl}_3)_2\{\text{EtS}(\text{CH}_2)_2\text{SEt}\}]$ suitable for single-crystal X-ray analysis were obtained by cooling the filtrate (CH_2Cl_2) from the complex preparation. Data collection used a Bruker-Nonius Kappa CCD diffractometer fitted with monochromated Mo- K_α radiation ($\lambda=0.71073 \text{ \AA}$), with the crystals held at 100 K in a nitrogen gas stream. Structure solution and refinement were straightforward,^{53, 54} with H atoms introduced into the model in idealized positions.

Crystal structure of $[(\text{GaCl}_3)_2\{\text{tBuTe}(\text{CH}_2)_3\text{Te}^t\text{Bu}\}]$: formula = $\text{C}_{11}\text{H}_{24}\text{Cl}_6\text{Ga}_2\text{Te}_2$, $M = 763.64$, crystal system triclinic, space group $P-1$ (no. 2), $a = 6.4351(18)$, $b = 13.119(4)$, $c = 14.261(5) \text{ \AA}$, $\alpha = 83.81(2)$, $\beta = 88.486(17)$, $\gamma = 83.745(16)^\circ$, $V = 1189.6(6) \text{ \AA}^3$, $\mu = 5.334 \text{ mm}^{-1}$, $Z = 2$, total no. of reflections measured = 17609, $R_{\text{int}} = 0.082$, 5173 unique reflections, 190 independent parameters, $R_1 (I > 2\sigma I) = 0.070$, $R_1 (\text{all data}) = 0.095$, $wR_2 (I > 2\sigma I) = 0.098$, $wR_2 (\text{all data}) = 0.108$.

$[(\text{GaCl}_3)_2\{\text{EtS}(\text{CH}_2)_2\text{SEt}\}]$: formula = $\text{C}_6\text{H}_{14}\text{Cl}_6\text{Ga}_2\text{S}_2$, $M = 502.43$, crystal system triclinic, space group $P-1$ (no. 2), $a = 6.168(4)$, $b = 6.895(4)$, $c = 11.666(7) \text{ \AA}$, $\alpha = 102.229(8)$, $\beta = 93.561(5)$, $\gamma = 113.384(10)^\circ$, $V = 439.1(4) \text{ \AA}^3$, $\mu = 4.193 \text{ mm}^{-1}$, $Z = 1$, total no. of reflections measured = 4880, $R_{\text{int}} = 0.010$, 2552 unique reflections, 73 independent parameters, $R_1 (I > 2\sigma I) = 0.055$, $R_1 (\text{all data}) = 0.124$, $wR_2 (I > 2\sigma I) = 0.078$, $wR_2 (\text{all data}) = 0.099$

LPCVD onto SiO_2 or TiN substrates

In a typical experiment the reagent (*ca.* 100 mg) and substrates were loaded into a closed-end silica tube in a glove-box (precursor at the closed end, followed by either SiO_2 or TiN substrates positioned end-to-end through the heated region). The tube was set in a furnace such that the precursor was at the edge of the heated zone; the tube was evacuated, then heated to 773 K (actual temperature in the hot zone *ca.* 767 K) under 0.1 mmHg and the furnace was allowed to stabilize. The sample position was maintained until most of the precursor had evaporated (some residual black material remained), *i.e.* *ca.* 1 h. The tube was then cooled to room temperature and transferred to the glove box where the tiles were removed and stored under an N_2 atmosphere prior to analysis.

The LPCVD experiments using the selenoether precursors $[(\text{GaCl}_3)_2\{\text{}^n\text{BuSeCH}_2\text{CH}_2\text{Se}^n\text{Bu}\}]$ and $[\text{GaCl}_3(\text{}^n\text{Bu}_2\text{Se})]$ produced matt orange films and gave good coverage over 6–7 tiles. Both precursors gave Ga_2Se_3 films, with no significant differences in appearance or properties observed across the tiles. Similar films were also obtained using $[\text{GaBr}_3(\text{}^n\text{Bu}_2\text{Se})]$. Samples were generally well adhered to the tiles. Excellent reproducibility was obtained and films were visually very similar between depositions conducted with furnace temperature settings between 773 and 873 K, although lower temperatures (723 K) led to high Cl contamination in the EDX spectra of the deposited films, hence 773 K was selected as the preferred deposition temperature for the main work. Similar characterization data were obtained from several different samples.

The LPCVD experiments using the telluroether precursors $[\text{GaCl}_3(\text{Te}^n\text{Bu}_2)]$ and $[(\text{GaCl}_3)_2\{\text{}^n\text{BuTe}(\text{CH}_2)_3\text{Te}^n\text{Bu}\}]$ produced shiny dark grey films with coverage of *ca.* 1–3 tiles per experiment. When freshly prepared precursor samples were used, these gave single phase Ga_2Te_3 films, but when older samples were used the deposited films were shown by XRD to contain both Ga_2Te_3 and Te in varying ratios – see Discussion. Samples were generally very well adhered to the tiles. Good reproducibility was obtained and similar characterization data were obtained from several different samples.

LPCVD onto patterned TiN/SiO₂ substrates using $[\text{GaCl}_3(\text{Te}^n\text{Bu}_2)]$

TiN/SiO₂ patterned substrates (1 x 5 x 25 mm) were loaded with 5 mg of reagent into a closed-end silica tube in a glove-box as described above, and depositions were performed similarly over *ca.* 30 mins.

3.4 References

1. Gurnani, C.; Levason, W.; Ratnani, R.; Reid, G.; Webster, M., *Dalton Trans.* **2008**, 6274-6282.
2. de Groot, C. H.; Gurnani, C.; Hector, A. L.; Huang, R.; Jura, M.; Levason, W.; Reid, G., *Chem. Mater.* **2012**, *24*, 4442-4449.
3. Carmalt, C. J.; Parkin, I. P.; Peters, E. S., *Polyhedron* **2003**, *22*, 1263-1269.
4. Ritch, J. S.; Chivers, T.; Afzaal, M.; O'Brien, P., *Chem. Soc. Rev.* **2007**, *36*, 1622-1631.
5. Afzaal, M.; O'Brien, P., *J. Mater. Chem.* **2006**, *16*, 1597-1602.
6. Ramasamy, K.; Kuznetsov, V. L.; Gopal, K.; Malik, M. A.; Raftery, J.; Edwards, P. P.; O'Brien, P., *Chem. Mater.* **2013**, *25*, 266-276.
7. McKarns, P. J.; Lewkebandara, T. S.; Yap, G. P. A.; Liable-Sands, L. M.; Rheingold, A. L.; Winter, C. H., *Inorg. Chem.* **1998**, *37*, 418-424.
8. Reid, S. D.; Hector, A. L.; Levason, W.; Reid, G.; Waller, B. J.; Webster, M., *Dalton Trans.* **2007**, 4769-4777.
9. Nomura, R.; Inazawa, S. j.; Kanaya, K.; Matsuda, H., *Polyhedron* **1989**, *8*, 763-767.
10. Nomura, R.; Fujii, S.; Kanaya, K.; Matsuda, H., *Polyhedron* **1990**, *9*, 361-366.
11. Ng, T. L.; Maung, N.; Fan, G.; Poole, I. B.; Williams, J. O.; Wright, A. C.; Foster, D. F.; Cole-Hamilton, D. J., *Chem. Vap. Deposition* **1996**, *2*, 185-189.
12. Yu, S. M.; Yoo, J. H.; Patole, S. P.; Lee, J. H.; Yoo, J.-B., *Electron. Mater. Lett.* **2012**, *8*, 245-250.
13. Nomura, R.; Konishi, K.; Matsuda, H., *Thin Solid Films* **1991**, *198*, 339-345.
14. MacInnes, A. N.; Power, M. B.; Hepp, A. F.; Barron, A. R., *J. Organomet. Chem.* **1993**, *449*, 95-104.
15. MacInnes, A. N.; Cleaver, W. M.; Barron, A. R.; Power, M. B.; Hepp, A. F., *Adv. Mater. Opt. Electron.* **1992**, *1*, 229-233.
16. Park, J.-H.; Afzaal, M.; Helliwell, M.; Malik, M. A.; O'Brien, P.; Raftery, J., *Chem. Mater.* **2003**, *15*, 4205-4210.
17. Afzaal, M.; Crouch, D.; O'Brien, P., *Mater. Sci. Eng., B* **2005**, *116*, 391-394.
18. Haggata, S. W.; Malik, M. A.; Motevalli, M.; O'Brien, P.; Knowles, J. C., *Chem. Mater.* **1995**, *7*, 716-724.

19. O'Brien, P.; Otway, D. J.; Walsh, J. R., *Chem. Vap. Deposition* **1997**, *3*, 227-229.
20. O'Brien, P.; Otway, D. J.; Walsh, J. R., *Thin Solid Films* **1998**, *315*, 57-61.
21. Afzaal, M.; Malik, M. A.; O'Brien, P., *Chem. Commun.* **2004**, *0*, 334-335.
22. Bessergenev, V. G.; Ivanova, E. N.; Kovalevskaya, Y. A.; Gromilov, S. A.; Kirichenko, V. N., *Inorg. Mater.* **1996**, *32*, 592-596.
23. A. Horley, G.; O'Brien, P.; Park, J.-H.; J. P. White, A.; J. Williams, D., *J. Mater. Chem.* **1999**, *9*, 1289-1292.
24. A. Horley, G.; Chunggaze, M.; O'Brien, P.; J. P. White, A.; J. Williams, D., *J. Chem. Soc., Dalton Trans.* **1998**, 4205-4210.
25. Schulz, S.; Gillan, E. G.; Ross, J. L.; Rogers, L. M.; Rogers, R. D.; Barron, A. R., *Organometallics* **1996**, *15*, 4880-4883.
26. Stoll, S. L.; Gillan, E. G.; Barron, A. R., *Chem. Vap. Deposition* **1996**, *2*, 182-184.
27. Cheon, J.; Arnold, J.; Yu, K.-M.; Bourret, E. D., *Chem. Mater.* **1995**, *7*, 2273-2276.
28. MacInnes, A. N.; Power, M. B.; Barron, A. R., *Chem. Mater.* **1993**, *5*, 1344-1351.
29. Gillan, E. G.; Barron, A. R., *Chem. Mater.* **1997**, *9*, 3037-3048.
30. Gysling, H. J.; Wernberg, A. A.; Blanton, T. N., *Chem. Mater.* **1992**, *4*, 900-905.
31. Barron, A. R., *Adv. Mater. Opt. Electron.* **1995**, *5*, 245-258.
32. Garje, S. S.; Copsy, M. C.; Afzaal, M.; O'Brien, P.; Chivers, T., *J. Mater. Chem.* **2006**, *16*, 4542-4547.
33. Garje, S. S.; Eisler, D. J.; Ritch, J. S.; Afzaal, M.; O'Brien, P.; Chivers, T., *J. Am. Chem. Soc.* **2006**, *128*, 3120-3121.
34. Garje, S. S.; Ritch, J. S.; Eisler, D. J.; Afzaal, M.; O'Brien, P.; Chivers, T., *J. Mater. Chem.* **2006**, *16*, 966-969.
35. Nakamoto, K., *Infrared and Raman Spectra of Inorganic and Coordination Compounds*. Fourth ed.; Wiley-Interscience: New York, USA, 1986.
36. Mason, J., *Multinuclear NMR*. Plenum Press: New York, USA, 1989.
37. Mantina, M.; Chamberlin, A. C.; Valero, R.; Cramer, C. J.; Truhlar, D. G., *J. Phys. Chem. A* **2009**, *113*, 5806-5812.
38. Lübbers, D.; Leute, V., *J. Solid State Chem.* **1982**, *43*, 339-345.

39. Yamada, A.; Kojima, N.; Takahashi, K.; Okamoto, T.; Konagai, M., *Jpn J. Appl. Phys.* **2** **1992**, *31*, L186-L188.
40. Finkman, E.; Tauc, J.; Kershaw, R.; Wold, A., *Phys. Rev. B* **1975**, *11*, 3785-3794.
41. Julien, C.; Ivanov, I.; Ecrepont, C.; Guittard, M., *Phys. Status Solidi A* **1994**, *145*, 207-215.
42. Fletcher, D. A.; McMeeking, R. F.; Parkin, D., *J. Chem. Inf. Comput. Sci.* **1996**, *36*, 746-749.
43. Hahn, H.; Klingler, W., *Z. Anorg. Chem.* **1949**, *259*, 135-142.
44. Guymont, M.; Tomas, A.; Guittard, M., *Philos. Mag. A* **1992**, *66*, 133-139.
45. Schubert, U.; Huesing, N., *Synthesis of Inorganic Materials*. Third ed.; Wiley-VCH: Weinheim, Germany, 2012.
46. Yamanaka, S.; Ishimaru, M.; Charoenphakdee, A.; Matsumoto, H.; Kurosaki, K., *J. Electron. Mater.* **2009**, *38*, 1392-1396.
47. Kurosaki, K.; Matsumoto, H.; Charoenphakdee, A.; Yamanaka, S.; Ishimaru, M.; Hirotsu, Y., *Appl. Phys. Lett.* **2008**, *93*, 012101-3.
48. Popović, S.; Čelustka, B.; Ružic-Toroš, Ž.; Broz, D., *Phys. Status Solidi A* **1977**, *41*, 255-262.
49. Belal, A. E.; El-shaikh, H. A.; Ashraf, I. A., *Cryst. Res. Technol.* **1995**, *30*, 135-139.
50. Rusu, M.; Wiesner, S.; Lindner, S.; Strub, E.; Röhrich, J.; Würz, R.; Fritsch, W.; Bohne, W.; Th, S.-N.; Lux-Steiner, M. C.; Ch, G.; Heuken, M., *J. Phys.: Condens. Matter* **2003**, *15*, 8185.
51. Abdurakhmanova, A. A.; Aliev, M. I., *Phys. Status Solidi B* **1966**, *17*, 375-380.
52. Sen, S.; Bose, D. N., *Solid State Commun.* **1984**, *50*, 39-42.
53. Sheldrick, G. M. *SHELXS-97, Program for crystal structure solution*, University of Göttingen, Germany, 1997.
54. Sheldrick, G. M. *SHELXL-97, Program for crystal structure refinement*, University of Göttingen, Germany, 1997.

4 Chemical Vapour Deposition of Gallium Sulfide

4.1 Introduction

Chapter 3 investigated the use of gallium thioether complexes to deposit Ga₂S₃ without success. This chapter aims to use two thiolate based single source precursor, [Ga(SR)₂(μ-SR)]₂ (R = ⁱPr, ^tBu), to deposit thin films of Ga₂S₃. The syntheses and LPCVD of these precursors have previously been reported.^{1, 2} The aim is to build on the previous work by investigating the phase change properties of the deposited Ga₂S₃ films. As the thin films of Ga₂S₃ can be deposited as a cubic phase and then annealed to give a monoclinic phase, it will be easier to investigate their phase change properties than the films discussed in Chapter 3. The phase change properties will be investigated by thermal annealing of the thin films, which can be studied by XRD and Raman spectroscopy and laser annealing of very small areas of the films, which can be studied by microfocus XRD. There has been very little previous research into the phase change properties of Ga₂S₃.

4.1.1 Properties of gallium sulfide

Two forms of gallium sulfide exist with the formulae GaS and Ga₂S₃. GaS is an indirect band gap semiconductor (2.53 eV),^{3, 4} whereas Ga₂S₃ is a direct band gap semiconductor ($E_g = 3.4$ eV for α -Ga₂S₃, 2.5 eV for β -Ga₂S₃).⁵ Ga₂S₃ has exhibited blue-green luminescence at room temperature and several studies of the luminescence of doped and undoped Ga₂S₃ has been carried out due to its potential use in blue light emitting devices.⁶⁻⁹ There is also interest in gallium sulfide as there is a large amount of research into lanthanum gallium sulfide glasses which can be easily doped with other metals. These materials have excellent properties for optical lenses, optical amplification for telecommunications and laser fabrication and are non-toxic.¹⁰⁻¹³

4.1.2 Structure of Ga₂S₃

Several different phases of Ga₂S₃ have been found to exist.¹⁴⁻¹⁷ There exists some confusion in the literature as to the name of each phase, for example Hahn and Klingler¹⁴ report a cubic phase as α -Ga₂S₃, whereas this same phase is γ -Ga₂S₃ according to Tomas *et al.*, who claim that the α form has a wurtzite structure.¹⁶

The first crystal phases of Ga₂S₃ were reported by Hahn and Klingler in 1949.¹⁴ They reported the existence of a cubic phase ($F\bar{4}3m$; $a = 5.18 \text{ \AA}$), which they named α -Ga₂S₃ that is stable at low temperatures, and a high temperature hexagonal phase ($P6_3mc$; $a = 3.685$, $c = 6.028 \text{ \AA}$) based on a wurtzite structure, which they named β -Ga₂S₃. They stated that the transition temperature between the two phases is between 550 and 600 °C. In 1955, Hahn and Frank then reported an additional structure type of Ga₂S₃ with a hexagonal crystal system ($P6_1$), which is based on a modification of the wurtzite structure with lattice parameters of $a\sqrt{3}$ and $3c$ of the simple wurtzite structure ($a = 6.37$, $c = 18.0 \text{ \AA}$).¹⁸ A similar structural modification of a wurtzite form had already been observed for Al₂S₃ so it was logical that Ga₂S₃ might also adopt this form.¹⁹ In the conclusion in their paper, Hahn and Frank renamed the previously reported cubic phase γ -Ga₂S₃ and called the new form with the wurtzite superstructure α -Ga₂S₃.

In 1961, Goodyear *et al.* produced samples of bulk Ga₂S₃, which they studied by single crystal and powder X-ray diffraction and found the data to be almost identical to that of Hahn and Frank¹⁸ but with extra reflections that did not fit with the hexagonal $P6_1$ space group. Using their data, Goodyear *et al.* determined the structure of α -Ga₂S₃ as being C centred monoclinic ($a = 12.637$, $b = 6.41$, $c = 7.03 \text{ \AA}$, $\beta = 131.07^\circ$) and concluded that it has no relationship to the wurtzite structure.²⁰ In 1963, Goodyear and Steigmann reported a refined version of the monoclinic phase of α -Ga₂S₃ ($a = 11.14$, $b = 6.411$, $c = 7.038 \text{ \AA}$, $\beta = 121.22^\circ$), which was based on the same data but using a more conventional and convenient cell.¹⁷ This allowed for identification of the space group as Cc and the structure can be described as a distorted wurtzite form. A 1976 paper by Collin *et al.* reviewed and attempted to reproduce the literature on the preparation and structural determination of Ga₂S₃.¹⁵ They characterised a different monoclinic (Bb) form of Ga₂S₃ ($a = 11.094$, $b = 9.578$, $c = 6.395 \text{ \AA}$, $\beta = 141.15^\circ$) and could not reproduce the monoclinic form reported by Goodyear and Steigmann, instead identifying two triclinic

forms with similar a , b , c and β values but with α and γ being close to but not exactly 90°. The ICSD was able to transform the data into the Cc cell, which matches that reported by Goodyear and Steigmann and that is listed as the standardised structure. The authors were also able to identify polymorphism within Ga_2S_3 by melting crystals of Ga_2S_3 and cooling them at different rates. They were unable to assign the phases, however.

In 1979, Chilouet *et al.* reported that they obtained the zinc blende structure type γ - Ga_2S_3 at temperatures below 950 °C and the wurtzite form β - Ga_2S_3 at temperatures above 1000 °C.²¹

In 1987, Tomas *et al.* summarised the prior literature on the structures of Ga_2S_3 , describing four structural types that are listed in Table 4.1.¹⁶ They also described the relationship between the monoclinic (Bb) and wurtzite forms, assuming that the minor distortion in the monoclinic form is ignored (Equation 4.1). The same authors also report that the α and β forms only exist above 885 °C and the γ form only exists when there is a very small defect of sulfur to give a sub-stoichiometric form ($\text{GaS}_{1.38}$).²² They suggested that the four polymorphs of Ga_2S_3 are all dependent on temperature and composition and present a phase diagram to demonstrate where the transitions between polymorphs occur.

Name	Crystal system	Space group	Structure type	Lattice parameters
α - Ga_2S_3	Hexagonal	$P6_1$	Wurtzite superstructure	6.385(1), 18.040(1) Å
α' - Ga_2S_3	Monoclinic	Cc	Superstructure of α - Ga_2S_3	11.107(2), 6.395(1), 7.021(1) Å 121.17(3) °
		Bb	Superstructure of α - Ga_2S_3	11.094(2), 9.578(2), 6.395(1) Å 141.15(1) °
β - Ga_2S_3	Hexagonal	$P6_3mc$	Wurtzite	3.67(1), 6.01(1) Å
γ - Ga_2S_3	Cubic	$F-43m$	Zinc blende	5.17(1) Å

Table 4.1 – Crystal phases of Ga_2S_3 . The Bb phase is widely reported but the Cc setting is the standardised form.

$$a_m = 3a_w; b_m = \sqrt{(2a_w)^2 + c_w^2}; c_m = a_w\sqrt{3}$$

$$\alpha = \beta = \gamma = 90^\circ$$

Equation 4.1 – Relationship between the monoclinic and wurtzite forms of Ga₂S₃

More recently, Jones *et al.* published a crystal structure of monoclinic (*Cc*) Ga₂S₃ ($a = 11.107$, $b = 6.395$, $c = 7.021$ Å, $\beta = 121.17^\circ$) that matches the unit cell given by Goodyear and Steigmann.²³

4.1.3 CVD of gallium sulfide

The single source precursor used for this work, [Ga(SⁱPr)₂(μ-SⁱPr)]₂, was first synthesised by Suh *et al.*¹ and they also used it for a series of vapour deposition experiments.² The low melting point (~60 °C) allows for use of the precursor in a conventional bubbler assembly. Suh *et al.* carried out depositions at 350 – 610 °C on to silicon, glass and yttria-stabilised zirconia (YSZ) substrates. Rutherford backscattering spectroscopy, XPS and EDX spectroscopy were used to determine that the film composition was Ga₂S₃ and that carbon and oxygen contamination was very low (< 1 atom %). Deposition on to glass substrates produced γ-Ga₂S₃ with the degree of crystallinity increasing as the deposition temperature increased (Figure 4.1). The deposition at 610 °C showed some preferred orientation in the (111) direction. Attempts to grow highly oriented films by using YSZ (111) as a substrate were successful, resulting in highly oriented films at 550 and 610 °C. Using silicon as a substrate led to the formation of α-Ga₂S₃ and the films were comprised of platelike crystals.

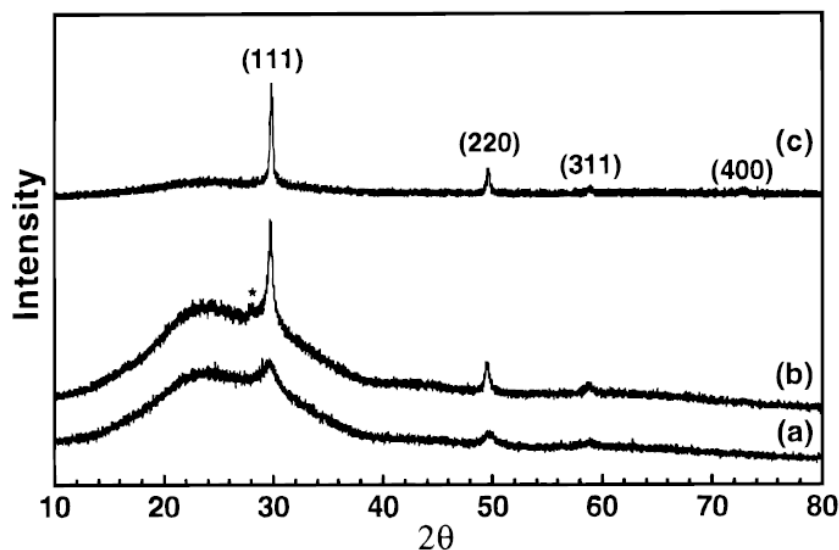
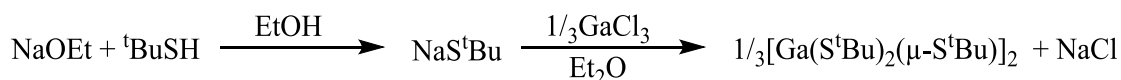


Figure 4.1 – XRD pattern of γ - Ga_2S_3 deposited at different temperatures [(a) = 400 °C; (b) = 500 °C; (c) = 610 °C] onto glass showing an increase in crystallinity with temperature. Image reproduced with permission.²

α - Ga_2S_3 has also been deposited using the thiocarboxylate compounds $[\text{Ga}(\text{SCOMe})_3(3,5\text{-lutidine})]$ and $[\text{Ga}(\text{SCOMe})_2\text{Me}(3,5\text{-lutidine})]$.²⁴ The depositions were carried out at 275 – 310 °C and gave good quality, stoichiometric Ga_2S_3 . $[\text{Ga}(\text{S}_2\text{CNMeHex})_3]$, an air stable solid, has also been used to deposit thin films of α - Ga_2S_3 .²⁵ Using this compound for AACVD produced poor quality films but using LPCVD produced films with much better crystallinity and morphology. At 500 °C it was possible to grow thin films on GaAs substrates but not on glass. $[\text{Cp}^*\text{Ga}(\mu_3\text{-S})]_4$ ($\text{Cp}^* = \text{C}_5\text{Me}_5$) has been used to deposit thin films of amorphous Ga_2S_3 at ~300 °C on silicon and GaAs substrates, which crystallises as γ - Ga_2S_3 upon annealing at 500 °C.²⁶ Barron and co-workers reported in 1993 that at 475 °C, $[\text{Ga}(\text{tBu})_2(\mu\text{-S}^t\text{Bu})]_2$ produced amorphous Ga_2S_3 , whereas at 400 °C it formed GaS.²⁷

Nanoparticles of β - Ga_2S_3 with a mean diameter of 12 nm have been deposited from $[\text{GaMe}(\text{SCH}_2\text{CH}_2\text{S})]_n$.²⁸ The nanoparticles were formed at 400 °C and heating at 500 °C formed a mixture of Ga_2S_3 and GaS.

Initially an alternative experimental route for the synthesis of $[\text{Ga}(\text{S}^t\text{Bu})_2(\mu\text{-S}^t\text{Bu})]_2$ was attempted *via* the route shown in Scheme 4.2. Although a white solid was obtained from the reaction, ^1H NMR spectroscopy showed only the presence of $^t\text{BuSH}$ and some unidentified impurities. $^t\text{BuSH}$ may have formed from hydrolysis of $[\text{Ga}(\text{S}^t\text{Bu})_2(\mu\text{-S}^t\text{Bu})]_2$ from trace amounts of water in the NMR solvent. Due to the difficulties in confirming the formation of $[\text{Ga}(\text{S}^t\text{Bu})_2(\mu\text{-S}^t\text{Bu})]_2$ *via* this synthesis route, the method reported by Suh *et al.* was used instead.¹



Scheme 4.2 – Attempted synthesis of $[\text{Ga}(\text{S}^t\text{Bu})_2(\mu\text{-S}^t\text{Bu})]_2$

A comparison of acidities show that amides have higher proton affinities than the corresponding alkoxides (Table 4.2), suggesting that using LDA to deprotonate the thiol has a greater chance of success than the using sodium ethoxide.³⁰

R^-	$\Delta H_{\text{acid}}(\text{RH})$ (kcal mol^{-1})
Me_2N^-	396.4 ± 0.9
CH_3O^-	381.9 ± 0.5
CH_3S^-	356.9 ± 2.2

Table 4.2 – Acidities of dimethyl amide, methoxide and methyl thiolate

All precursors used in this work were synthesised by the routes reported by Suh *et al.*¹ The precursor identity and purity was confirmed by ^1H NMR spectroscopy prior to use for LPCVD.

4.2.2 Thin film deposition and characterisation

LPCVD experiments using the thiolate complex $[\text{Ga}(\text{S}^i\text{Pr})_2(\mu\text{-S}^i\text{Pr})]_2$ were undertaken with the furnace temperature set at 723 K, leading to complete evaporation of the precursor compound and deposition of very pale yellow films onto SiO_2 substrates.

Depositions used ~25 mg of precursor, producing films over 3-4 tiles closest to the precursor. These films were used for compositional and structural analysis.

723 K was chosen as the furnace temperature as temperature profiling showed that this gave a temperature of ~663 K in the deposition zone. The XRD pattern published by Suh *et al.* shows that a poorly crystalline film is deposited at 673 K and higher deposition temperatures give more crystalline films (Figure 4.1).²

SEM images show that the films are uniform and smooth with no observable features (Figure 4.3a). LPCVD using 25 mg of $[\text{Ga}(\text{S}^{\text{i}}\text{Pr})_2(\mu\text{-S}^{\text{i}}\text{Pr})_2]$ gave a film approximately 200 nm thick as determined by SEM (Figure 4.3b). EDX analysis of the thin films show Ga:S ratios very close to 2:3. After annealing at 800 °C under N_2 some cracking of the films was observed by SEM but otherwise there was no apparent difference in the morphology of the films and the Ga:S ratio was unaffected.

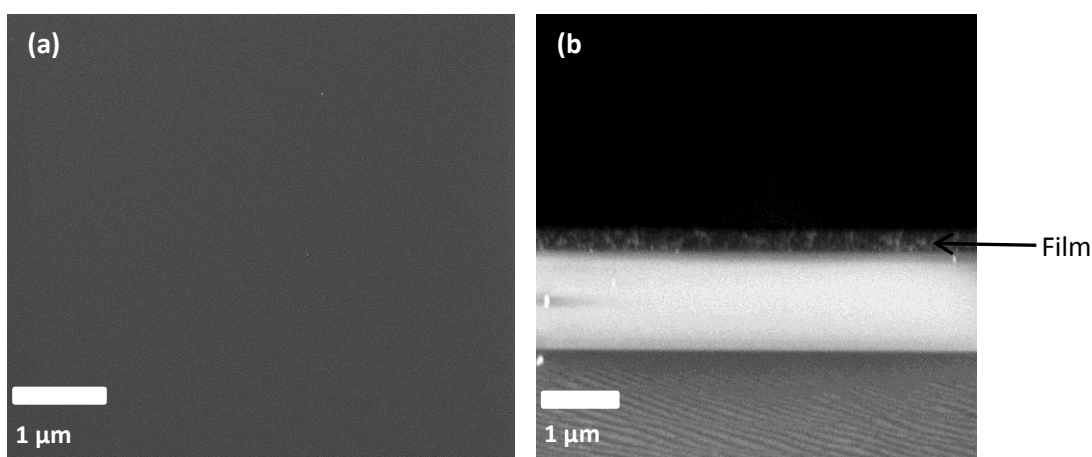


Figure 4.3 – (a) Top and (b) cross-sectional SEM images of a thin film of Ga_2S_3 deposited from $[\text{Ga}(\text{S}^{\text{i}}\text{Pr})_2(\mu\text{-S}^{\text{i}}\text{Pr})_2]$ at 723 K onto SiO_2 . (a) shows the film to have no observable features.

XRD analysis of a thin film deposited at 400 °C shows broad peaks that can be assigned as the cubic $F\text{-}43m$ phase (Figure 4.4).¹⁸ The data are shown after background

subtraction and peak positions match well with literature patterns, although there is a weak reflection at $2\theta = 16.7^\circ$, which is the correct position for a (100) reflection. This reflection is disallowed so this may suggest some defect ordering. The additional peak at $2\theta = 55^\circ$ does not fit the pattern and cannot be identified as any other phase of Ga_2S_3 and cannot be assigned as any other material. Lattice parameters were calculated as $a = 5.1719(1) \text{ \AA}$ and the crystallite size was determined as $3.2(9) \text{ nm}$ by lattice parameter refinement by individual peak fitting using the Rigaku PDXL 2 software.³¹ The crystallite size calculation is not corrected for instrumental broadening effects.

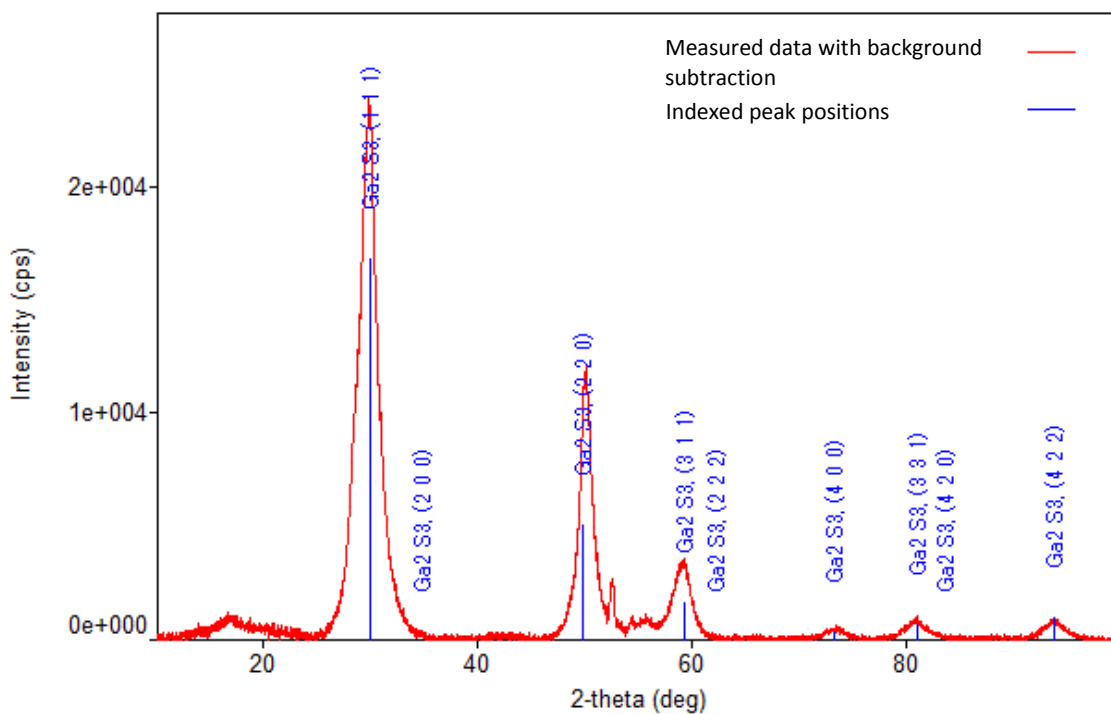


Figure 4.4 – XRD pattern of Ga_2S_3 thin film deposited at 400°C with background subtraction and peak positions corresponding to $F\text{-}43m$ Ga_2S_3

XRD analysis of a thin film annealed under an N_2 atmosphere at 800°C for 300 seconds shows much sharper peaks that match with the previously published monoclinic Cc phase (Figure 4.5).¹⁵ The calculated and observed data match very well. Lattice parameters were calculated by lattice parameter refinement by individual peak fitting using the Rigaku PDXL 2 software as $a = 11.11(1)$, $b = 6.406(6)$, $c = 7.038(5) \text{ \AA}$, $\beta = 121.18(3)^\circ$ and the crystallite size was determined as $12(4) \text{ nm}$.

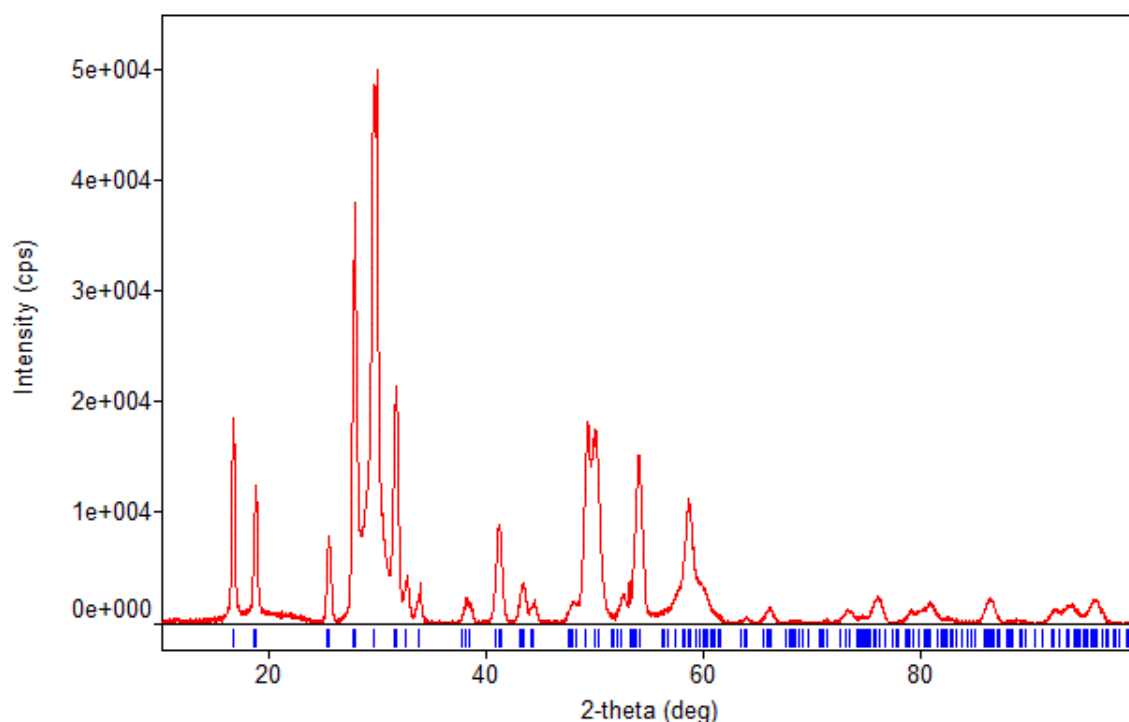


Figure 4.5 – XRD pattern of Ga₂S₃ thin film annealed at 800 °C with background subtraction and peak positions corresponding to *Cc* Ga₂S₃

Figure 4.6 shows the results from an *in situ* annealing XRD. This demonstrates how the as-deposited Ga₂S₃ changes from a cubic phase to monoclinic as the temperature increases. The peak shape is broader than in figures 4.4 and 4.5 as it was not possible to perform this experiment in grazing incident angle mode due to the restraints imposed by the furnace used to anneal the sample *in situ*. At 450 °C the peaks are starting to sharpen but there is no evidence for the monoclinic phase. At 500 °C the intensity of the cubic peak at $2\theta = \sim 29^\circ$ starts to decrease and a peak corresponding to that of the monoclinic phase at $2\theta = \sim 34^\circ$ begins to appear. This becomes more pronounced at 550 °C. By 600 °C the peaks corresponding to the cubic phase are no longer visible but two peaks corresponding to the monoclinic phase are now evident. By continuing to anneal the sample to 650 °C, the peaks become sharper. No further change is observed on heating to 800 °C. These observations are consistent with Hahn and Klingler, who reported that the transition occurs between 550 and 600 °C.¹⁴ Their analysis was based on the behaviour of bulk samples of Ga₂S₃, which may behave differently to thin films.

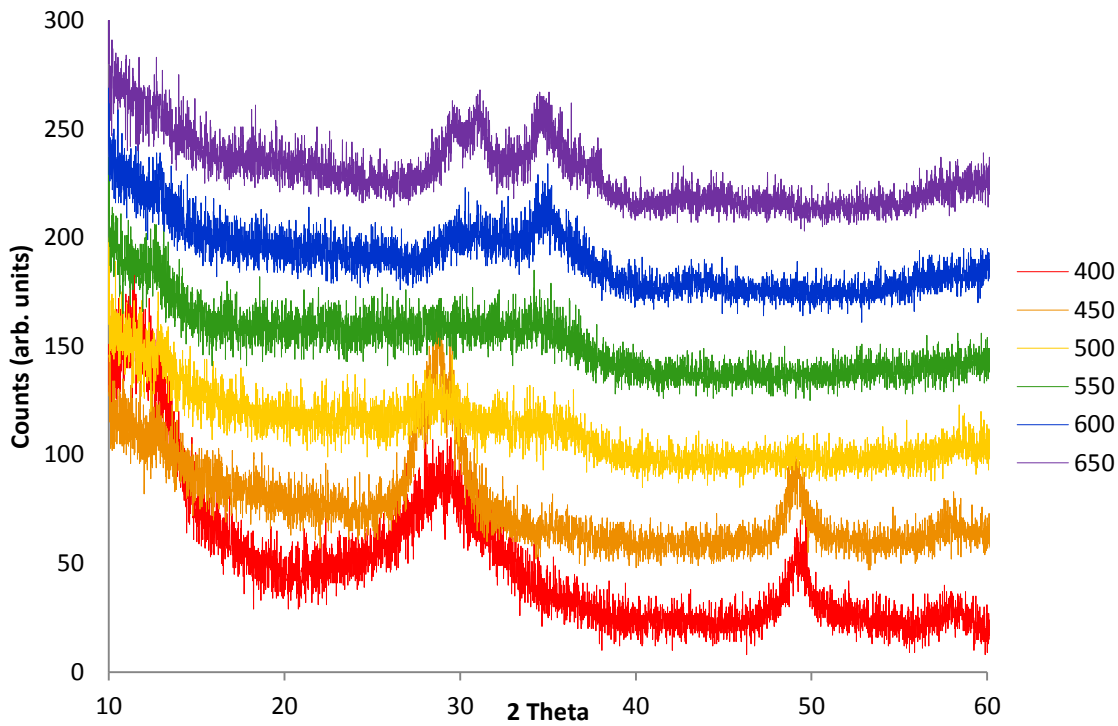


Figure 4.6 – Phase transition of Ga_2S_3 as annealing temperature increases. The legend shows the annealing temperature of the film in $^\circ\text{C}$.

Raman spectroscopy on the films before and after annealing (Figure 4.7) also shows that the as-deposited film is poorly crystalline, as many of the features are ill-defined. After annealing at $800\text{ }^\circ\text{C}$, there is a significant increase in the crystallinity of the film and peaks can be assigned at $235\text{ (}\nu_3\text{ mode)}$ and $385\text{ (}\nu_1\text{ mode)}$ cm^{-1} . These match well with literature data.^{32, 33}

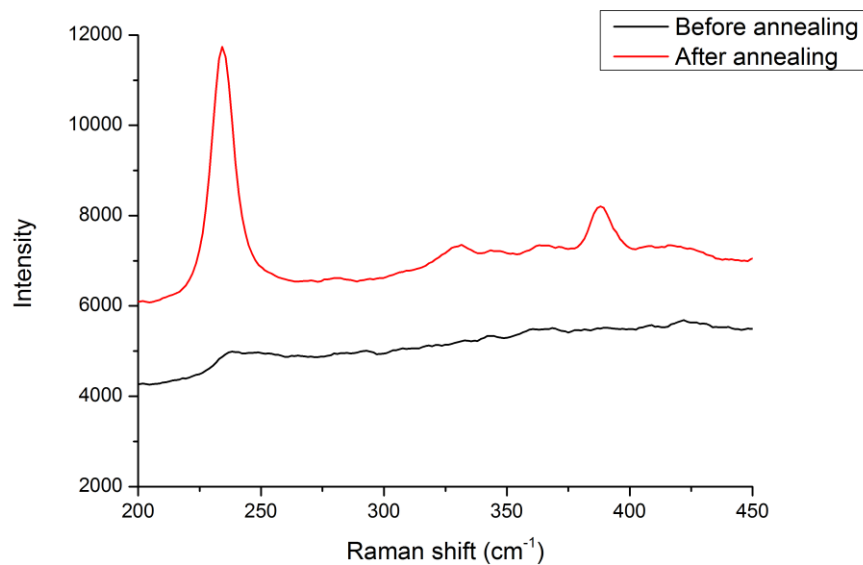


Figure 4.7 – Raman spectra of a Ga₂S₃ thin film before (black) and after (red) annealing

Electrical conductivity measurements were also carried out on the films. The as-deposited films had a resistance that was above the measurable value for the instrument used ($> 10^{10} \Omega$). As the film thickness has been measured as 200 nm, it can be calculated that the thin film will have a resistivity greater than $2 \times 10^5 \Omega \cdot \text{cm}$. For the annealed films, a resistivity of $\sim 1 \times 10^3 \Omega \cdot \text{cm}$ was measured, however there was some difficulty in obtaining consistent results over several measurements due to the cracking of the film that occurred on annealing.

Selective deposition onto photolithographically patterned TiN/SiO₂ substrates using [Ga(SⁱPr)₂(μ -SⁱPr)]₂ was attempted at a range of temperatures (450 – 900 °C) but was unsuccessful. In all cases, a very smooth, uniform film was deposited over all areas of the tile with no indication of preferential deposition (Figure 4.8). EDX analysis confirmed that Ga₂S₃ was present both inside and outside of the holes.

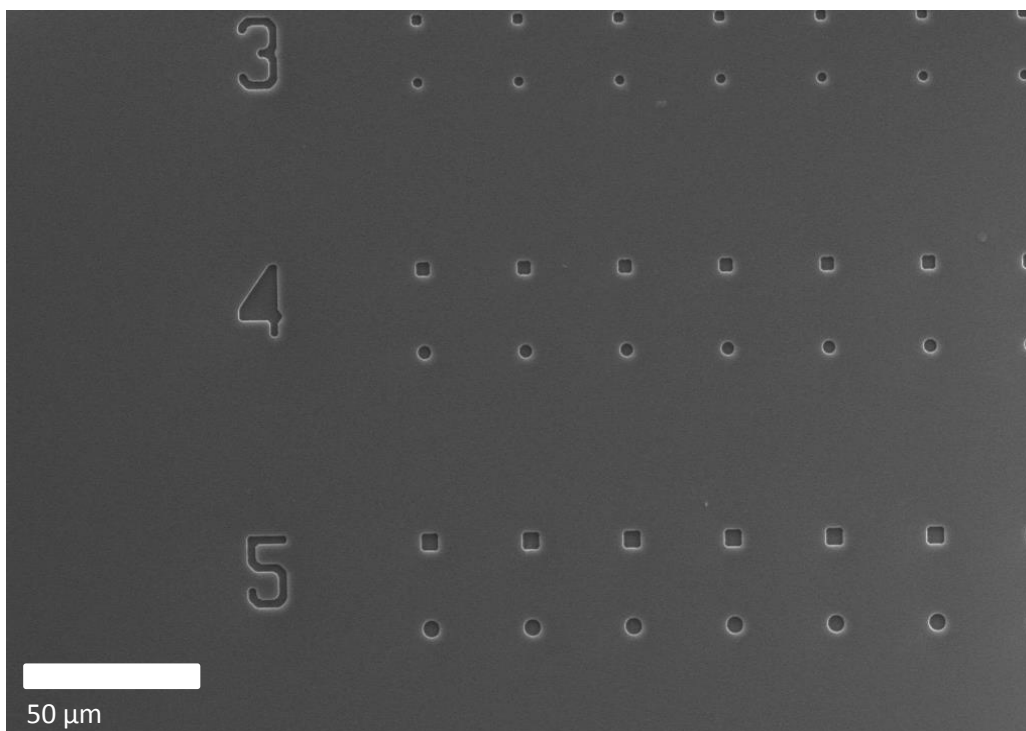


Figure 4.8 – Thin film of Ga_2S_3 deposited onto a photolithographically patterned TiN/ SiO_2 substrate at 723 K showing no evidence of selective deposition onto TiN or SiO_2

4.2.3 $[\text{Ga}(\text{S}^t\text{Bu})_2(\mu\text{-S}^t\text{Bu})]_2$

The synthesis of $[\text{Ga}(\text{S}^t\text{Bu})_2(\mu\text{-S}^t\text{Bu})]_2$ has also been reported by Suh *et al.*¹ This was investigated as an alternative potential precursor for the LPCVD of Ga_2S_3 thin films. Initial deposition attempts at 673 – 873 K and 0.1 mmHg were unsuccessful with no deposition on the substrates and a large quantity of residue left from the precursor. Analysis by EDX spectroscopy showed that this residue is Ga_2S_3 and XRD analysis confirmed that it is $\gamma\text{-Ga}_2\text{S}_3$. Suh *et al.* report that their attempts to sublime $[\text{Ga}(\text{S}^t\text{Bu})_2(\mu\text{-S}^t\text{Bu})]_2$ under vacuum led to deposition. This compound therefore seems to have insufficient volatility to be a suitable single source precursor for LPCVD.

4.2.4 Microfocus XRD experiments

Thin films of Ga_2S_3 were deposited at 723 K onto 0.5 mm thick silica using 40 mg of $[\text{Ga}(\text{S}^i\text{Pr})_2(\mu\text{-S}^i\text{Pr})]_2$. These films were then capped with a 50 nm thick layer of SiO_2 to

prevent oxidation. Small areas of the film (5 – 10 μm diameter) were then laser annealed with laser currents of 90, 100, 110 and 120 mA for 50 ms by Mr Jonathon Maddock. The aim was to investigate whether laser annealing would be a suitable method of initiating a phase change in the material and whether the relative amounts of the cubic and monoclinic phases in the thin films varied by using different laser powers. Microfocus ($2 \times 4 \mu\text{m}$) XRD was then performed at beam line I18, Diamond Light Source in order to establish the effects of the laser annealing. The data were collected in transmission mode through the capping layer, thin film and substrate.

Figure 4.9 shows a typical dataset recorded. As the data are collected by transmitting the beam through the sample and the SiO_2 substrate, the background makes a significant contribution. This made performing a simple background subtraction very difficult. In order to get the best background subtraction for phase refinement, a partial background subtraction was performed using the data collected from a sample that had not been laser annealed and then the background fit was refined using GSAS software.

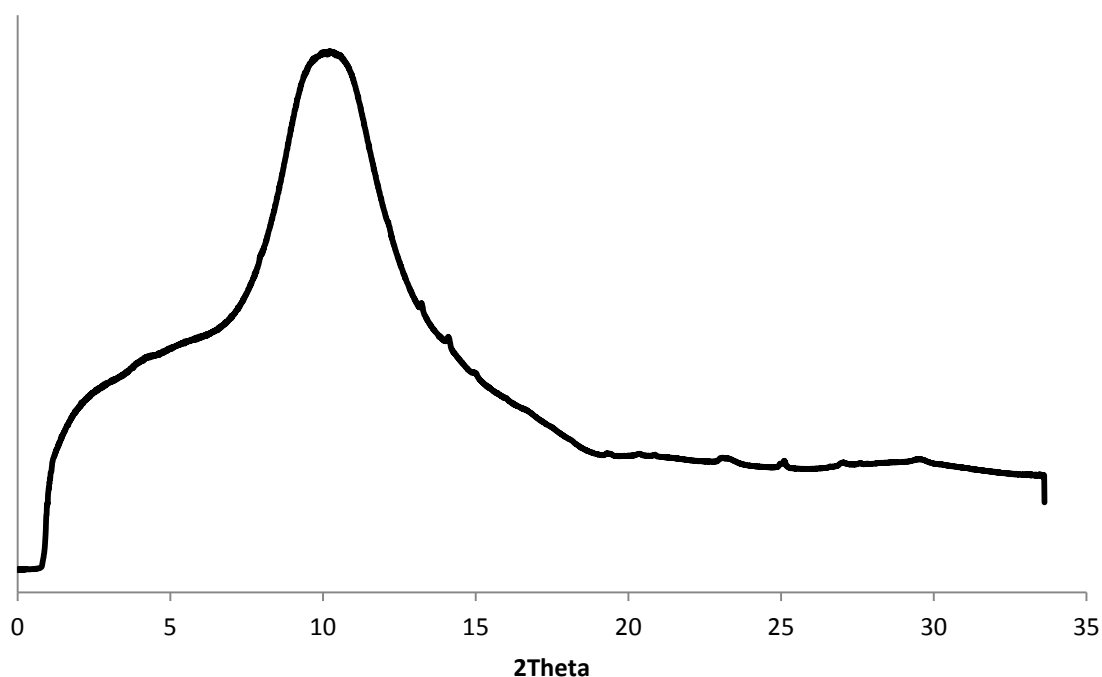


Figure 4.9 – Uncorrected XRD profile of a Ga_2S_3 thin film laser annealed at 110 mA. The broad features below ~ 20 2θ are due to the SiO_2 substrate. Small peaks visible from ~ 13 2θ are due to the Ga_2S_3 thin film.

Figure 4.10 shows a stacked plot of four samples annealed at different laser powers. Due to the very small crystallite size in the cubic phase, the peaks for this phase are very broad and they are often coincident with the monoclinic phase, creating broad features under the sharper monoclinic peaks. As the laser power increases, the amount of the monoclinic phase in the sample increases, which is evident in a sharpening of the peaks corresponding to the monoclinic phase. At 110 mA a third phase starts to grow in, which becomes more apparent in the sample annealed at 120 mA. This third phase is particularly evident between $2\theta = 15$ and 18° and is weakly present at lower laser powers too. This phase is unidentified but does not correspond to SiO_2 or any known phases of gallium sulfide, oxide, nitride, oxysulfide or silicate. Although the samples were capped with a layer of SiO_2 , it is possible that this degrades at high laser powers, exposing the sample and allowing sample degradation. Due to the presence of this extra phase, as well as difficulties encountered in data analysis due to the significant background contribution from the substrate, comparisons between the samples annealed at different laser powers and literature data must be done with care to avoid over-analysis of the data.

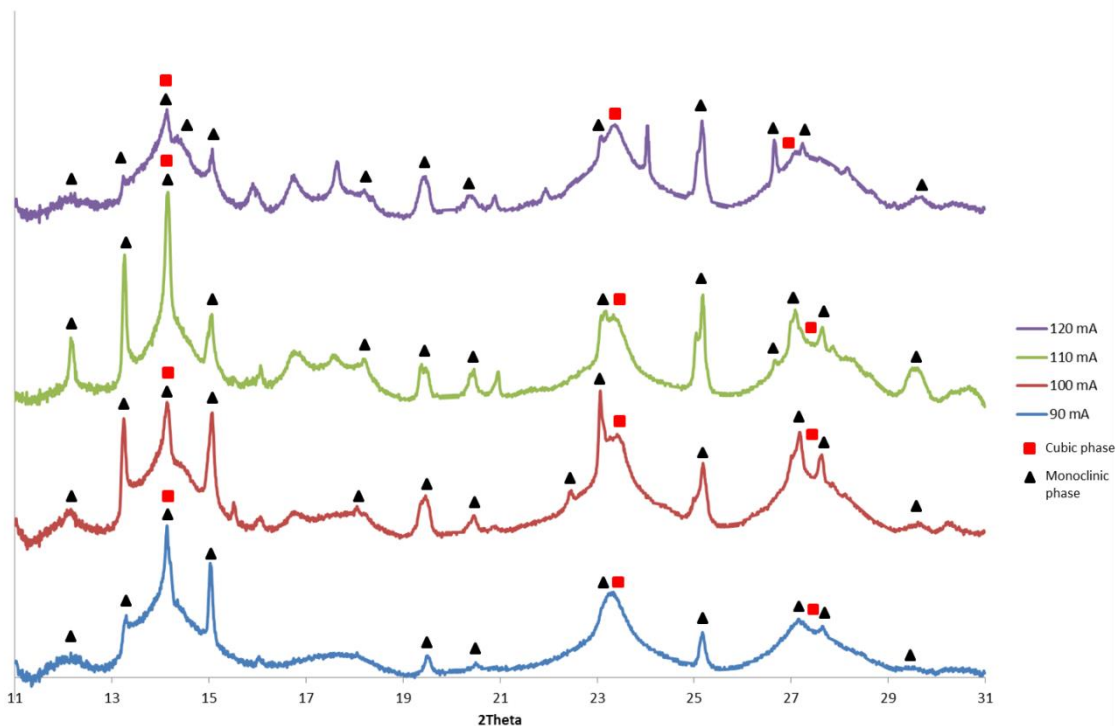


Figure 4.10 – Stacked plot showing how phase composition of the film changes with laser annealing power. A background subtraction has been applied to the data.

Due to the significant presence of a third phase in the sample annealed at 120 mA, it was not possible to perform a reliable phase refinement on the sample. Phase refinements on the samples annealed at 90, 100 and 110 mA were carried out for data over the range $2\theta = 11-31^\circ$. A section of data between $2\theta = \sim 16-19^\circ$ was omitted as this section contained peaks corresponding to the unidentified phase and did not contribute to either phase of Ga_2S_3 , which made fitting and refining the data for Ga_2S_3 more difficult. Removal of this section of data should not impact on the quality of the fit to either phase of Ga_2S_3 as neither has significant peaks in this region.

Phase refinement on the samples that were laser annealed at 90 and 100 mA showed no change in the relative percentages of the cubic (81%) and monoclinic (19%) phases (Figures 4.11 and 4.12).

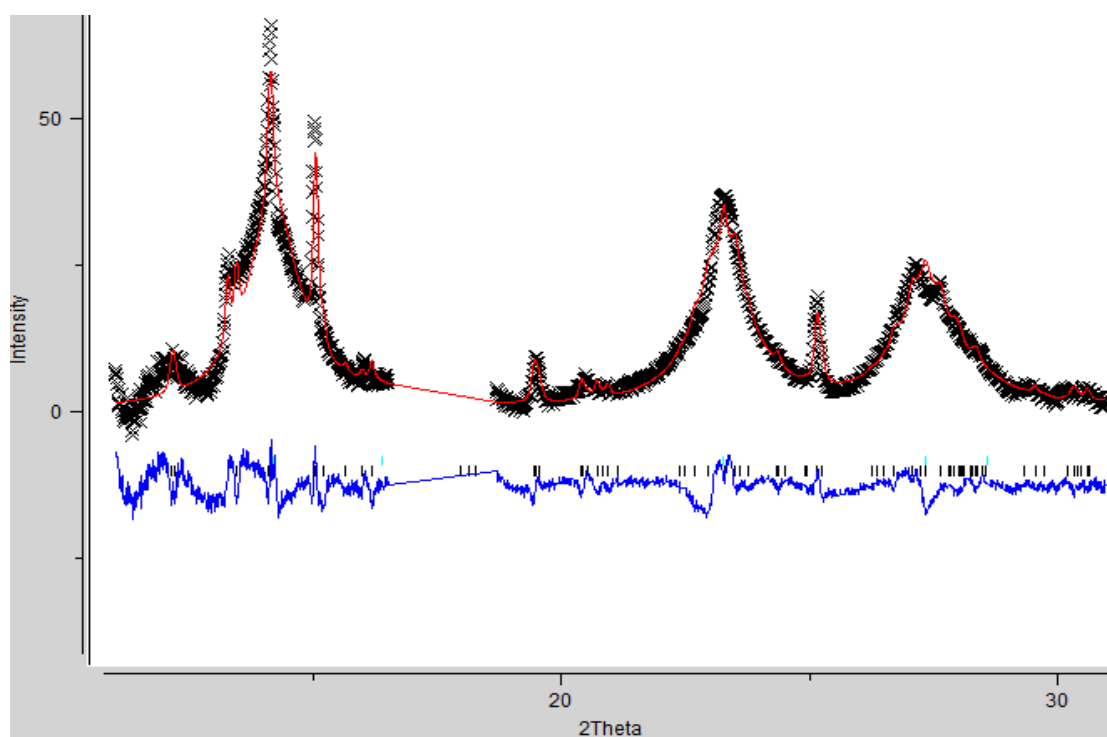


Figure 4.11 – Phase fit for Ga_2S_3 annealed at 90 mA. Collected data are shown in black; calculated fit is in red; difference between calculated and actual data are in blue; tick marks indicate peak positions for $F-43m$ and Cc phases of Ga_2S_3 . Data between $2\theta = \sim 16-19^\circ$ are omitted as peaks in this region belong to an unidentified phase and do not contribute to either phase of Ga_2S_3 . Residuals are below 1%.

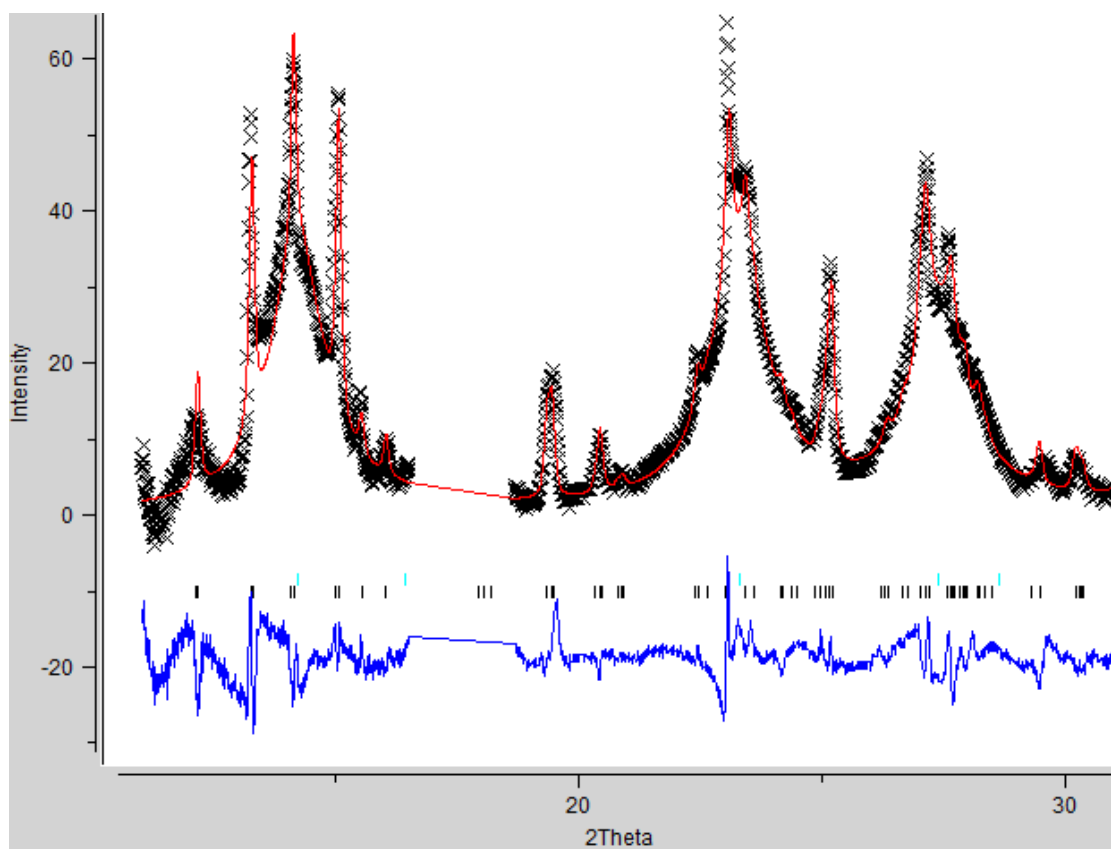


Figure 4.12 – Phase fit for Ga_2S_3 annealed at 100 mA. Collected data are shown in black; calculated fit is in red; difference between calculated and actual data are in blue; tick marks indicate peak positions for $F\text{-}43m$ and Cc phases of Ga_2S_3 . Data between $2\theta = \sim 16\text{-}19^\circ$ are omitted as peaks in this region belong to an unidentified phase and do not contribute to either phase of Ga_2S_3 . Residuals are below 1%.

The sample annealed at 110 mA shows an increased percentage of the monoclinic phase (23%) relative to the cubic phase (77%) than the samples that had been annealed at the lower laser powers (90 and 100 mA, 19% cubic) (Figure 4.13). This increase in the amount of the monoclinic phase present is expected with higher laser power.

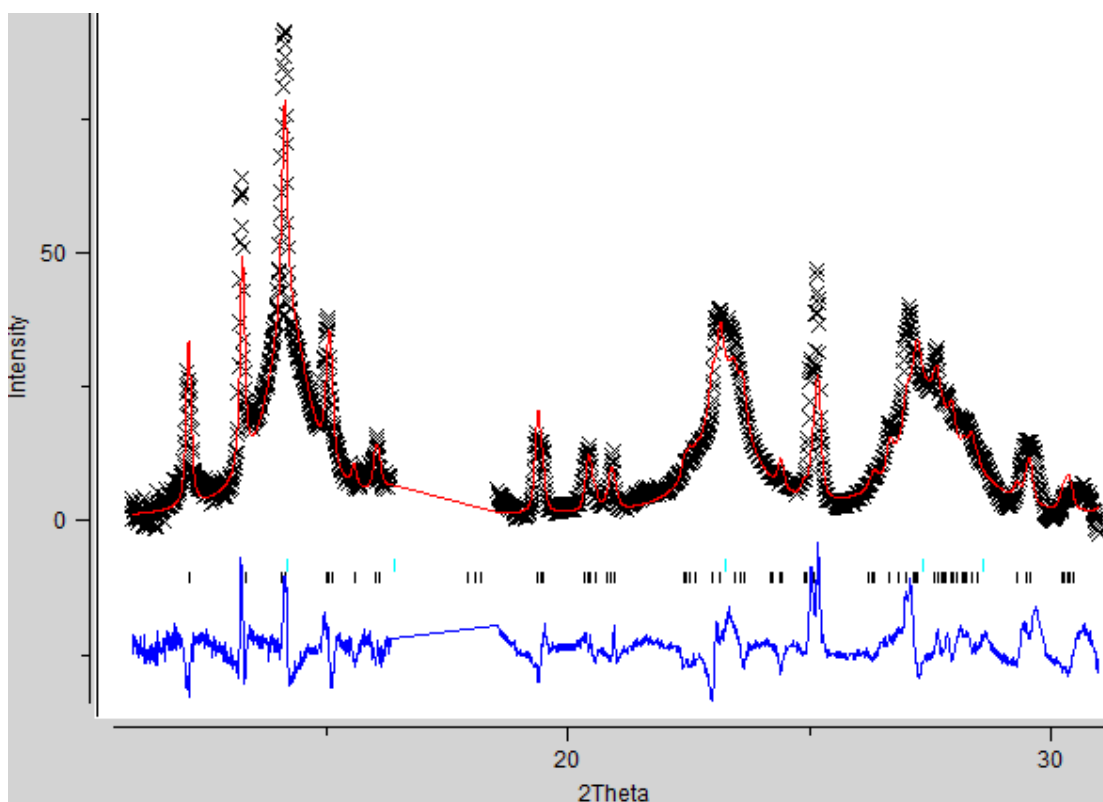


Figure 4.13 – Phase fit for Ga_2S_3 annealed at 110 mA. Collected data are shown in black; calculated fit is in red; difference between calculated and actual data are in blue; tick marks indicate peak positions for *F-43m* and *Cc* phases of Ga_2S_3 . Data between $2\theta = \sim 16\text{-}19^\circ$ are omitted as peaks in this region belong to an unidentified phase and do not contribute to either phase of Ga_2S_3 . Residuals are below 1%.

The phase fractions and calculated lattice parameters for each data set are summarised in Table 4.3. The lattice parameter for the *F-43m* phase is most similar to the literature value for the sample annealed at 100 mA, although the samples annealed at 90 and 110 mA are within the error of the literature value.¹⁴ There is more variance in the refined values for the *Cc* phase. For the samples annealed at 90 and 110 mA, the *a*, *c* and β parameters are larger than the literature values and the *b* parameter is slightly smaller, even when errors are taken into consideration.¹⁵ The sample annealed at 100 mA has the closest match to the literature values for *Cc* Ga_2S_3 . The refined data for each sample, however, is comparable to the literature data. The data indicate that 100 mA may be the optimum laser power for annealing the films. It is possible that increasing the annealing time at 100 mA may increase the percentage of the film converted to the monoclinic

phase, while maintaining optimum film quality. It was not possible to investigate that effect as part of this work but it would be interesting to study if this work, or similar, were pursued further.

Laser Power	90 mA	100 mA	110 mA
Weight % of <i>F-43m</i> phase	81	81	77
<i>F-43m</i> lattice parameter	5.183(2) Å	5.168(1) Å	5.188(2) Å
Weight % of <i>Cc</i> phase	19	19	23
<i>Cc</i> lattice parameters	$a = 11.126(4)$ $b = 6.312(2)$ $c = 7.055(2)$ Å $\beta = 121.75(1)^\circ$	$a = 11.091(3)$ $b = 6.377(1)$ $c = 7.022(2)$ Å $\beta = 121.34(1)^\circ$	$a = 11.136(4)$ $b = 6.371(2)$ $c = 7.053(1)$ Å $\beta = 121.47(1)^\circ$

Table 4.3 – Refined phase fractions and lattice parameters for thin film samples of Ga₂S₃ laser annealed at 90, 100 and 110 mA. Literature values: $a = 5.17(1)$ Å (*F-43m*); $a = 11.107(2)$, $b = 6.395(1)$, $c = 7.021(1)$ Å, $\beta = 121.17(3)^\circ$ (*Cc*).

4.2.5 Conclusions

It is possible to deposit thin films of cubic Ga₂S₃ using [Ga(SⁱPr)₂(μ-SⁱPr)]₂ at 723 K and 0.05 mmHg. By annealing the films at higher temperatures (> 873 K), a phase change from cubic to monoclinic occurs. At intermediate temperatures (773 – 873 K) both phases are present. This agrees with the earliest literature report on the phases of Ga₂S₃, although later reports state that the transition happens at higher temperatures, which may be due to the form of the Ga₂S₃ (i.e. bulk vs. thin film). It is also possible to use laser annealing to effect this phase change, with higher laser powers giving greater quantities of the monoclinic phase. Although [Ga(S^tBu)₂(μ-S^tBu)]₂ decomposes to give Ga₂S₃ when heated under vacuum, it was not found to be a suitable single source precursor for the deposition of thin films of Ga₂S₃ due to its low volatility.

4.3 Experimental

[Ga(SⁱPr)₂(μ-SⁱPr)]₂ was prepared according to the method described by Suh *et al.*¹

[Ga(NⁱPr₂)₃] was prepared *via* a modification of the synthesis for [Ga(NCy₂)₃] described by Pauls and Neumüller.²⁹

Microfocus XRD patterns were collected at beam line I18 of the Diamond Light Source using 16.8 keV (0.738 Å) X-rays focussed to a 2 × 4 μm FWHM spot. An aligned optical microscope was used to locate regions of interest on the sample and diffraction patterns were collected through the 0.5 mm SiO₂ substrate using a 4000 × 2500 pixel CCD detector. Data collected on an unannealed film were used to subtract the substrate contributions to the signal and the background subtraction was refined using GSAS software.

4.4 References

1. Suh, S.; Hardesty, J. H.; Albright, T. A.; Hoffman, D. M., *Inorg. Chem.* **1999**, *38*, 1627-1633.
2. Suh, S.; Hoffman, D. M., *Chem. Mater.* **2000**, *12*, 2794-2797.
3. Ho, C. H.; Lin, S. L., *J. Appl. Phys.* **2006**, *100*, 083508-1-083508-6.
4. Ho, C. H.; Lin, S. L., *J. Appl. Phys.* **2006**, *100*, 083508-083508-6.
5. Madelung, O., *Semiconductors: Data Handbook*. Third ed.; Springer: Berlin, Germany, 2004.
6. Lee, J.-S.; Won, Y.-H.; Kim, H.-N.; Kim, C.-D.; Kim, W.-T., *Solid State Commun.* **1996**, *97*, 1101-1104.
7. Yoon, C.-S.; Medina, F. D.; Martinez, L.; Park, T.-Y.; Jin, M.-S.; Kim, W.-T., *Appl. Phys. Lett.* **2003**, *83*, 1947-1949.
8. Aono, T.; Kase, K., *Solid State Commun.* **1992**, *81*, 303-305.
9. Aono, T.; Kase, K., *Solid State Commun.* **1992**, *83*, 749-752.
10. Li, R.; Seddon, A. B., *J. Non-Cryst. Solids* **1999**, *256-257*, 17-24.
11. Seddon, A. B.; Furniss, D.; Sims, D. J., *Proc. SPIE* **1999**, 160-168.
12. Schweizer, T.; Brady, D.; Hewak, D. W., *Opt. Express* **1997**, *1*, 102-107.
13. Takebe, H.; Kitagawa, R.; Hewak, D. W., *J. Ceram. Soc. Jpn.* **2005**, *113*, 37-43.
14. Hahn, H.; Klingler, W., *Z. Anorg. Chem.* **1949**, *259*, 135-142.
15. Collin, G.; Flahaut, J.; Guittard, M.; Loireau-Lozach, A.-M., *Mater. Res. Bull.* **1976**, *11*, 285-292.
16. Tomas, A.; Pardo, M. P.; Guittard, M.; Guymont, M.; Famery, R., *Mater. Res. Bull.* **1987**, *22*, 1549-1554.
17. Goodyear, J.; Steigmann, G. A., *Acta Crystallogr.* **1963**, *16*, 946-949.
18. Hahn, H.; Frank, G., *Z. Anorg. Allg. Chem.* **1955**, *278*, 333-339.
19. Geiersberger, K.; Galster, H., *Angew. Chem.* **1952**, *64*, 81-82.
20. Goodyear, J.; Duffin, W. J.; Steigmann, G. A., *Acta Crystallogr.* **1961**, *14*, 1168-1170.
21. Chilouet, A.; Mazurier, A.; Guittard, M., *Mater. Res. Bull.* **1979**, *14*, 1119-1124.
22. Pardo, M. P.; Tomas, A.; Guittard, M., *Mater. Res. Bull.* **1987**, *22*, 1677-1684.
23. Jones, C. Y.; Bryan, J. C.; Kirschbaum, K.; Edwards, J. G., *Z. Krist.-New Cryst. Struct.* **2001**, *216*, 327-328.

24. Shang, G.; Hampden-Smith, M. J.; Duesler, E. N., *Chem. Commun.* **1996**, 1733-1734.
25. Lazell, M. R.; O'Brien, P.; Otway, D. J.; Park, J.-H., *Chem. Mater.* **1999**, *11*, 3430-3432.
26. Schulz, S.; Gillan, E. G.; Ross, J. L.; Rogers, L. M.; Rogers, R. D.; Barron, A. R., *Organometallics* **1996**, *15*, 4880-4883.
27. MacInnes, A. N.; Power, M. B.; Barron, A. R., *Chem. Mater.* **1993**, *5*, 1344-1351.
28. Dutta, D. P.; Sharma, G.; Tyagi, A. K.; Kulshreshtha, S. K., *Mater. Sci. Eng., B* **2007**, *138*, 60-64.
29. Pauls, J.; Neumüller, B., *Z. Anorg. Allg. Chem.* **2001**, *627*, 583-588.
30. Fattahi, A.; Kass, S. R., *J. Org. Chem.* **2004**, *69*, 9176-9183.
31. *The Rigaku Journal* **2012**, *28*, 29-30.
32. Kadono, K.; Higuchi, H.; Takahashi, M.; Kawamoto, Y.; Tanaka, H., *J. Non-Cryst. Solids* **1995**, *184*, 309-313.
33. Haizheng, T.; Xiujian, Z.; Chengbin, J., *J. Mol. Struct.* **2004**, *697*, 23-27.

5 Coordination Complexes of Aluminium Halides with Acyclic and Macrocyclic Chalcogenoethers

5.1 Introduction

Previous research has investigated the coordination complexes of the Group 13 halides, GaX_3 and InX_3 ($\text{X} = \text{Cl}, \text{Br}, \text{I}$) with chalcogenoether ligands¹⁻³ but there has been very limited work on the coordination complexes of AlX_3 (see 1.3.1) in particular with chalcogenoethers.⁴ The aims of this chapter are to synthesise and characterise a range of coordination complexes of AlX_3 with chalcogenoether ligands to allow comparisons to be made with the heavier Group 13 halide analogues and to explore the potential of selected compounds as single source CVD precursors to deposit aluminium selenide and aluminium telluride.

Chapter summary: $[\text{AlCl}_3(\text{Me}_2\text{S})_n]$ ($n = 1, 2$) has previously been synthesised but not characterised by ^{27}Al NMR or Raman spectroscopy. All other aluminium halide complexes described in the results and discussion section of this chapter are novel complexes. Complexes of this type have not previously been investigated as single source CVD precursors.

5.1.1 Uses of aluminium compounds

Aluminium halides find extensive use in activating and catalysing organic reactions due to their high Lewis acidity.⁵ Aluminium halide complexes can be used for medical imaging by labelling with ^{18}F .^{6,7} There are also a range of III-V materials incorporating Al. These binary and ternary compounds are semiconductors used in LEDs, photodetectors and field effect transistors.⁵ Aluminium coordination complexes with porphyrin, Schiff base, phenolate and alkoxide ligands have also been used as catalysts for epoxide-carbon dioxide copolymerisations.⁸

There have been very few studies on the uses of aluminium chalcogenide materials. There is a report of the synthesis of aluminium selenide nanocrystals.⁹ The nanocrystals were prepared by reacting triethylaluminium with trioctylphosphine/trioctylphosphine oxide which was added to selenium powder in trioctylphosphine. The nanocrystals were bright UV-blue luminescent, which may make them useful in light collecting and emitting devices, in particular those for collection of higher energy solar photons. The only other recent work investigates the molecular beam epitaxy of AlSe¹⁰ and Al₂Se₃¹¹ from Al₂Se₃ granules onto Si(111) as the lattice mismatch between Al₂Se₃ and Si is only 1.3%, leading to the possibility of easy integration of Al₂Se₃ with silicon technology. Al₂Te₃ thin films produced by sputtering were investigated as a potential phase change memory material.¹² The studies found that, although Al₂Te₃ has good thermal stability, it has poor memory switching ability. The pseudo-binary material Al₂Te₃-Sb₂Te₃, however, has both good thermal stability and good memory switching ability.¹²

5.1.2 Coordination complexes with macrocycles

The coordination chemistry of aluminium halides with acyclic ligands is discussed in 1.3.1. Currently there are no reports of the coordination chemistry of aluminium halides with chalcogenoether macrocyclic ligands. There are several examples of complexes of aluminium halides with functionalised aza-macrocycles as these complexes are very stable, making them of particular interest as potential candidates for medical imaging following ¹⁸F labelling.^{6, 13-15} By using the 1,4,7-triazacyclononane-1,4,7-triacetic acid (NOTA) macrocycle, McBride and co-workers were able to attach the macrocycle to a peptide to allow for *in vivo* studies.⁷ The ¹⁸F labelling is performed *via* halide exchange by reaction of the macrocycle with a solution of AlCl₃ in sodium acetate buffer solution and then adding a solution of the ¹⁸F⁻ source.

There has been some research into complexes of alkyl aluminium halides with macrocycles. Atwood *et al.* carried out the reaction of AlCl₂Et with 12-crown-4 and 18-crown-6 to yield the ionic species [AlCl₂(crown)][AlCl₃Et] (crown = 12-crown-4 or 18-crown-6).¹⁶ The crystallographically characterised product of the reaction with 18-crown-6 was a hydrolysis product with a hydroxyl bridged [ClAl(μ-OH)₂AlCl]²⁺ unit in

the centre of the macrocycle.¹⁷ Self *et al.* also carried out the reaction of AlClEt_2 with diaza-18-crown-6 to produce $[(\text{EtAl})_2(\text{diaza-18-crown-6})][\text{EtAlCl}_3]_2$.¹⁸ The reaction of AlCl_2Et with [14]ane N_4 yielded a species in which the nitrogen donor atoms of the macrocycle have been deprotonated and with two $[\text{AlEt}]^{2+}$ units coordinated endocyclically and two AlCl_2Et molecules coordinated exocyclically (Figure 5.1).¹⁹ R_2AlX will react with crown ethers to give the ionic species $[\text{R}_2\text{Al}(\text{15-crown-5})][\text{R}_2\text{AlX}_2]$ ($\text{R} = \text{Me, Et, Pr; X} = \text{Br, I}$).²⁰ $[\text{Me}_3\text{Al}(\text{[12]aneS}_4)]$ has been crystallographically characterised showing one AlMe_3 coordinated exocyclically to one sulfur donor atom but with a longer range interaction to a sulfur donor on an adjacent [12]ane S_4 unit.²¹ The 1:1 complex forms despite the use of a 4:1 ratio AlMe_3 to [12]ane S_4 . In contrast, reaction of an excess of AlMe_3 with [14]ane S_4 yields the 4:1 complex, $[(\text{AlMe}_3)_4\{\text{[14]aneS}_4\}]$, with each sulfur donor atom coordinated exocyclically to one AlMe_3 .²² There are more structures reported with aluminium alkyls and a range of crown ethers²³⁻²⁸ and [14]ane N_4 ²⁹⁻³² but none with aluminium halides.

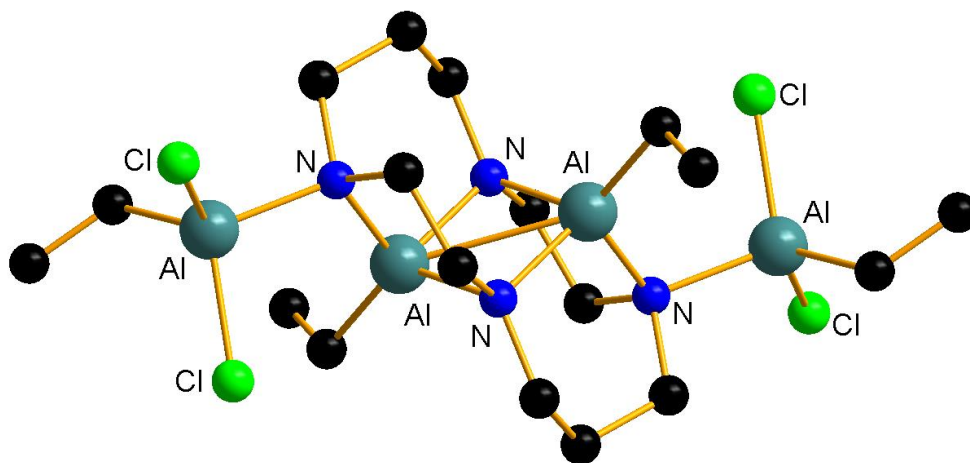


Figure 5.1 – Structure of $[(\mu_3\text{-AlEt})_2(1,4,8,11\text{-tetraazacyclotetradecane-1,4,8,11-tetraide})(\text{AlCl}_2\text{Et})_2]$

5.2 Results and discussion

All reactions were carried out under anhydrous conditions using dry CH_2Cl_2 (AlCl_3) or dry toluene to prevent halide exchange with the solvent (AlBr_3 and AlI_3). Previously halide exchange has only reported at elevated temperatures ($>80\text{ }^\circ\text{C}$)³³ but other, unpublished work within the research group has found that halide exchange can also occur at room temperature. $[\text{AlCl}_3(\text{Me}_2\text{S})]$ and $[\text{AlCl}_3(\text{}^n\text{Bu}_2\text{E})]$ ($\text{E} = \text{Se}, \text{Te}$) were obtained as oils, whereas all other products were obtained as white solids or yellow solids (AlI_3 complexes, $[(\text{AlCl}_3)_2\{\text{C}_6\text{H}_4(\text{CH}_2\text{SEt})_2\}]$ and $[\text{AlCl}_3(\text{Me}_2\text{Te})]$).

All complexes were highly air and moisture sensitive, particularly in solution. Many of the spectra were recorded several times in order to check for consistency and eliminate any problems caused by hydrolysis. Often the ^{27}Al NMR spectra showed the presence of variable amounts of $[\text{AlX}_4]^-$. As the amount varies from sample to sample, it is most likely to be due to moisture sensitivity rather than a rearrangement in solution. There were also difficulties in obtaining satisfactory microanalysis results for some compounds, despite several attempts. The analyst reported difficulties in handling the compounds due to their extreme sensitivity.

Interpretation of some of the IR spectra of the coordination complexes was more difficult than for analogous GaCl_3 complexes. The IR spectra often show that the expected bands (i.e. based on C_{3v} symmetry of $[\text{AlX}_3(\text{L})]$) are split. This is interpreted as arising from a lowering of symmetry caused by intermolecular interactions. The other possible interpretation is that there may be coupling with ligand modes of similar frequency.³⁴ If this were the case, the couplings should be very different between the chloride and iodide complexes. Comparison of the Cl/Br/I systems does not support this hypothesis, hence this is unlikely to be the cause. The splitting is more probably due to solid state effects as well as coupling with lighter atoms. The aluminium halide complexes are also more polar than the analogous gallium halide complexes, increasing the interaction of individual molecules with the bulk, which can cause frequencies to shift and increase coupling. These difficulties were not encountered for gallium and

indium halides, presumably as the larger and heavier metals are less affected by their environment.

Lewis *et al.* reported a discussion and interpretation of the IR spectra of some aluminium and gallium trihalides, including $[\text{AlX}_3(\text{Me}_2\text{S})]$ ($\text{X} = \text{Cl}, \text{Br}$).³⁵ Nakamoto reports the IR and Raman active stretches of $[\text{AlCl}_4]^-$ as 348 (Raman) and 498 cm^{-1} ,³⁶ however, $[\text{nBu}_4\text{N}][\text{AlCl}_4]$ was also synthesised in this work to use as a standard reference compound since no interactions are expected between $[\text{AlCl}_4]^-$ and the cation in this salt. This gave a strong absorption at 488 cm^{-1} and a very weak absorption at 347 cm^{-1} in the IR spectra. ^{27}Al NMR spectroscopy of this compound also confirmed that $[\text{AlCl}_4]^-$ appears as a sharp resonance at 103 ppm in both CH_2Cl_2 and MeCN.

5.2.1 Complexes with monodentate ligands

Reaction of AlCl_3 with the monodentate chalcogenoethers Me_2E ($\text{E} = \text{S}, \text{Se}, \text{Te}$) was carried out in a 1:1 stoichiometry to yield neutral 1:1 adducts with a distorted tetrahedral geometry. This was confirmed by IR spectroscopy, which showed Al-Cl stretches indicative of an $[\text{AlCl}_3(\text{L})]$ environment. The presence of $[\text{AlCl}_3(\text{L})]$ was also confirmed by ^{27}Al NMR spectroscopy ($\delta = 111, 108, 105$ for $\text{E} = \text{S}, \text{Se}, \text{Te}$ respectively). ^1H NMR spectroscopy showed a high frequency coordination shift of 0.4 – 0.5 ppm relative to free ligand for each dimethyl chalcogenide resonance.

For $\text{E} = \text{Se}, \text{Te}$, the distorted tetrahedral geometry was confirmed by single crystal X-ray diffraction (Figure 5.2). Both species crystallise in the same space group ($Pbcm$) and $[\text{AlCl}_3(\text{SeMe}_2)]$ is isostructural with $[\text{GaCl}_3(\text{SeMe}_2)]$.¹ $[\text{AlCl}_3(\text{TeMe}_2)]$ has almost identical a and c lattice parameters to $[\text{AlCl}_3(\text{SeMe}_2)]$ but the b length is $\sim 0.5 \text{ \AA}$ longer ($12.603(7)$ vs. $13.114(3) \text{ \AA}$). The Al-Se bond length is $2.488(2) \text{ \AA}$ compared to $2.687(1) \text{ \AA}$ for Al-Te. The difference in the covalent radii between Se and Te is 0.18 \AA (1.20 vs. 1.38 \AA)³⁷ therefore a difference in bond length of 0.2 \AA is not significant enough to indicate that there is much difference in the Al-E bond strengths in the two complexes. The bond length for Ga-Se in $[\text{GaCl}_3(\text{SeMe}_2)]$ is $2.464(1) \text{ \AA}$, which is very similar to the

Al-Se bond length (0.02 Å shorter).¹ The Ga-Te bond length in [(GaCl₃)₂(^tBuTe(CH₂)₃Te^tBu)], the only crystallographically characterised telluroether complex of a gallium halide (which is also four-coordinate at Ga), is 2.638(1) Å, 0.05 Å shorter than the Al-Te bond length in [AlCl₃(TeMe₂)].³⁸ This may indicate that there is a stronger bond between gallium and the chalcogenoether donor atom than for aluminium. This may be expected due to aluminium(III) being a harder metal centre than gallium(III) and the slightly better size match of gallium will allow for better orbital overlap with tellurium and hence a stronger bond.

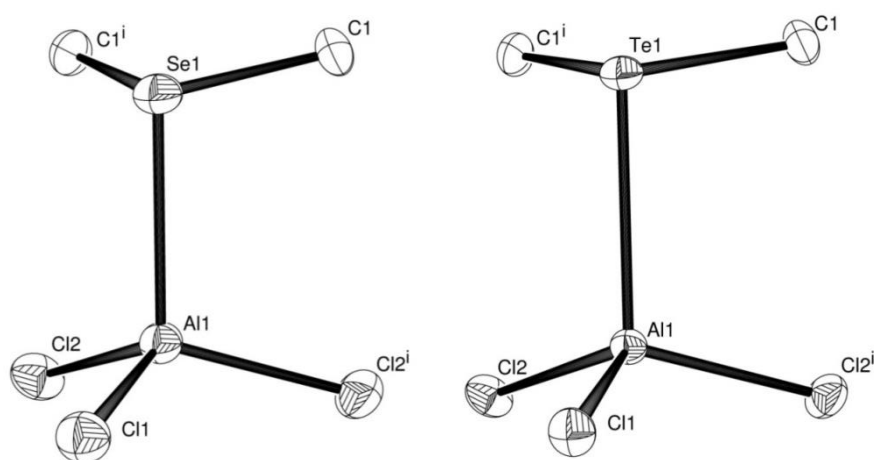


Figure 5.2 - Crystal structures of [AlCl₃(Me₂Se)] and [AlCl₃(Me₂Te)] with atom numbering scheme. Ellipsoids are shown at the 50% probability level and H atoms are omitted for clarity. Both molecules have 2-fold symmetry. Symmetry operation: $i = x, y, 1/2 - z$.

Se1-Al1	2.488(2)	Te1-Al1	2.687(1)
Al1-Cl1	2.118(3)	Al1-Cl1	2.129(1)
Al1-Cl2	2.113(2)	Al1-Cl2	2.121(1)
Cl1-Al1-Cl2	111.37(6)	Cl1-Al1-Cl2	111.16(3)
Cl2-Al1-Cl2	115.29(11)	Cl2-Al1-Cl2	115.18(5)
Cl1-Al1-Se1	105.20(8)	Cl1-Al1-Te1	106.21(4)
Cl2-Al1-Se1	106.42(6)	Cl2-Al1-Te1	106.24(3)
Cl1-Al1-Cl2	111.37(6)	Cl1-Al1-Cl2	111.16(3)

Table 5.1 – Selected bond distances (Å) and angles (°) for [AlCl₃(Me₂Se)] and [AlCl₃(Me₂Te)] (Figure 5.2)

^{27}Al , ^{77}Se and ^{125}Te NMR spectroscopic experiments were carried out in order to identify whether adding additional equivalents of ligand would produce new complexes with higher ligand to metal ratios. $[\text{AlCl}_3(\text{Me}_2\text{S})]$ exhibits a signal at 111 ppm in the ^{27}Al NMR spectrum. Addition of one additional equivalent of Me_2S causes this resonance to shift to 73 ppm. Typically 5-coordinate aluminium species have a ^{27}Al NMR signal at lower frequency than 4-coordinate species³⁹ so this new resonance is assigned to the formation of a 5-coordinate $[\text{AlCl}_3(\text{Me}_2\text{S})_2]$ complex. Addition of further equivalents of Me_2S do not cause any further coordination shift, indicating that a 6-coordinate species does not form, possibly due to steric crowding. Low temperature ($-95\text{ }^\circ\text{C}$) ^1H NMR spectroscopic studies in CH_2Cl_2 support the assignment of the existence of a 5-coordinate species but do not show evidence of a 6-coordinate species. $[\text{AlCl}_3(\text{Me}_2\text{S})]$ has a ^1H NMR shift of 2.53 ppm, which is a sharp singlet. Addition of one extra equivalent of Me_2S causes the signal to shift to 2.43 ppm and broaden slightly ($w_{1/2} = \sim 40\text{ Hz}$). Addition of one further equivalent of Me_2S causes further broadening of the signal and shifts the peak to 2.33 ppm ($w_{1/2} = \sim 200\text{ Hz}$), however cooling the solution to $-95\text{ }^\circ\text{C}$ causes this peak to split into two (2.24, 2.20 ppm). This suggests that the species in solution is the 5-coordinate complex that is exchanging with free ligand (2.13 ppm at $25\text{ }^\circ\text{C}$), rather than a 6-coordinate species. Similar *in situ* ^1H NMR spectroscopic experiments conducted on the Me_2Se and Me_2Te complexes do not show any evidence for the formation of 2:1 or 3:1 adducts. The ^1H NMR spectrum after addition of an extra equivalent of ligand to $[\text{AlCl}_3(\text{Me}_2\text{E})]$ ($\text{E} = \text{Se}, \text{Te}$) shows the 1:1 adduct and free ligand, even with cooling to $-95\text{ }^\circ\text{C}$. This is likely due to the weaker donor strength of these ligands compared to Me_2S as well as the larger size of Se and Te leading to increased steric crowding.

The *n*-butyl derivatives $[\text{AlCl}_3(\text{}^n\text{Bu}_2\text{E})]$ ($\text{E} = \text{Se}, \text{Te}$) were also synthesised as potential single source precursors for LPCVD. Their characterisation data matched well with that of the equivalent methyl substituted complexes. The complexes are yellow oils so it was not possible to obtain a crystal structure but microanalysis data support the formation of 1:1 complexes. IR spectra in the Al-X region matched with those of the dimethyl chalcogenide complexes and ^{77}Se and ^{125}Te NMR similarly showed low frequency coordination shifts.

The telluroether complexes are not stable when stored at room temperature over a period of days to weeks, even if stored in an N₂ filled glove box. The yellow oil will gradually become darker and a large quantity of black solid (elemental Te) forms. A sample of [AlCl₃(ⁿBu₂Te)] that had been stored in the glove box for several weeks and had visibly decomposed was analysed by ESI⁺ mass spectrometry, showing the presence of [ⁿBu₃Te]⁺, which was also present in the ¹²⁵Te NMR spectrum of the same sample [¹²⁵Te{¹H} NMR (CDCl₃): δ = 491; ES⁺ MS (MeCN): *m/z* = 301]. Similar decomposition has previously been observed with [GaCl₃(ⁿBu₂Te)].³⁸

Crystals of [Me₂SH][AlCl₄] (Figure 5.3) were obtained unexpectedly by leaving a solution of [AlCl₃(Me₂S)] in CH₂Cl₂ for one week at -18 °C. This species was subsequently prepared by taking a solution of [AlCl₃(Me₂S)] in anhydrous CH₂Cl₂ and bubbling HCl gas through it. The H--Cl distance of 2.51(3) Å shows that there are significant hydrogen bonding interactions that stabilise this species. The C3-S2-C4 bond angle is 104.6(1)°, which is a significant change from the C-S-C bond angle in Me₂S of 99.1°. ⁴⁰ The IR spectrum exhibits a broad peak at 2482 cm⁻¹, which is attributable to an S-H stretch. This is in agreement with an S-H stretch occurring at 2548(30) cm⁻¹ in [Me₂SH][SbF₆].^{41, 42} The shift to lower wavenumbers is probably caused by hydrogen bonding.

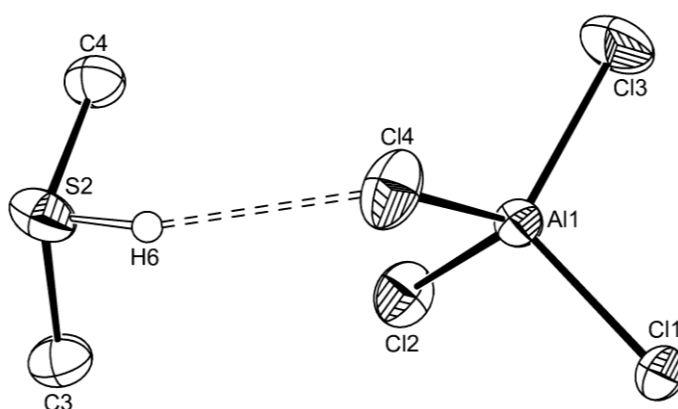


Figure 5.3 – The structure of [Me₂SH][AlCl₄] showing the S2 centred cation and the H-bond (dashed bond) to an adjacent Cl atom. Ellipsoids are drawn at the 50% probability level and H atoms on C are not shown. The other cation is similar.

The crystal structure of $[\text{Me}_2\text{SH}][\text{AlCl}_4]$ is a rare example of a crystallographically characterised protonated sulfonium cation.^{43, 44} $[\text{Me}_2\text{SH}][\text{Cl}(\text{HCl})_n]$ ($n = 3$ or 4) have been obtained from the reaction of Me_2S with liquid HCl at low temperatures.⁴³ [o - $\text{C}_6\text{H}_4(\text{CH}_2\text{SMe})_2$] $\text{H}[\text{NbF}_6]$ and [9]ane S_3] $\text{H}[\text{NbF}_6]$ were obtained from the reaction of o - $\text{C}_6\text{H}_4(\text{CH}_2\text{SMe})_2$ and 9]ane S_3 , respectively, with NbF_5 in a chlorocarbon solvent and refrigeration of the solution for two weeks.⁴⁴ In addition, Olah and co-workers reported the protonation of thiols and thioethers by strong mineral acids⁴⁵⁻⁴⁸ and vibrational spectroscopy has been used to study thioethers that have been protonated by HCl in chlorocarbon solvents or low temperature matrices.⁴⁹⁻⁵¹

AlBr_3 was reacted with Me_2E ($\text{E} = \text{S}, \text{Se}, \text{Te}$) and AlI_3 was reacted with Me_2S in order to establish whether changing the halide on aluminium would affect the coordination chemistry. All products were isolated as white or pale yellow solids from reaction mixtures in toluene. Chlorinated solvents were not suitable for the reactions of AlBr_3 and AlI_3 as they can undergo halide exchange with the solvent. ^1H NMR spectra of the AlBr_3 complexes showed larger coordination shifts than for the corresponding AlCl_3 complexes with the greatest difference apparent for the Me_2Te complex which displayed a resonance at 2.66 ppm, compared to 2.19 ppm for $[\text{AlCl}_3(\text{Me}_2\text{Te})]$ and 1.81 ppm for Me_2Te itself. ^{27}Al NMR and IR spectroscopic studies supported the formation of a distorted tetrahedral complex, analogous to that characterised for AlCl_3 , with no evidence for the presence of $[\text{AlBr}_4]^-$ or $[\text{AlI}_4]^-$. Microanalysis data also supported the formation of a 1:1 complex in each case. These conclusions were also supported by the crystal structure of $[\text{AlBr}_3(\text{Me}_2\text{Te})]$ (Figure 5.4), which has a distorted tetrahedral geometry.

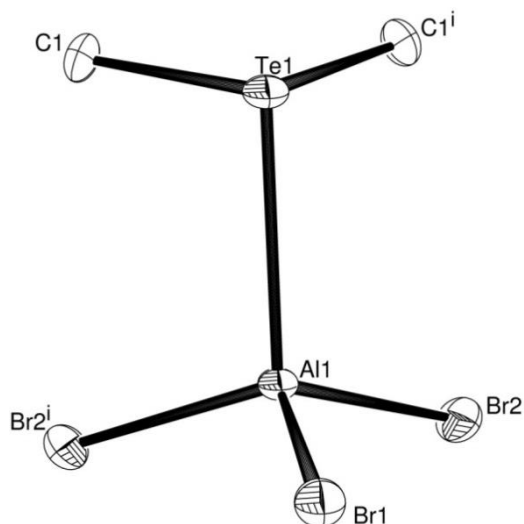


Figure 5.4 – Crystal structure of $[\text{AlBr}_3(\text{Me}_2\text{Te})]$ with atom numbering scheme. Ellipsoids are shown at the 50% probability level and H atoms are omitted for clarity. The molecule has 2-fold symmetry. Symmetry operation: $i = x, y, 3/2 - z$.

Te1-Al1	2.692(4)	Br1-Al1-Br2	111.19(9)
Al1-Br1	2.286(3)	Br2-Al1-Br2	114.01(15)
Al1-Br2	2.287(2)	Br1-Al1-Te1	106.34(12)
		Br2-Al1-Te1	106.80(9)

Table 5.2 – Selected bond distances (Å) and angles ($^\circ$) for $[\text{AlBr}_3(\text{Me}_2\text{Te})]$ (Figure 5.4)

The Al-Te bond distances in $[\text{AlCl}_3(\text{Me}_2\text{Te})]$ and $[\text{AlBr}_3(\text{Me}_2\text{Te})]$ are almost identical and the difference in the Al-Cl and Al-Br bond lengths ($\sim 0.16 \text{ \AA}$) is similar to that expected from the difference in the covalent radii of Cl and Br (0.18 \AA).³⁷ The similarity in bond lengths between the two complexes in the solid state suggests that the bond strengths and hence electron accepting abilities of AlCl_3 and AlBr_3 from Me_2Te are similar. The solution data do not support this conclusion as ^1H NMR coordination shifts were greater for $[\text{AlBr}_3(\text{Me}_2\text{Te})]$ than $[\text{AlCl}_3(\text{Me}_2\text{Te})]$, implying that AlBr_3 is more electron withdrawing than AlCl_3 in the respective complexes. It is possible that packing effects in the solid state have influenced the bond lengths.

Low temperature ^1H NMR and ^{27}Al NMR spectroscopic studies on $[\text{AlBr}_3(\text{Me}_2\text{S})]$ with additional equivalents of Me_2S did not give any evidence for the formation of any new species such as $[\text{AlBr}_3(\text{Me}_2\text{S})_2]$, possibly due to greater steric crowding of the aluminium centre with the larger bromide ligands compared to chloride, as well as the weaker Lewis acidity of AlBr_3 than AlCl_3 .

5.2.2 Complexes with bi- and tri- dentate ligands

Following the successful formation of a series of adducts of AlX_3 with selected monodentate chalcogenoethers, a series of complexes of with bi- and tri-dentate chalcogenoethers were synthesised in order to be able to compare more fully the coordination chemistry of AlX_3 with GaX_3 and InX_3 .

Reaction of the bidentate ligands $\text{CH}_3\text{E}(\text{CH}_2)_2\text{ECH}_3$ ($\text{E} = \text{S}, \text{Se}$) with AlCl_3 in anhydrous CH_2Cl_2 produced crystals, which single crystal X-ray diffraction shows to have the composition $[\text{AlCl}_2(\text{CH}_3\text{E}(\text{CH}_2)_2\text{ECH}_3)_2][\text{AlCl}_4]$ (Figure 5.5). The reaction was initially performed with a 2:1 ratio of AlCl_3 to ligand, as it was anticipated that AlCl_3 might adopt the same structure as the GaCl_3 analogue. The reaction product from this reaction had a 1:1 stoichiometry and subsequent reactions were performed using a 1:1 stoichiometry and identical characterisation data were obtained in both cases.

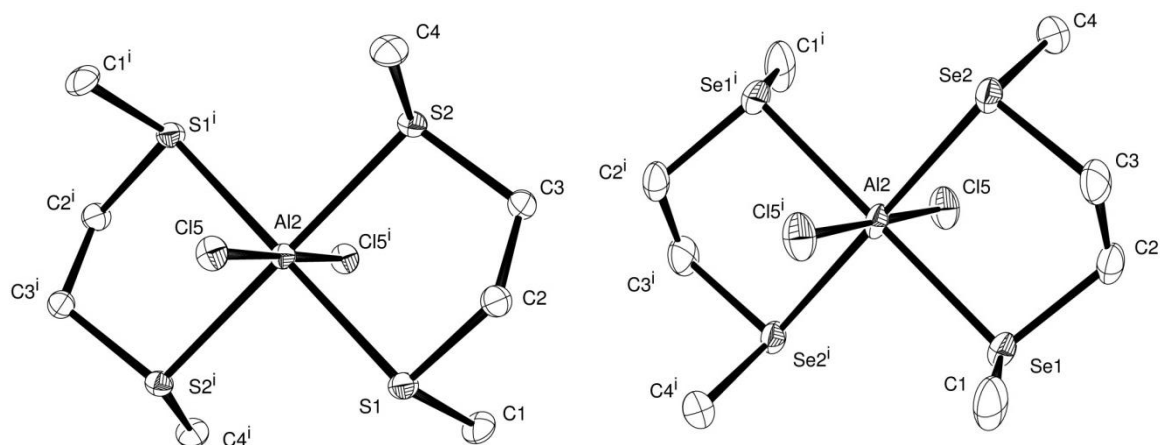


Figure 5.5 – View of the cations in $[\text{AlCl}_2(\text{CH}_3\text{E}(\text{CH}_2)_2\text{ECH}_3)_2][\text{AlCl}_4]$ ($\text{E} = \text{S}$ (left), Se (right)). Ellipsoids are shown at the 50% probability level and H atoms are omitted for clarity. Symmetry operation: $i = 2-x, -y, 1-z$ ($\text{E} = \text{S}$); $i = 1-x, 1-y, 1-z$ ($\text{E} = \text{Se}$).

Al2-Cl5	2.214(1)	Al2-Cl5	2.212(2)
Al2-S1	2.460(1)	Al2-Se1	2.595(2)
Al2-S2	2.481(2)	Al2-Se2	2.623(1)
S1-Al2-S2	87.92(4)	Se1 Al2 Se2	88.11(4)
S1-Al2-S2	92.08(4)	Se1 Al2 Se2	91.89(4)
Cl5-Al- S1	94.49(2)	Cl5-Al2-Se1	94.50(6)
Cl5-Al2-S1	85.51(2)	Cl5-Al2-Se1	85.50(6)
Cl5-Al2-S2	86.50(3)	Cl5-Al2-Se2	86.51(6)
Cl5-Al2-S2	93.50(3)	Cl5-Al2-Se2	93.49(6)

Table 5.3 – Selected bond distances (\AA) and angles ($^\circ$) for $[\text{AlCl}_2(\text{CH}_3\text{S}(\text{CH}_2)_2\text{SCH}_3)_2]^+$ and $[\text{AlCl}_2(\text{CH}_3\text{Se}(\text{CH}_2)_2\text{SeCH}_3)_2]^+$ (Figure 5.5)

The two crystal structures adopt different space groups, with $[\text{AlCl}_2(\text{CH}_3\text{S}(\text{CH}_2)_2\text{SCH}_3)_2][\text{AlCl}_4]$ having a triclinic unit cell, whereas $[\text{AlCl}_2(\text{CH}_3\text{Se}(\text{CH}_2)_2\text{SeCH}_3)_2][\text{AlCl}_4]$ has a higher symmetry monoclinic unit cell, as the two complexes pack differently (Figure 5.6). The difference in packing is probably dictated by the presence of short contacts in the selenoether complex that are not present in the thioether complex. There are short contacts $\text{Se2}\cdots\text{Se2}'$ (3.436 \AA) and $\text{Se3}\cdots\text{Se3}''$ (3.542 \AA). These link Al2 centred cations into chains through Se2 (along the a direction)

and similarly the Al₃ centred cations are linked into chains through Se₃ (again along the *a* direction). Both crystal structures have a plane of symmetry through the centre of the [AlCl₂]⁺ unit. The bond angles show that the geometry at the aluminium centre is not perfectly octahedral, with angles varying between 85.5 and 94.5 °. Al-S bond lengths (2.460(1) and 2.481(2) Å) are shorter than the Al-Se bond lengths (2.595(2) and 2.623(1) Å), which is to be expected from the smaller van der Waals radius of S (1.05 Å) than Se (1.20 Å).³⁷

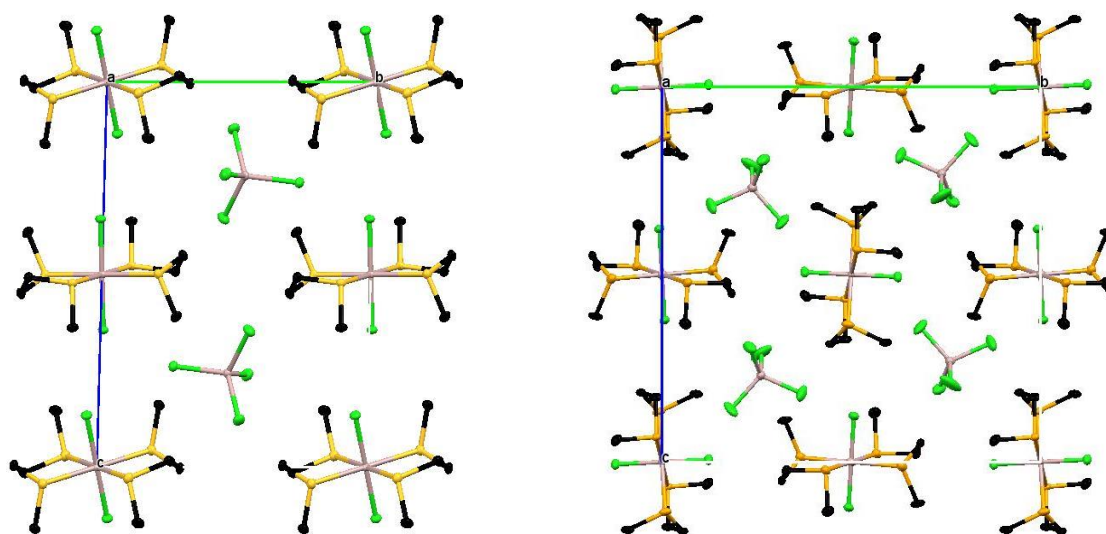


Figure 5.6 – View along the *a* axis of the packing diagrams of [AlCl₂(CH₃S(CH₂)₂SCH₃)₂][AlCl₄] (left) and [AlCl₂(CH₃Se(CH₂)₂SeCH₃)₂][AlCl₄] (right)

This contrasts with the neutral 2:1 adduct [(GaCl₃)₂(CH₃E(CH₂)₂ECH₃)], which has been previously characterised,¹ and the chloro-bridged dimer that has been characterised with InCl₃.² The structures of [AlCl₂(CH₃E(CH₂)₂ECH₃)₂][AlCl₄] are analogous to the products of the reaction between InX₃ and RE(CH₂)₂ER (X = Cl, E = S, R = ⁱPr; X = Br, E = S, Se; R = Me, ⁱPr).²

IR spectroscopic data are in agreement with the crystal structure, showing strong peaks at 488 cm⁻¹, corresponding to [AlCl₄]⁻. The solution data on these complexes are more

complicated. ^1H NMR spectra show two strong singlets that are shifted from free ligand and assigned as the CH_3 and CH_2 resonances for the ligand. There are also several broad signals that split into multiplets on cooling of the sample to $-90\text{ }^\circ\text{C}$. These signals may be attributed to the conformationally locked methyl groups, which can have five different possible stereoisomers that would lead to eight different methyl resonances, although in practice not all of these may be present and many of the resonances would overlap. It is also possible that in solution the complex does not retain an octahedral geometry but instead the chalcogen donor coordinates to one AlCl_3 . This is supported by the ^{27}Al NMR spectroscopy. $[\text{AlCl}_2(\text{CH}_3\text{S}(\text{CH}_2)_2\text{SCH}_3)_2][\text{AlCl}_4]$ showed two resonances, which are assigned as tetrahedrally coordinated $[\text{AlCl}_3(\text{L})]$ ($\delta = 105\text{ ppm}$) and pseudo octahedral $[\text{AlCl}_2(\text{CH}_3\text{S}(\text{CH}_2)_2\text{SCH}_3)_2]^+$ ($\delta = 37\text{ ppm}$). ^{27}Al NMR spectroscopy of $[\text{AlCl}_2(\text{CH}_3\text{Se}(\text{CH}_2)_2\text{SeCH}_3)_2][\text{AlCl}_4]$ showed tetrahedrally coordinated $[\text{AlCl}_3(\text{L})]$ ($\delta = 107\text{ ppm}$). It was not possible to isolate a tetrahedrally coordinated species as $[\text{AlCl}_2(\text{CH}_3\text{E}(\text{CH}_2)_2\text{ECH}_3)_2][\text{AlCl}_4]$ were the reaction products whether the reaction was done in a 1:1 or 2:1 metal to ligand ratio.

The 1:1 reaction of AlBr_3 and AlI_3 with $\text{CH}_3\text{S}(\text{CH}_2)_2\text{SCH}_3$ was also performed in order to establish whether the same behaviour was observed for these complexes. In each case the IR spectroscopic data showed peaks corresponding to $[\text{AlX}_4]^-$ ($\text{X} = \text{Br}, \text{I}$) and ^{27}Al NMR spectroscopy showed only $[\text{AlX}_4]^-$. It is therefore likely that these complexes adopt the same structure as seen for the reaction of AlCl_3 with $\text{CH}_3\text{S}(\text{CH}_2)_2\text{SCH}_3$. ^1H NMR spectroscopy of $[\text{AlI}_2(\text{CH}_3\text{S}(\text{CH}_2)_2\text{SCH}_3)_2][\text{AlI}_4]$ shows two sharp signals at 3.12 (CH_2) and 2.27 (CH_3) ppm as well as two broad signals (2.77, 2.17 ppm) with ~ 6 times the integral corresponding to free ligand, suggesting that the complex is exchanging significantly in solution.

A crystal structure of $[\text{AlI}_2(\text{CH}_3\text{S}(\text{CH}_2)_2\text{SCH}_3)_2][\text{AlI}_4]$ was obtained (Figure 5.7), which confirmed that the cation adopts an octahedral geometry at aluminium, the first crystallographically characterised octahedral aluminium iodide species. The crystal structure also confirms the presence of $[\text{AlI}_4]^-$. In contrast to the $[\text{AlCl}_2(\text{CH}_3\text{S}(\text{CH}_2)_2\text{SCH}_3)_2][\text{AlCl}_4]$ structure where the chloride ligands are in a *trans* geometry, the iodide ligands adopt a *cis* geometry. There are no short range interactions

that may influence the geometry so it is likely that the difference arises from a more complex combination of factors, such as solvent effects or kinetics.

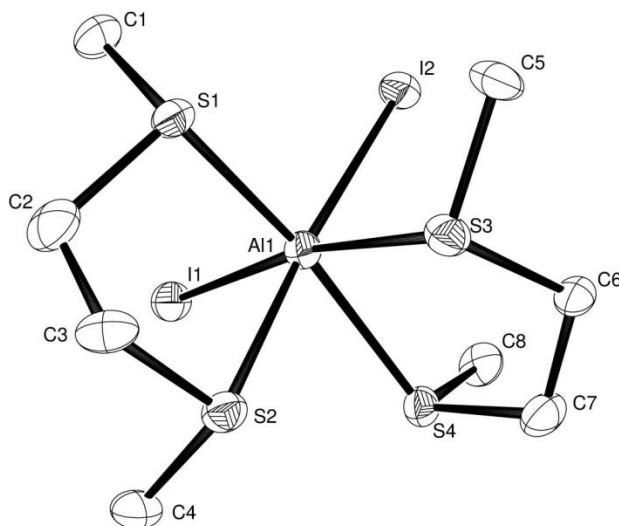


Figure 5.7 – Crystal structure of the cation in $[\text{AlI}_2(\text{CH}_3\text{S}(\text{CH}_2)_2\text{SCH}_3)_2][\text{AlI}_4]$.

Ellipsoids are shown at the 50% probability level and H atoms are omitted for clarity.

Al1-S1	2.431(4)	S2-Al1-S3	76.13(15)
Al1-S2	2.546(5)	S2-Al1-S4	79.23(14)
Al1-S3	2.533(5)	S1-Al1-I1	99.18(14)
Al1-S4	2.448(4)	S1-Al1-I2	94.43(14)
Al1-I1	2.611(4)	S2-Al1-I1	93.68(14)
Al1-I2	2.634(4)	S2-Al1-I2	168.98(18)
I1-Al1-I2	97.33(13)	S3-Al1-I1	168.64(17)
S1-Al1-S2	83.46(16)	S3-Al1-I2	92.92(14)
S3-Al1-S4	83.25(14)	S4-Al1-I1	89.98(14)
S1-Al1-S3	84.83(16)	S4-Al1-I2	101.02(15)
S1-Al1-S4	160.9(2)		

Table 5.4 – Selected bond distances (Å) and angles (°) for $[\text{AlI}_2(\text{CH}_3\text{S}(\text{CH}_2)_2\text{SCH}_3)_2]^+$ (Figure 5.7)

The Al-S bond lengths in the iodide complex (2.43 – 2.55 Å) are a similar length to those found in the chloride complex (2.46, 2.48 Å). There is a significant *trans* influence that is present in the iodide complex due to the different geometry which puts two sulfur donor atoms *trans* to the iodide ligands and two sulfur donor atoms *cis* to the iodide ligands. The two sulfur donor atoms that are *cis* to iodide have Al-S bond lengths that are approximately 0.1 Å longer than the *trans* Al-S bond lengths.

The reaction of two equivalents of AlCl₃ with the ditelluroether ^tBuTe(CH₂)₃Te^tBu in CH₂Cl₂ produced a mixture of species. ¹H NMR spectroscopy showed multiple signals for the *t*-butyl groups and the CH₂ bridge. Multiple signals were also observed in the ¹²⁵Te NMR spectrum, which also showed free ligand. ²⁷Al NMR spectroscopy indicated the presence of [AlCl₄]⁻. Very air sensitive, yellow crystals were isolated of one of the decomposition products (Figure 5.8), which consists of a ligand has lost a *t*-butyl group to become positively charged, forming a Te-Te bond to a tellurium donor of an adjacent ligand, as well as forming a bond to the other tellurium atom in the same [^tBuTe(CH₂)₃Te]⁺ cation, creating a 5 membered ring. There is an [AlCl₄]⁻ unit for charge balance. However, this is not likely to be the only product present in the reaction mixture. It is likely that the high Lewis acidity of AlCl₃ combined with weak Te-C bonds promotes bond cleavage, particularly if the Al-Te interactions are weak.

There are few examples of crystallographically characterised 5 membered rings with Te-Te bonds, most examples using 1,8 functionalised naphthalene rings in order to prearrange the tellurium atoms for bonding. Functionalised tetracenes have also been used with similar results. In these examples the Te-Te bond distance is much shorter (~2.65 – 2.75 Å).⁵²⁻⁵⁵ A ditelluroolane derivative, 2-oxa-6,7-ditelluraspiro[3.4]octane, has a Te-Te bond distance of 2.74 Å.⁵⁶ In comparison, the Te-Te bond length in Me₂Te₂ has been reported as 2.71(2) Å⁵⁷ and [Me₂TeTeMe]⁺ has a bond length of 2.73(1) Å.⁵⁸

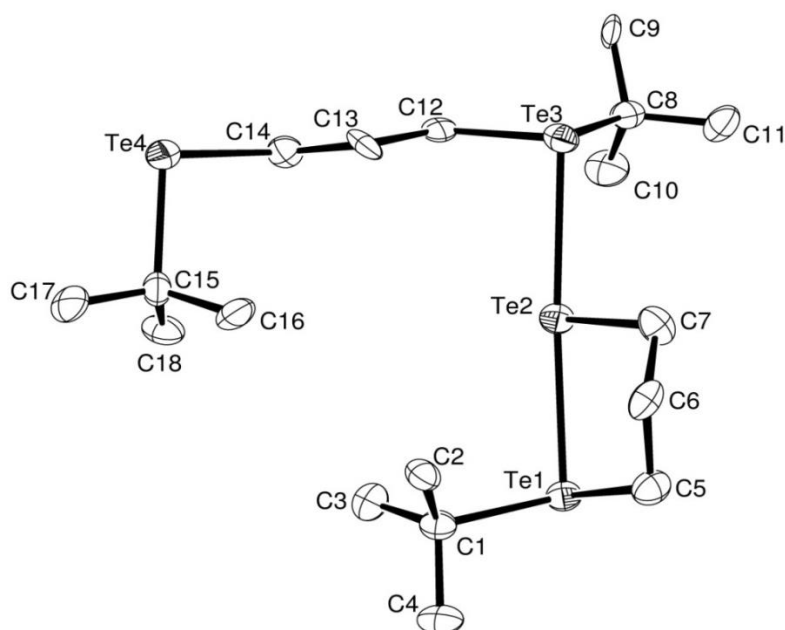


Figure 5.8 – Crystal structure of the cation in $[\text{tBuTe}(\text{CH}_2)_3\text{Te}(\text{tBu})\text{Te}(\text{CH}_2)_3\text{Te}^{\text{tBu}}][\text{AlCl}_4]$. Ellipsoids are shown at the 40% probability level and H atoms are omitted for clarity.

Te1-Te2	2.937(2)	Te4-C15	2.223(17)
Te2-Te3	2.990(2)	C1-Te1-C5	100.1(7)
Te1-C1	2.200(19)	C1-Te1-Te2	100.5(4)
Te1-C5	2.154(18)	Te1-Te2-Te3	170.33(6)
Te2-C7	2.153(17)	C7-Te2-Te3	88.4(5)
Te3-C8	2.193(19)	Te2-Te3-C8	100.3(5)
Te3-C12	2.130(18)	C8-Te3-C12	94.6(7)
Te4-C14	2.177(18)	C14-Te4-C15	99.0(7)

Table 5.5 – Selected bond distances (Å) and angles (°) for $[\text{tBuTe}(\text{CH}_2)_3\text{Te}(\text{tBu})\text{Te}(\text{CH}_2)_3\text{Te}^{\text{tBu}}]^+$ (Figure 5.8)

Reaction of AlCl_3 with the bidentate ligand $o\text{-C}_6\text{H}_4(\text{CH}_2\text{SEt})_2$ results in the formation of the ligand bridged adduct $[(\text{AlCl}_3)_2(o\text{-C}_6\text{H}_4(\text{CH}_2\text{SEt})_2)]$, which exhibits distorted tetrahedral coordination of one AlCl_3 unit at each S donor (Figure 5.9). This structural motif was also observed in the complex of this ligand with GaCl_3 .³ In that structure the

Ga-S bond length was 2.351(2) Å, slightly shorter than the Al-S bond length of 2.367(4) Å. This is the shortest Al-S bond length observed in the set of crystallographically characterised complexes reported here. The wider bite angle of the sulfur donor atoms in this ligand compared to MeS(CH₂)₂SMe may mean that it is better set up for coordinating to one AlCl₃ on each sulfur donor rather than chelating in the same manner MeS(CH₂)₂SMe. For a small metal, such as Al, it would be unlikely that a seven membered chelate ring would form.

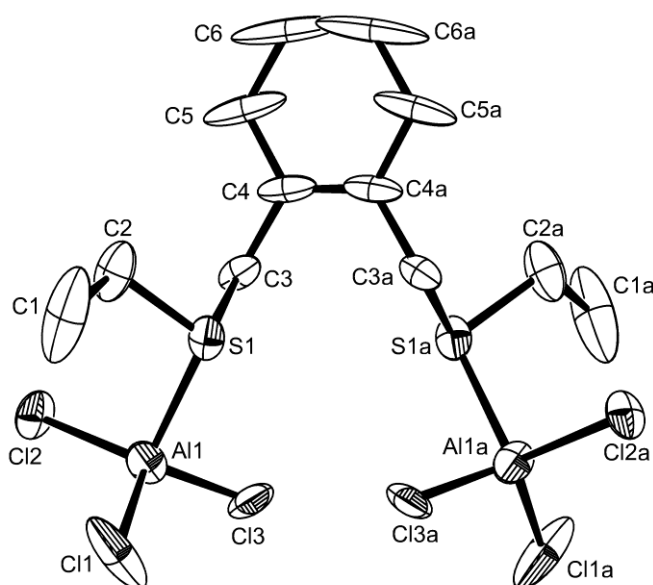


Figure 5.9 – The structure of [*o*-C₆H₄(CH₂SEt)₂](AlCl₃)₂] showing the atom labelling scheme. The displacement ellipsoids are drawn at the 40% probability level and H atoms are omitted for clarity. The molecule has 2-fold symmetry. Symmetry operation: $a = -x, y, 1/2 - z$.

Al1-Cl1	2.100(4)	Cl1-Al1-Cl3	114.8(2)
Al1-Cl2	2.122(3)	Cl2-Al1-Cl3	112.95(17)
Al1-Cl3	2.123(5)	Cl1-Al1-S1	105.8(2)
Al1-S1	2.367(4)	Cl2-Al1-S1	105.40(16)
Cl1-Al1-Cl2	114.00(17)	Cl3-Al1-S1	102.32(14)

Table 5.6 – Selected bond lengths (Å) and angles (°) for [(AlCl₃)₂(*o*-C₆H₄(CH₂SEt)₂)] (Figure 5.9)

There were initial difficulties in solving the single crystal data as the data displayed characteristics indicative of a modulated structure. Initial indexing suggested a cell with lattice parameters $a = 18.75(2)$, $b = 32.43(2)$, $c = 13.61(1)$ Å, which is similar to the unit cell of $[(\text{GaCl}_3)_2(o\text{-C}_6\text{H}_4(\text{CH}_2\text{SEt})_2)]$ but with a tripling of the b length.³ A structure solution was attempted with the smaller cell. The data were transformed removing all reflections with k not equal to $3n$ ($n = \text{integer}$) and the b cell dimension adjusted to a smaller value. The smaller cell had $b = (32.43(2))/3 = 10.81(1)$ Å. 33429 reflections were measured initially and after removing hkl layers with k not equal to $3n$ there remained 9449 reflections. Absences of the smaller cell corresponded to $C2/c$ or Cc and a solution readily appeared using Shelxs in $C2/c$. A modulated structure was also observed for $[(\text{GaCl}_3)_2(o\text{-C}_6\text{H}_4(\text{CH}_2\text{SEt})_2)]$, although in that example the ratio of large b to small b was close to 5, indicating a different modulation.³

In contrast, use of the selenoether ligand $o\text{-C}_6\text{H}_4(\text{CH}_2\text{SeMe})_2$ forms the selenonium tetrachloroaluminate species $[o\text{-C}_6\text{H}_4\text{CH}_2\text{Se}(\text{Me})\text{CH}_2][\text{AlCl}_4]$ (Figure 2.12). This cation had previously been seen when $[(\text{GaCl}_3)_2(o\text{-C}_6\text{H}_4(\text{CH}_2\text{SeMe})_2)]$ had been left to stand in CH_2Cl_2 .¹ Group 4 metal chlorides have also been reported to induce fragmentation of the $o\text{-C}_6\text{H}_4(\text{CH}_2\text{SeMe})_2$ ligand but with formation of a different selenonium salt with the formula $[\text{C}_{17}\text{H}_{19}\text{Se}]_2[\text{TiCl}_6]$ (Figure 5.10).⁵⁹ $[o\text{-C}_6\text{H}_4\text{CH}_2\text{Se}(\text{Me})\text{CH}_2][\text{AlCl}_4]$ adopts the same unit cell as the tetrachlorogallate salt,¹ which is unsurprising as there is little difference in size between the $[\text{AlCl}_4]^-$ anion and the $[\text{GaCl}_4]^-$ anion so crystal packing is unlikely to differ. As AlCl_3 is a stronger Lewis acid than GaCl_3 , it is more likely to promote the formation of the selenonium salt, whose formation is favoured due to the stability of the 5-membered ring that is formed.

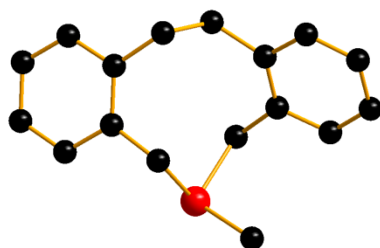


Figure 5.10 – Structure of one of the cations in $[\text{C}_{17}\text{H}_{19}\text{Se}]_2[\text{TiCl}_6]$

The presence of $[\text{AlCl}_4]^-$ is confirmed by both ^{27}Al NMR spectroscopy ($\delta = 103$ ppm) and IR spectroscopy (491 cm^{-1}). ^{77}Se NMR spectroscopy shows a signal at 383 ppm, a significant high frequency shift from $o\text{-C}_6\text{H}_4(\text{CH}_2\text{SeMe})_2$ at 149 ppm.⁶⁰ This is consistent with the previously reported ^{77}Se NMR spectroscopy of $[o\text{-C}_6\text{H}_4\text{CH}_2\text{Se}(\text{Me})\text{CH}_2][\text{InCl}_4]$ that had a shift of 384 ppm.² ESI mass spectrometry also confirmed the formation of $[\text{AlCl}_4]^-$ ($M^- = 169$) and $[o\text{-C}_6\text{H}_4\text{CH}_2\text{Se}(\text{Me})\text{CH}_2]^+$ ($M^+ = 199$), which has a distinctive isotope pattern (Figure 5.11).

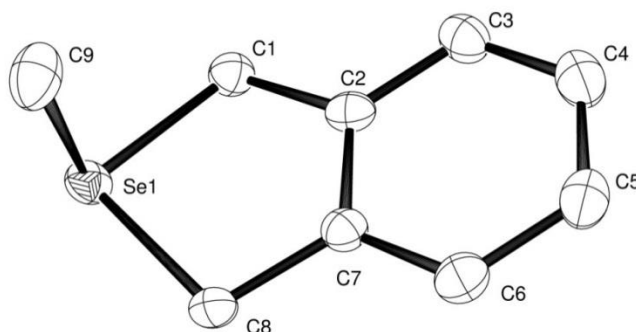


Figure 5.11 – View of the cation in $[o\text{-C}_6\text{H}_4\text{CH}_2\text{Se}(\text{Me})\text{CH}_2][\text{AlCl}_4]$ showing the atom labelling scheme. The displacement ellipsoids are drawn at the 50% probability level and H atoms are omitted for clarity.

Se1-C1	1.952(3)	C8-Se1-C1	90.44(14)
Se1-C8	1.946(3)	C9-Se1-C1	96.69(16)
Se1-C9	1.928(4)	C9-Se1-C8	97.18(16)

Table 5.7 – Selected bond lengths (Å) and angles ($^\circ$) for $[o\text{-C}_6\text{H}_4\text{CH}_2\text{Se}(\text{Me})\text{CH}_2]^+$ (Figure 5.11)

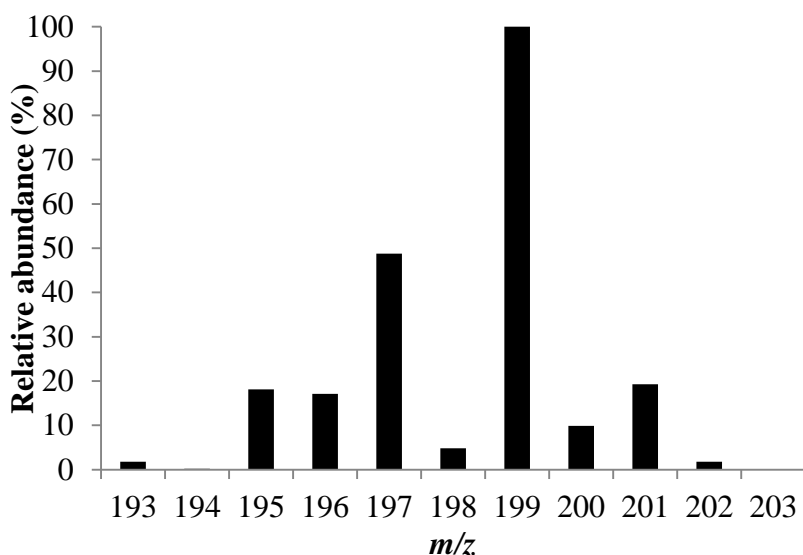


Figure 5.12 – Calculated mass spectrometry isotope pattern for [*o*-C₆H₄CH₂Se(Me)CH₂]⁺

The reaction of one equivalent of AlCl₃ with one equivalent of the tripodal sulfur donor ligand MeC(CH₂SMe)₃ was also investigated. It was anticipated that the product of this reaction would be an octahedral species with *fac*-coordination of the MeC(CH₂SMe)₃ ligand. Figure 5.14, however, shows that the product of the 1:1 complex is a 1D chain polymer with distorted trigonal bipyramidal coordination at Al, with *trans* S donor atoms and planar arrangement of Cl ligands. One of the sulfur donor atoms is uncoordinated and does not exhibit longer range interactions to other 1D chains. A similar 1D chain polymer was observed from the reaction of SbCl₃ with MeC(CH₂SMe)₃, although the coordination geometry at Sb, which has a lone pair, was distorted square pyramidal with the S donor atoms *cis* to each other.⁶¹

The Al-S bond lengths range between 2.467(3) and 2.489(3) Å, approximately 0.1 Å longer than for [(AlCl₃)₂(*o*-C₆H₄(CH₂SEt)₂)], although more consistent with the Al-S bond lengths in [AlCl₂(CH₃S(CH₂)₂SCH₃)₂][AlCl₄]. This is consistent with the expectation that higher coordination numbers lead to longer bond lengths. Solution state data were not able to provide any additional information on this complex as the chain polymer would have to break up in order to dissolve. This is confirmed by the presence of [AlCl₄]⁻ in the ²⁷Al NMR spectrum, which is likely to be a hydrolysis product.

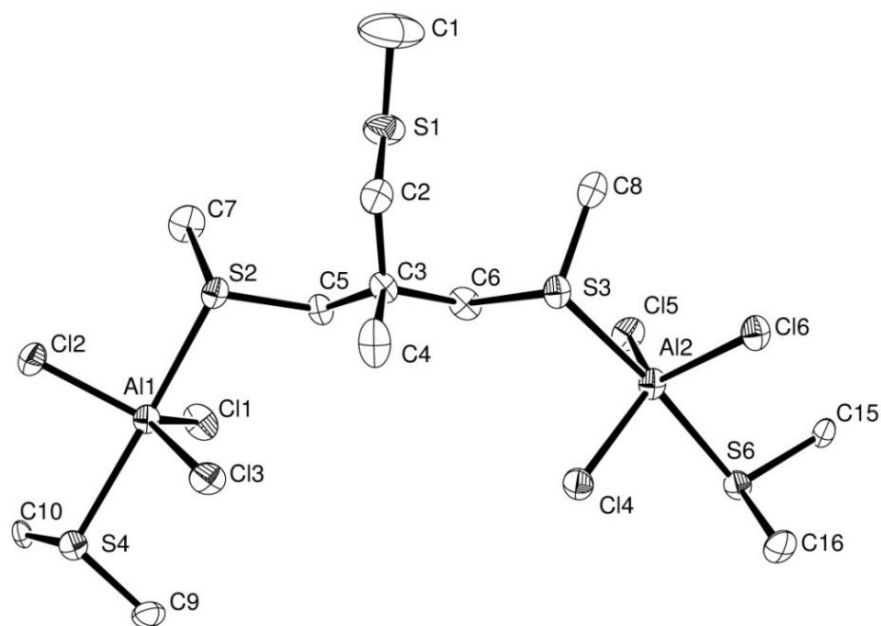


Figure 5.13 – View of part of the 1D chain polymer $[\text{AlCl}_3(\text{MeC}(\text{CH}_2\text{SMe})_3)]$ showing the atom labelling scheme. The displacement ellipsoids are drawn at the 50% probability level and H atoms are omitted for clarity.

Al1-S2	2.489(3)	Cl2-Al1-Cl3	124.20(13)
Al1-S4	2.475(3)	Cl1-Al1-S2	95.32(11)
Al2-S3	2.467(3)	Cl2-Al1-S2	89.30(11)
Al2-S6	2.489(3)	Cl3-Al1-S2	86.51(10)
Al1-Cl1	2.151(3)	Cl1-Al1-S4	94.95(11)
Al1-Cl2	2.152(3)	Cl2-Al1-S4	88.32(11)
Al1-Cl3	2.154(3)	Cl3-Al1-S4	86.30(10)
Al2-Cl4	2.167(3)	Cl4-Al2-S3	86.89(11)
Al2-Cl5	2.159(3)	Cl5-Al2-S3	94.47(10)
Al2-Cl6	2.161(3)	Cl6-Al2-S3	89.40(11)
S4-Al1-S2	169.42(11)	Cl4-Al2-S6	86.76(11)
S3-Al2-S6	173.41(12)	Cl5-Al2-S6	90.22(10)
Cl1-Al2-Cl2	117.04(12)	Cl6-Al2-S6	92.57(10)
Cl1-Al1-Cl3	118.75(13)		

Table 5.8 – Selected bond distances (Å) and angles (°) for $[\text{AlCl}_3(\text{MeC}(\text{CH}_2\text{SMe})_3)]$ (Figure 5.13)

The reaction was also carried out with three equivalents of AlCl_3 to one equivalent of $\text{MeC}(\text{CH}_2\text{SMe})_3$ to see if it was also possible to form the $[(\text{AlCl}_3)_3(\text{MeC}(\text{CH}_2\text{SMe})_3)]$ complex with one AlCl_3 unit tetrahedrally coordinated to each sulfur donor, as was observed for GaCl_3 .¹ It was not possible to isolate a pure product from this reaction, however solution data support the formation of a species with tetrahedral coordination at Al. ^{27}Al NMR spectroscopy shows a very broad peak at 108 ppm ($w_{1/2} = \sim 1800$ Hz), indicative of tetrahedral coordination. ^1H NMR spectroscopy shows that the complex formed has significant shifts from free ligand (3.15 (CH_2), 2.65 (SCH_3) and 1.41 (CCH_3) ppm vs. 2.60, 2.15 and 1.05 ppm).⁶²

5.2.3 Complexes with macrocyclic ligands

The reaction of [9]ane S_3 with AlCl_3 was carried out in a 1:1 ratio. Addition of a solution of [9]ane S_3 in anhydrous CH_2Cl_2 to a suspension of AlCl_3 in anhydrous CH_2Cl_2 did not show any colour change or any indication that the AlCl_3 had been complexed and taken into solution. After stirring for several hours, the white solid was collected by filtration. Elemental analysis on this showed a large excess of AlCl_3 (approximately 8 AlCl_3 : 1 [9]ane S_3). This reaction was then repeated with the addition of anhydrous CH_3CN in order to increase the solubility of the AlCl_3 and promote complexation. Addition of CH_3CN with stirring to a suspension of AlCl_3 and [9]ane S_3 in CH_2Cl_2 yielded a colourless solution. Attempts to grow crystals from the solution yielded only [9]ane S_3 . It is likely that the hard N donor of CH_3CN , present in excess, forms an adduct with AlCl_3 in preference to the soft S donor of [9]ane S_3 .⁶³ This reaction was next attempted using toluene as a solvent. With heating, it is possible to dissolve AlCl_3 in toluene to form a bright yellow solution. Addition of a solution of [9]ane S_3 to this solution caused immediate loss of the yellow colour and the formation of a white precipitate. Poor solubility of the complex in chlorocarbon solvents necessitated the use of CD_3CN as a solvent for NMR spectroscopy. Despite this being a weakly coordinating solvent, the complex dissociated in solution to give free ligand (^1H NMR spectroscopy) and $[\text{AlCl}_4]^-$ (^{27}Al NMR spectroscopy). IR spectroscopy shows three bands at 444, 408 and 375 cm^{-1} . These bands occur at lower wavenumbers than has been observed for the tetrahedral coordination complexes of AlCl_3 , indicating a higher coordination number. There is no evidence for $[\text{AlCl}_4]^-$ in the IR spectrum.

The reaction of two equivalents of AlCl_3 with one equivalent of [14]aneS₄ was carried out. Addition of a solution of [14]aneS₄ to a suspension of AlCl_3 in anhydrous CH_2Cl_2 caused all reactants to go into solution, although a large volume of white precipitate rapidly formed. Microanalysis data support the formation of a 2:1 complex and IR spectroscopy shows evidence of $[\text{AlCl}_4]^-$, suggesting that the complex formed is $[\text{AlCl}_2(\text{[14]aneS}_4)][\text{AlCl}_4]$ as was seen with the reaction of GaCl_3 with several of the 16 membered chalcogenoether macrocycles, although the reaction of GaCl_3 with [14]aneS₄ yielded a 1:1 product.³ ^1H NMR spectroscopy does not yield any additional information as there is no shift from free ligand, suggesting that the complex is dissociated in the coordinating CD_3CN solvent. The poor solubility of the complex in chlorocarbon solvents precluded the acquisition of an NMR spectrum in these non-coordinating solvents. A crystal structure was obtained, which shows $[\text{AlCl}_2(\text{[14]aneS}_4)][\text{AlCl}_4]$ with a distorted octahedral cation at the centre of the macrocycle with *cis* chlorides (Figure 5.14). There are three cations in the asymmetric unit with one exhibiting some disorder in the carbon backbone of the macrocycle. The same geometry was observed in the analogous indium chloride complex $[\text{InCl}_2(\text{[14]aneS}_4)][\text{InCl}_4]$.²

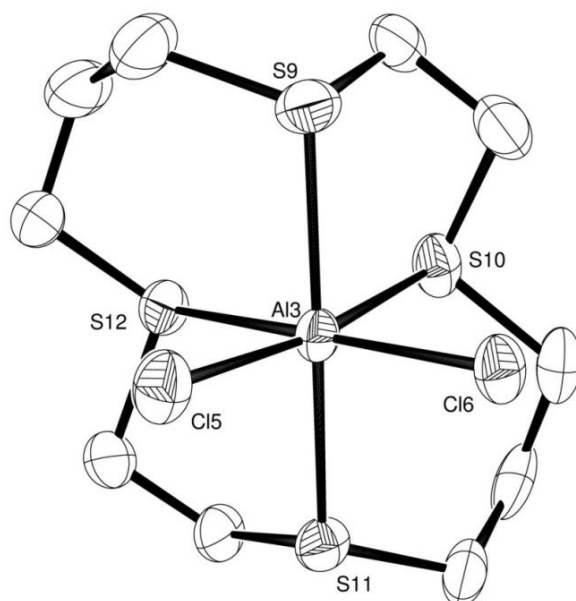


Figure 5.14 – View of one of the cations in $[\text{AlCl}_2([\text{14]aneS}_4)]^+[\text{AlCl}_4]^-$ showing the atom labelling scheme. The displacement ellipsoids are drawn at the 50% probability level and H atoms are omitted for clarity.

Al-Cl	2.197(3) – 2.220(7)	S-Al-S	77.19(9) – 92.09(19)
Al-S	2.382(3) – 2.450(6)	Cl-Al-S	167.3(3) – 170.9(3)
Cl-Al-Cl	98.0(3) – 98.9(1)	Cl-Al-S	90.4(3) – 94.1(3)
S-Al-S	173.09(11) – 173.6(2)		

Table 5.9 – Selected bond lengths and angles for $[\text{AlCl}_2([\text{14]aneS}_4)]^+$ (Figure 5.14).

Values are shown as a range due to the presence of three cations in the asymmetric unit.

The reaction of two equivalents of AlCl_3 with one equivalent of $[\text{16]aneSe}_4$ proceeded in a similar manner to the reaction with $[\text{14]aneS}_4$. Poor solubility of the complex in chlorocarbon solvents hindered attempts to gain informative NMR spectroscopic data. The use of CD_3CN as an NMR solvent resulted in ^1H and ^{77}Se NMR spectra that did not show any shift from free ligand. ^{27}Al NMR spectroscopy showed the presence of $[\text{AlCl}_4]^-$, which was also evident in the IR spectrum. Microanalysis data supported the formation of a complex with a ratio of two AlCl_3 to one $[\text{16]aneSe}_4$. The proposed reaction product is $[\text{AlCl}_2([\text{16]aneSe}_4)]^+[\text{AlCl}_4]^-$ reactions of GaCl_3 and InCl_3 with $[\text{16]aneSe}_4$ also yielded 2:1 complexes with the formulae $[\text{MCl}_2([\text{16]aneSe}_4)]^+[\text{MCl}_4]^-$ with *trans* chloride ligands in $[\text{MCl}_2([\text{16]aneSe}_4)]^+$.³

5.2.4 Chemical vapour deposition

Owing to previous success in using neutral chalcogenoether adducts of GaCl₃ to deposit thin films of Ga₂Se₃ and Ga₂Te₃,³⁸ several coordination complexes of AlCl₃ were synthesised as potential single source precursors to Al₂E₃. Ligands with ⁿBu substituents were selected as these had previously been shown to be more effective than ligands with Me substituents but the ligands are still easy to synthesise.³⁸

[AlCl₃(ⁿBu₂E)] (E = Se, Te) were synthesised as yellow oils. Characterisation data were similar to the [AlCl₃(Me₂E)] (E = Se, Te) complexes, indicating that the complexes are neutral, tetrahedral adducts. Microanalytical data support the formation of 1:1 complexes.

LPCVD of both single source precursors was attempted at temperatures between 723 and 873 K. In all cases the precursor evaporated cleanly, having changed colour to dark brown during the evaporation. There was no deposition on the tiles and some elemental selenium or tellurium was deposited on the tube at the exit of the furnace.

Thermogravimetric analysis (TGA) of [AlCl₃(ⁿBu₂Se)] showed a mass loss of 89%, which occurred in two steps between 100 – 250 °C and 250 – 520 °C, although the majority of the mass loss occurred by 300 °C. TGA of [AlCl₃(ⁿBu₂Te)] showed a mass loss of 83%, which occurred in two steps between 100 – 300 °C (60% loss) and 500 – 650 °C.

It is possible that the strength of the Al-E (E = Se, Te) bond is too weak to make these complexes suitable single source precursors for LPCVD. TGA did not indicate, however, that the ligand was being distilled off and so it is likely that the decomposition pathway is more complicated than can be deduced from TGA.

5.2.5 Conclusions

A wider range of coordination numbers and geometries have been characterised for the complexes of AlCl_3 with acyclic chalcogenoether ligands than for the complexes of GaX_3 with the same ligands. The use of monodentate ligands such as Me_2E ($\text{E} = \text{S}, \text{Se}, \text{Te}$) leads to the formation of 4-coordinate, distorted tetrahedral species and NMR spectroscopy shows that using extra equivalents of Me_2S leads to the formation of a 5-coordinate complex. The use of bidentate ligands can produce 4-coordinate, neutral complexes ($o\text{-C}_6\text{H}_4(\text{CH}_2\text{SEt})_2$) or 6-coordinate cationic species ($\text{MeE}(\text{CH}_2)_2\text{EMe}$), depending on the bite angle of the ligand. The use of the tridentate ligand $\text{MeC}(\text{CH}_2\text{SMe})_3$ did not produce the expected 6 coordinate octahedral species but led to trigonal bipyramidal coordination at aluminium with one uncoordinated S donor. This range of coordination numbers and environments is unexpected based on previous examples with gallium halides. AlBr_3 and AlI_3 appear to form analogous coordination complexes with monodentate ligands, although they cannot access higher coordination numbers by using excess equivalents of Me_2S . The Lewis acidity of AlCl_3 can also promote Se-C and Te-C bond cleavage in certain ligands. Previously coordination complexes of GaCl_3 have been shown to be suitable single source precursors, however the analogous complexes of AlCl_3 are not suitable for LPCVD of aluminium selenide and aluminium telluride.

5.3 Experimental

Raman spectroscopy data are only supplied for certain complexes due to terminal failure of the departmental Raman spectrometer while these complexes were being studied. Due to the sensitivity of the complexes, it was not feasible to send the samples out of the department for analysis.

[AlCl₃(Me₂S)]

Me₂S (0.093 g, 1.5 mmol) was added dropwise to a suspension of AlCl₃ (0.2 g, 1.5 mmol) in anhydrous CH₂Cl₂ (15 mL) with stirring to give a colourless solution. After 30 minutes, all solvent was removed *in vacuo* to give a pale yellow oil. Yield 0.260 g, 89%. Anal Calcd for C₂H₆AlCl₃S: C, 12.3; H, 3.1. Found: C, 12.4; H, 3.1%. ¹H NMR (CDCl₃, 295 K): 2.53 (s, [6H]). ²⁷Al NMR (CDCl₃, 295 K): 111, (213 K) 110. IR (cm⁻¹): 541 (s), 410 (m). Raman (cm⁻¹): 404 (m).

[AlBr₃(Me₂S)]

AlBr₃ (0.1 g, 0.37 mmol) was dissolved in toluene (10 mL) to give a pale yellow solution. Me₂S (0.023 g, 0.37 mmol) was added dropwise to give a colourless solution. After stirring for 15 minutes, all solvent was removed *in vacuo* to give a white solid. Yield 0.097 g, 79%. Anal Calcd for C₂H₆AlBr₃S: C, 7.3; H, 1.8. Found: C, 6.4; H, 2.0%. ¹H NMR (CD₂Cl₂, 295 K): 2.77 (s, [6H]). ²⁷Al NMR (CD₂Cl₂, 295 K): 81, (185 K) 81. IR (cm⁻¹, Nujol): 392 (br).

[AlI₃(Me₂S)]

AlI₃ (0.2 g, 0.5 mmol) was dissolved in toluene (10 mL) to give a pale yellow solution. Me₂S (0.030 g, 0.5 mmol) was added dropwise to give a colourless solution. After stirring for 15 minutes, all solvent was removed *in vacuo* to give a pale yellow solid. Yield 0.172 g, 75%. Anal Calcd for C₂H₆AlI₃S: C, 5.1; H, 1.3. Found: C, 5.0; H, 1.3%.

^1H NMR (CD_2Cl_2 , 295 K): 2.44 (s, [6H]). ^{27}Al NMR (CD_2Cl_2 , 295 K): 49; (185 K) 81. IR (cm^{-1} , Nujol): 336 (br).

[AlCl₄][Me₂SH]

Me₂S (0.093 g, 1.5 mmol) was added dropwise to a suspension of AlCl₃ (0.2 g, 1.5 mmol) in anhydrous CH₂Cl₂ (25 mL) with stirring to give a colourless solution. HCl was slowly bubbled through the solution for ~30 seconds. After stirring for 30 minutes, some white precipitate formed. The white solid was collected by filtration and dried *in vacuo*. The volume of the pale yellow filtrate was reduced to ~10 mL. Colourless crystals suitable for single crystal X-ray diffraction were obtained after storage at -18°C for 24 hours. Anal Calcd for C₂H₇AlCl₄S: C, 10.4; H, 3.0. Found: C, 10.5; H, 2.9%. IR (cm^{-1} , Nujol): 2482 (br, w), 488 (br), 467 (br), 395 (s).

[AlCl₂(MeSCH₂CH₂SMe)₂][AlCl₄]

MeSCH₂CH₂SMe (0.183 g, 1.5 mmol) was added dropwise to a suspension of AlCl₃ (0.2 g, 1.5 mmol) in anhydrous CH₂Cl₂ (15 mL) with stirring to give a colourless solution. After 30 minutes the volume of solvent was reduced *in vacuo* to ~5 mL. A large quantity of white solid precipitated after storage at -18°C for 24 hours. The solid was collected by filtration and dried *in vacuo*. Yield 0.260 g, 68%. Anal Calcd for C₈H₂₀Al₂Cl₆S₄: C, 18.8; H, 3.9. Found: C, 18.3; H, 3.8%. ^1H NMR (CD_2Cl_2 , 295 K): 3.07 (s, [4H]), 2.25 (s, [6H]). ^{27}Al NMR (CDCl_3 , 295 K): 105, 37. IR (cm^{-1} , Nujol): 489 (s), 463 (m) 346 (w). Raman (cm^{-1}): 490 (w), 350 (s), 295 (s).

[AlBr₂(MeSCH₂CH₂SMe)₂][AlBr₄]

MeSCH₂CH₂SMe (0.090 g, 0.75 mmol) was added dropwise to a pale yellow solution of AlBr₃ (0.200 g, 0.75 mmol) in toluene (15 mL) with stirring to give a colourless solution and some white precipitate. After 30 minutes the reaction mixture was filtered and the white solid dried *in vacuo*. Yield 0.209 g, 72 %. Anal Calcd for C₈H₂₀Al₂Br₆S₄: C, 12.3; H, 2.6. Found: C, 11.7; H, 2.9%. ^1H NMR (CD_2Cl_2 , 295 K): 3.10 (s, [4H]),

2.26 (s, [6H]). ^{27}Al NMR (CD_2Cl_2 , 295 K): 81, (283 K) 81. IR (cm^{-1} , Nujol): 405 (s, br), 355 (s, br).

$[\text{AlI}_2(\text{MeSCH}_2\text{CH}_2\text{SMe})_2][\text{AlI}_4]$

$\text{MeSCH}_2\text{CH}_2\text{SMe}$ (0.061 g, 0.5 mmol) was added dropwise to a pale yellow solution of AlI_3 (0.200 g, 0.5 mmol) in toluene (15 mL) with stirring to give an orange solution and some pale yellow precipitate. After 30 minutes the reaction mixture was filtered and the pale yellow solid dried *in vacuo*. Crystals suitable for single crystal X-ray diffraction were obtained after storage of the filtrate at -18°C for 48 hours. Yield 0.192 g, 74 %. Anal Calcd for $\text{C}_8\text{H}_{20}\text{Al}_2\text{I}_6\text{S}_4$: C, 9.1; H, 1.9. Found: C, 8.9; H, 3.3%. ^1H NMR (CD_2Cl_2 , 295 K): 3.12 (s, [4H]), 2.27 (s, [6H]). ^{27}Al NMR (CD_2Cl_2 , 295 K): -23, (283 K) -23. IR (cm^{-1} , Nujol): 338 (s).

$\{\text{AlCl}_3[\text{MeC}(\text{CH}_2\text{SMe})_3]\}$

$\text{MeC}(\text{CH}_2\text{SMe})_3$ (0.158 g, 0.75 mmol) was added dropwise to a suspension of AlCl_3 (0.1 g, 0.75 mmol) in anhydrous CH_2Cl_2 (10 mL) with stirring to give a colourless solution. After 30 minutes the volume of solvent was reduced *in vacuo* to ~ 5 mL. Colourless crystals suitable for single crystal X-ray diffraction were obtained after storage at -18°C for 48 hours. Yield 0.181 g, 70%. Anal Calcd for $\text{C}_8\text{H}_{18}\text{AlCl}_3\text{S}_3$: C, 27.9; H, 5.3. Found: C, 26.9; H, 4.9%. ^1H NMR (CDCl_3 , 295 K): 2.76 (s, [6H]), 2.25 (s, [9H]), 1.16 (s, [3H]). IR (cm^{-1} , Nujol): 533 (s), 491 (s).

$[(\text{AlCl}_3)_2\{\text{C}_6\text{H}_4(\text{CH}_2\text{SEt})_2\}]$

o- $\text{C}_6\text{H}_4(\text{CH}_2\text{SEt})_2$ (0.170 g, 0.75 mmol) was added dropwise to a suspension of AlCl_3 (0.2 g, 1.5 mmol) in anhydrous CH_2Cl_2 (15 mL) with stirring to give a yellow solution. After 30 minutes the volume of solvent was reduced *in vacuo* to ~ 5 mL. Storage at -18°C for 24 hours produced yellow crystals. Yield 0.222 g, 60%. Anal Calcd for $\text{C}_{12}\text{H}_{18}\text{Al}_2\text{Cl}_6\text{S}_2$: C, 29.2; H, 3.7. Found: C, 29.3; H, 3.7%. ^1H NMR (CDCl_3 , 295 K): 7.47 (m, [4H]), 4.37 (s, [4H]), 3.08 (q, [4H]), 1.49 (t, [6H]). ^{27}Al NMR (CDCl_3 , 295 K):

111 ($w_{1/2} = 900$ Hz). IR (cm^{-1} , Nujol): 565-500 (vbr, s), 394 (s). Raman (cm^{-1}): 518 (m), 402 (m).

[AlCl₃([9]aneS₃)]

A solution of [9]aneS₃ (0.135 g, 0.75 mmol) in anhydrous toluene (10 mL) was added to a solution of AlCl₃ (0.1 g, 0.75 mmol) in anhydrous toluene (10 mL) with stirring to give a colourless solution and a large quantity of white precipitate. After 60 minutes, the precipitate was collected by filtration and dried *in vacuo*. Yield 0.160 g, 68%. Anal Calcd for C₆H₁₂AlCl₃S₃: C, 23.0; H, 3.9. Found: C, 23.1; H, 3.9%. ¹H NMR (CD₃CN, 295 K): 3.10 (s, [12H]) (free ligand). IR (cm^{-1} , Nujol): 408 (s), 375 (m).

[AlCl₂([14]aneS₄)] [AlCl₄]

A solution of [14]aneS₄ (0.099 g, 0.37 mmol) in anhydrous CH₂Cl₂ (10 mL) was added to a suspension of AlCl₃ (0.1 g, 0.75 mmol) in anhydrous CH₂Cl₂ (10 mL) with stirring to give a colourless solution. After approximately 5 minutes a large quantity of white precipitate formed. After 60 minutes, the precipitate was collected by filtration and dried *in vacuo*. Yield 0.140 g, 70%. Anal Calcd for C₁₀H₂₀Al₂Cl₆S₄: C, 22.4; H, 3.8. Found: C, 22.6; H, 3.7%. ¹H NMR (CD₃CN, 295 K): 2.74 (s, [8H]), 2.60 (m, [8H]), 1.88 (m, [4H]) (free ligand). IR (cm^{-1} , Nujol): 481 (br, s), 419 (m).

[AlCl₃(Me₂Se)]

Me₂Se (0.163 g, 1.5 mmol) was added dropwise to a suspension of AlCl₃ (0.2 g, 1.5 mmol) in anhydrous CH₂Cl₂ (15 mL) with stirring to give a colourless solution. After 30 minutes, the volume of solvent was reduced *in vacuo* to ~5 mL. Storage at -18°C for 24 hours produced colourless crystals. Yield 0.298 g, 82%. Anal Calcd for C₂H₆AlCl₃Se: C, 9.9; H, 2.5. Found: C, 10.0; H, 2.6%. ¹H NMR (CDCl₃, 295 K): 2.42 (s, [6H]). ²⁷Al NMR (CDCl₃, 295 K): 110, (183 K) 110. ⁷⁷Se NMR (CDCl₃, 273 K): -11, (183 K) -14. IR (cm^{-1} , Nujol): 531 (s), 399 (s). Raman (cm^{-1}): 521 (w), 399 (s).

[AlBr₃(Me₂Se)]

AlBr₃ (0.1 g, 0.37 mmol) was dissolved in toluene (10 mL) to give a pale yellow solution. Me₂Se (0.040 g, 0.37 mmol) was added dropwise to give a colourless solution. After stirring for 15 minutes, all solvent was removed *in vacuo* to give a white solid. Yield 0.112 g, 80%. Anal Calcd for C₂H₆AlBr₃Se: C, 6.4; H, 1.6. Found: C, 6.1; H, 1.9%. ¹H NMR (CD₂Cl₂, 295 K): 2.47 (s, [6H]). ²⁷Al NMR (CD₂Cl₂, 295 K): 99. IR (cm⁻¹, Nujol): 446 (s), 397 (s).

[AlCl₃(ⁿBu₂Se)]

A solution of ⁿBu₂Se (0.289 g, 1.5 mmol) in anhydrous CH₂Cl₂ (7 mL) was added dropwise to a suspension of AlCl₃ (0.2 g, 1.5 mmol) in anhydrous CH₂Cl₂ (8 mL) with stirring to give a colourless solution. After 30 minutes, all solvent was removed *in vacuo* to yield a pale yellow oil. Yield 0.357 g, 73%. Anal Calcd for C₈H₁₈AlCl₃Se: C, 29.4; H, 5.6. Found: C, 29.7; H, 5.8%. ¹H NMR (CD₂Cl₂, 295 K): 3.03 (t, [4H]), 1.82 (m, [4H]), 1.46 (m, [4H]), 0.97 (t, [6H]). ²⁷Al NMR (CD₂Cl₂, 295 K): 110. ⁷⁷Se NMR (CDCl₃, 295 K): 102. IR (cm⁻¹): 539 (s), 399 (m).

[AlCl₂(MeSeCH₂CH₂SeMe)₂][AlCl₄]

MeSeCH₂CH₂SeMe (0.162 g, 0.75 mmol) was added dropwise to a suspension of AlCl₃ (0.1 g, 0.75 mmol) in anhydrous CH₂Cl₂ (10 mL) with stirring to give a yellow solution. After 30 minutes the volume of solvent was reduced *in vacuo* to ~5 mL. Storage at -18°C for 24 hours produced colourless crystals. Yield 0.183 g, 69%. Anal Calcd for C₈H₂₀Al₂Cl₆Se₄: C, 13.7; H, 2.9. Found: C, 12.8; H, 2.7%. ¹H NMR (CDCl₃, 295 K): 3.21 (s, [4H]), 2.36 (s, [6H]). ²⁷Al NMR (CDCl₃, 295 K): 108. ⁷⁷Se NMR (CDCl₃, 295 K): 95. IR (cm⁻¹, Nujol): 488 (s).

[*o*-C₆H₄CH₂Se(Me)CH₂][AlCl₄]

o-C₆H₄(CH₂SeCH₃)₂ (0.121 g, 0.38 mmol) was added dropwise to a suspension of AlCl₃ (0.1 g, 0.75 mmol) in anhydrous CH₂Cl₂ (10 mL) with stirring to give a yellow solution.

After 30 minutes all solvent was removed *in vacuo* to yield an orange oil. On standing, crystals suitable for X-ray diffraction formed. Yield 0.172 g, 78%. ^{27}Al NMR (CDCl_3 , 295 K): 103. ^{77}Se NMR (CDCl_3 , 295 K): 383. IR (cm^{-1} , Nujol): 491 (s), 348 (w). ES^+ MS (MeCN): $m/z = 199$; ES^- MS (MeCN): $m/z = 169$.

[AlCl₂([16]aneSe₄)] [AlCl₄]

A solution of [16]aneSe₄ (0.181 g, 0.37 mmol) in anhydrous CH_2Cl_2 (10 mL) was added to a suspension of AlCl_3 (0.1 g, 0.75 mmol) in anhydrous CH_2Cl_2 (10 mL) with stirring to give a colourless solution. After approximately 5 minutes a large quantity of white precipitate formed. After 60 minutes, the precipitate was collected by filtration and dried *in vacuo*. Yield 0.196 g, 70%. Anal Calcd for $\text{C}_{12}\text{H}_{24}\text{Al}_2\text{Cl}_6\text{Se}_4$: C, 19.2; H, 3.2. Found: C, 19.0; H, 3.1%. ^1H NMR (CD_3CN , 295 K): 2.67 (t, [16H]), 2.00 (p, [8H]) (free ligand). IR (cm^{-1}): 483 (s).

[AlCl₃(Me₂Te)]

Me_2Te (0.118 g, 0.75 mmol) was added dropwise to a suspension of AlCl_3 (0.1 g, 0.75 mmol) in anhydrous CH_2Cl_2 (10 mL) with stirring to give a colourless solution. After 30 minutes, the volume of solvent was reduced *in vacuo* to ~5 mL. Storage at -18°C for 24 hours produced yellow crystals. Yield: 0.135 g, 62%. Anal Calcd for $\text{C}_2\text{H}_6\text{AlCl}_3\text{Te}$: C, 8.3; H, 2.1. Found: C, 8.6; H, 2.1%. ^1H NMR (CD_2Cl_2 , 295 K): 2.19 (s, [6H]). ^{27}Al NMR (CD_2Cl_2 , 295 K): 105. ^{125}Te NMR (CDCl_3): not observed at 295 – 183 K. IR (cm^{-1} , Nujol): 491 (s), 395 (m).

[AlBr₃(Me₂Te)]

AlBr_3 (0.1 g, 0.37 mmol) was dissolved in toluene (10 mL) to give a pale yellow solution. Me_2Te (0.058 g, 0.37 mmol) was added dropwise to give a paler yellow solution. After stirring for 15 minutes, all solvent was removed *in vacuo* to give a yellow solid. Yield 0.107g, 68%. Anal Calcd for $\text{C}_2\text{H}_6\text{AlBr}_3\text{Te}$: C, 5.7; H, 1.4. Found:

C, 5.7; H, 1.8%. ^1H NMR (CD_2Cl_2 , 295 K): 2.66 (s, [6H]). ^{27}Al NMR (CD_2Cl_2 , 295 K): 92. ^{125}Te NMR: not observed. IR (cm^{-1} , Nujol): 404 (m), 391 (m).

[AlCl₃(ⁿBu₂Te)]

A solution of ⁿBu₂Te (0.181 g, 0.75 mmol) in anhydrous CH₂Cl₂ (7 mL) was added dropwise to a suspension of AlCl₃ (0.1 g, 0.75 mmol) in anhydrous CH₂Cl₂ (8 mL) with stirring to give a yellow solution. After 15 minutes, all solvent was removed *in vacuo* to yield a yellow oil. Yield 0.218 g, 78%. Anal Calcd for C₈H₁₈AlCl₃Te: C, 25.6; H, 4.8. Found: C, 26.1; H, 5.1%. ^1H NMR (CD_2Cl_2 , 295 K): 2.95 (t, [4H]), 1.83 (m, [4H]), 1.43 (m, [4H]), 0.96 (t, [6H]). ^{27}Al NMR (CD_2Cl_2 , 295 K): 107. ^{125}Te NMR (CDCl_3): not observed at 295 – 183 K. IR (cm^{-1}): 526 (s), 495 (s), 395 (m).

Table 5.10 Crystal data and structure refinement details^a

Compound	[AlCl ₃ (Me ₂ Se)]	[AlCl ₃ (Me ₂ Te)]	[AlCl ₄][Me ₂ SH]
Formula	C ₂ H ₆ AlCl ₃ Se	C ₂ H ₆ AlCl ₃ Te	C ₂ H ₇ AlCl ₄ S
<i>M</i>	242.36	291.00	231.92
crystal system	orthorhombic	orthorhombic	monoclinic
Space group	<i>Pbcm</i> (no. 57)	<i>Pbcm</i> (no. 57)	<i>P2₁/c</i> (no. 14)
<i>a</i> [Å]	6.205(4)	6.248(1)	14.3783(7)
<i>b</i> [Å]	12.603(8)	13.114(3)	10.9075(7)
<i>c</i> [Å]	10.479(6)	10.514(2)	12.3742(5)
α [deg]	90	90	90
β [deg]	90	90	90.260(3)
γ [deg]	90	90	90
<i>U</i> [Å ³]	819.6(8)	861.4(3)	1940.64(17)
<i>Z</i>	4	4	8
μ (Mo K α) [mm ⁻¹]	5.564	4.388	1.443
total reflns	4909	3839	11008
unique reflns	1315	1312	4432
<i>R</i> _{int}	0.103	0.018	0.035
no. of params, restraints	38, 0	38, 0	153, 0
<i>R</i> ₁ ^b [<i>I</i> _o > 2 σ (<i>I</i> _o)]	0.055	0.018	0.045
<i>R</i> ₁ [all data]	0.065	0.022	0.055
<i>wR</i> ₂ ^b [<i>I</i> _o > 2 σ (<i>I</i> _o)]	0.137	0.034	0.156
<i>wR</i> ₂ [all data]	0.148	0.035	0.189

^a Common items: temperature = 100 K; wavelength (Mo K α) = 0.71073 Å; θ (max) = 27.5°.

^b $R_1 = \Sigma ||F_o| - |F_c|| / \Sigma |F_o|$. $wR_2 = [\Sigma w(F_o^2 - F_c^2)^2 / \Sigma wF_o^4]^{1/2}$

Table 5.10 cont.

Compound	[AlBr ₃ (Me ₂ Te)]	[AlCl ₂ (CH ₃ S(CH ₂) ₂ SCH ₃) ₂][AlCl ₄]	[AlCl ₂ (CH ₃ Se(CH ₂) ₂ SeCH ₃) ₂][AlCl ₄]
Formula	C ₂ H ₆ AlBr ₃ Te	C ₈ H ₂₀ Al ₂ Cl ₆ S ₄	C ₈ H ₂₀ Al ₂ Cl ₆ Se ₄
<i>M</i>	424.38	511.14	698.74
crystal system	orthorhombic	triclinic	monoclinic
Space group	<i>Pbcm</i> (no. 57)	<i>P</i> -1 (no. 2)	<i>P</i> 2 ₁ / <i>c</i> (no. 14)
<i>a</i> [Å]	6.562(3)	6.708(5)	7.122(4)
<i>b</i> [Å]	13.400(5)	10.583(5)	17.744(8)
<i>c</i> [Å]	10.724(4)	15.383(5)	17.582(8)
α [deg]	90	90.070(5)	90
β [deg]	90	102.422(5)	93.169(8)
γ [deg]	90	96.512(5)	90
<i>U</i> [Å ³]	943.0(6)	1059.2(10)	2218.5(18)
<i>Z</i>	4	2	4
μ (Mo K α) [mm ⁻¹]	15.870	1.276	7.405
total no. reflns	8126	11612	10277
unique reflns	1140	6072	5039
<i>R</i> _{int}	0.297	0.026	0.114
no. of params, restraints	38, 0	188, 0	188, 0
<i>R</i> ₁ ^b [<i>I</i> _o > 2 σ (<i>I</i> _o)]	0.065	0.046	0.077
<i>R</i> ₁ [all data]	0.068	0.059	0.091
<i>wR</i> ₂ ^b [<i>I</i> _o > 2 σ (<i>I</i> _o)]	0.163	0.072	0.196
<i>wR</i> ₂ [all data]	0.168	0.077	0.207

Table 5.10 cont.

Compound	[AlI ₂ (CH ₃ S(CH ₂) ₂ SCH ₃) ₂][AlI ₄]	[^t BuTe(CH ₂) ₃ Te(^t Bu)Te(CH ₂) ₃ Te ^t Bu][AlCl ₄]	[{ <i>o</i> -C ₆ H ₄ (CH ₂ SEt) ₂ }(AlCl ₃) ₂]
Formula	C ₈ H ₂₀ Al ₂ I ₆ S ₄	C ₁₈ H ₃₉ AlCl ₄ Te ₄	C ₁₂ H ₁₈ Al ₂ Cl ₆ S ₂
<i>M</i>	1059.84	934.67	493.04
crystal system	monoclinic	triclinic	monoclinic
Space group	<i>P</i> 2 ₁ / <i>c</i> (no. 14)	<i>P</i> -1 (no. 2)	<i>C</i> 2/ <i>c</i> (no. 15)
<i>a</i> [Å]	14.825(3)	10.016(1)	18.7450(16)
<i>b</i> [Å]	12.181(2)	12.524(2)	10.810(10)
<i>c</i> [Å]	15.150(4)	14.049(2)	13.608(12)
α [deg]	90	113.209(8)	90
β [deg]	108.449(8)	90.417(6)	125.779(1)
γ [deg]	90	105.465(7)	90
<i>U</i> [Å ³]	2595.3(10)	1548.3(3)	2237(3)
<i>Z</i>	4	2	4
μ(Mo Kα) [mm ⁻¹]	7.563	4.109	1.026
total no. reflns	24085	11817	8120
unique reflns	5928	5448	2199
<i>R</i> _{int}	0.152	0.149	0.041
no. of params, restraints	185, 0	253, 144	100, 3
<i>R</i> ₁ ^b [<i>I</i> _o > 2σ(<i>I</i> _o)]	0.057	0.083	0.108
<i>R</i> ₁ [all data]	0.135	0.188	0.121
<i>wR</i> ₂ ^b [<i>I</i> _o > 2σ(<i>I</i> _o)]	0.106	0.126	0.258
<i>wR</i> ₂ [all data]	0.115	0.162	0.277

Table 5.10 cont.

Compound	[<i>o</i> -C ₆ H ₄ CH ₂ Se(Me)CH ₂][AlCl ₄]	[AlCl ₃ (MeC(CH ₂ SMe) ₃)]	[AlCl ₂ ([14]aneS ₄)[AlCl ₄]
Formula	C ₉ H ₁₁ AlCl ₄ Se	C ₁₆ H ₃₆ Al ₂ Cl ₆ S ₆	C ₃₀ H ₆₀ Al ₂ Cl ₁₈ S ₁₂
<i>M</i>	366.92	687.47	1605.48
crystal system	monoclinic	monoclinic	monoclinic
Space group	<i>P</i> 2 ₁ / <i>c</i> (no. 14)	<i>P</i> 2 ₁ / <i>c</i> (no. 14)	<i>P</i> 2 ₁ / <i>n</i> (no. 14)
<i>a</i> [Å]	7.4218(19)	16.131(7)	21.849(2)
<i>b</i> [Å]	14.027(3)	8.310(3)	11.869(1)
<i>c</i> [Å]	13.481(3)	24.976(11)	26.054(2)
α [deg]	90	90	90
β [deg]	94.415(6)	107.156(8)	100.82
γ [deg]	90	90	90
<i>U</i> [Å ³]	1399.2(6)	3199(2)	6636.3(9)
<i>Z</i>	4	4	4
μ(Mo Kα) [mm ⁻¹]	3.477	0.991	1.226
total no. reflns	11574	10176	21108
unique reflns	5425	4613	11544
<i>R</i> _{int}	0.031	0.133	0.241
no. of params, restraints	137, 0	279, 0	644, 765
<i>R</i> ₁ ^b [<i>I</i> _o > 2σ(<i>I</i> _o)]	0.058	0.085	0.122
<i>R</i> ₁ [all data]	0.078	0.103	0.305
<i>wR</i> ₂ ^b [<i>I</i> _o > 2σ(<i>I</i> _o)]	0.119	0.193	0.236
<i>wR</i> ₂ [all data]	0.132	0.207	0.335

5.4 References

1. Gurnani, C.; Levason, W.; Ratnani, R.; Reid, G.; Webster, M., *Dalton Trans.* **2008**, 6274-6282.
2. Gurnani, C.; Jura, M.; Levason, W.; Ratnani, R.; Reid, G.; Webster, M., *Dalton Trans.* **2009**, 1611-1619.
3. George, K.; Jura, M.; Levason, W.; Light, M. E.; Ollivere, L. P.; Reid, G., *Inorg. Chem.* **2012**, *51*, 2231-2240.
4. Richards, R. L.; Thompson, A., *J. Chem. Soc. A* **1967**, 1248-1252.
5. Aldridge, S.; Downs, A. J., *The Group 13 Metals Aluminium, Gallium, Indium and Thallium*. Wiley: Chichester, UK, 2011.
6. McBride, W. J.; Sharkey, R. M.; Karacay, H.; D'Souza, C. A.; Rossi, E. A.; Laverman, P.; Chang, C.-H.; Boerman, O. C.; Goldenberg, D. M., *J. Nucl. Med.* **2009**, *50*, 991-998.
7. McBride, W. J.; D'Souza, C. A.; Sharkey, R. M.; Karacay, H.; Rossi, E. A.; Chang, C.-H.; Goldenberg, D. M., *Bioconjugate Chem.* **2010**, *21*, 1331-1340.
8. Ikpo, N.; Flogeras, J. C.; Kerton, F. M., *Dalton Trans.* **2013**, 8998-9006.
9. Balitskii, O. A.; Demchenko, P. Y.; Mijowska, E.; Cendrowski, K., *Mater. Res. Bull.* **2013**, *48*, 916-919.
10. Adams, J. A.; Bostwick, A.; Ohta, T.; Ohuchi, F. S.; Olmstead, M. A., *Phys. Rev. B* **2005**, *71*, 195308-1-195308-8.
11. Lu, C.-Y.; Adams, J. A.; Yu, Q.; Ohta, T.; Olmstead, M. A.; Ohuchi, F. S., *Phys. Rev. B* **2008**, *78*, 075321-1-075321-6.
12. Ren, K.; Rao, F.; Song, Z.; Lv, S.; Cheng, Y.; Wu, L.; Peng, C.; Zhou, X.; Xia, M.; Liu, B.; Feng, S., *Appl. Phys. Lett.* **2012**, *100*, 052105-1-052105-3.
13. Bylikin, S. Y.; Robson, D. A.; Male, N. A. H.; Rees, L. H.; Mountford, P.; Schroder, M., *J. Chem. Soc., Dalton Trans.* **2001**, 170-180.
14. Bossek, U.; Hanke, D.; Wieghardt, K.; Nuber, B., *Polyhedron* **1993**, *12*, 1-5.
15. Shetty, D.; Choi, S. Y.; Jeong, J. M.; Lee, J. Y.; Hoigebazar, L.; Lee, Y.-S.; Lee, D. S.; Chung, J.-K.; Lee, M. C.; Chung, Y. K., *Chem. Commun.* **2011**, *47*, 9732-9734.
16. Atwood, J.; Elgamal, H.; Robinson, G.; Bott, S.; Weeks, J.; Hunter, W., *J. Inclusion Phenom.* **1984**, *2*, 367-376.
17. Atwood, J. L.; Bott, S. G.; May, M. T., *J. Coord. Chem.* **1991**, *23*, 313-320.

18. Self, M. F.; Pennington, W. T.; Laske, J. A.; Robinson, G. H., *Organometallics* **1991**, *10*, 36-38.
19. Robinson, G. H.; Sangokoya, S. A., *Organometallics* **1988**, *7*, 1453-1454.
20. Richey, H. G.; Bergstresser, G. L., *Organometallics* **1988**, *7*, 1459-1465.
21. Robinson, G. H.; Sangokoya, S. A., *J. Am. Chem. Soc.* **1988**, *110*, 1494-1497.
22. Robinson, G. H.; Zhang, H.; Atwood, J. L., *Organometallics* **1987**, *6*, 887-889.
23. Cui, C.; Giesbrecht, G. R.; Schmidt, J. A. R.; Arnold, J., *Inorg. Chim. Acta* **2003**, *351*, 404-408.
24. Atwood, J.; Priester, R.; Rogers, R.; Canada, L., *J. Inclusion Phenom.* **1983**, *1*, 61-69.
25. Zhang, H.; Mitchell Means, C.; Carlene Means, N.; Atwood, J., *J. Cryst. Spectrosc.* **1985**, *15*, 445-452.
26. Robinson, G. H.; Hunter, W. E.; Bott, S. G.; Atwood, J. L., *J. Organomet. Chem.* **1987**, *326*, 9-16.
27. Atwood, J. L.; Hrncir, D. C.; Shakir, R.; Dalton, M. S.; Priester, R. D.; Rogers, R. D., *Organometallics* **1982**, *1*, 1021-1025.
28. Robinson, G.; Bott, S.; Elgamal, H.; Hunter, W.; Atwood, J., *J. Inclusion Phenom.* **1985**, *3*, 65-69.
29. Robinson, G. H.; Rae, A. D.; Campana, C. F.; Byram, S. K., *Organometallics* **1987**, *6*, 1227-1230.
30. Self, M. F.; Pennington, W. T.; Robinson, G. H., *Acta Crystallogr. C* **1991**, *47*, 1309-1310.
31. Robinson, G. H.; Pennington, W. T.; Lee, B.; Self, M. F.; Hrncir, D. C., *Inorg. Chem.* **1991**, *30*, 809-812.
32. Self, M. F.; Pennington, W. T.; Robinson, G. H., *Inorg. Chim. Acta* **1990**, *175*, 151-153.
33. Burford, N.; Royan, B. W.; Spence, R. E. v. H.; Cameron, T. S.; Linden, A.; Rogers, R. D., *J. Chem. Soc., Dalton Trans.* **1990**, 1521-1528.
34. Ebsworth, E. A. V.; Rankin, D. W. H.; Craddock, S., *Structural Methods in Inorganic Chemistry*. Blackwell Scientific: Chichester, UK, 1987.
35. Lewis, J.; Miller, J. R.; Richards, R. L.; Thompson, A., *J. Chem. Soc.* **1965**, 5850-5860.
36. Nakamoto, K., *Infrared and Raman Spectra of Inorganic and Coordination Compounds*. Fourth ed.; Wiley-Interscience: New York, USA, 1986.

37. Cordero, B.; Gomez, V.; Platero-Prats, A. E.; Reves, M.; Echeverria, J.; Cremades, E.; Barragan, F.; Alvarez, S., *Dalton Trans.* **2008**, 2832-2838.
38. George, K.; de Groot, C. H.; Gurnani, C.; Hector, A. L.; Huang, R.; Jura, M.; Levason, W.; Reid, G., *Chem. Mater.* **2013**, *25*, 1829-1836.
39. Mason, J., *Multinuclear NMR*. Plenum Press: New York, USA, 1989.
40. McMurry, J., *Organic Chemistry*. Seventh ed.; Thomson Learning: California, USA, 2008.
41. Minkwitz, R.; Gerhard, V.; Norkat, T., *Z. Naturforsch., B: Chem. Sci.* **1989**, *44*, 1337-1342.
42. Minkwitz, R.; Lohmann, U.; Borrmann, H., *Z. Anorg. Allg. Chem.* **1996**, *622*, 889-894.
43. Mootz, D.; Deeg, A., *Z. Anorg. Allg. Chem.* **1992**, *615*, 109-113.
44. Jura, M.; Levason, W.; Reid, G.; Webster, M., *Dalton Trans.* **2009**, 7610-7612.
45. Olah, G. A.; Demember, J. R.; Mo, Y. K.; Svoboda, J. J.; Schillin, P.; Olah, J. A., *J. Am. Chem. Soc.* **1974**, *96*, 884-892.
46. Olah, G. A.; Prakash, G. K. S.; Marcelli, M.; Lammertsma, K., *J. Phys. Chem.* **1988**, *92*, 878-880.
47. Olah, G. A.; Szilagyi, P. J., *J. Org. Chem.* **1971**, *36*, 1121-1126.
48. Olah, G. A.; O'Brien, D. H.; Pittman, C. U., Jr., *J. Am. Chem. Soc.* **1967**, *89*, 2996-3001.
49. Burdham, R. A.; Ludman, C. J.; Lynch, R. J.; Waddington, T. C., *J. Magn. Reson.* **1979**, *34*, 223-231.
50. Graindourze, M.; Maes, G., *J. Mol. Spectrosc.* **1985**, *114*, 97-104.
51. Maes, G.; Graindourze, M., *J. Mol. Spectrosc.* **1985**, *113*, 410-425.
52. Aucott, S. M.; Milton, H. L.; Robertson, S. D.; Slawin, A. M. Z.; Woollins, J. D., *Heteroat. Chem.* **2004**, *15*, 530-542.
53. Cui, H.; Okano, Y.; Zhou, B.; Kobayashi, A.; Kobayashi, H., *J. Am. Chem. Soc.* **2008**, *130*, 3738-3739.
54. Fujiwara, E.; Fujiwara, H.; Narymbetov, B. Z.; Kobayashi, H.; Nakata, M.; Torii, H.; Kobayashi, A.; Takimiya, K.; Otsubo, T.; Ogura, F., *Eur. J. Inorg. Chem.* **2005**, *2005*, 3435-3449.
55. Sandman, D. J.; Stark, J. C.; Foxman, B. M., *Organometallics* **1982**, *1*, 739-742.
56. Lakshmikantham, M. V.; Cava, M. P.; Gunther, W. H. H.; Nugara, P. N.; Belmore, K. A.; Atwood, J. L.; Craig, P., *J. Am. Chem. Soc.* **1993**, *115*, 885-887.

57. Mundt, O.; Becker, G.; Baumgarten, J.; Riffel, H.; Simon, A., *Z. Anorg. Allg. Chem.* **2006**, *632*, 1687-1709.
58. Poleschner, H.; Seppelt, K., *Angew. Chem. Int. Ed.* **2008**, *47*, 6461-6464.
59. Reid, S. D.; Hector, A. L.; Levason, W.; Reid, G.; Waller, B. J.; Webster, M., *Dalton Trans.* **2007**, 4769-4777.
60. Levason, W.; Nirwan, M.; Ratnani, R.; Reid, G.; Tsoureas, N.; Webster, M., *Dalton Trans.* **2007**, 439-448.
61. Barton, A. J.; Hill, N. J.; Levason, W.; Reid, G., *J. Chem. Soc., Dalton Trans.* **2001**, 1621-1627.
62. Brodersen, K.; Rölz, W.; Jordan, G.; Gerbeth, R.; Ellermann, J., *Chem. Ber.* **1978**, *111*, 132-142.
63. Beattie, I. R.; Jones, P. J.; Howard, J. A. K.; Smart, L. E.; Gilmore, C. J.; Akitt, J. W., *J. Chem. Soc., Dalton Trans.* **1979**, 528-535.

6 Chemical Vapour Deposition of Gallium Arsenide and Gallium Phosphide Thin Films

6.1 Introduction

Gallium phosphide and gallium arsenide are materials that are widely used in the optoelectronics industry due to their semiconducting properties (see 1.1). The aims of this chapter are to investigate the use of $[\text{}^n\text{Bu}_2\text{Ga}(\mu\text{-E}^t\text{Bu}_2)_2\text{Ga}^n\text{Bu}_2]$ (E = P, As) (Figure 6.1) as a single source precursor for the LPCVD of GaP and GaAs. These precursors were first synthesised by Cowley *et al.*³ This continues work previously undertaken within the group that explored the use of $[\text{}^n\text{Bu}_2\text{M}(\mu\text{-E}^t\text{Bu}_2)_2\text{M}^n\text{Bu}_2]$ (M = Ga, In; E = P, As) as single source precursors for the supercritical chemical fluid deposition of III-V materials^{1,2} (6.1.2) in order to compare their properties as single source precursors for chemical vapour deposition. The thin films will then be characterised by XRD, EDX, SEM, XPS and Raman spectroscopy and photoluminescence to determine the film quality. Although these precursors have previously been used for LPCVD, the CVD rig that is being used is less complex and the characterisation of the thin films will be more extensive. $[\text{Ga}(\text{P}^t\text{Bu}_2)_3]$, which is a known compound, is also investigated as a novel single source LPCVD precursor.

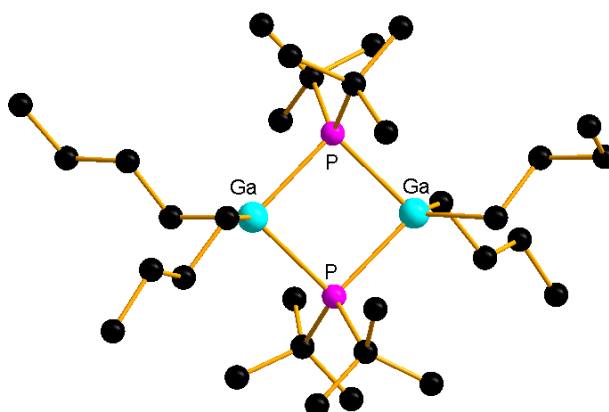


Figure 6.1 – Structure of $[\text{}^n\text{Bu}_2\text{Ga}(\mu\text{-P}^t\text{Bu}_2)_2\text{Ga}^n\text{Bu}_2]$. The other dimeric precursors discussed in this chapter adopt the same structure.

6.1.1 LPCVD of III-V materials using single source precursors

The industrial synthetic route to III-V thin films is a dual source route involving the use of separate Group 13 and 15 precursors, either elemental or molecular. The most commonly used route in industry involves reacting a Group 13 trialkyl (e.g. GaMe₃) with a Group 15 hydride (e.g. PH₃ or AsH₃). These reagents produce films with very low levels of carbon contamination due to the large quantity of active atomic hydrogen produced in the pyrolysis of the Group 15 hydride.⁴ Although this route is very effective, the precursors used are highly toxic and pyrophoric. There has therefore been a considerable interest in using safer precursors, such as Et₂AsH or ^tBuAsH₂ in place of AsH₃, or developing single source precursors. Single source precursors have been shown to be safer to handle but due to the quality of the films produced they have not yet made a significant impact in the industrial growth of III-V films.⁵ Although single source precursors are unlikely to be widely used in industry, they have been shown to be useful for certain applications, for example depositions in confined spaces such as nanopores, the formation of quantum dots and the growth of nanowires, as described below.⁶⁻¹⁰

Initial attempts to develop single source precursors for III-V materials began in the 1980s when Maury and Constant used adducts of the formulae [ClR₂Ga(ER'₃)] (E = P, As; R and R' = Me, Et).¹¹⁻¹³ By utilising Et₂PH during the MOCVD of [ClEt₂Ga(AsEt₃)] they were also able to produce the ternary system GaAs_{1-x}P_x (0 < x < 0.6).¹⁴ Epitaxial GaAs has been grown from [R₂ClGa(AsEt₃)] (R = Me, Et)¹⁵ and [{Et₂ClGa(AsEt₂)}₂CH₂]¹². [(C₆F₅)Me₂Ga(AsEt₃)] has also been successfully used to deposit GaAs¹² and compounds of the formula [(C₆F₅)_{3-x}Me_xGa(AsEt₃)] (x = 0 or 2) were investigated to see if using electron withdrawing substituents such as C₆F₅ would alter the strength of the Ga-As bond and hence affect the CVD properties of the precursor.^{16, 17}

Precursors with covalent M-P bonds, including [Et₂MPEt₂]₃ (M = Ga, In), cyclic trimeric molecules¹⁸ and [(Me₃SiCH₂)₂MPPh₂] (M = Ga, In) and [(Me₃CCH₂)₂InPPh₂]¹⁹ have been successfully used to deposit thin films of GaP and InP. Coates and Beachley

were among the first to synthesise single source precursors for III-V materials with covalent M-E bonds by utilising the reaction of Me_3M ($\text{M} = \text{Al}, \text{Ga}, \text{In}$) with Ph_2EH ($\text{E} = \text{P}, \text{As}$) to form complexes of the type $[(\text{Me}_2\text{M}(\mu\text{-EPh}_2)_n)]_2$.²⁰ Wells and co-workers also developed the use of single source precursors with covalent M-E bonds, synthesising complexes with the formulae $[\text{GaBr}\{\mu\text{-As}(\text{Me}_3\text{SiCH}_2)_2\}_2]_2$;²¹ $[\text{GaBr}_2\{\mu\text{-As}(\text{Me}_3\text{SiCH}_2)_2\}_3]$, a complex with a six membered gallium-arsenic ring;²² and $[\text{Ph}_2\text{Ga}\{\mu\text{-As}(\text{SiMe}_3)_2\}_2\text{Ga}(\text{Ph})_2(\mu\text{-X})]$ ($\text{X} = \text{Cl}, \text{Br}$) which has mixed halogen and arsenic bridging.^{23, 24} They also developed the nanoparticulate precursors $[\text{X}_2\text{Ga}\{\mu\text{-P}(\text{SiMe}_3)_2\}_2]$ ($\text{X} = \text{Cl}, \text{Br}, \text{I}$) and $[(\text{Cl}_3\text{Ga}_2\text{P})_n]$, which decompose at low temperatures (300 – 320 °C) under vacuum^{25, 26} as well as $[\text{H}_2\text{Ga}\{\mu\text{-E}(\text{SiMe}_3)_2\}_3]$ ($\text{E} = \text{P}, \text{As}$), which gives nanoparticles of GaP and GaAs approximately 5 nm in diameter after thermolysis in xylene at 450 °C.²⁷ Other single source precursors for MAs nanoparticles ($\text{M} = \text{Ga}, \text{In}$), include $[\text{GaMe}_2(\mu\text{-As}^t\text{Bu}_2)]_2$ and $[\text{InEt}_2(\mu\text{-As}^t\text{Bu}_2)]_2$, which are grown in hexadecylamine at 120 °C and 280 °C, respectively.^{28, 29} The GaAs nanoparticles were approximately 3.2 nm in diameter whereas the InAs nanoparticles were approximately 8.8 nm in diameter.

Cowley and co-workers have significantly developed single source precursors with covalent M-E bonds for the chemical vapour deposition (CVD) of III-V semiconductors. The dimeric precursor $[\text{Me}_2\text{Ga}(\mu\text{-}^t\text{Bu}_2\text{As})]_2$, with H_2 as a carrier gas, produced good quality films of GaAs with carbon contamination less than 1000 ppm, as measured by XPS.³⁰ The sample also exhibited band gap photoluminescence, but the authors concluded that the quality of the film deposited was insufficient for device work due to the limitations of the apparatus. Trimeric single source precursors such as $[\text{Me}_2\text{Ga}(\mu\text{-As}^i\text{Pr}_2)]_3$ were also investigated but have not been used successfully to deposit thin films of GaAs due to facile elimination of the tetraalkyldiarsine.³¹ $[\text{Ga}(\text{As}^t\text{Bu}_2)_3]$ has been used to deposit good quality GaAs films, which Cowley stated were “the best we have obtained so far” owing to the very low levels of carbon contamination and “modest” (480 °C at 6×10^{-5} Torr) reactor conditions.^{31, 32} There has also been work done on developing precursors for the deposition of GaP but the literature provides limited discussion of their growth by CVD.^{3, 33-35} The thermal decomposition of $[\text{Bu}_2\text{Ga}(\mu\text{-PH}_2)]_3$ was investigated to show that it was possible to deposit GaP at lower temperatures than previously achieved (248 °C) but the conditions

were not optimised and the carbon content was found to be approximately 10%.³⁴

Cowley and co-workers have also developed single source precursors for other III-V materials including [ⁱBuAl(μ_3 -PSiPh₃)₄]₄ for the deposition of AlP,³⁶ [Et₂Ga(μ -NH₂)₃]₃ for GaN,³⁷⁻³⁹ [ⁱPr(ⁱPr₂P)In(μ -PⁱPr₂)₂]₂ for InP^{35, 40} and [Me₂In(μ -Sb^tBu₂)₃]₃ for InSb⁴¹.

6.1.2 Supercritical chemical fluid deposition

Supercritical fluids have several unique properties that make them suited to the deposition of materials into nanostructured templates, including their zero surface tension, gas-like mass transport rates and ability to act like a solvent, enabling them to easily fill nanopores. Transport of the precursor also eliminates the volatility concerns that occur in some CVD techniques.^{42, 43} This technique has been used successfully to deposit a range of metals, including Cu, Ni, Pt, Pd, Au, Rh, Ru, Co and Ir.⁴⁴⁻⁴⁶ There has also been significant work on the deposition of metal oxide thin films, particularly of dielectric materials such as ZrO₂, HfO₂ and MnO₂ using SCFD.^{47, 48} Very little work, however, has been done on the supercritical chemical fluid deposition (SCFD) of compound semiconductors. Bulk GaN has been deposited on seed crystals using an ammonothermal method. This method is only suited to the deposition of nitride semiconductors due to the harsh nature of the supercritical ammonia. Thin films of InP have been deposited by dual source SCFD, using PPh₃ and In[(C₆H₄)CH₂N(CH₃)₂]₃ in CO₂, C₂F₆ and Xe.⁴⁹ High quality films of CdS, as evidenced by strong, narrow line-width bandedge photoluminescence, have been deposited using a single source precursor.⁵⁰ These films exhibited optoelectronic properties comparable to that of single crystal CdS.

Previous work in the Southampton group has investigated the use of [ⁿBu₂M(μ -E^tBu₂)₂MⁿBu₂]₃ (M = Ga, In; E = P, As) as single source precursors for supercritical chemical fluid deposition (SCFD) of thin films.^{1, 2} These compounds were chosen as promising precursors for SCFD as the long alkyl chains are likely to impart good solubility in (low dielectric constant) supercritical CO₂. Using a homogeneous hexane/CO₂ fluid led to the successful deposition of thick mats of InP and InAs nanowires at 512 K and 4.4 MPa. The InP nanowires obtained were single crystalline

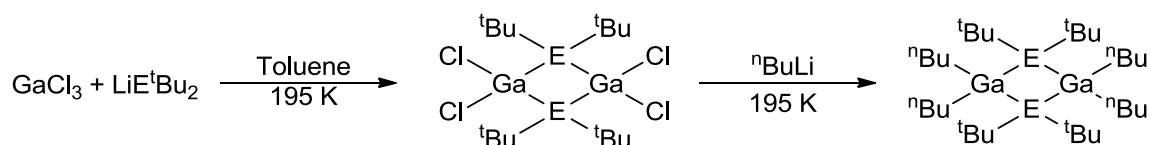
and exhibited band-edge luminescence, along with the underlying InP films. Carbon contamination of the films was reduced by using sc-CHF₃ as a carrier at 773 K and 4 MPa. As part of this work [ⁿBu₂In(μ-E'Bu₂)₂InⁿBu₂] was also investigated as a precursor for the LPCVD (0.05 mmHg) of InP and InAs. Cubic InP was obtained at 723 – 873 K but films deposited at 723 and 773 K had significant amounts of indium metal, as shown by XRD and WDX analysis. Cubic InAs was obtained at 723 and 773 K with no contamination from In metal. The films, however, were powdery and poorly adhered.

Attempts to deposit GaP and GaAs under similar SCFD conditions (773 K, 12 MPa) using [ⁿBu₂Ga(μ-E'Bu₂)₂GaⁿBu₂] (E = P, As) were not as successful and produced amorphous films with high levels of carbon contamination.² The Ga:P ratios were highly variable and no As was detected by EDX from the deposits obtained from the arsenide reagent. These depositions were probably less successful due to the higher reactivity of Ga relative to In in the supercritical fluid, which caused solvent degradation, producing the high levels of carbon contamination.

6.2 Results and discussion

6.2.1 Dimeric [${}^n\text{Bu}_2\text{Ga}(\mu\text{-E}^t\text{Bu}_2)_2\text{Ga}{}^n\text{Bu}_2$] precursors

The [${}^n\text{Bu}_2\text{Ga}(\mu\text{-E}^t\text{Bu}_2)_2\text{Ga}{}^n\text{Bu}_2$] precursors were synthesised by Dr Fei Cheng using a method described by Cowley and co-workers³ (Scheme 6.1) to give air sensitive white powders. This method avoids the direct use of alkyl gallium reagents, which are highly pyrophoric, in favour of alkylating reagents such as ${}^n\text{BuLi}$, which are arguably easier to handle. The precursors could be easily synthesised on a scale of several grams and were stable over a period of years if stored in a dry, N_2 filled glove box. To check that decomposition or oxidation had not occurred, purity was ascertained by ${}^1\text{H}$ NMR and ${}^{31}\text{P}\{{}^1\text{H}\}$ NMR ($\text{E} = \text{P}$) spectroscopy (δ 32.9).



Scheme 6.1 – Synthesis of [${}^n\text{Bu}_2\text{Ga}(\mu\text{-E}^t\text{Bu}_2)_2\text{Ga}{}^n\text{Bu}_2$] ($\text{E} = \text{P}, \text{As}$) as reported by Cowley and co-workers³

LPCVD of [${}^n\text{Bu}_2\text{Ga}(\mu\text{-E}^t\text{Bu}_2)_2\text{Ga}{}^n\text{Bu}_2$] at 673 – 823 K led to the deposition of shiny silvery films ($\text{E} = \text{As}$) or shiny yellow films ($\text{E} = \text{P}$) with good coverage over several silica tiles. This temperature range was chosen as it had been effective for previous LPCVD experiments using [${}^n\text{Bu}_2\text{In}(\mu\text{-E}^t\text{Bu}_2)_2\text{In}{}^n\text{Bu}_2$].² The experiments were highly reproducible and each deposition produced films that were visually very similar and characterisation data obtained were comparable. The majority of depositions were done at 773 K and most of the characterisation data discussed herein will focus on samples deposited at this temperature as representative of the films obtained.

XRD measurements on the materials deposited from [${}^n\text{Bu}_2\text{Ga}(\mu\text{-E}^t\text{Bu}_2)_2\text{Ga}{}^n\text{Bu}_2$] at 773 K confirmed them to be cubic GaP ($a = 5.465(4) - 5.503(9)$ Å) (Figure 6.2) and cubic GaAs ($a = 5.465(4) - 5.496(5)$ Å) (Figure 6.3) respectively (literature values for bulk

GaP and GaAs are $5.358 - 5.473 \text{ \AA}$ and $5.508 - 5.750 \text{ \AA}$)⁵¹, with no evidence of other phases. There is no significant variation with deposition temperature (Figure 6.4) and no evidence from the X-ray diffraction patterns or peak intensities for preferred orientation of the crystallites.

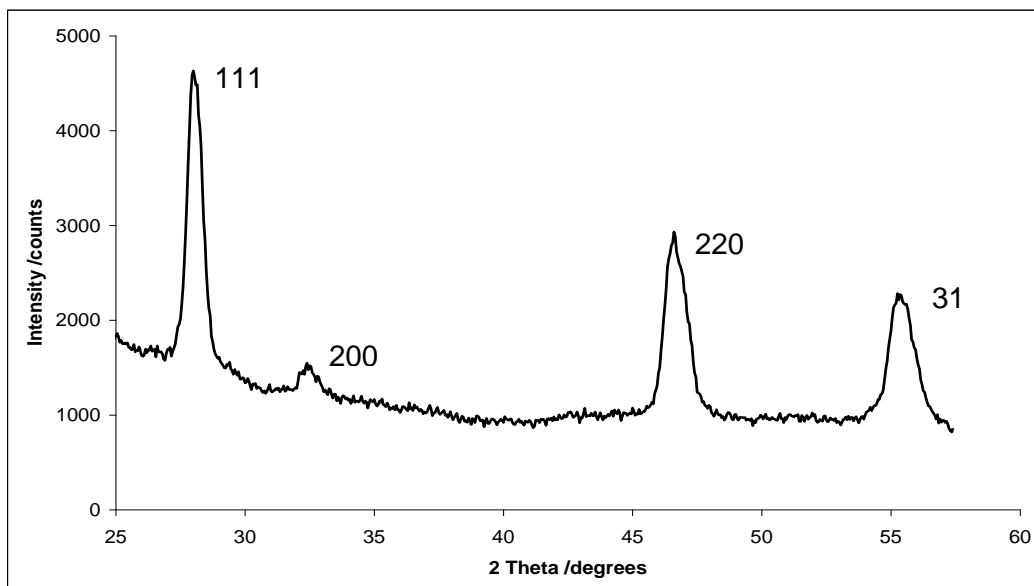


Figure 6.2 - XRD pattern obtained from a GaP thin film grown on silica at 773 K by LPCVD from [${}^n\text{Bu}_2\text{Ga}(\mu\text{-P}^t\text{Bu}_2)_2\text{Ga}{}^n\text{Bu}_2$]

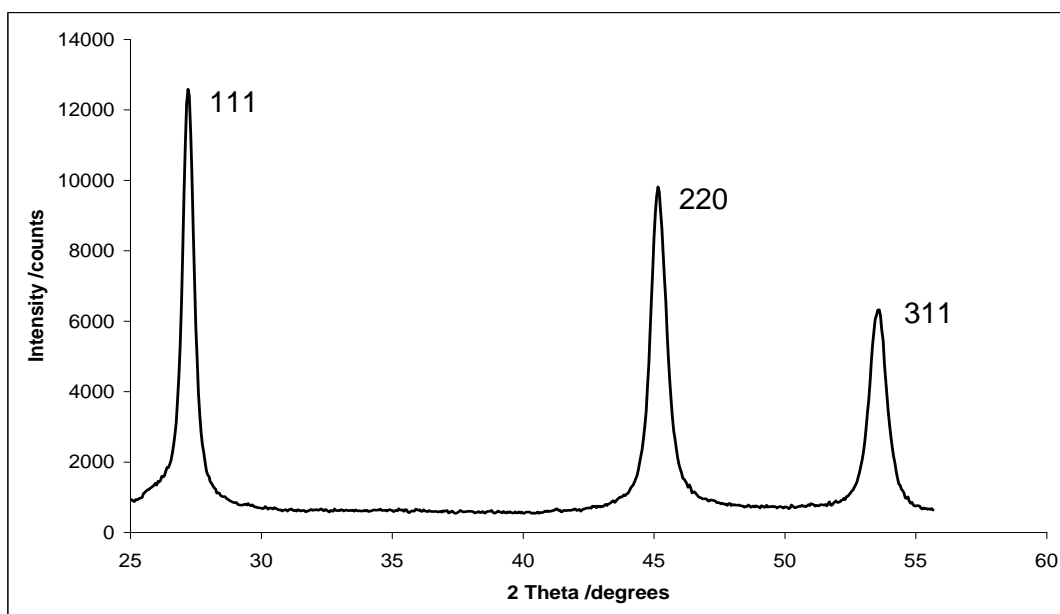


Figure 6.3 - XRD pattern obtained from a GaAs thin film grown on silica at 773 K by LPCVD from [${}^n\text{Bu}_2\text{Ga}(\mu\text{-As}^t\text{Bu}_2)_2\text{Ga}{}^n\text{Bu}_2$]

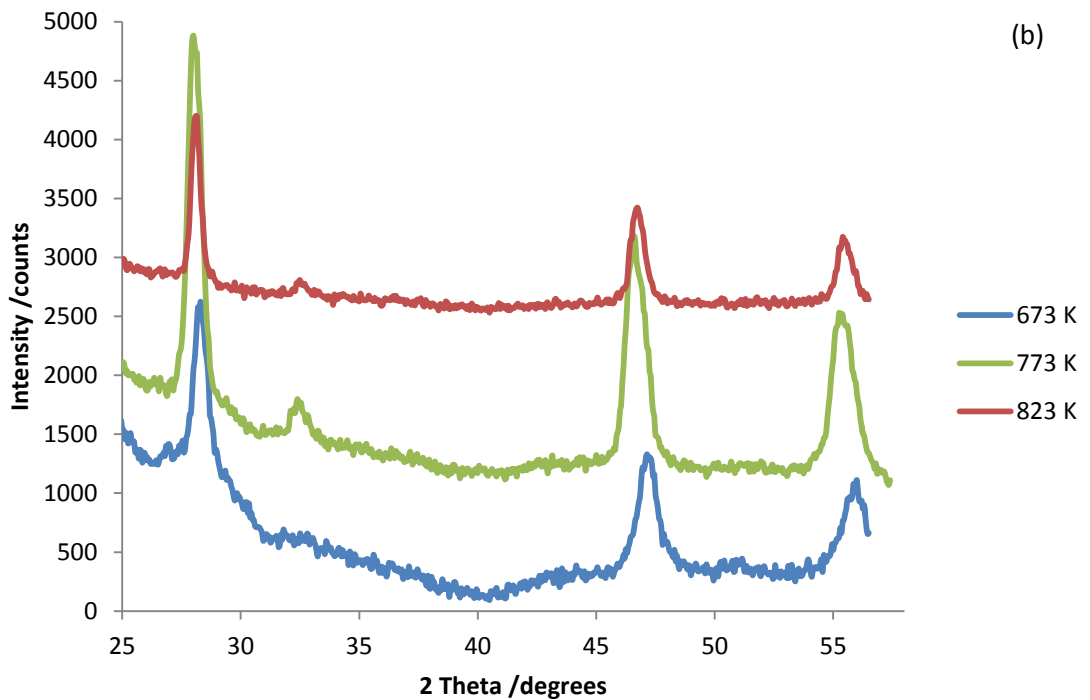
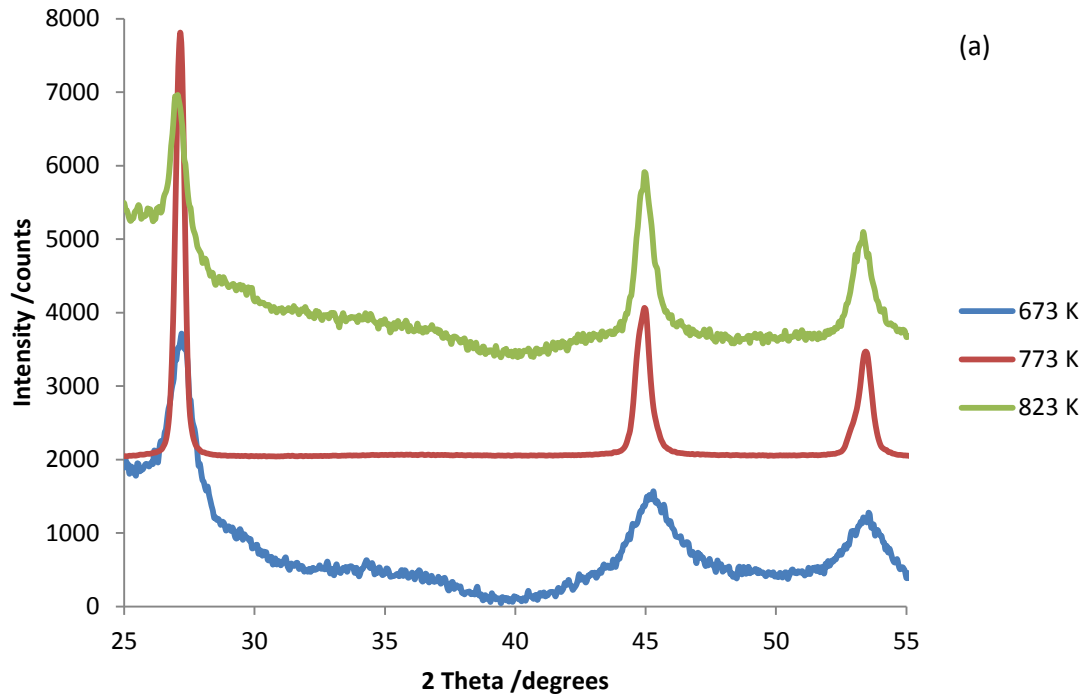


Figure 6.4 - XRD patterns from GaAs thin films (a) deposited from $[{}^n\text{Bu}_2\text{Ga}(\mu\text{-As}^t\text{Bu}_2)_2\text{Ga}^n\text{Bu}_2]$ at 673, 773 and 823 K and GaP thin films (b) deposited from $[{}^n\text{Bu}_2\text{Ga}(\mu\text{-P}^t\text{Bu}_2)_2\text{Ga}^n\text{Bu}_2]$ at 673, 773 and 823 K

Raman spectra recorded by John Nesbitt from the same thin film samples each show two bands (Figure 6.5), GaP at 367 and 402 cm^{-1} and GaAs at 270 and 291 cm^{-1} , which are entirely in agreement with literature values for the transverse optical (TO) and longitudinal optical (LO) phonons in each material respectively.^{52,53} Raman measurements taken at several locations on the sample showed variations in the relative amplitudes of the TO and LO peaks, as well as small shifts in the peak frequencies, which are due to the microcrystallinity of the sample.

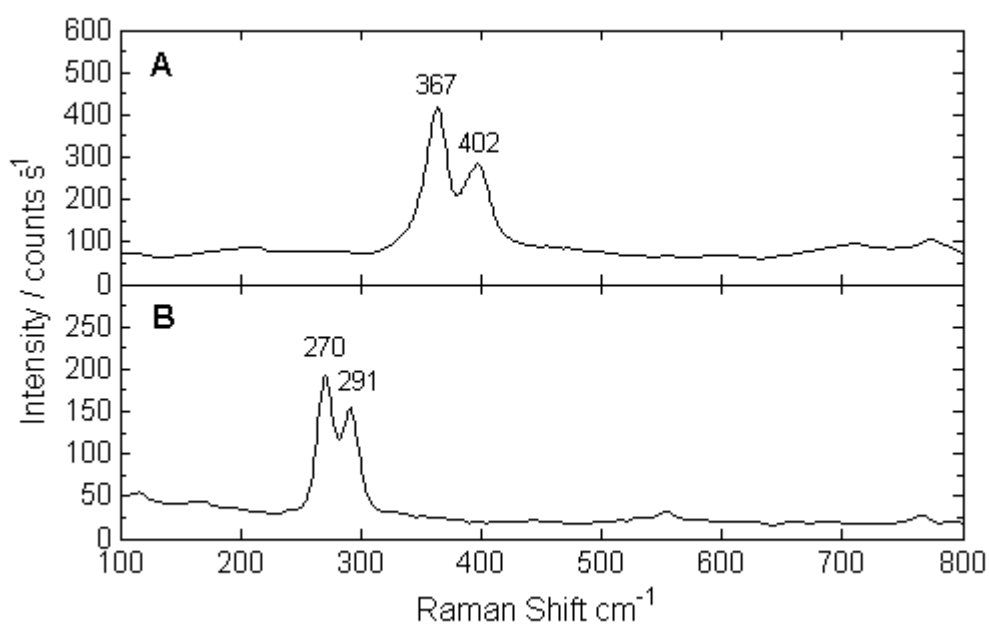


Figure 6.5 - Raman spectra of GaP (A) and GaAs (B) thin films grown by LPCVD at 773 K from [${}^n\text{Bu}_2\text{Ga}(\mu\text{-E}^i\text{Bu}_2)_2\text{Ga}{}^n\text{Bu}_2$]

SEM analysis on the more reflective GaP films showed a regular morphology formed of a dense mat of columnar nano-rods with growth direction approximately perpendicular to the substrate surface (Figure 6.6), which would suggest preferred orientation but this is not evident in the XRD spectra of these samples. Typical GaP films grown at 773 K using 100 mg of precursor were $\sim 1 \mu\text{m}$ thick. The GaAs film morphology was much denser and smoother than the GaP film morphology (Figure 6.6).

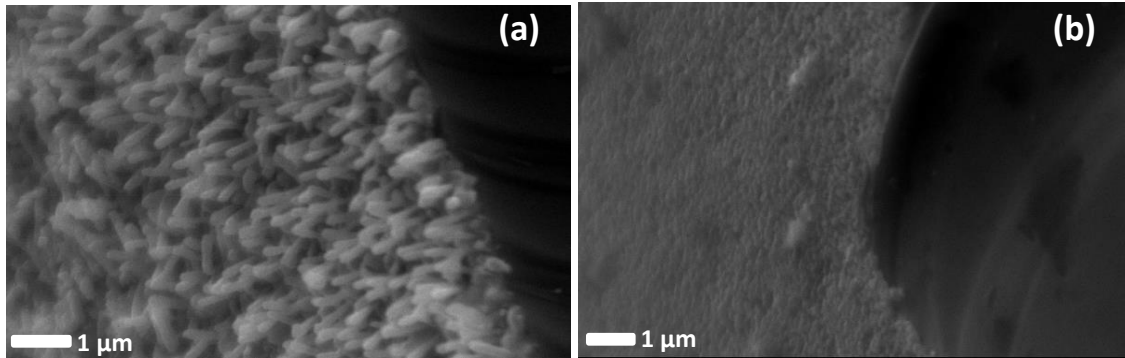


Figure 6.6 - SEM cross-section images of (a) GaP and (b) GaAs films deposited on silica at 773 K by LPCVD from [${}^n\text{Bu}_2\text{Ga}(\mu\text{-E}^t\text{Bu}_2)_2\text{Ga}^n\text{Bu}_2$]. Tiles were fractured through the films and the darker regions on the right hand side of the images are the fractured tile edge.

AFM measurements (Figures 6.7 and 6.8) were consistent with the SEM data, revealing that the GaP film surfaces are considerably rougher than the GaAs films produced under the same experimental conditions (GaAs rms roughness = 8.0 nm (2 x 2 micron scan)). The needle-like morphology of the GaP surface precluded accurate determination of its rms roughness.

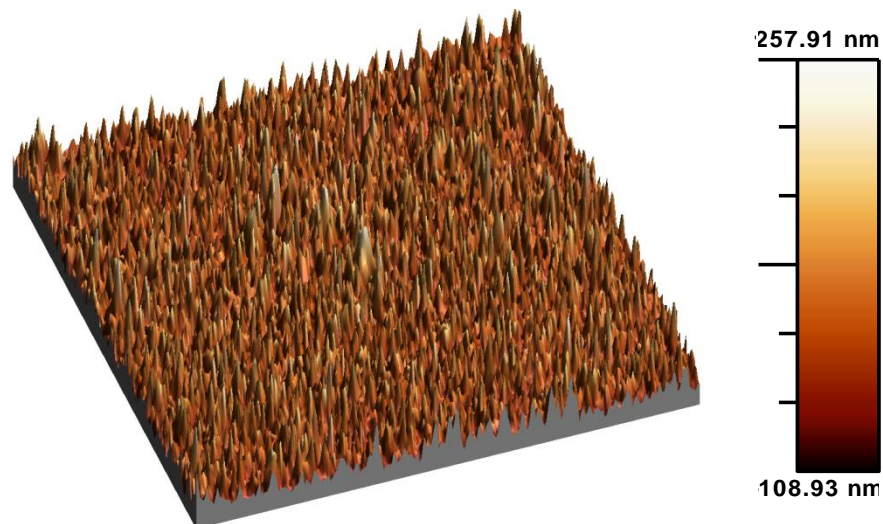


Figure 6.7 - 3D AFM image (20 μm x 20 μm) of a GaP film grown at 773 K

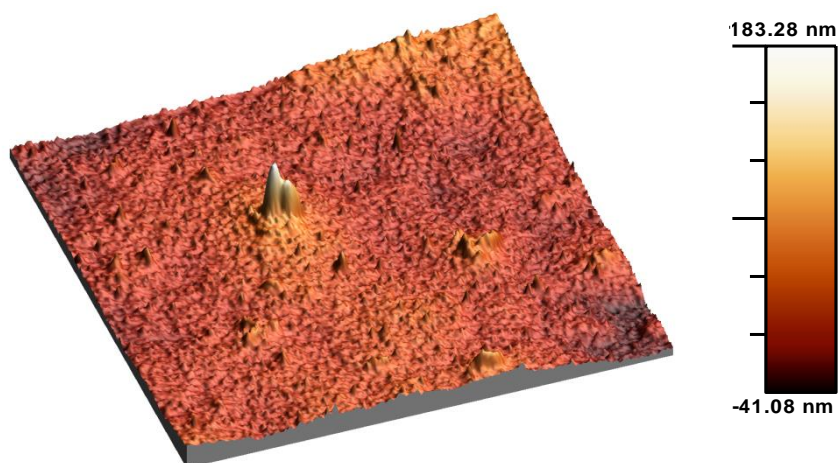


Figure 6.8 - 3D AFM image (20 μm x 20 μm) of a GaAs film grown at 773 K

The elemental composition of these deposited materials was probed by EDX analysis which showed Ga:P and Ga:As ratios closest to 1:1.0 for samples deposited at higher temperatures (773 and 823 K; Table 6.1). XPS measurements on unetched films showed P- or As-deficient compositions. Only one Ga and one P or As environment was observed in these GaE films. For GaAs both O (15.9 Wt%) and C (4.6 Wt%) were also evident. With the expectation that the presence of oxygen and the pnictogen deficiency were due to reactions of the surface with air, the samples were Ar ion etched. This resulted in significant reductions in the oxygen and carbon signals (to 10% and 1.8 wt% respectively). The rod-like morphology of the GaP samples is likely to lead to inherently higher C and O levels pre-etching, as observed, and this also precluded effective etching of the whole of their surfaces, hence reliable %C and %O determinations from the GaP samples were not possible by XPS.

Temperature /K	Ga:As ratio	Temperature /K	Ga:P ratio
623	1:1.16	723	1:1.15
723	1:1.12	773	1:0.98
773	1:0.99	823	1:1.00
823	1:0.99		

Table 6.1 - EDX data for GaE films deposited by LPCVD from [$^n\text{Bu}_2\text{Ga}(\mu\text{-E}^t\text{Bu}_2)_2\text{Ga}^n\text{Bu}_2$] (E = P or As) prior to surface etching

In order to probe the electronic quality of the films, photoluminescence measurements were also undertaken on a number of the GaP and GaAs thin film samples by John Nesbitt. The GaP samples gave photoluminescence whose magnitude and form was comparable with that from a single crystalline sample (99.99%, Aldrich) (Figure 6.9), suggesting that the deposited material has good electronic quality. However the GaAs samples gave no measurable luminescence. As the film stoichiometry is 1:1 and low levels of impurities were detected it is unlikely to be due to poor film quality. One probable explanation for this is that the GaAs is formed from nano-crystallites whose surfaces act as non-radiative recombination sites. For this reason the photoluminescence measurements were repeated with samples which had been freshly etched with 12 mol dm^{-3} HCl (for GaAs) or 12 mol dm^{-3} H₂SO₄ (for GaP) for 6 s and 10 s respectively, to try and remove the non-radiative recombination sites.^{54, 55} The etching had little effect for the GaP samples and references. In the case of GaAs the etching increased the intensity of the luminescence from the single crystal reference by approximately a factor of six, however the deposited GaAs samples still produced no luminescence. Whilst this may indicate these samples consist of defective GaAs, it is also possible that the dense nature of the films means that the etchant was unable to reach most of the crystallite interfaces.

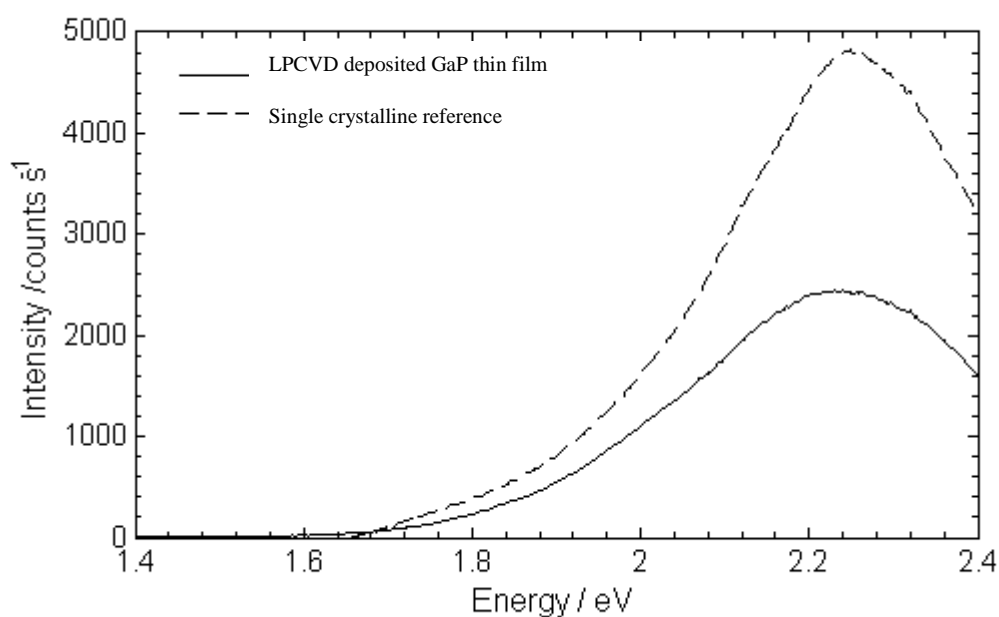


Figure 6.9 - Luminescence spectrum of GaP film grown at 773 K by LPCVD from [ⁿBu₂Ga(μ-P^tBu₂)₂GaⁿBu₂] compared to a single crystal reference sample

As it was not possible to obtain information about the band gap of the deposited GaAs films from photoluminescence spectroscopy, an optical transmission measurement was carried out, which can also provide information about the band gap. The optical transmission measurement from a shiny GaAs film is presented in Figure 6.10. Whilst a precise determination of the onset of absorption in the film is difficult, the onset has certainly occurred by 1.46 eV; the accepted band gap of bulk GaAs. This suggests there may be sub-band gap absorption which would agree with the conclusion from the photoluminescence measurements that the GaAs films are not of high optical quality. The GaP films are scatterry and so for these films absorbance measurements were performed using an integrating sphere based system. The result from these measurements is shown in Figure 6.11. Whilst these measurements do not show a clear onset of absorption at 2.27 eV, the GaP direct band gap E_g , there is a clear feature at approximately 2.78 eV, the GaP zone centre band gap E_o .⁵⁶ This, combined with the PL measurements which show emission at E_o , strongly indicate that the optical properties of these films are in agreement with the accepted band structure of GaP.⁵⁶

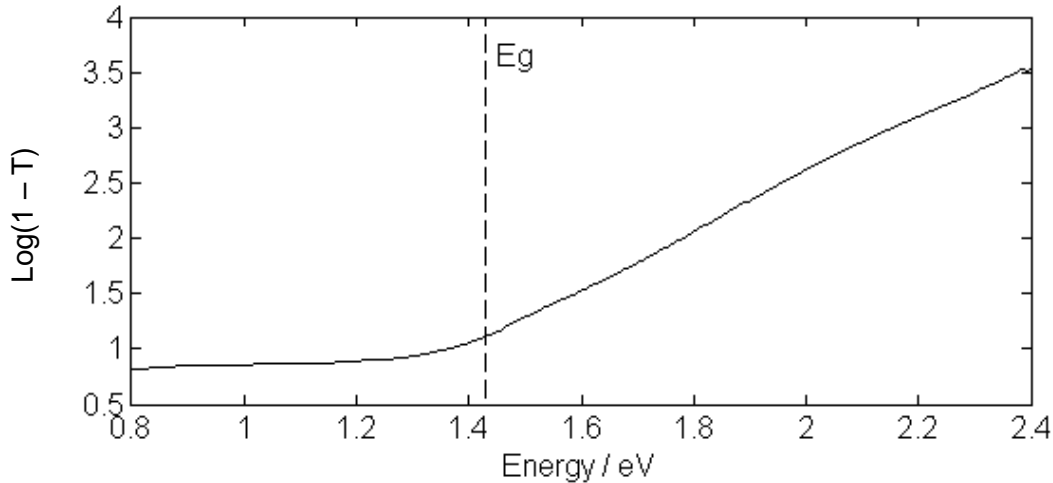


Figure 6.10 - Transmission spectrum of GaAs film grown at 773 K

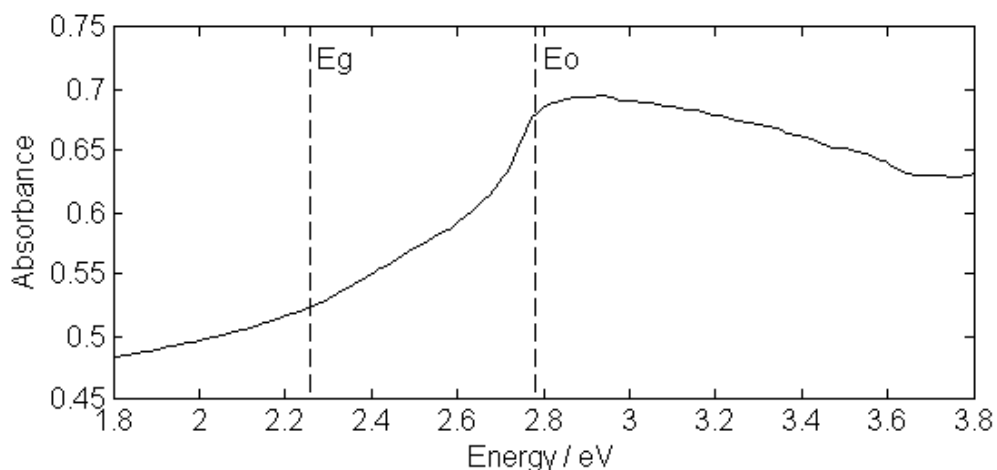


Figure 6.11 – Diffuse reflectance spectrum of GaP film grown at 773 K

6.2.2 [Ga(P^tBu₂)₃] precursor

[Ga(P^tBu₂)₃] (Figure 6.11) was also synthesised and investigated as a potential precursor for the deposition of GaP thin films as the higher P:Ga ratio should reduce the likelihood of depositing phosphorus deficient films. Although the films deposited using [PⁿBu₂Ga(μ-P^tBu₂)₂GaⁿBu₂] were not phosphorus deficient, this has been a reported problem encountered in the CVD of GaP thin films.^{30, 35} This precursor had previously been used with some success to make GaP nanoparticles.⁶ These nanoparticles were synthesised by dissolving [Ga(P^tBu₂)₃] in 4-ethylpyridine, slowly heating to 167 °C and leaving for up to one week. The particles were isolated by centrifuging and precipitation from light petroleum (40-60). This work concluded that the nanocrystals obtained were poorly crystalline and polydispersed, so this technique requires further optimisation in order to achieve the monodispersed, single crystal nanoparticles desired. A similar method was employed using [In(P^tBu₂)₃] to produce monodispersed quantum dots of InP with an average diameter of 7.24 ± 1.24 nm.⁹ In this case the precursor was also heated to 167 °C in 4-ethylpyridine but for a shorter period of time (30 minutes).

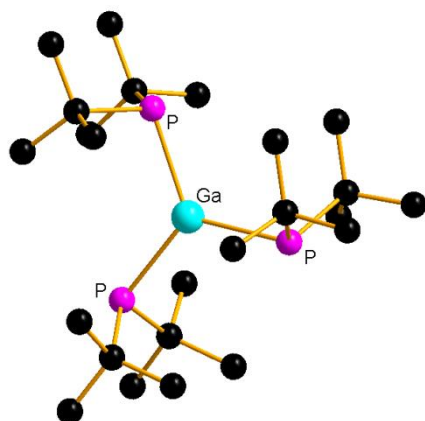
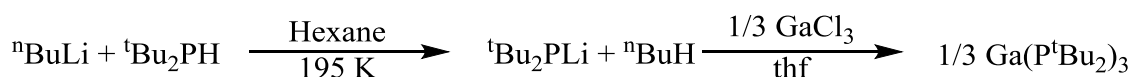


Figure 6.12 – Structure of [Ga(P^tBu₂)₃]

[Ga(P^tBu₂)₃] was synthesised *via* the route shown in Scheme 6.2, which has previously been reported by Cowley and co-workers,³ to yield an extremely air and moisture sensitive red crystalline solid, which required very careful handling. Despite several attempts, it was not possible to determine the purity of the sample by ³¹P{¹H} NMR spectroscopy prior to using it for CVD, as an NMR sample prepared in anhydrous C₆D₆ in a glovebox under N₂ had completely oxidised and decolourised within the NMR tube within minutes of the sealed sample being removed from the glove box.



Scheme 6.2 – Synthesis of [Ga(P^tBu₂)₃] as reported by Cowley and co-workers³

The LPCVD of [Ga(P^tBu₂)₃] was performed under similar conditions to that of [ⁿBu₂Ga(E^tBu₂)₂GaⁿBu₂]. The colour of the precursor was checked to ensure that it had not oxidised (a change from red to white) prior to each CVD experiment commencing. The experiments were carried out at 773 K and 0.05 mmHg onto silica substrates. Thin, shiny yellow films were deposited on the slides closest to the precursor and a significant amount of yellow powder remained where the precursor had been positioned in the tube. The films were found to be crystalline GaP by XRD (Figure 6.12) and EDX analysis

showed Ga:P ratios of 1:1.0. There was some minor variation in composition across the tiles ($< \pm 0.1$ in the ratio of Ga:P by EDX). XRD and EDX analysis on the yellow powder showed it to consist mostly of GaP with some contamination from GaPO_4 and other impurities. It was therefore concluded that as the majority of the precursor did not sublime and diffuse through the tube, the sublimation and decomposition temperature of the precursor are similar. Although the films obtained were of good quality, the coverage was poor compared to films deposited using $[\text{}^n\text{Bu}_2\text{Ga}(\mu\text{-P}^t\text{Bu}_2)_2\text{Ga}^n\text{Bu}_2]$ as a precursor. The poor volatility of the precursor, combined with its extreme sensitivity, makes it unsuitable for further investigation as a precursor for LPCVD.

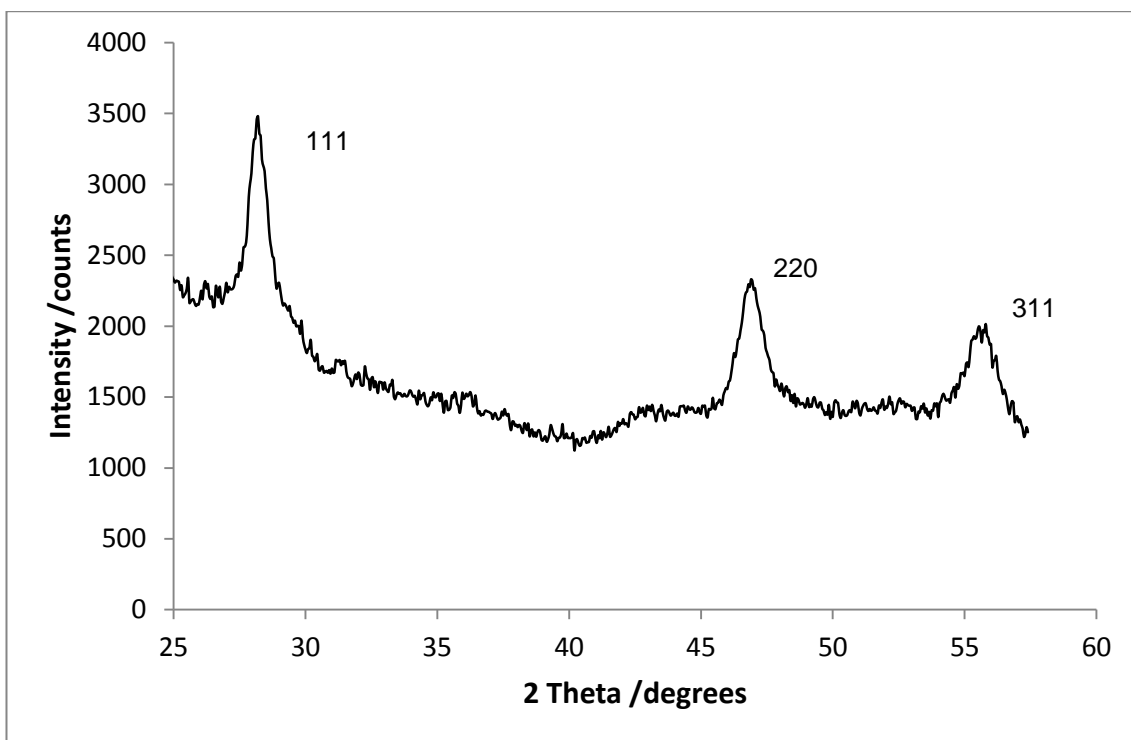


Figure 6.13 - XRD pattern from GaP film deposited from $\text{Ga}(\text{P}^t\text{Bu}_2)_3$ at 773 K

6.2.3 Conclusions

This work has shown that $[\text{}^n\text{Bu}_2\text{Ga}(\text{E}^t\text{Bu}_2)_2\text{Ga}^n\text{Bu}_2]$ are very promising precursors for the deposition of GaE, giving good quality, crystalline thin films with low %C and %O

with excellent reproducibility. These compounds have been shown to be better LPCVD precursors than the analogous In compounds. The deposition conditions used and the film quality obtained are comparable with other, good quality reported single source precursors.³⁰ The precursors are also easier handle than traditional dual source precursors. $[\text{Ga}(\text{P}^t\text{Bu}_2)_3]$, however, was shown to be a poor precursor for the LPCVD of GaP due to its low volatility, although it does decompose to give GaP.

6.3 Experimental

LPCVD of [ⁿBu₂Ga(E^tBu₂)₂GaⁿBu₂] (E = P, As)

In a typical experiment 0.100 g of reagent and silica substrates were loaded into a quartz tube in a glove-box. The tube was then set in a furnace and evacuated, then heated to achieve deposition at 773 K under 0.05 mmHg (66 Pa). The sublimation temperature of the reagents was approximately 573 K. Upon completion of the deposition experiment, the tube was cooled to room temperature and transferred to the glove box where the tiles were removed and stored under an N₂ atmosphere for analysis. Similar experiments were conducted at 623, 673, 723 and 823 K.

LPCVD of Ga(P^tBu₂)₃

In a typical experiment 0.100 g of reagent and silica substrates were loaded into a quartz tube in a glove-box. The tube was then set in a furnace and evacuated, then heated to achieve deposition at 773 K under 0.05 mmHg (66 Pa).

Samples deposited at lower temperatures tended to have a more matt appearance, whereas higher temperatures gave reflective films, and EDX measurements revealed Ga:E ratios closer to 1:1 from the higher temperature depositions. GaAs films obtained were grey, shiny and reflective with powdery regions on substrates closest to the precursor. The majority of the GaP films were yellow or greyish and powdery, but films deposited at higher temperatures (773 K) were yellow, shiny and reflective and these were the ones subjected to more detailed analysis, including photoluminescence measurements. The films selected for further characterisation were generally on substrates located 50-100 mm from the precursor in the quartz tube. Samples were generally very well adhered to the tiles as evidenced by the fact the film remained intact even when removed from an SEM stub to which they had been attached by carbon tape. Excellent reproducibility was obtained and films were visually very similar between depositions conducted at the same temperature. Similar characterisation data were obtained from several different samples.

6.4 References

1. Aksomaityte, G.; Cheng, F.; Hector, A. L.; Hyde, J. R.; Levason, W.; Reid, G.; Smith, D. C.; Wilson, J. W.; Zhang, W. J., *Chem. Mater.* **2010**, *22*, 4246-4253.
2. Cheng, F.; George, K.; Hector, A. L.; Jura, M.; Kroner, A.; Levason, W.; Nesbitt, J.; Reid, G.; Smith, D. C.; Wilson, J. W., *Chem. Mater.* **2011**, *23*, 5217-5222.
3. Arif, A. M.; Benac, B. L.; Cowley, A. H.; Geerts, R.; Jones, R. A.; Kidd, K. B.; Power, J. M.; Schwab, S. T., *J. Chem. Soc. Chem. Comm.* **1986**, 1543-1545.
4. Jones, A. C., *Chem. Soc. Rev.* **1997**, *26*, 101-110.
5. Aldridge, S.; Downs, A. J., *The Group 13 Metals Aluminium, Gallium, Indium and Thallium*. Wiley: Chichester, UK, 2011.
6. Green, M.; O'Brien, P., *J. Mater. Chem.* **2004**, *14*, 629-636.
7. Pickett, N. L.; O'Brien, P., *Chem. Rec.* **2001**, *1*, 467-479.
8. Banerjee, C.; Hughes, D. L.; Bochmann, M.; Nann, T., *Dalton Trans.* **2012**, *41*, 7244-7248.
9. Green, M.; O'Brien, P., *Chem. Commun.* **1998**, 2459-2460.
10. Wells, R.; Gladfelter, W., *J. Cluster Sci.* **1997**, *8*, 217-238.
11. Maury, F.; Constant, G.; Fontaine, P.; Biberian, J. P., *J. Cryst. Growth* **1986**, *78*, 185-188.
12. Maury, F.; Elhammadi, A.; Constant, G., *J. Cryst. Growth* **1984**, *68*, 88-95.
13. Zaouk, A.; Salvétat, E.; Sakaya, J.; Maury, F.; Constant, G., *J. Cryst. Growth* **1981**, *55*, 135-144.
14. Maury, F.; Constant, G., *J. Cryst. Growth* **1983**, *62*, 568-576.
15. Zaouk, A.; Calsou, R.; Constant, G., *Ann. Chim.-Sci. Mat.* **1984**, *9*, 587-592.
16. Maury, F.; Elhammadi, A., *J. Cryst. Growth* **1988**, *91*, 97-104.
17. Elhammadi, A.; Maury, F.; Muller, G.; Bensoam, J.; Constant, G., *Acad. Sci. Paris, Ser. II* **1984**, *299*, 1255-1257.
18. Maury, F.; Constant, G., *Polyhedron* **1984**, *3*, 581-584.
19. Beachley Jr, O. T.; Kopasz, J. P.; Zhang, H.; Hunter, W. E.; Atwood, J. L., *J. Organomet. Chem.* **1987**, *325*, 69-81.
20. Beachley, O. T.; Coates, G. E., *J. Chem. Soc.* **1965**, 3241-3247.
21. Purdy, A. P.; Wells, R. L.; McPhail, A. T.; Pitt, C. G., *Organometallics* **1987**, *6*, 2099-2105.

22. Wells, R. L.; Purdy, A. P.; McPhail, A. T.; Pitt, C. G., *J. Organomet. Chem.* **1988**, *354*, 287-292.
23. Holley, W. K.; Wells, R. L.; Shafieezad, S.; McPhail, A. T.; Pitt, C. G., *J. Organomet. Chem.* **1990**, *381*, 15-27.
24. Wells, R. L.; Holley, W. K.; Shafieezad, S.; McPhail, A. T.; Pitt, C. G., *Phosphorus Sulfur Silicon Relat. Elem.* **1989**, *41*, 15-19.
25. Wells, R. L.; Self, M. F.; McPhail, A. T.; Aubuchon, S. R.; Woudenberg, R. C.; Jasinski, J. P., *Organometallics* **1993**, *12*, 2832-2834.
26. Aubuchon, S. R.; McPhail, A. T.; Wells, R. L.; Giambra, J. A.; Bowser, J. R., *Chem. Mater.* **1994**, *6*, 82-86.
27. Janik, J. F.; Wells, R. L.; Young, V. G.; Rheingold, A. L.; Guzei, I. A., *J. Am. Chem. Soc.* **1998**, *120*, 532-537.
28. Malik, M. A.; Afzaal, M.; O'Brien, P.; Bangert, U.; Hamilton, B., *Mater. Sci. Technol.* **2004**, *20*, 959-963.
29. Malik, M. A.; O'Brien, P.; Helliwell, M., *J. Mater. Chem.* **2005**, *15*, 1463-1467.
30. Miller, J. E.; Kidd, K. B.; Cowley, A. H.; Jones, R. A.; Ekerdt, J. G.; Gysling, H. J.; Wernberg, A. A.; Blanton, T. N., *Chem. Mater.* **1990**, *2*, 589-593.
31. Cowley, A. H.; Jones, R. A., *Polyhedron* **1994**, *13*, 1149-1157.
32. Lakhotia, V.; Heitzinger, J. M.; Cowley, A. H.; Jones, R. A.; Ekerdt, J. G., *Chem. Mater.* **1994**, *6*, 871-874.
33. Arif, A. M.; Benac, B. L.; Cowley, A. H.; Jones, R. A.; Kidd, K. B.; Nunn, C. M., *New J. Chem.* **1988**, *12*, 553-557.
34. Cowley, A. H.; Harris, P. R.; Jones, R. A.; Nunn, C. M., *Organometallics* **1991**, *10*, 652-656.
35. Atwood, D. A.; Atwood, V. O.; Cowley, A. H.; Gobran, H. R.; Jones, R. A.; Smeal, T. M.; Carrano, C. J., *Organometallics* **1993**, *12*, 3517-3521.
36. Cowley, A. H.; Jones, R. A.; Mardones, M. A.; Atwood, J. L.; Bott, S. G., *Angew. Chem. Int. Ed.* **1990**, *29*, 1409-1410.
37. Park, H. S.; Waezsada, S. D.; Cowley, A. H.; Roesky, H. W., *Chem. Mater.* **1998**, *10*, 2251-2257.
38. Neumayer, D. A.; Cowley, A. H.; Decken, A.; Jones, R. A.; Lakhotia, V.; Ekerdt, J. G., *J. Am. Chem. Soc.* **1995**, *117*, 5893-5894.
39. Lakhotia, V.; Neumayer, D. A.; Cowley, A. H.; Jones, R. A.; Ekerdt, J. G., *Chem. Mater.* **1995**, *7*, 546-552.

40. Atwood, D. A.; Cowley, A. H.; Jones, R. A.; Mardones, M. A., *J. Organomet. Chem.* **1993**, *449*, C1-C2.
41. Cowley, A. H.; Jones, R. A.; Nunn, C. M.; Westmoreland, D. L., *Chem. Mater.* **1990**, *2*, 221-222.
42. Majimel, M.; Marre, S.; Garrido, E.; Aymonier, C., *Chem. Vap. Deposition* **2011**, *17*, 342-352.
43. Romang, A. H.; Watkins, J. J., *Chem. Rev.* **2010**, *110*, 459-478.
44. Blackburn, J. M.; Long, D. P.; Cabañas, A.; Watkins, J. J., *Science* **2001**, *294*, 141-145.
45. Long, D. P.; Blackburn, J. M.; Watkins, J. J., *Adv. Mater.* **2000**, *12*, 913-915.
46. O'Neil, A.; Watkins, J. J., *Chem. Mater.* **2006**, *18*, 5652-5658.
47. Wei, Q.; You, E.; Hendricks, N. R.; Briseno, A. L.; Watkins, J. J., *ACS Appl. Mater. Interfaces* **2012**, *4*, 2322-2324.
48. O'Neil, A.; Watkins, J. J., *Chem. Mater.* **2007**, *19*, 5460-5466.
49. Popov, V. K.; Bagratashvili, V. N.; Antonov, E. N.; Lemenovski, D. A., *Thin Solid Films* **1996**, *279*, 66-69.
50. Yang, J.; Hyde, J. R.; Wilson, J. W.; Mallik, K.; Sazio, P. J.; O'Brien, P.; Malik, M. A.; Afzaal, M.; Nguyen, C. Q.; George, M. W.; Howdle, S. M.; Smith, D. C., *Adv. Mater.* **2009**, *21*, 4115-4119.
51. Fletcher, D. A.; McMeeking, R. F.; Parkin, D., Inorganic Crystal Structure Database (ICSD) Fachinformationszentrum Karlsruhe (FIZ), accessed via the United Kingdom Chemical Database Service. In *J. Chem. Inf. Comput. Sci.* , 1996; Vol. 36, p 746.
52. Fu, L.-T.; Chen, Z.-G.; Zou, J.; Cong, H.-T.; Lu, G.-Q., *J. Appl. Phys.* **2010**, *107*, 124321-5.
53. Campos, C. E. M.; Pizani, P. S., *Appl. Surf. Sci.* **2002**, *200*, 111-116.
54. Adachi, S.; Oe, K., *J. Electrochem. Soc.* **1983**, *130*, 2427-2435.
55. Tjerkstra, R. W., *Electrochem. Solid-State Lett.* **2006**, *9*, C81-C84.
56. Madelung, O., *Semiconductors: Data Handbook*. Third ed.; Springer: Berlin, Germany, 2004.

7 Conclusions and Outlook

This thesis aimed to develop the coordination chemistry of Group 13 halides with neutral chalcogenoethers by building on the work that has previously been reported.^{1,2} By having a greater understanding of the coordination complexes that can be formed, it may be possible to use this knowledge to develop better single source precursors for the low pressure chemical vapour deposition of III-VI materials, which are important materials due to their semi-conducting properties and potential as phase change memory materials. This thesis has shown that using acyclic ligands with ⁿBu substituents in place of Me substituents can produce suitable single source precursors in many cases without significantly changing the nature of the coordination complex. Not all coordination complexes are suitable and this appears to be dictated by the strength of the metal-chalcogen bond, which is sufficiently strong in Ga-E (E = Se, Te) but not in Ga-S or Al-E (E = Se, Te) complexes, in which case anionic ligands may be more effective.

Previously, only neutral complexes of GaX₃ (X = Cl, Br, I) with acyclic chalcogenoether ligands with distorted tetrahedral coordination at Ga have been reported, despite using ligands of differing denticities and different metal to ligand ratios.¹ This thesis has found that by using macrocyclic chalcogenoethers, it is possible to access higher coordination numbers and ionic species. The complexes [MCl₂([16]aneE₄)] [MCl₄] (M = Ga, E = S, Se; M = In, E = Se) exhibited octahedral coordination, whereas [GaCl₃([14]aneS₄)] was the first example of a trigonal bipyramidal complex of GaCl₃ with three planar chloride ligands. GaCl₃ was also found to promote the one and two electron oxidation of [8]aneSe₂.

Neutral, selenoether complexes have been used successfully to deposit thin films of metal selenides.³⁻⁵ This thesis has developed this work by demonstrating the use of two precursors for the LPCVD of Ga₂Se₃ ([GaCl₃(ⁿBu₂Se)] and [(GaCl₃)₂{ⁿBuSe(CH₂)₂SeⁿBu}]) and two precursors for the deposition of Ga₂Te₃

([GaCl₃(ⁿBu₂Te)] and [(GaCl₃)₂{ⁿBuTe(CH₂)₃TeⁿBu}]) at 773 K and 0.05 mmHg. This is first reported example of a telluroether complex being used to deposit a metal telluride. This is also the first reported example of a single source precursor for the deposition of Ga₂Te₃ thin films without contamination from Te or GaTe. The films deposited were crystalline and have been shown to be good quality by EDX, XRD and Raman spectroscopy, as well as Hall measurements. Due to the roughness of the films and the inability to deposit good quality, amorphous films from the precursors, however, the phase change memory properties of the films were not tested further.

Literature reports indicate that Ga₂S₃ can undergo a phase change by heating but there is disagreement on the temperature at which this phase change occurs.⁶⁻⁹ [Ga(SⁱPr)₂(μ-SⁱPr)]₂, which has previously been reported as a single source precursor for the LPCVD of Ga₂S₃,^{10, 11} was selected as a suitable precursor as it could deposit Ga₂S₃ at temperatures lower than the reported phase change temperatures. The as-deposited films were found to be cubic (*F*-43*m*) by XRD and could be converted into a monoclinic (*Cc*) phase by annealing at 800 °C. Variable temperature XRD shows that the phase transition occurs between 500 and 600 °C. Laser annealing could also be used to induce a phase change, with higher laser powers converting a higher proportion of the film to the monoclinic phase. The films deposited using this precursor were smoother than the Ga₂Se₃ and Ga₂Te₃ thin films, making them more suitable for device fabrication. Hall measurements on the as-deposited films found that the resistivity was too high to be measured but annealing the films caused the resistivity to decrease.

There has been very limited work reported on the coordination chemistry of AlX₃ with soft donor ligands. This work therefore began by investigating the coordination chemistry of AlX₃ (X = Cl, Br, I) with the monodentate ligands Me₂E (S, Se, Te). These ligands form 1:1 neutral complexes with C_{3v} symmetry at Al. The 5-coordinate species [AlCl₃(Me₂S)₂] was accessed by adding an extra equivalent of Me₂S but this was the only example of a 5-coordinate complex for these systems. [Me₂SH][AlCl₄] was reported as a rare example of a crystallographically characterised sulfonium salt, showing H-bonding to Cl. The use of bidentate ligands produced both neutral complexes ([AlCl₃)₂{*o*-C₆H₄(CH₂SEt)₂}) and 6-coordinate ionic species

$[\text{AlX}_2(\text{MeECH}_2\text{CH}_2\text{EMe})_2][\text{AlCl}_4]$). The tridentate ligand, $\text{MeC}(\text{CH}_2\text{SMe})_3$, did not coordinate to AlCl_3 in the anticipated *fac*-octahedral geometry but instead formed the 1D chain polymer $[\text{AlCl}_3(\text{MeC}(\text{CH}_2\text{SMe})_3)]$. The poor solubility of macrocyclic complexes of AlCl_3 precluded easy characterisation but the formulae of the complexes were confirmed as $[\text{AlCl}_3([\text{9}]ane\text{S}_3)]$, $[\text{AlCl}_2([\text{14}]ane\text{S}_4)][\text{AlCl}_4]$ and $[\text{AlCl}_2([\text{16}]ane\text{Se}_4)][\text{AlCl}_4]$. The identity of $[\text{AlCl}_2([\text{14}]ane\text{S}_4)][\text{AlCl}_4]$ was confirmed by single crystal X-ray diffraction. The Lewis acidity of AlCl_3 was also found to promote ligand fragmentation, producing the previously reported selenonium cation, $[\text{o-C}_6\text{H}_4\text{CH}_2\text{Se}(\text{Me})\text{CH}_2]^+$, and the novel telluronium cation, $[\text{tBuTe}(\text{CH}_2)_3\text{Te}(\text{tBu})\text{Te}(\text{CH}_2)_3\text{Te}(\text{tBu})]^+$. Based on the successful use of GaCl_3 coordination complexes for the deposition of Ga_2E_3 , the analogous complexes, $[\text{AlCl}_3(\text{Bu}_2\text{E})]$ ($\text{E} = \text{Se}, \text{Te}$), were synthesised. These complexes were not suitable single source precursors for the LPCVD of aluminium chalcogenides as no deposition occurred. This is likely due to the weaker Al-E bond strength compared to that of Ga-E.

$[\text{Bu}_2\text{M}(\mu\text{-E}'\text{Bu}_2)_2\text{M}'\text{Bu}_2]$ ($\text{M} = \text{Ga}, \text{In}$; $\text{E} = \text{P}, \text{As}$) have been used for the deposition of thin films of ME *via* supercritical chemical fluid deposition with better quality films obtain for InE than GaE.¹² These precursors had also been investigated as precursors for the LPCVD of InE with limited success. This work aimed to use $[\text{Bu}_2\text{Ga}(\mu\text{-E}'\text{Bu}_2)_2\text{Ga}'\text{Bu}_2]$ ($\text{E} = \text{P}, \text{As}$) to deposit GaE *via* LPCVD to compare with the previous work. Good quality films of GaP and GaAs were obtained at 773 K. The films were characterised by XRD, Raman, SEM and EDX spectroscopy, AFM and photoluminescence. The direct band gap of the GaP thin films was found to match the literature, whereas the GaAs thin films exhibited some sub-band gap luminescence

This thesis has demonstrated that the coordination chemistry of the Group 13 halides with neutral chalcogenoether ligands is varied with a wide range of chemistry accessible by choosing the appropriate ligand. It is also possible to design coordination complexes that can be used as single source precursors for the LPCVD of gallium chalcogenides. Further work is required in order to optimise the precursors for the deposition of thin films that are suitable for device fabrication. The Ga_2Se_3 and Ga_2Te_3 thin films have promising electronic characteristics (resistivity) whereas Ga_2S_3 films are significantly

smoother and can easily be annealed by heat or laser power to undergo a phase change. Future work should aim to develop a precursor that deposits films with the best characteristics of the Ga₂E₃ (E = Se, Te) and Ga₂S₃ films reported in this thesis. A gallium selenolate or tellurolate based precursor may be a suitable precursor to investigate for this purpose.

References

1. Gurnani, C.; Levason, W.; Ratnani, R.; Reid, G.; Webster, M., *Dalton Trans.* 2008, 6274-6282.
2. Gurnani, C.; Jura, M.; Levason, W.; Ratnani, R.; Reid, G.; Webster, M., *Dalton Trans.* 2009, 1611-1619.
3. de Groot, C. H.; Gurnani, C.; Hector, A. L.; Huang, R.; Jura, M.; Levason, W.; Reid, G., *Chem. Mater.* 2012, 24, 4442-4449.
4. McKarns, P. J.; Lewkebandara, T. S.; Yap, G. P. A.; Liable-Sands, L. M.; Rheingold, A. L.; Winter, C. H., *Inorg. Chem.* 1998, 37, 418-424.
5. Hector, A. L.; Jura, M.; Levason, W.; Reid, S. D.; Reid, G., *New J. Chem.* 2009, 33, 641-645.
6. Hahn, H.; Frank, G., *Z. Anorg. Allg. Chem.* 1955, 278, 333-339.
7. Collin, G.; Flahaut, J.; Guittard, M.; Loireau-Lozach, A.-M., *Mater. Res. Bull.* 1976, 11, 285-292.
8. Goodyear, J.; Steigmann, G. A., *Acta Crystallogr.* 1963, 16, 946-949.
9. Pardo, M. P.; Tomas, A.; Guittard, M., *Mater. Res. Bull.* 1987, 22, 1677-1684.
10. Suh, S.; Hardesty, J. H.; Albright, T. A.; Hoffman, D. M., *Inorg. Chem.* 1999, 38, 1627-1633.
11. Suh, S.; Hoffman, D. M., *Chem. Mater.* 2000, 12, 2794-2797.
12. Aksomaityte, G.; Cheng, F.; Hector, A. L.; Hyde, J. R.; Levason, W.; Reid, G.; Smith, D. C.; Wilson, J. W.; Zhang, W. J., *Chem. Mater.* 2010, 22, 4246-4253.

Appendix 1 – General Experimental Techniques

All reactions were conducted using Schlenk, vacuum line and glove-box techniques under a dry nitrogen atmosphere. The reagents were stored and manipulated using a glove box with a dry N₂ atmosphere. Solvents were dried and degassed prior to use. Et₂O and thf were distilled over Na/benzophenone ketyl; hexane, toluene and benzene were distilled over Na wire; CH₂Cl₂, CHCl₃ and MeCN were distilled over CaH; acetone was dried over molecular sieves (4 Å). Reagents were purchased from Sigma-Aldrich, Strem or Alfa Aesar and used as received. [8]aneSe₂, [16]aneSe₄, [24]aneSe₆, ⁿBu₂Se, ⁿBu₂Te, Me₂Te and LiP^tBu₂ were prepared by literature methods.¹⁻³ *o*-C₆H₄(CH₂SEt)₂, MeC(CH₂SMe)₃, ⁿBuTe(CH₂)₃TeⁿBu, MeSe(CH₂)₂SeMe, ⁿBuSe(CH₂)₂SeⁿBu, *o*-C₆H₄(CH₂SeMe)₂ were available in the laboratory, having been previously prepared by other group members by literature methods.^{2, 4-6} [(GaCl₃)₂{ⁿBuSeCH₂CH₂SeⁿBu}], [GaCl₃(TeMe₂)], [ⁿBu₂Ga(E^tBu₂)₂GaⁿBu₂] (E = P, As) and [Ga(P^tBu₂)₃] were prepared by literature methods.^{7, 8} The preparation of other ligands and precursors is described in the experimental text.

Good laboratory practice was followed at all times, including the use of fume cupboards to handle volatile or hazardous substances, and the use of appropriate personal protective equipment. Organo-phosphorus, -arsenic, -selenium and -tellurium compounds are toxic, and were handled with care in small quantities, being treated with aqueous sodium hypochlorite prior to disposal. Organic residues were separated into those containing chlorinated and unchlorinated solvents and sent away for incineration. Aqueous residues were washed down the sink in dilute form.

Reagent and complex characterisation

Infrared spectra were recorded over the range 4000-200 cm⁻¹ using a Perkin-Elmer Spectrum 100 spectrometer. Samples were prepared as Nujol mulls (unless otherwise stated) between CsI plates. Raman spectra were obtained using a Perkin-Elmer FT2000R with a Nd:YAG laser. NMR spectra were recorded using Bruker AV300 or DPX400 spectrometers. ¹H and ¹³C spectra were referenced to the solvent resonance, ²⁷Al to aqueous [Al(H₂O)₆]³⁺, ³¹P{¹H} to 85% H₃PO₄, ⁷¹Ga to aqueous [Ga(H₂O)₆]³⁺ at pH = 1,

^{77}Se to Me_2Se , ^{115}In to aqueous $[\text{In}(\text{H}_2\text{O})_6]^{3+}$ at $\text{pH} = 1$, ^{125}Te to Me_2Te . Microanalyses were undertaken by Medac Ltd or London Metropolitan University. Electrospray (ES) MS data were obtained from solutions in MeCN using a VG Biotech Platform. Single crystal X-ray data were collected using two different systems: a Bruker-Nonius Kappa CCD diffractometer with molybdenum FR591 rotating anode, monochromated using 10cm confocal mirrors, or a Rigaku AFC12 goniometer equipped with an enhanced sensitivity (HG) Saturn724+ detector mounted at the window of an FR-E+ SuperBright molybdenum rotating anode generator with HF or VHF Varimax optics. All used Mo-K α radiation ($\lambda = 0.71073 \text{ \AA}$). Crystals were held at either 120 K or 100 K under a nitrogen gas stream (Oxford Cryostream). Solution and refinement of structures was carried out as standard using SHELX-97,⁹⁻¹¹ with hydrogen atoms added to the model in calculated positions using default C-H distances. Where additional restraints were required, details are provided in the cif file for each structure.

Thin film characterisation (Chapters 3 and 4)

XRD patterns were collected in grazing incidence ($\theta_I = 5^\circ$) using Bruker D8 with GADDS and Rigaku SmartLab diffractometers (both Cu-K α_1). *In situ* annealing experiments were done using a Rigaku SmartLab diffractometer in Theta/2Theta geometry, using an Anton Paar HTK hot stage under a He atmosphere. Raman scattering spectra of the deposited films were measured at room temperature on a Renishaw InVia Micro Raman Spectrometer using a helium-neon laser with a wavelength of 532 nm. The incident laser power was adjusted to ~1 mW for all samples. Scanning electron microscopy (SEM) was performed on samples at an accelerating voltage of 10 kV using a Zeiss EVO LS 25, and energy dispersive X-ray (EDX) data were obtained with an Oxford INCAx-act X-ray detector. The cross-section SEM measurements were carried out with a field emission SEM (Jeol JSM 7500F) at an accelerating voltage of 2 kV. Atomic force microscopy (AFM) was conducted using a Veeco Dimension 3100 in tapping mode. Hall measurements were performed at room temperature on a Nanometrics HL5500PC with a current of 1 mA. Hall measurements, Raman spectroscopy and some EDX and SEM measurements were carried out by Mr Ruomeng Huang in Electronics and Computer Science at the University of Southampton. TGA measurements used a Mettler-Toledo TGA851e mounted in a glove box for air-sensitive material handling. The scan rate was 10 degrees per minute.

Thin film characterisation (Chapter 6)

SEM was performed on gold coated samples at an accelerating voltage of 20 kV using a JEOL JSM 5910 and EDX data on carbon coated samples were obtained with an Oxford INCA300 detector. Raman measurements were taken at an excitation energy of 3.09 eV, which was produced by a Coherent Inc. mode locked Mira 900 Ti:sapphire laser and Second Harmonic Generator (SHG) by Mr John Nesbitt. The bandwidth of the pulses was 0.30 nm which were produced at a repetition rate of 80 MHz. The Raman microscope was set up in a co-linear alignment where an OLYMPUS LMPlan50xIR objective was used to focus an 8 mW beam to a spot size of $\approx 1 \mu\text{m}^2$ on the sample and subsequently collect the scattered Raman light. The Raman signal was detected with a Princeton Instruments Pi-Action TriVista triple spectrometer fitted with a Roper Scientific ST133B nitrogen cooled CCD. Photoluminescence measurements were made with a 405 nm excitation from a diode laser (Sanyo, DL-3146-151) by Mr John Nesbitt. A power density of 8.7 W cm^{-2} was used. The emission was collected and collimated by 0.25 NA lens, passed through a 45° laser line mirror (CVI TLM1-400-45P-2037) to remove the intense laser light, and then focused into an optical fibre and analysed using a UV-visible spectrometer (Ocean Optics, HR4000). The throughput of the system was corrected for using a fibre coupled tungsten-halogen white light source placed at the position of the sample. Atomic force microscopy was conducted using a Veeco Dimension 3100 in tapping mode. Absorption spectra were recorded using the diffuse reflectance attachment of a Perkin Elmer Lambda19 spectrometer. XPS data were obtained using a Scienta ESCA300 photoelectron spectrometer with a rotating anode Al K_α ($h\nu = 1486.7 \text{ eV}$) X-ray source at the National Centre for Electron Spectroscopy and Surface Analysis (NCESS), Daresbury Laboratory, U.K. Samples were etched using argon ion bombardment for 300 s at 3 keV. Where necessary, sample charging was eliminated by use of an electron flood gun delivering 5 eV electrons. The Ga 2p and 3p, As 2p and 3p, P 2s and 2p, C 1s and O 1s spectra were collected. The CasaXPS package was used for data analysis. Data were referenced to the C 1s peak, which was assigned a binding energy of 284.8 eV.

Substrate preparation

Substrates were fabricated by Mr Ruomeng Huang (unless otherwise stated). TiN films with thickness of 50 nm were deposited on a p-type Si (100) wafer by the medium

frequency plasma assisted magnetron sputtering method (Leybold HELIOS Pro) at room temperature. This process combines reactive middle frequency sputtering with an additional RF plasma source. During each rotation of the plate holding the substrate, a thin layer of Ti was deposited from dual magnetron metal targets (99.99 % purity) using a power of 3000 W in an Ar atmosphere. The thin film was then transformed into a nitride layer by passing the substrate underneath the N₂ plasma of the RF source. The N₂ and Ar flow rates were maintained at 30 and 35 sccm respectively and a high drive speed of 180 rpm was applied to enhance the film uniformity. The deposition rate was found to be 0.161 nm s⁻¹. SiO₂ films with thickness of 1 μm were also deposited by medium frequency dual magnetron sputtering using pure Si targets (99.99% purity) at a MF magnetron power of 4350 W in an O₂/Ar atmosphere. The O₂ and Ar flow rates were maintained at 20 and 40 sccm, respectively. The layer was then further oxidized using an O₂ plasma in the additional RF plasma source operating at 2000 W with an O₂ flow rate of 30 sccm. A drive speed of 180 rpm yielded a deposition rate of 0.3 nm s⁻¹. The patterned samples were fabricated via a photolithographic process followed by a reactive-ion etching of SiO₂. The pattern was pre-designed on a mask with template hole-sizes ranging from 1 μm to 100 μm. The photolithography was carried out using an EVG 620TB with a positive resist S1813. The etching was performed by a RIE80+ with CHF₃ and Ar. The etching rate was found to be 0.37 nm s⁻¹.

The silica tile substrates (*ca.* 1 × 5 × 25 mm) were obtained commercially. Prior to deposition, they were cleaned with acetone and deionized water and dried at 100°C overnight. The TiN and patterned TiN/SiO₂ substrates were cleaned by dipping into acetone and isopropanol for 15 minutes each.

Furnace temperature profiling

Furnace temperature was profiled at all deposition temperatures in order to establish the temperature in the hot zone. A temperature probe was inserted into a CVD tube, which was mounted in the tube furnace. The tube furnace was set to the desired temperature and the temperature of the furnace measured at 10 mm intervals by moving the temperature probe and allowing it to equilibrate before recording the temperature.

References

1. Batchelor, R. J.; Einstein, F. W. B.; Gay, I. D.; Gu, J. H.; Johnston, B. D.; Pinto, B. M., *J. Am. Chem. Soc.* **1989**, *111*, 6582-6591.
2. Brodersen, K.; Rölz, W.; Jordan, G.; Gerbeth, R.; Ellermann, J., *Chem. Ber.* **1978**, *111*, 132-142.
3. Kuhn, N.; Faupel, P.; Zauder, E., *J. Organomet. Chem.* **1986**, *302*, C4-C6.
4. Levason, W.; Nirwan, M.; Ratnani, R.; Reid, G.; Tsoureas, N.; Webster, M., *Dalton Trans.* **2007**, 439-448.
5. Hope, E. G.; Kemmitt, T.; Levason, W., *Organometallics* **1987**, *6*, 206-207.
6. Gulliver, D. J.; Hope, E. G.; Levason, W.; Murray, S. G.; Potter, D. M.; Marshall, G. L., *J. Chem. Soc. Perk. Trans. 2* **1984**, 429-434.
7. Gurnani, C.; Levason, W.; Ratnani, R.; Reid, G.; Webster, M., *Dalton Trans.* **2008**, 6274-6282.
8. Arif, A. M.; Benac, B. L.; Cowley, A. H.; Geerts, R.; Jones, R. A.; Kidd, K. B.; Power, J. M.; Schwab, S. T., *J. Chem. Soc. Chem. Comm.* **1986**, 1543-1545.
9. Sheldrick, G. M., *SHELXS-97, program for crystal structure solution* **1997**, University of Göttingen, Germany.
10. Sheldrick, G. M., *SHELXL-97, program for crystal structure refinement* **1997**, University of Göttingen, Germany.
11. Flack, H. D., *Acta Crystallogr. Sect. A* **1983**, *39*, 876-881.